Binary Neutron Star Merger Simulations

DISSERTATION

zur Erlangung des akamedischen Grades
doctor rerum naturalium (Dr. rer. nat.)

seit 1558

vorgelegt dem Rat der
PHYSIKALISCH-ASTRONOMISCHEN FAKULTÄT
der
FRIEDRICH-SCHILLER-UNIVERSITÄT JENA
von

Tim Dietrich (M.Sc.)
geboren am 23.04.1988 in Dessau

Gutacher:

1. Prof. Dr. Bernd Brügmann (Friedrich-Schiller-Universität Jena)
2. Prof. Dr. Stephan Rosswog (Stockholm University)
3. Prof. Dr. Mark Hannam (Cardiff Univeristy)

Tag der Disputation: 26.01.2016

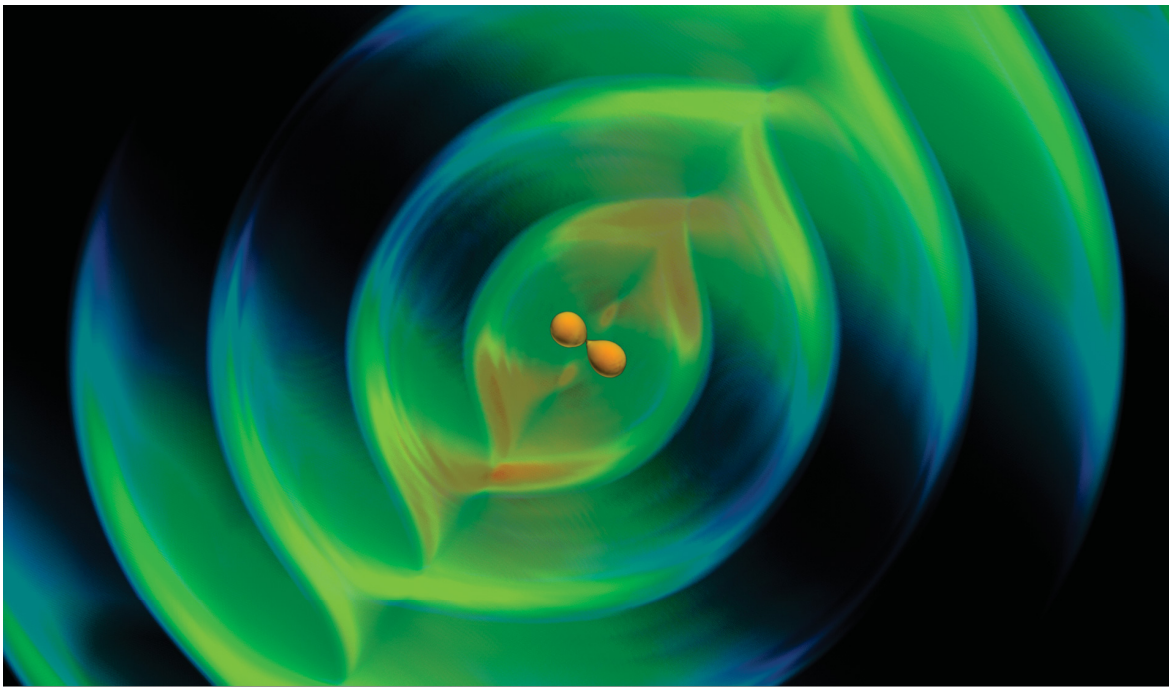

Visualization of the Gravitational wave signal (curvature scalar Ψ_4) and the density profile of a binary neutron star merger simulation.

The same system is also shown in the flip-book in the upper right corners.

Abbreviations and Notation

Throughout this work geometrized units are employed with $c = G = M_\odot = 1$. In some cases, $c, G, M_\odot$ are given explicitly for better understanding. We use Greek letters for four-dimensional indices running from 0 to 3 and Latin letters for three-dimensional indices running from 1 to 3.

We refer to most references using the first authors and the year of publication, except for references to our own publications for which we use Arabic numerals.

The following abbreviations are used throughout the thesis, in most cases these abbreviations are also introduced in the text at their first appearance:

ADM	Arnowitt-Deser-Misner
AMR	Adaptive Mesh refinement
BAM	Bi-functional Adaptive Mesh (code name)
BBH	Binary black hole
BC	Berger-Collela
BH	Black hole
BNS	Binary neutron star
BO	Berger-Oliger
BSSN	Baumgarte-Shapiro-Shibata-Nakamura
CFL	Courant-Friedrichs-Lewy
CRV	Constant rotational velocity
CTS	Conformal thin-sandwich
ENO	Essentially non-oscillatory
EOB	Effective-one-body
EOS	Equation of state
GRHD	General relativistic hydrodynamics
GW	Gravitational wave
HMNS	Hypermassive neutron star
LIGO	Laser Interferometer Gravitational Wave Observatory
LORENE	Langage objet pour la relativité numérique (code name)

LSO	Last stable orbit
MNS	Massive neutron star
NLO	Next-to-leading order
NNLO	Next-to-next-to-leading order
NQC	Next-to-quasi-circular
NR	Numerical relativity
P	Prolongation
PDE	Partial differential equation
PN	Post-Newtonian
PSD	Power spectral density
R	Restriction
RHS	Right hand side
RNS	Rapidly Rotating Neutron Star (code name)
SMNS	Supramassive neutron star
TOV	Tolman-Oppenheimer-Volkoff
WENO	Weighted essentially non-oscillatory

Abstract

Binary neutron star mergers are associated with a variety of observable phenomena in the gravitational and electromagnetic spectra and are of great importance in a number of different physical subjects, e.g. high energy and gravitational physics. In this thesis, we are investigating binary neutron star systems in the last milliseconds before and after their merger. In such systems gravity is strong and has to be described by Einstein's full Theory of General Relativity. Because of the complexity of the governing equations of general relativity and relativistic hydrodynamics no analytical solutions exist. Thus, the usage of numerical methods is inevitable.

Throughout the thesis we consider different configurations by varying the spin, the equation of state, and the mass-ratio. In particular, we present the first consistent, constraint solved simulations of spinning binary neutron stars in full general relativity and the highest mass ratios simulated to date. Additionally, new numerical methods were implemented in the existing BAM code, most notably a refluxing algorithm which ensures mass conservation across mesh refinement boundaries. This algorithm allowed us to perform the most accurate simulations of the gravitational collapse of a rotating neutron star.

In addition to pure numerical waveform modeling, we used high-resolution simulations to validate an improved tidal effective-one-body model and show that the new formalism can predict the waveform accurately up to the moment of merger. Furthermore, the effective-one-body model predicts quasi-universal relations, which we found also in full general relativistic simulations for the inspiral and even in the postmerger phase.

Contents

1 Introduction **3**

2 Basic Equations and Numerical methods **7**
2.1 Numerical relativity in a nutshell 7
2.1.1 3+1-Decomposition 7
2.1.2 Slicing conditions 9
2.1.3 Einstein's Field Equations in 3+1-form 10
2.1.4 Hydrodynamical equations 15
2.2 Numerical methods 18
2.2.1 Method of Lines 18
2.2.2 Flux computation and shock capturing methods 20
2.2.3 Primitive reconstruction and atmosphere treatment 21
2.2.4 Adaptive mesh refinement 22

3 Rotating neutron star collapse **27**
3.1 Collapse dynamics 27
3.2 Gravitational waveform 29
3.3 The end state: a spinning trumpet 33

4 Spinning neutron stars in the CRV-approach **35**
4.1 Construction of constant rotational velocity stars 35
4.2 Single CRV-stars 39
4.3 Binaries within the CRV-approach 42
4.4 Spinning neutron star evolutions 46
4.4.1 Orbital motion 47
4.4.2 Merger remnant 51
4.4.3 Gravitational radiation 55

5 BNS mergers for different EOSs and mass-ratios **59**
5.1 Influence of the EOS and the mass ratio 60
5.1.1 Assessment of conservative AMR 66
5.1.2 Ejecta 67

5.1.3 Gravitational waves 68
5.2 A stiff $1.0M_\odot - 1.5M_\odot$ binary 70
5.3 A $q = 2.06$ configuration 75

6 Gravitational waveform modeling **81**
6.1 The Effective-One-Body model 81
6.1.1 Basics of the EOB model 81
6.1.2 Tidal EOB models 83
6.1.3 Comparison of the Tidal EOB model and numerical results . . 86
6.2 Quasi-universal relations in BNS simulations 90
6.2.1 The late inspiral and merger 91
6.2.2 The post-merger spectrum 94

7 Conclusion **97**

A Simulation analysis **101**
A.1 Gravitational wave extraction 101
A.2 Merger and post-merger analysis 101

B Testbeds for the conservative mesh refinement **105**

C Numerical flux computation tests **111**
C.1 Flux computation and reconstruction algorithms 112
C.1.1 Higher-order LLF scheme 112
C.1.2 Reconstruction algorithm 113
C.2 Single star tests 114
C.3 Binary neutron stars 117

D SGRID **123**
D.1 Grid configuration 123
D.2 Iteration procedure 124
D.3 Code novelties 125

Bibliography **127**

Publications **143**

Additional Material **147**

Chapter 1

Introduction

Binary neutron star (BNS) mergers are extreme events associated with a large variety of observable phenomena in the gravitational and electromagnetic spectra, e.g. [Eichler et al., 1989; Andersson et al., 2013; Rosswog, 2015]. The coalescence is primarily driven by the emission of gravitational waves (GWs), which carry away energy, linear momentum and angular momentum, such that the two objects orbit around each other until they finally merge. Although there is indirect evidence for the existence of GWs by the radio observation of double pulsars [Hulse and Taylor, 1975; Weisberg et al., 2010; Burgay et al., 2003; Lyne et al., 2004; Kramer et al., 2006], the direct detection of a GW signal is still pending.

The expected GW signal emitted during the final stages of the coalescence, merger and post-merger lies in parts within the band of the advanced ground-based laser interferometer LIGO [LIGO] and Virgo [VIRGO], which start to operate at sensitivities where detections are expected in the near future [Abadie et al., 2010; Aasi et al., 2013]. These experiments will be followed by the Kamioka GW Detector (KAGRA) [KAGRA], LIGO-India [IND], and, later, by the eLISA mission [Amaro-Seoane et al., 2012; LISA] and the Einstein telescope [ET]. One of the most promising sources for the first detection of GWs are BNS mergers. Advanced configurations of LIGO/Virgo will see BNS mergers up to a distance of ~ 200 Mpc, corresponding to 0.4 to 400 events per year [Abadie et al., 2010; Aasi et al., 2013]. Even though these systems can radiate up to $\sim 10\%$ of their total mass-energy in GWs [Hemberger et al., 2013], the signals one expects to receive on Earth are still weak and hard to measure. Accurate templates for the GWs are therefore urgently required in order to be able to detect them in the detector's noise. Furthermore, after one has made a detection, these templates also allow to infer the properties of the source from its waveform.

When the binary's components are well-separated, analytical models, e.g. the post-Newtonian expansion [Blanchet, 2014], can generate these template waveforms. However, for the last few orbits even high-order post-Newtonian descriptions are too inaccurate and a full numerical solution of the non-linear field equations is needed

to develop accurate templates or to tune and validate analytical approximations like the effective-one-body (EOB) model [Buonanno and Damour, 1999]. Directly after merger, no accurate analytical description of the system exists at all.

BNS mergers result most likely in a supramassive or hypermassive neutron star supported by differential rotation and thermal pressure. Usually this star oscillates until it collapses into a black hole or forms a stable differentially rotating neutron star. Until the final stable configuration is reached GWs are emitted. The waves convey unique information about the sources, and in particular, they allow the measurement of masses, spins, and the unknown equation of state (EOS) of dense, cold nuclear matter [Read et al., 2009b; Damour et al., 2012b; Del Pozzo et al., 2013].

In addition to GWs we expect several electromagnetic counterparts during and following BNS mergers. Thus, the joint observations of the gravitational and electromagnetic emissions would maximize the scientific outcome [Metzger and Berger, 2012]. In particular, neutron star mergers are usually associated with short-gamma ray bursts and afterglows [Paczynski, 1986; Eichler et al., 1989]. Although the precise injection mechanism is not identified, BNS mergers are the most plausible triggers of these powerful events. Furthermore, ejecta from BNS mergers are very likely the origin of heavy nuclei ($A \gtrsim 140$) via rapid neutron-capture processes [Lattimer and Schramm, 1974; Rosswog et al., 1999; Goriely et al., 2011]. The radioactive decay of some of these newly produced heavy elements is likely to lead to strong electromagnetic transients called kilonova (or macronova) events [Li and Paczynski, 1998; Metzger et al., 2010; Tanvir et al., 2013; Yang et al., 2015]. A large amount of energy is also released in form of neutrinos, produced by the merger remnant either via shocks [Waxman, 2004; Dermer and Holmes, 2005] and neutron-rich outflows [Bahcall and Meszaros, 2000], or, in case of low energy neutrinos, in the hot dense regions of the hypermassive neutron star [Dessart et al., 2009; Perego et al., 2014]. Unfortunately, because of the steep energy dependence of the interaction cross sections and their energies of ~ 20 MeV neutrinos are hard to detect.

BNS mergers can be modeled by general relativistic hydrodynamics simulations in dynamical spacetimes, i.e. by solving the full set of Einstein's field equations coupled to the equations governing the matter fields. These simulations are computationally challenging and need to run on high performance computing facilities.

General relativistic simulations are typically performed in the framework of 3+1 numerical relativity using finite volume or finite differencing methods on Cartesian grids, and explicit time evolutions, see [Faber and Rasio, 2012] for a review about BNS merger simulations. Over the last years BNS simulations were improved significantly, notably by including more realistic equations of state from piecewise polytropes [Shibata et al., 2005] to finite temperature EOSs [Sekiguchi et al., 2011b; Sekiguchi

et al., 2011a], ideal and resistive magnetohydrodynamics [Anderson et al., 2008; Liu et al., 2008; Giacomazzo et al., 2009; Kiuchi et al., 2014a; Dionysopoulou et al., 2015], and neutrino cooling [Sekiguchi et al., 2011b; Galeazzi et al., 2013; Sekiguchi et al., 2015], some simulations include most of these improvements at once [Neilsen et al., 2014; Palenzuela et al., 2015].

Two important ingredients for most simulations are (i) a reliable adaptive mesh refinement strategy and (ii) a robust treatment of the shocks and discontinuities, which can occur in BNS merger simulations. Also finite element [Sopuerta et al., 2006; Sopuerta and Laguna, 2006], pseudo-spectral [SpEC; Tichy, 2006], and discontinuous Galerkin methods [Radice and Rezzolla, 2011], [Die14] start to play a role in general relativistic simulations.

The following thesis deals with the numerical investigation of BNS mergers employing the general relativistic BAM code and is organized as follows: In chapter 2, the most important equations and numerical methods are introduced. We describe in detail the mesh refinement strategy, which was improved during the PhD thesis [Die8]. In chapter 3 we perform a detailed study of the rotating neutron star collapse [Die7] based on the most accurate simulations to date. The emitted GW signal is discussed and we compare the spacetime with results obtained from pure vacuum evolutions [Die9].

We continue in chapter 4 with the investigation of spinning neutron stars and review the constant rotational velocity approach of [Tichy, 2011] and discuss single stars and binaries in this approach under the assumption of conformal flatness [Die13]. Furthermore, the first dynamical simulations of BNS systems [Die6] with astrophysical reasonable spins are presented.

In chapter 5 we discuss the influence of the EOS and the mass ratio. We perform a large number of equal and unequal mass simulations including a $1.0M_\odot - 1.5M_\odot$ and a $0.94M_\odot - 1.94M_\odot$ configuration; see [Die8; Die13]. The dynamical ejecta mechanism is studied in detail. Additionally, we use these simulations to test the conservative mesh refinement algorithm in BNS merger simulations.

In chapter 6 gravitational waveforms obtained by our numerical simulations are compared with results of the effective-one-body model [Die2] and we prove that the quasi-universal relations, predicted by the effective-one-body model during inspiral and merger, exist also in full general relativity simulations [Die1; Die10] and are even present beyond the moment of merger [Die3].

For additional information we include in the appendix important quantities for the analysis of our simulations, single neutron star test beds for the conservative mesh refinement [Die8], a discussion about different flux computation methods [Die15], and a short description of the SGRID code [Die13].

For further results obtained during this thesis, we refer the reader to the published articles, see e.g., [Die13] for the first-precessing BNS merger simulation; [Die14] for a discontinuous Galerkin implementation in BAMPS; [Die5] for a description of the GW collapse of self-interacting gravitational fields or [Die4; Die9] for studies about the moving puncture approach in axisymmetry which started already during the Master thesis and were finalized during the PhD thesis. We do not present these results here because of the restrictive page limit and to focus uniquely on BNS mergers or closely related topics.

Chapter 2

Numerical Relativity: Basic Equations and Numerical Methods

Within this thesis we perform numerical simulations of compact objects. To allow such simulations, we have to recast Einstein's field equations in a suitable form. This procedure will be described in the first part of the chapter, Sec. 2.1, where we summarize important equations for numerical relativity (NR) simulations. We will not discuss the underlying principles of Einstein's theory of General Relativity and refer the reader to the textbooks of [Misner et al., 1973; Wald, 1984; Schutz, 1985; d'Inverno, 1992; Carroll, 2003]. In Sec. 2.2, the second part of this chapter, we describe shortly the most important numerical methods employed in this work.

2.1 Numerical relativity in a nutshell

Einstein's field equations

$$G_{\mu\nu} = R_{\mu\nu} - \frac{1}{2} R g_{\mu\nu} = 8\pi T_{\mu\nu} \tag{2.1}$$

are written down in a fully covariant way. But, for numerical simulations it is preferable to perform dynamical simulations of given initial data in time. One approach to achieve this is the *3+1 decomposition*, i.e. the foliation of the four-dimensional manifold by three-dimensional spacelike hypersurfaces, see e.g. [Alcubierre, 2008; Baumgarte and Shapiro, 2010; Gourgoulhon, 2012; Rezzolla and Zanotti, 2013] for detailed textbook explanations.

2.1.1 3+1-Decomposition

Given an n-dimensional manifold $\mathcal{M}$, we can define a hypersurface of $\mathcal{M}$ as an $(n-1)$ - dimensional submanifold Σ of $\mathcal{M}$ with the embedding $\Phi : \hat{\Sigma} \to \mathcal{M}$, where $\hat{\Sigma}$ denotes an $(n-1)$ -dimensional manifold; cf. [Gourgoulhon, 2012]. In this context, it is possible to foliate $\mathcal{M}$ by hypersurfaces, if there exists a smooth scalar function t on

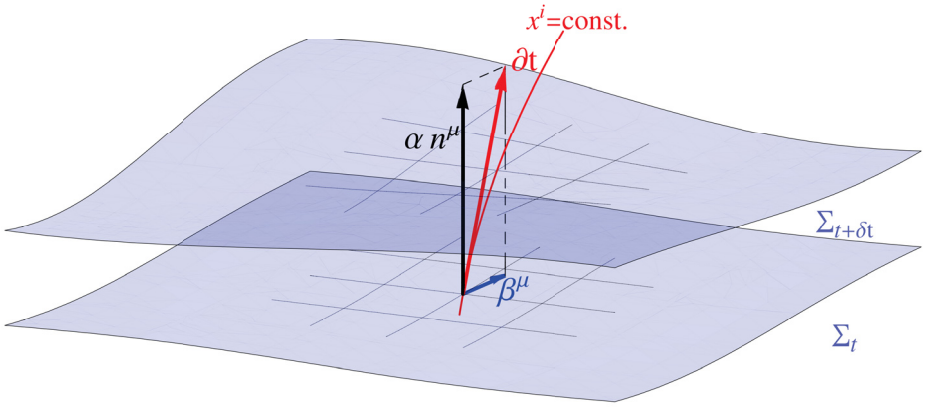

Figure 2.1: Visualization of the foliation of the four-dimensional manifold $\mathcal{M}$ by three-dimensional hypersurfaces Σ_t. On each hypersurface we introduced coordinates x^i. The lapse α and shift β^μ determine the change of the coordinates from Σ_t to $\Sigma_{t+\delta t}$.

$\mathcal{M}$ with a non-zero gradient such that every level surface is a hypersurface (Fig. 2.1).

The parameter t can be interpreted as the coordinate time on the hypersurface $\Sigma_t = \Sigma(t)$. The normal vector to $\Sigma(t)$ is given by

$$n_\mu = -\alpha \nabla_\mu t. \tag{2.2}$$

From the normalization condition of timelike vectors, one gets $\alpha^2 = -1/g^{tt}$. We restrict $\alpha > 0$ to ensure that n^μ is future directed. The proportionality constant α is typically called *lapse* function [Wheeler, 1964]. With the help of the normal vector n^μ, we define the associated metric on the hypersurface $\Sigma(t)$

$$\gamma_{\mu\nu} = g_{\mu\nu} + n_\mu n_\nu \tag{2.3}$$

and the corresponding inverse

$$\gamma^{\mu\nu} = g^{\mu\nu} + n^\mu n^\nu. \tag{2.4}$$

The coordinates x^i of $\Sigma(t)$ can be generalized to $x^\mu = (t, x^i)$, i.e. to a coordinate system in $\mathcal{M}$.

At each point x^μ we define the difference between the normal vector n^μ and ∂_t as the *shift* vector β^μ (blue vector in Fig. 2.1). The normal vector and co-vector expressed in a coordinate basis as functions of the shift β^μ and the lapse α are

$$n^\mu = \left(\frac{1}{\alpha}, -\frac{\beta^i}{\alpha}\right), \tag{2.5}$$

$$n_\mu = (-\alpha, 0, 0, 0)\,. \tag{2.6}$$

Inserting equation (2.6) in (2.3) leads to the four-dimensional line element in 3+1-form:

$$\mathrm{d}s^2 = (-\alpha^2 + \beta_i\beta^i)\mathrm{d}t^2 + 2\beta_i \mathrm{d}t\mathrm{d}x^i + \gamma_{ij}\mathrm{d}x^i\mathrm{d}x^j. \tag{2.7}$$

Additionally, we introduce the extrinsic curvature, which characterizes the embedding of the hypersurface Σ in $\mathcal{M}$:

$$K_{\mu\nu} = -P^\sigma_\mu \nabla_\sigma n_\nu, \tag{2.8}$$

where we used the spatial projection operator $P^\mu_\nu = \delta^\mu_\nu + n^\mu n_\nu$, which enforces that $K_{\mu\nu}$ is purely spatial. In general, every tensor can be split in a purely spatial part (i.e. contained completely in $\Sigma(t)$) by the spatial projection operator P^μ_ν and a purely timelike part by the operator $N^\mu_\nu = -n^\mu n_\nu$.

2.1.2 Slicing conditions

The slicing condition defines the particular foliation of the spacetime. The choice is crucial for a successful simulation. Singularities inside black holes, gauge shocks[1], and slice stretching (e.g. [Reimann, 2004; Reimann, 2005]) have to be avoided. Furthermore, one has to ensure that the evolution system combined with the slicing conditions builds a well-posed partial differential equation (PDE) problem to enable a stable numerical setup.

A widely used condition is the Bona-Massó slicing [Bona et al., 1995]

$$(\partial_t - \mathcal{L}_{\boldsymbol{\beta}})\alpha = -\alpha^2 f(\alpha) K, \tag{2.9}$$

with $f > 0$, where $\mathcal{L}_{\boldsymbol{\beta}}$ denotes the Lie-derivative along $\boldsymbol{\beta}$ and K is the trace of the extrinsic curvature. It is important to mention that Eq. (2.9) together with the Bona-Massó reformulation of Einstein's field equations build a hyperbolic system [Bona et al., 1995; Bona et al., 1997]. No gauge shocks occur [Alcubierre, 1997; Alcubierre, 2003] if

$$1 - f(\alpha) - \frac{\alpha}{2}\frac{\mathrm{d}f}{\mathrm{d}\alpha} = 0, \tag{2.10}$$

and spacetime singularities are avoided for $n < 0$, when $f \propto \alpha^n$, see [Bona et al., 1997]. We summarize different examples of the Bona-Massó slicing condition in Tab. 2.1.

In this thesis we will use exclusively the 1+log-slicing condition

$$(\partial_t - \mathcal{L}_{\boldsymbol{\beta}})\alpha = -2\alpha K, \tag{2.11}$$

due to the fact that singularities are avoided (at zeroth order [Alcubierre, 2003]) and

[1] We define gauge shocks as coordinate singularities for which the lapse becomes discontinuous caused by the crossing of characteristic lines; cf. [Alcubierre, 2003].

Table 2.1: Different slicing conditions and their main properties.

Name	Condition	f in Eq. (2.9)	avoiding gauge shocks	singularity avoiding
geodesic slicing	$\alpha = 1$	$f = 0$	no	no
maximal slicing	$K = 0$	$f \to \infty$	yes	yes
harmonic slicing	$(\partial_t - \mathcal{L}_{\boldsymbol{\beta}})\alpha = -\alpha^2 K$	$f = 1$	yes	marginally
1+log slicing	$(\partial_t - \mathcal{L}_{\boldsymbol{\beta}})\alpha = -2\alpha K$	$f = \frac{2}{\alpha}$	at zeroth order	strongly

that no gauge shocks can occur.

Finally, we have to mention that the usage of Eq. (2.11) is computationally cheap, while instead of solving an elliptic equation, as for example needed for the maximal slicing, we can simply evolve the lapse in time.

For the shift vector β^i we employ the Gamma-driver shift condition [Alcubierre et al., 2003; van Meter et al., 2006] in its integrated form

$$(\partial_t - \beta^j \partial_j)\beta^i = \mu_S \tilde{\Gamma}^i - \eta \beta^i, \tag{2.12}$$

with the conformal connection $\tilde{\Gamma}^i$, Eq. (2.29), and the damping parameter η. The gauge parameter μ_S is fixed to $1/\alpha^2$ in our simulations. Without a proper shift condition "time lines" (x^i = const. in Fig. 2.1) tend to fall into the black hole thereby reducing the resolution significantly. The particular choice of Eq. (2.12) counteracts this effect and allows long-term stable simulations of black holes and neutron stars. The combination of Eq. (2.11) and Eq. (2.12) is usually called *moving-puncture* gauge/coordinates. Together with the BSSN or Z4c formulation of Einstein's Equations (Sec. 2.1.3) it forms a strongly hyperbolic evolution system [Beyer and Sarbach, 2004; Gundlach and Martin-Garcia, 2006; van Meter et al., 2006].

2.1.3 Einstein's Field Equations in 3+1-form

ADM-Equations

The dynamics of the gravitational field are embedded in Einstein's field equations. We start by considering the ADM formalism [Arnowitt et al., 1962] to split the field equations (2.1) in 3+1-form ending up with a system of evolution and constraint equations.

First, we bring the right hand side (RHS) of Einstein's field equations, i.e. the energy-momentum tensor, into 3+1-form. This can be done with the following

projections:

$$S_{\mu\nu} = P^{\sigma}_{\mu} P^{\rho}_{\nu} T_{\sigma\rho}, \tag{2.13a}$$
$$S_{\mu} = -P^{\sigma}_{\mu} n^{\rho} T_{\sigma\rho}, \tag{2.13b}$$
$$S = S^{\mu} S_{\mu}, \tag{2.13c}$$
$$E = n^{\mu} n^{\nu} T_{\mu\nu}, \tag{2.13d}$$

where $S_{\mu\nu}$ is the spatial part of $T_{\mu\nu}$, S_{μ} is the momentum density, and E the energy density (measured by the Eulerian observer with the four-velocity n^{ν}).

The split of the Riemann tensor is based on the Gauss-Codazzi (2.14a) and the Codazzi-Mainardi (2.14b) equations:

$$P^{\delta}_{\alpha} P^{\kappa}_{\beta} P^{\lambda}_{\mu} P^{\sigma}_{\nu} {}^{(4)}R_{\delta\kappa\lambda\sigma} = {}^{(3)}R_{\alpha\beta\mu\nu} + K_{\alpha\mu} K_{\beta\nu} - K_{\alpha\nu} K_{\beta\mu} \tag{2.14a}$$
$$P^{\delta}_{\alpha} P^{\kappa}_{\beta} P^{\lambda}_{\mu} n^{\sigma} {}^{(4)}R_{\delta\kappa\lambda\sigma} = D_{\beta} K_{\alpha\mu} - D_{\alpha} K_{\beta\mu}, \tag{2.14b}$$

where $P^{\alpha\beta} = \gamma^{\beta\omega} P^{\alpha}_{\omega} = \gamma^{\alpha\beta}$, ${}^{(3)}R_{\alpha\beta\gamma\delta}$ is the three-dimensional Riemann tensor and D_{μ} denotes the three-dimensional covariant derivative after projecting the standard covariant derivative onto the space orthogonal to n^{α}, i.e. after a projection of all indices.

From the contracted Gauss relation, which follows from Eq. (2.14a), and Einstein's field Equations, we obtain:

$$\gamma^{\alpha\gamma} \gamma^{\beta\delta} {}^{(4)}R_{\alpha\beta\gamma\delta} = {}^{(3)}R + K^2 - K_{\alpha\beta} K^{\alpha\beta} = 2 n^{\alpha} n^{\beta} G_{\alpha\beta} = 16\pi E. \tag{2.15}$$

Contracting equation (2.14b) we achieve

$$\gamma^{\alpha\mu} n^{\nu} {}^{(4)}R_{\mu\nu} = D^{\alpha} K - D_{\mu} K^{\alpha\mu} = \gamma^{\alpha\mu} n^{\nu} G_{\mu\nu} = 8\pi S^{\alpha}. \tag{2.16}$$

The four equations

$$ {}^{(3)}R + K^2 - K_{\alpha\beta} K^{\alpha\beta} = 16\pi E, \tag{2.17}$$
$$D_j K^{ij} - D^i K = 8\pi S^i, \tag{2.18}$$

are called *Hamiltonian* and *Momentum Constraints*, respectively. These equations have to be fulfilled for all time slices. Therefore, they also need to be solved to construct initial data.

To find the evolution equation for the induced metric

$$\partial_t \gamma_{ij} = -2\alpha K_{ij} + D_i \beta_j + D_j \beta_i, \tag{2.19}$$

let us recall the definition of the extrinsic curvature:

$$K_{\alpha\beta} = \frac{1}{2}(K_{\alpha\beta} + K_{\beta\alpha}) = -\frac{1}{2}\left(n^\mu n_\beta \nabla_\mu n_\alpha + \nabla_\beta n_\alpha + n^\mu n_\alpha \nabla_\mu n_\beta + \nabla_\alpha n_\beta\right) = -\frac{1}{2}\left(n^\mu \nabla_\mu (n_\alpha n_\beta) + g_{\alpha\mu}\nabla_\beta n^\mu + g_{\beta\mu}\nabla_\alpha n^\mu\right) = -\frac{1}{2}\left(n^\mu \nabla_\mu \gamma_{\alpha\beta} + \gamma_{\alpha\mu}\nabla_\beta n^\mu + \gamma_{\beta\mu}\nabla_\alpha n^\mu\right) = -\frac{1}{2}\mathcal{L}_{\boldsymbol{n}}\gamma_{\alpha\beta} = -\frac{1}{2\alpha}\left(\mathcal{L}_{\boldsymbol{t}} - \mathcal{L}_{\boldsymbol{\beta}}\right)\gamma_{\alpha\beta} = -\frac{1}{2\alpha}\left(\partial_t \gamma_{\alpha\beta} - D_\alpha \beta_\beta - D_\beta \beta_\alpha\right). \tag{2.20}$$

The evolution equation for the extrinsic curvature

$$\partial_t K_{ij} = -D_i D_j \alpha + \beta^k \partial_k K_{ij} + K_{ik}\partial_j \beta^k + K_{kj}\partial_i \beta^k + \alpha\left({}^{(3)}R_{ij} + K K_{ij} - 2K_{ik}K^k{}_j\right) + 4\pi\alpha\left(\gamma_{ij}(S-E) - 2S_{ij}\right) \tag{2.21}$$

can be derived in the following way: Contracting the Riemann tensor twice with the normal vector and using Eq. (2.14a) yields

$$P^\mu_\alpha P^\nu_\beta n^\rho n^\sigma {}^{(4)}R_{\mu\rho\nu\sigma} = \mathcal{L}_{\boldsymbol{n}} K_{\alpha\beta} + \frac{1}{\alpha} D_\alpha D_\beta \alpha + K^\lambda{}_\beta K_{\alpha\lambda}, \tag{2.22}$$

$$P^\mu_\alpha P^\nu_\beta (n^\rho n^{\lambda (4)}R_{\mu\rho\nu\lambda} + {}^{(4)}R_{\mu\nu}) = {}^{(3)}R_{\alpha\beta} + K K_{\alpha\beta} - K^\lambda{}_\beta K_{\alpha\lambda}. \tag{2.23}$$

Inserting (2.22) in (2.23), we get

$$\mathcal{L}_{\boldsymbol{n}} K_{\alpha\beta} = -\frac{1}{\alpha} D_\alpha D_\beta \alpha - P^\mu_\alpha P^{\nu (4)}_\beta R_{\mu\nu} + {}^{(3)}R_{\alpha\beta} + K K_{\alpha\beta} - 2K^\lambda{}_\beta K_{\alpha\lambda}, \tag{2.24}$$

which can be easily transformed to the evolution equations (2.21). The equations (2.17,2.18,2.19,2.21) are called the ADM-equations named after Arnowitt, Deser, and Misner [Arnowitt et al., 1962]. The actual representation used in this thesis was derived by York [York, 1979], since is better suited for numerical simulations than the original approach.

The BSSN evolution scheme

Unfortunately, the ADM equations presented above combined with the common slicing conditions are only weakly hyperbolic [Kidder et al., 2001]. Thus, they do not possess the necessary well-posedness for long numerical simulations. Nakamura, Oohara and Kojima [Nakamura et al., 1987] reformulated the ADM equations in 1987, which led to a more stable evolution scheme. Baumgarte, Shapiro [Baumgarte and Shapiro, 1998] and Shibata, Nakamura [Shibata and Nakamura, 1995] improved this formulation in 1998. The new evolution system is called BSSNOK or just BSSN formalism.

In the following we present the particular formulation of the BSSN equations used in BAM.

As a first step, we consider a conformal rescaling of the spatial metric

$$\bar{\gamma}_{ij} = \psi^{-4}\gamma_{ij}. \tag{2.25}$$

Here ψ^4 is an auxiliary variable, but since the number of degrees of freedom have to remain the same, we are allowed to impose $\bar{\gamma} = 1$ or equivalent $\psi = (\det(\gamma))^{\frac{1}{12}}$. The extrinsic curvature K_{ij} is split in a trace-free part A_{ij} and the trace K:

$$K_{ij} = A_{ij} + \frac{1}{3}\gamma_{ij}K. \tag{2.26}$$

The trace-free part is transformed according to

$$\bar{A}_{ij} = \psi^2 A_{ij}. \tag{2.27}$$

Applying (2.25)-(2.27) the constraint equations become

$$\bar{D}^i\bar{D}_i\psi - \frac{1}{12}\psi^5 K^2 + \frac{1}{8}\psi^{-7}\bar{A}_{ij}\bar{A}^{ij} - \frac{1}{8}\psi\ {}^{(3)}\bar{R} = -2\pi\psi^5 E, \tag{2.28a}$$

$$\bar{D}_j\bar{A}^{ij} - \frac{2}{3}\psi^6\bar{\gamma}^{ij}\bar{D}_j K = 8\pi\psi^{10}S^i. \tag{2.28b}$$

For the evolution equations we use $\tilde{A}_{ij} = \psi^{-6}\bar{A}_{ij}$, $\tilde{\gamma}_{ij} = \bar{\gamma}_{ij}$, the conformal connection functions

$$\tilde{\Gamma}^i = -\partial_j\tilde{\gamma}^{ij} \tag{2.29}$$

and the conformal factor $\chi = \psi^{-4}$. For the conformal factor we get

$$(\partial_t - \mathcal{L}_{\boldsymbol{\beta}})\chi = \frac{2}{3}\chi\left(\alpha K - D_i\beta^i\right). \tag{2.30}$$

For the derivation of the other evolution equations we use the ADM equations constructed above and add multiples of the constraint equations:

$$(\partial_t - \mathcal{L}_{\boldsymbol{\beta}})\tilde{\gamma}_{ij} = -2\alpha\tilde{A}_{ij}, \tag{2.31}$$

$$(\partial_t - \mathcal{L}_{\boldsymbol{\beta}})\tilde{A}_{ij} = \chi\left(-D_iD_j\alpha + \alpha\ {}^{(3)}R_{ij} - 8\pi\alpha S_{ij}\right)^{\text{TF}} + \alpha(K\tilde{A}_{ij} - 2\tilde{A}_{ik}\tilde{A}^k_j), \tag{2.32}$$

$$(\partial_t - \mathcal{L}_{\boldsymbol{\beta}})K = -D^iD_i\alpha + \alpha(\tilde{A}_{ij}\tilde{A}^{ij} + \frac{1}{3}K^2) + 4\pi\alpha(E+S), \tag{2.33}$$

$$\begin{aligned}\partial_t\tilde{\Gamma}^i = {}& \tilde{\gamma}^{jk}\partial_j\partial_k\beta^i + \frac{1}{3}\tilde{\gamma}^{ij}\partial_j\partial_k\beta^k - 2\tilde{A}^{ij}\partial_j\alpha + \beta^j\partial_j\tilde{\Gamma}^i + \frac{2}{3}\tilde{\Gamma}^i\partial_j\beta^j \\ & - \tilde{\Gamma}^j\partial_j\beta^i + 2\alpha(\tilde{\Gamma}^i_{jk}\tilde{A}^{jk} - \frac{3}{2}\tilde{A}^{ij}\partial_j\ln(\chi) - \frac{2}{3}\tilde{\gamma}^{ij}\partial_j K - 8\pi\tilde{\gamma}^{ij}S_j).\end{aligned} \tag{2.34}$$

The Z4c -evolution system

Another evolution system implemented in BAM and used in this thesis is the Z4c formulation, see [Bernuzzi and Hilditch, 2010; Hilditch et al., 2013] for a detailed description.

Einstein's Equations can be rewritten as

$$R_{\alpha\beta} + \nabla_\alpha Z_\beta + \nabla_\beta Z_\alpha = 8\pi \left(T_{\alpha\beta} - \frac{1}{2} g_{\alpha\beta} T \right) + \kappa_1 \left(t_\alpha Z_\beta + t_\beta Z_\alpha - (1+\kappa_2) g_{\alpha\beta} \right) t_\gamma Z^\gamma, \tag{2.35}$$

where Z_α is a four-vector consisting of constraints, t_α is a timelike vector, and κ_1, κ_2 damping parameters. When the constraints vanish (2.35) is equivalent to (2.1). Performing a 3+1-split, introducing a conformal decomposition, discarding non-principal and non-damping terms leads to

$$\tilde{\gamma}_{ij} = \chi \gamma_{ij} \tag{2.36}$$

$$\tilde{A}_{ij} = \chi (K_{ij} - \frac{1}{3} \gamma_{ij} K) \tag{2.37}$$

$$\hat{K} = \gamma^{ij} K_{ij} - 2\Theta, \tag{2.38}$$

with $\Theta = -n_\alpha Z^\alpha$. Plugging (2.36)-(2.38) in (2.35) we end up with

$$\partial_t \chi = \frac{2}{3} \chi \left(\alpha (\hat{K} + 2\Theta) - D_i \beta^i \right) \tag{2.39}$$

$$\partial_t \tilde{\gamma}_{ij} = -2\alpha \tilde{A}_{ij} + \beta^k \partial_k \tilde{\gamma}_{ij} + 2\tilde{\gamma}_{k(i} \partial_{j)} \beta^k - \frac{2}{3} \tilde{\gamma}_{ij} \partial_k \beta^k, \tag{2.40}$$

$$\begin{aligned} \partial_t \hat{K} = & -D^i D_i \alpha + \alpha \left(\tilde{A}_{ij} \tilde{A}^{ij} + \frac{1}{3} (\hat{K} + 2\Theta)^2 \right) \\ & + 4\pi\alpha (S + E) + \beta^k \partial_k \hat{K} + \alpha \kappa_1 (1 - \kappa_2) \Theta \end{aligned} \tag{2.41}$$

$$\begin{aligned} \partial_t \tilde{A}_{ij} = & \chi \left(-D_i D_j \alpha + \alpha \left({}^{(3)}R_{ij} - 8\pi S_{ij} \right) \right)^{TF} + \alpha \left((\hat{K} + 2\Theta) \tilde{A}_{ij} - 2 \tilde{A}^k{}_j \tilde{A}_{kj} \right) \\ & + \beta^k \partial_k \tilde{A}_{ij} + 2 \tilde{A}_{k(i} \partial_{j)} \beta^k - \frac{2}{3} \tilde{A}_{ij} \partial_k \beta^k \end{aligned} \tag{2.42}$$

$$\begin{aligned} \partial_t \tilde{\Gamma}^i = & -2\tilde{A}^{ik} \partial_k \alpha + 2\alpha \left(\tilde{\Gamma}^i_{kl} \tilde{A}^{kl} - \frac{3}{2} \tilde{A}^{ik} \partial_k \ln(\chi) - \frac{1}{3} \tilde{\gamma}^{ik} \partial_k (\hat{K} + 2\Theta) - 8\pi \tilde{\gamma}^{ik} S_k \right) \\ & + \tilde{\gamma}^{kl} \partial_k \partial_l \beta^i + \frac{1}{3} \tilde{\gamma}^{ik} \partial_l \partial_k \beta^l - 2\alpha \kappa_1 (\tilde{\Gamma}^i - \bar{\Gamma}^i) \\ & + \beta^k \partial_k \tilde{\Gamma}^i - \bar{\Gamma}^k \partial_k \beta^i + \frac{2}{3} \bar{\Gamma}^i \partial_k \beta^k, \end{aligned} \tag{2.43}$$

$$\begin{aligned} \partial_t \Theta = & \frac{\alpha}{2} \left({}^{(3)}R - \tilde{A}_{ij} \tilde{A}^{ij} + \frac{2}{3} (\hat{K} + 2\Theta)^2 \right) \\ & - \alpha \left(8\pi E + \kappa_1 (2 + \kappa_2) \Theta \right) + \beta^i \partial_i \Theta, \end{aligned} \tag{2.44}$$

with $\tilde{\Gamma}^i = 2\tilde{\gamma}^{ik} Z_k + \tilde{\gamma}^{ij} \tilde{\gamma}^{kl} \tilde{\gamma}_{jk,l}$ and $\bar{\Gamma}^i = \tilde{\gamma}^{kl} \tilde{\Gamma}^i_{,kl}$; cf. [Hilditch et al., 2013].

Although we break the 4-covariance of the system, we stay close to the BSSN evolution system. The important advantages of the Z4c system are the constraint

damping property and that no zero-speed characteristic variables in the constraint subsystem exist. These effects make the Z4c formulation the preferred choice for our simulations. Additionally, constraint preserving boundary conditions were derived for this system [Ruiz et al., 2011] and are already implemented in BAM. We want to mention that an approach similar to Z4c was suggested with the CCZ4 system, where also non-principal terms are included [Alic et al., 2012].

The conformal thin-sandwich approach

The BSSN and the Z4c formulation, presented above, allow long term stable numerical simulations of compact binaries. However, as a prerequisite, we need accurate and constraint satisfying initial data. For this purpose we will use the *conformal thin-sandwich* (CTS) approach in Sec. 4.2 and 4.3. Starting with the constraint equations in its conformal decomposed form, Eqs. (2.28), and additionally assuming that

$$\bar{A}^{ij} = \frac{\psi^6}{2\alpha}((\bar{L}\beta)^{ij} - \bar{u}^{ij}), \tag{2.45}$$

with $\bar{u}_{ij} = \partial_t \bar{\gamma}_{ij}$, $\bar{u}^{ij}\bar{\gamma}_{ij} = 0$ and $(\bar{L}\beta)^{ij} = \bar{D}^i\beta^j + \bar{D}^j\beta^i - \frac{2}{3}\delta^{ij}\bar{D}_k\beta^k$, brings the momentum constraint to the form

$$(\bar{\Delta}_L\beta)^i - (\bar{L}\beta)^{ij}\bar{D}_j \ln(\alpha\psi^{-6}) = \alpha\psi^{-6}\bar{D}_j\left(\frac{\bar{u}^{ij}\psi^6}{\alpha}\right) + \frac{4}{3}\alpha\bar{D}^i K + 16\pi\alpha\psi^4 S^i, \tag{2.46}$$

where $(\bar{\Delta}_L\beta)^i$ denotes the vector Laplacian. It is important to notice that for the extended conformal thin-sandwich approach, employed in Sec. 4.1, we have to consider the additional equation

$$\bar{D}^i\bar{D}_i(\alpha\psi) = \alpha\psi\left(\frac{7}{8}\psi^{-8}\bar{A}_{ij}\bar{A}^{ij} + \frac{5}{12}\psi^4 K^2 + \frac{1}{8}{}^{(3)}\bar{R} + 2\pi\psi^4\left(E + 2S\right)\right) - \psi^5\partial_t K + \psi^5\beta^i\bar{D}_i K, \tag{2.47}$$

which is a combination of the evolution equation of K and the Hamiltonian constraint. Thus, we solve five instead of four equations, but we are allowed to choose $\bar{\gamma}_{ij}, \bar{u}_{ij}, K, \partial_t K$ freely. To obtain data, which are also in hydrodynamical equilibrium, we have to solve the constraint equations together with the matter equations, which we introduce in the following section.

2.1.4 Hydrodynamical equations

So far we have introduced schemes for the description of the spacetime geometry, but still missing are the evolution equations for the matter variables. For this purpose, we use the 3+1 conservative Eulerian formulation of GRHD; see [Font, 2007; Rezzolla and Zanotti, 2013] for references and detailed explanations. The fundamental equations governing the matter fields arise from the energy-momentum conservation

law

$$\nabla_\nu T^{\mu\nu} = 0 \tag{2.48}$$

and the conservation of the rest mass. Assuming the energy-momentum tensor of a perfect fluid

$$T^{\mu\nu} = \rho h u^\mu u^\nu + p g^{\mu\nu}, \tag{2.49}$$

with u^μ as the 4-velocity, p the pressure, and h the enthalpy. Eq. (2.48) can be written as the relativistic Euler equations

$$\rho h u^\nu \nabla_\nu u^\mu = -(g^{\mu\nu} + u^\mu u^\nu)\nabla_\nu p, \tag{2.50}$$

and the requirement of constant rest mass leads to the continuity equation

$$\nabla_\nu(\rho u^\nu) = 0. \tag{2.51}$$

Following the "Valencia formulation" of [Banyuls et al., 1997] we introduce the *primitive* variables as $\mathbf{w} = (\rho, v_i, \epsilon)$ (the proper rest-mass density, the fluid velocity, and the internal energy density measured by a Lagrangian observer) and the corresponding *conservative* variables $\mathbf{q} = (D, S_i, E)$ (the conserved rest mass, momentum, and internal energy density of the Eulerian observer)[2]:

$$D = \rho W \tag{2.52a}$$
$$S_i = \rho h W^2 v_i \tag{2.52b}$$
$$E = \rho h W^2 - p \tag{2.52c}$$
$$\tau = E - D, \tag{2.52d}$$

with $W = 1/\sqrt{1 - \gamma_{kl} v^k v^l}$ being the Lorentz factor. The enthalpy can be expressed as $h = 1 + \epsilon + p/\rho$. The first-order, flux conservative, hyperbolic system is

$$\frac{1}{\sqrt{-g}}\left(\frac{\partial(\sqrt{\gamma}\mathbf{q})}{\partial x^0} + \frac{\partial(\sqrt{-g}\mathbf{F}^i)}{\partial x^i}\right) = \mathbf{S}, \tag{2.53}$$

where

$$\mathbf{q} = \mathbf{q}(\mathbf{w}) = (D, S_j, \tau) \tag{2.54a}$$
$$\mathbf{F}^i = \mathbf{F}^i(\mathbf{w}) = \left(D\left(v^i - \frac{\beta^i}{\alpha}\right), S_j\left(v^i - \frac{\beta^i}{\alpha}\right) + p\delta^i_j, \tau\left(v^i - \frac{\beta^i}{\alpha}\right) + pv^i\right) \tag{2.54b}$$
$$\mathbf{S} = \mathbf{S}(\mathbf{w}) = \left(0, T^{\mu\nu}\left(\partial_\mu g_{\nu j} - \Gamma^\sigma_{\nu\mu} g_{\sigma j}\right), \alpha\left(T^{\mu 0}\partial_\mu(\log(\alpha)) - T^{\mu\nu}\Gamma^0_{\nu\mu}\right)\right). \tag{2.54c}$$

The implementation of Eq. (2.53) in BAM was the main topic of the PhD thesis

[2]Notice that instead of E we use τ as a conserved variable similar to [Banyuls et al., 1997].

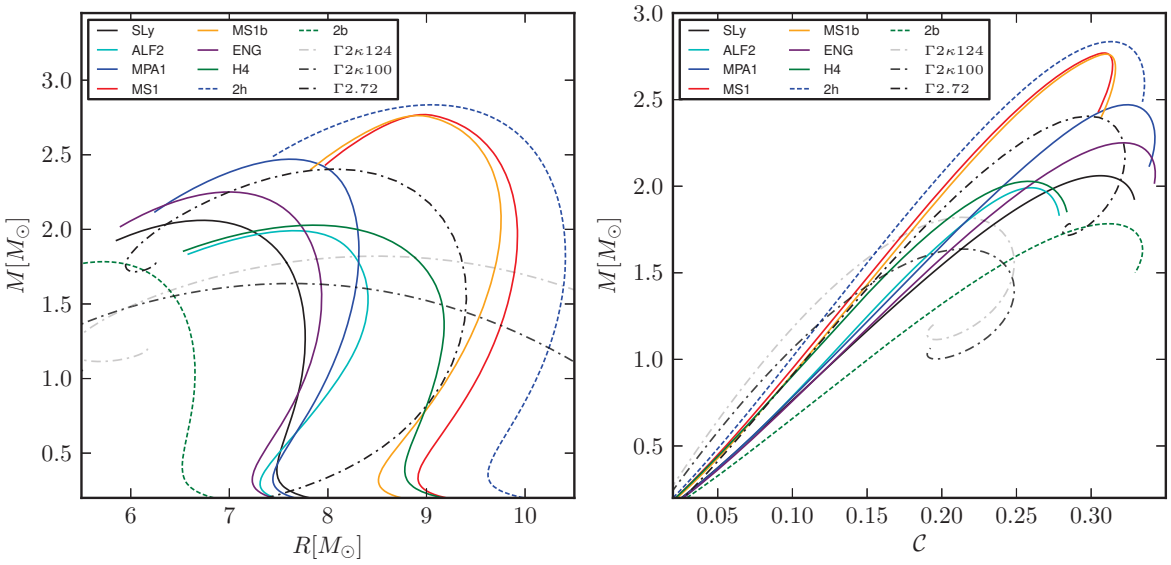

Figure 2.2: The mass-radius relation (left) and the mass-compactness relation (right) for spherically symmetric TOV-stars depending on the EOS. The different dashing differentiate simple polytropes and piecewise polytropes with 2 or 4 pieces. More details are listed in Table 2.2.

of M. Thierfelder [Thierfelder, 2011]. Therefore, we do not repeat the governing equations here and just refer to [Thierfelder, 2011; Thierfelder et al., 2011a] for further details.

Equations of State

The evolution system is finally closed by an EOS of the form $p = P(\rho, \epsilon)$, where we use one of the following possibilities:

$$\begin{aligned}
&\text{(i)} && \text{polytropic EOS} && P(\rho) = \kappa\rho^{\Gamma}, && && \text{(2.55a)}\\
&\text{(ii)} && \text{ideal gas} && P(\rho,\epsilon) = (\Gamma-1)\rho\epsilon, && && \text{(2.55b)}\\
&\text{(iii)} && \text{piecewise-polytropic EOS} && P(\rho) = \kappa_i\rho^{\Gamma_i}; && \rho \in (\rho_i, \rho_{i+1}), && \text{(2.55c)}\\
&\text{(iv)} && \text{piecewise-polytropic EOS +} && P(\rho,\epsilon) = \kappa_i\rho^{\Gamma_i} + && && \\
& && \text{thermal contribution} && (\Gamma_{th}-1)\rho\epsilon_{th}; && \rho \in (\rho_i, \rho_{i+1}), && \text{(2.55d)}
\end{aligned}$$

with $\epsilon_{th} = \epsilon - \epsilon_{cold}$ and ϵ_{cold} is computed from the barotropic (polytropic) EOS.

Several barotropic, zero-temperature EOSs developed to describe neutron star matter, can be fitted with piecewise-polytropes as outlined in [Read et al., 2009a]. It is possible to extend the barotropic EOSs with an additional thermal pressure [Shibata et al., 2005; Bauswein et al., 2010]. In this thesis we set $\Gamma_{th} = 1.75$ unless otherwise stated. All employed EOSs for our simulations are summarized in Tab. 2.2 and shown in Fig. 2.2.

Table 2.2: Properties of the EOSs used in this work. All piecewise-polytrope EOSs use a crust with $\kappa_{\text{crust}} = 8.948185 \times 10^{-2}$ and $\Gamma_{\text{crust}} = 1.35692$. The columns refer to: the name of the EOS, the maximum density in the crust, the three polytropic exponents for the individual pieces, and the maximum supported gravitational mass M^{max}, baryonic mass $M_{\text{b}}^{\text{max}}$, the compactness of an isolated nonrotating star $\mathcal{C}^{\text{max}}$ with M^{max}, and the maximum adiabatic speed of sound c_s^{max} within the maximum stable neutron star configuration, respectively. [We define the compactness by $\mathcal{C} := M/R$, where R is the star's radius (in Schwarzschild coordinates) and M is its gravitational mass.] The divisions for the individual parts for the piecewise polytropes are at $\rho_1 = 8.12123 \times 10^{-4}$ and $\rho_2 = 1.62040 \times 10^{-3}$; see [Read et al., 2009a] for more details about these particular EOSs.

EOS	$\rho_{\text{crust}}/10^{-4}$	Γ_1	Γ_2	Γ_3	M^{max}	$M_{\text{b}}^{\text{max}}$	$\mathcal{C}^{\text{max}}$	c_s^{max}
SLy	2.36953	3.005	2.988	2.851	2.06	2.46	0.31	1.00
ALF2	3.15606	4.070	2.411	1.890	1.99	2.32	0.26	0.65
ENG	2.99450	3.514	3.130	3.168	2.25	2.73	0.32	1.11
H4	1.43830	2.909	2.246	2.144	2.03	2.33	0.26	0.72
MPA1	2.71930	3.446	3.572	2.887	2.47	3.04	0.32	1.05
MS1	1.52594	3.224	3.033	1.325	2.77	3.35	0.31	1.00
MS1b	1.84169	3.456	3.011	1.425	2.76	3.35	0.31	0.99
2b	3.49296	3.000	–	–	1.78	2.14	0.31	1.05
2h	1.13813	3.000	–	–	2.83	3.41	0.31	1.06
$\Gamma 2\kappa 100$	$\Gamma = 2$,	$\kappa = 100$			1.64	1.80	0.21	0.62
$\Gamma 2\kappa 124$	$\Gamma = 2$,	$\kappa = 123.6489$			1.82	2.00	0.21	0.62
$\Gamma 2.72$	$\Gamma = 2.7203$,	$\kappa = 23841.43$			2.40	2.85	0.30	0.95

2.2 Numerical methods

In this part we summarize the numerical methods employed in this thesis. In particular we focus on different spatial discretization methods, the flux computation, the primitive reconstruction, and the mesh refinement strategy.

2.2.1 Method of Lines

The evolution equations presented in Sec. 2.1.3 together with matter equations in Sec. 2.1.4 describe a non-linear system of PDEs. We will follow the *method of lines*-approach assuming that time and space can be treated separately to solve the PDE system.

While the time is still continuous the spatial dimensions are already discretized. The RHS, which contains spatial derivatives of the evolved variables, can be evaluated in different ways. During this thesis, we worked with finite differencing as in BAM; a pseudo-spectral method (e.g. [Fornberg, 1998; Boyd, 2001]) as in SGRID and BAMPS; or a discontinuous Galerkin method as in BAMPS[3]. After discretizing the spatial dimensions we obtain a set of ordinary differential equations at each grid

[3] Because this thesis focuses on the BAM code and briefly presents results obtained with SGRID, we will review fundamental aspects of finite differencing and pseudo-spectral schemes. We will not review the results of [Die14] obtained with the BAMPS code. This will be explained in detail in the PhD thesis of M. Bugner.

point; the semi-discrete equations. Finally, the obtained system can be solved with any stable ordinary differential equation solver. In this thesis we use an explicit third and fourth order Runge-Kutta method and employ a Courant-Friedrichs-Lewy (CFL) condition of 0.25.

Finite differencing and finite volume methods

Probably the easiest approach for the discretization of the RHS, i.e. the discretization of the space dimensions, is the usage of finite differencing stencils. Let us consider that at every gridpoint x_j the solution $f(x)$ can be expressed as a Taylor series

$$f(x) = f(x_j) + (x - x_j)f'(x_j) + \frac{(x - x_j)^2}{2}f''(x_j) + \mathcal{O}\left((x - x_j)^3\right). \tag{2.56}$$

To compute the derivative $f'(x_j)$, we have to use the Taylor expansions at the neighboring gridpoints x_{j-1}, x_{j+1} similar to Eq. (2.56). Combining the resulting two equations we end up with a simple second order stencil

$$f'(x_j) = \frac{f(x_{j+1}) - f(x_{j-1})}{x_{j+1} - x_{j-1}} + \mathcal{O}\left((x_{j+1} - x_{j-1})^2\right). \tag{2.57}$$

Higher order and higher derivative stencils can be derived in a similar way using the information of more grid points. In the current BAM version finite differencing stencils up to 10th order for the geometrical variables and fourth order for the matter variables are implemented.

Pseudo-spectral methods

Let us consider the case, where our solution can be expressed as a series of test functions. The chosen orthogonal basis functions Φ_n should satisfy that the continuum derivative of the n-th basis function is a linear combination of the first $(n-1)$-th basis functions.

For a successful implementation we have to introduce a specific grid and its grid points x_j. We evaluate every necessary function on those grid points to create a discrete representation. The function $f(x)$ is expanded into a series $f(x) = \sum_n a_n \Phi_n$ and the coefficients are determined by the orthogonality relation $a_n = \int_A^B f(x)\Phi_n(x)\omega(x)\mathrm{d}x$, where the weight function $\omega(x)$ and the integration interval (A, B) depends on the exact choice of the polynomials. Since only a finite number of basis functions is used, we have to approximate f and compute it at the grid points

$$f_{N,j} = \sum_{n=0}^{N-1} a_n \Phi_{n,j}, \quad \text{with} \quad a_n = \sum_{j=0}^{N-1} f_{N,j}\Phi_{n,j}\omega_j, \tag{2.58}$$

with ω_j being the specific quadrature weights. In our example N represents both the

number of basis functions and the number of grid points.

The discrete derivative operator is finally defined as

$$\partial_x f_{N,j} = \sum_{n=0}^{N-1} a_n \partial_x \Phi_{n,j} = \sum_{n=0}^{N-1} b_n \Phi_{n,j}. \tag{2.59}$$

The coefficients for fixed n at the position j can be stored as a matrix, thus taking derivatives is a simple matrix multiplication. The main advantage of spectral methods is that in case of smooth functions an exponential convergence can be achieved, while for non-smooth or discontinuous functions the rate of convergence drops or the numerical method fails.

2.2.2 Flux computation and shock capturing methods

To solve the evolution equations of the matter fields, Eq. (2.53), we have to compute the flux at the cell boundaries between grid points. But in the presence of shocks or discontinuities this is a challenging task. We want to present important properties and aspects of high-resolution shock capturing schemes for the flux computation. We restrict our discussion to the basic description necessary to understand the employed schemes in our simulations. More details and other flux computation algorithms are discussed and tested in Appendix C.

We compute the fluxes in Eq. (2.53) similar to the description in [Shu and Osher, 1989; Thierfelder, 2011; Thierfelder et al., 2011a]. For simplicity we restrict our description to one dimension, but higher dimensions can be obtained treating each dimension separately. The divergence term in (2.53) is calculated using the conservative finite differencing formula

$$\frac{\partial \mathbf{F}}{\partial x}(x_i) = \frac{\left(\hat{\mathbf{F}}_{i+1/2} - \hat{\mathbf{F}}_{i-1/2}\right)}{\Delta x}\,, \tag{2.60}$$

where the numerical fluxes at the interfaces, $\hat{\mathbf{F}}_{i\pm1/2}$, are an approximation of the numerical flux function and $\Delta x = x_{i+1/2} - x_{i-1/2}$.

The numerical flux is computed according to the following steps:

(i) Recovery of the primitives $\mathbf{w}$ from the conservative variables $\mathbf{q}$ (Sec. 2.2.3);

(ii) Reconstruction of the primitives at the cell interfaces $i + 1/2$ with a high resolution shock capturing scheme

$$\mathrm{Rec}[(\mathbf{w}_{(i+1/2),\mathcal{S}})] \mapsto \mathbf{w}^{\pm}_{i+1/2}, \tag{2.61}$$

with $+/-$ denoting the right/left interface value point and $\mathcal{S}$ the stencil of the reconstruction.

(iii) Computation of the numerical flux with an approximate Riemann solver, where we use the Local Lax-Friedrich (LLF) flux

$$\hat{\mathbf{F}}_{i+1/2} = \frac{1}{2}\left(\mathbf{F}^{+} + \mathbf{F}^{-} - a^{(k)}(\mathbf{q}^{-} - \mathbf{q}^{+})\right), \tag{2.62}$$

with $a^{(k)} = \max(|\lambda^{(k)}|)$ denoting the maximum of the local characteristic speeds of the k-th field variable (eigenvalues λ of $\partial\hat{\mathbf{F}}/\partial\mathbf{q}$) at the interface $i + 1/2$. $\mathbf{F}^{\pm}$ is computed from $\mathbf{w}^{\pm}$ according to Eq. (2.54b).

Reconstruction methods

The fundamental idea behind the reconstruction algorithm is to select stencils according to the gradient of the solution. Within this work we focus on the WENOZ reconstruction [Borges et al., 2008], cf. Appendix. C.1. The MP5 [Suresh, 1997] scheme is tested in Appendix C as well. Other reconstruction methods such as the Total Variation Diminishing, linear MINMOD, Monotonized Centered, Piecewise Parabolic Method, and Convex-essentially-non-oscillatory schemes are also implemented in BAM, but not used in this thesis [Thierfelder, 2011; Thierfelder et al., 2011a; Bernuzzi et al., 2012b].

2.2.3 Primitive reconstruction and atmosphere treatment

As shown in Eq. (2.53) the conservative variables are evolved in time, but for the computation of the fluxes the primitive variables have to be known at every instance of time. Thus, it is necessary to recover at every time step and at every Runge-Kutta substep the primitive variables from the conservative ones. We can invert the definition of the conservative variables Eqs. (2.52) and obtain:

$$W(p) = \frac{\xi}{\xi^2 - S^2}, \tag{2.63a}$$

$$v^i(p) = \frac{S^i}{\xi}, \tag{2.63b}$$

$$\rho(p) = \frac{D}{W}, \tag{2.63c}$$

$$\epsilon(p) = \frac{\sqrt{\xi^2 - S^2} - Wp - D}{D}, \tag{2.63d}$$

with $\xi = \tau + D + p$. Unfortunately, the inversion can not be done explicitly, since the primitive variables given in Eq. (2.63) depend on the pressure p. Therefore, we have to determine the pressure and find a self-consistent solution. The pressure is determined by the particular form of the EOS Eq. (2.55) and has to fulfill

$$f(p) = p - P(\rho, \epsilon) \stackrel{!}{=} 0. \tag{2.64}$$

To solve this algebraic equation, we use a Newton-Raphson method with

$$p^{i+1} = p^i - \frac{f(p)}{f'(p)}, \tag{2.65a}$$

$$f'(p) = 1 - \frac{\partial P}{\partial \rho}\frac{\partial \rho}{\partial p} - \frac{\partial P}{\partial \epsilon}\frac{\partial \epsilon}{\partial p}, \tag{2.65b}$$

$$\frac{\partial \rho}{\partial p} = \frac{DS^2}{\xi^2\sqrt{\xi^2 - S^2}}, \tag{2.65c}$$

$$\frac{\partial \epsilon}{\partial p} = \frac{pS^2}{D(\xi^2 - S^2)^{3/2}}. \tag{2.65d}$$

As an initial guess p^0 we use the maximum of $S - D - \tau$ or the pressure of the previous timestep.

During the transformation from the conservative variables to the primitive ones we have to divide by the density ρ. This is one reason why we can not set the density outside the neutron stars to zero and have to introduce an artificial atmosphere. As described in [Thierfelder, 2011; Thierfelder et al., 2011a] a low-density static and barotropic atmosphere (henceforth simply called atmosphere) is used, where

$$\rho_{atm} = f_{atm}\ \max[\rho(t=0)]. \tag{2.66}$$

During the recovery of the primitive variables a point is set to atmosphere if the density is below the threshold

$$\rho_{thr} = f_{thr}\ \rho_{atm}. \tag{2.67}$$

It is important to notice that (i) all hydrodynamical simulations of BNSs in full general relativity use an atmosphere and (ii) the atmosphere treatment violates mass conservation. The latter point will be investigated in Appendix B in more detail.

2.2.4 Adaptive mesh refinement

In numerical relativity simulations several length scales have to be covered and resolved properly. Most notably, the strong-field region has to be modeled with sufficiently high resolution to allow long-term stable simulations. This region is covered with a grid spacing of $\sim 100\mathrm{m}$ in our simulations. However, the GW extraction should be done on regions sufficiently far away from the compact objects such that the approximations made to extract the GWs are valid. Thus, these region should extend up to $\sim 1000\mathrm{km}$ and the numerical domain has to span several orders of magnitude to model the near zone and the far-field properly. The most common approach for this purpose is an adaptive mesh-refinement (AMR) technique, which we describe below.

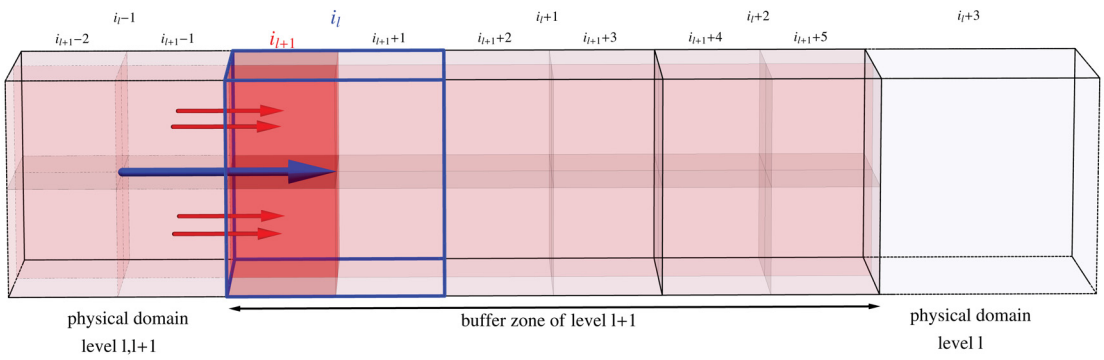

Figure 2.3: Sketch of the mesh refinement. We focus on the buffer region along the positive x direction. We employ six buffer points in level $l+1$. Prolongation (P) and correction (C) steps take place in this region. The *parent* cell is visualized by the blue bounding box, while the *child* cells are colored dark red. The fluxes across the physical domain and the refinement buffer zone are visualized with arrows. The parent cell (level l) receives the correction after level $l+1$ has been evolved; adapted from [Die8].

Berger-Oliger mesh refinement

BAM's AMR combines a box-in-box Cartesian AMR in the strong field region with a "cubed-sphere" multi-patch AMR in the wave-zone [Ronchi et al., 1996; Thornburg, 2004; Pollney et al., 2011]. The grid hierarchy consists of a fixed number L of refinement levels. Two different types of levels exist: the outermost levels, which are fixed and do not change during the simulation, and the inner refinement levels, which can either stay fixed or can be dynamically moved and adapted according to the technique of "moving boxes"; cf. [Yamamoto et al., 2008; Brügmann et al., 2008; Baiotti et al., 2008].

Whenever level l is evolved by one time step and we apply Berger-Oliger (BO) time stepping, level $l+1$ performs two steps due to a 2:1-refinement strategy. For such an evolution technique boundary conditions for every refinement level are needed, but only the physical boundary conditions on the outermost level $l=0$ are in principle "known", i.e. they can be derived from the outer boundary condition. Thus, following the standard BO algorithm, every refinement level $l>0$ includes buffer zones. We interpolate the buffer region of level $l+1$ by second order time interpolation using level l, see [Brügmann et al., 2008] for a detailed discussion.

To avoid divisions by zero at the origin, a staggered grid is used, such that the gridpoints of level l and $l+1$ do not coincide. In this thesis we use different methods for the interpolation from the coarse to the fine grid (*prolongation*) and the interpolation from the fine to the coarse grid (*restriction*) of the matter variables. For the geometrical quantities a fourth or sixth order Lagrangian interpolation is applied for both the restriction and the prolongation.

Berger-Colella mesh refinement

Independent of the particular interpolation scheme employed for the restriction and prolongation step, truncation errors lead to differences between the fluxes across mesh refinement boundaries on a finer grid and the corresponding fluxes calculated on the coarse grid. This introduces mass violations and can affect the accuracy of the simulation. But an additional *correction* (C) step can be introduced to enforce mass conservation. The idea to correct fluxes crossing refinement boundaries goes back to Berger-Colella [Berger and Colella, 1989] (BC) and is widely used in astrophysics and was adapted to numerical relativistic codes [East et al., 2012; Reisswig et al., 2013a]. The method has been used in different applications, e.g. in black hole - neutron star and in BNS systems [Stephens et al., 2011; East and Pretorius, 2012], massive star and core-collapse supernovae evolutions [Ott et al., 2013; Reisswig et al., 2013b; Abdikamalov et al., 2014], and in the rotating neutron star collapse [Reisswig et al., 2013a],[Die7]. Our implementation is based on [East et al., 2012] and described in detail in [Die8].

For clarity we will review the algorithm in one dimension, higher dimensions can be obtained by considering each dimension separately. In fact the only strict conservation law in Eq. (2.53) is the one for the rest mass density D, i.e. the first component of $\mathbf{q}$. However, the flux correction is applied for all conservative variables.

The discrete model equation for D is given by

$$D^{n+1}_{i,j,k} = D^{n}_{i,j,k} - \frac{\Delta t}{\Delta x}\left(F^{x}_{i+1/2,j,k} - F^{x}_{i-1/2,j,k}\right) \tag{2.68}$$

with $F^{x}_{i\pm1/2,j,k}$ denoting the x component of the numerical fluxes corresponding to D across the cell faces $(i \pm 1/2, j, k)$. The index n defines the time and Δt is the time step.

Considering two sequential refinement levels l and $l+1$ with $\Delta x_{l+1}/\Delta x_l = 1/2$ mass violation happens during a BO step because:

(i) the buffer zones of level $l+1$ are set by level l via prolongation;

(ii) the prolongation carries a certain truncation error, thus, the fluxes on $l+1$ and l are different;

(iii) after restriction from level $l+1$, the solution on level l is not consistent with the fluxes on l.

Figure 2.3 illustrates the buffer region of level $l+1$.

The changes $\delta D^{(l)}_{i,j,k}$ in $D^{(l)}$ on level l due to the flux going through the cell face $(i_l + 1/2, j_l, k_l)$ after the time step Δt is

$$\delta D^{(l)}_{i,j,k}(t+\Delta t) = -\frac{\Delta t}{\Delta x} F^{x}_{i_l+1/2,j_l,k_l}(t)\ . \tag{2.69}$$

Due to the 2:1-refinement strategy, level $l+1$ advances by two $\Delta t/2$ time steps:

$$\begin{aligned}\delta D^{(l+1)}_{i,j,k}(t+\Delta t) = &- \frac{\Delta t/2}{\Delta x/2} F^x_{i_{l+1}+1/2,j_{l+1},k_{l+1}}(t) \\ &- \frac{\Delta t/2}{\Delta x/2} F^x_{i_{l+1}+1/2,j_{l+1},k_{l+1}}(t+\Delta t/2).\end{aligned} \tag{2.70}$$

These two changes $\delta D^{(l)}_{i,j,k}(t+\Delta t)$ and $\delta D^{(l+1)}_{i,j,k}(t+\Delta t)$ differ due to truncation errors. Thus, the mass crossing the cell faces is different, $\delta M^{(l+1)} \neq \delta M^{(l)}$ and, after restriction, the mass conservation is violated proportional to $\delta M^{(l)} - \delta M^{(l+1)}$.

The original Berger-Colella algorithm corrects the solution at level l when the refinement level $l+1$ and l are aligned in time [Berger and Colella, 1989]. The additionally introduced correction operation

$$D^{(l)} \mapsto D^{(l)} + \Delta t/\Delta x \; \delta F^{x\ (l)}, \tag{2.71}$$

with $\delta F^{x\ (l)}$ being the flux correction stored on the cell face. $\delta F^{x\ (l)}$ is initialized with $-F^x_{i_l+1/2,j_l,k_l}$ before advancing level $l+1$ in time. During each time step of level $l+1$, it receives and sums up the contributions $F^x_{i_{l+1}+1/2,j_{l+1},k_{l+1}}$ (two contributions in our example). The C step finally guarantees consistency of the fluxes.

Our implementation follows [East et al., 2012], who proposed to store the mass correction $\delta M^{(l)}$ and not $\delta F^{(l)}$, and performed the correction as $D^{(l)} \mapsto D^{(l)} + \delta M^{(l)}/V^{(l)}$ on the cell volume $V^{(l)}$. This algorithm is simpler and only uses grid variables on cell centers instead of faces, which minimizes the necessary changes in the BAM code.

The correction procedure in BAM goes as follows:

(i) We define a mask labeling the cells involved in the C step; the innermost buffer points of level $l+1$ (red in Fig. 2.3) and the corresponding parent cells (blue in Fig. 2.3). The mask additionally stores the information about the box faces $(+x, -x, +y, -y, +z, -z)$. Notice that it is crucial to compute the mask after each regridding step.

(ii) After each evolution step of level l we store the mass change of the parent cells

$$\delta M^{(l)} = \pm V^{(l)} \delta D^{(l)}, \tag{2.72}$$

and, similarly, after each substep of level $l+1$, $\delta M^{(l+1)} = \mp V^{(l+1)} \delta D^{(l+1)}$. The particular sign depends on the entry in the mask, e.g. $+x$ surfaces refer to a positive sign in Eq. (2.72).

(iii) The contributions are summed up, when level l and $l+1$ are aligned in time,

and we correct the cell values

$$D^{(l)} \mapsto D^{(l)} + \frac{\delta M^{(l)}}{V^{(l)}} + \sum \frac{\delta M^{(l+1)}}{V^{(l+1)}}. \tag{2.73}$$

The effectiveness of the algorithm depends crucially on the choice for the restriction and prolongation operators. The restriction step of the hydrodynamical fields is conservative if the operation is performed using local averages. A conservative choice for the prolongation step is a linear interpolation including limiters in order to control oscillations. Although one might expect that for neutron star simulations high-order operators may be important for accuracy and faster convergence, we show in extensive tests in Appendix B that the best restriction/prolongation combination is indeed the conservative combination of average restriction and linear prolongation.

Chapter 3

Rotating neutron star collapse

In this chapter we review the findings of [Die7] and investigate the gravitational collapse of a rotating neutron star to a black hole. Such configurations are of astrophysical importance, since neutron stars close to the collapse threshold can be formed in stellar core collapses and BNS mergers e.g. [Ott et al., 2011; Thierfelder et al., 2011a].

Similar setups have been studied extensively in the literature in 2D under the assumption of axisymmetry [Stark and Piran, 1985; Nakamura et al., 1987; Shibata, 2003; Duez et al., 2006; Shibata et al., 2006; Stephens et al., 2007; Stephens et al., 2008] and in full 3D [Shibata et al., 2000; Duez et al., 2004; Baiotti et al., 2005; Baiotti et al., 2007; Giacomazzo et al., 2011b; Reisswig et al., 2013a]. Here we perform the highest-resolved simulations to date reaching resolutions of less than six meters in the central region of the neutron star.

3.1 Collapse dynamics

The particular setup we are going to investigate is the D4 model described in [Baiotti et al., 2005; Baiotti et al., 2007; Reisswig et al., 2013a]. This configuration is in an unstable equilibrium, i.e. beyond the radial stability point. The collapse can be introduced by an artificial pressure perturbation or low-resolved initial data. We decide to use high-resolved data and add a perturbation of 0.5%. Thus, we compute the initial data with the polytropic $\Gamma 2 \kappa 100$ EOS, but change to $\kappa = 99.5$ for the evolution using a Γ-law. The initial central rest-mass density is $\rho_c = 4.0869 \times 10^{-3}$, the axes-ratio 0.65, the gravitational mass $M = 1.8605 M_\odot$, and the baryonic mass $M_b = 2.0443 M_\odot$. The configuration is computed with the RNS code [Stergioulas and Friedman, 1995]. Applying an artificial pressure perturbation is the usual approach in the literature, see e.g. [Baiotti et al., 2005; Baiotti et al., 2007; Reisswig et al., 2013a] where a 2% and [Giacomazzo and Perna, 2012] where a 0.1% perturbation was applied. However, this always results in a constraint violation and an unphysical GW emitted at the beginning of the simulation. A clear distinction between the artificial and physical

Table 3.1: Grid configurations for the investigation of the rotating neutron star collapse: L number of total levels, n number of points per direction, $L_{\rm m}$ number of levels employing $n_{\rm m}$ points per direction (every level $l > 3$), h_f finest grid spacing, h_c coarsest grid spacing. The neutron star is covered completely by level $l = 5$, while its equatorial radius is $\sim 7.7 M_\odot \approx 11.4\mathrm{km}$. The outer boundary of the numerical domain is at $r_{\rm out} \sim 576 M_\odot \approx 852\mathrm{km}$. Table adopted from [Die7].

Name	L	n	$L_{\rm m}$	$n_{\rm m}$	h_f	h_c
G8	8	144	4	64	0.0625	8
G9L	9	108	5	48	0.04167	10.67
G9	9	144	5	64	0.03125	8
G9H	9	216	5	80	0.025	6.4
G10	10	144	6	64	0.015625	8
G11	11	144	7	64	0.0078125	8
G11H	11	216	7	96	0.0052083	5.33
G11F	11	288	7	128	0.00390625	4

part of the waveform is only possible for small perturbations as used in this work.

The grid configurations are described in Table 3.1. In all simulations quadrant symmetry is employed to reduce computational costs. However, we cross checked our results with full 3D simulations for the lowest-resolved simulations in Tab. 3.1.

We investigate the influence of (i) an increased number of refinement levels keeping the number of grid points inside a level fixed and (ii) an increased number of grid points inside a fixed number of levels. The former procedure allows us to better resolve the origin and the formed puncture in an efficient way; the latter has a larger effect on the waveforms due to higher resolutions in the wave extraction zone.

During collapse the central density increases (upper left panel of Fig. 3.1) and the central lapse decreases (bottom left panel). The central density reaches a maximum and matter "falls off" the numerical domain due to the moving puncture gauge [Thierfelder, 2011; Thierfelder et al., 2011b] and the formation of a black hole. To follow the collapse with sufficient resolution we have to use refinement levels inside the star, which is only possible with a conservative mesh refinement as described in Sec. 2.2.4 to avoid artificial mass violation and corruption of the numerical data.

With an increasing number of refinement levels the origin is better resolved, and consequently the maximum density (lapse) increases (decreases). The resolution effect (tested for the configurations G9 and G11) can be as large as the effect of including more refinement levels. Therefore, both parameters need to be tuned for an optimal grid setup. For higher resolutions the collapse happens earlier.

The baryonic mass conservation, and the L_2 norm of the Hamiltonian constraint $||\mathcal{H}||_2$ (right panels of Fig. 3.1) are used for an error estimate of the simulation. The relative error in the mass conservation is $\sim 10^{-5}$ at the time of collapse. The Hamiltonian constraint (and also the momentum constraints) show their maximum at the moment of black hole formation. With increasing resolution (more grid

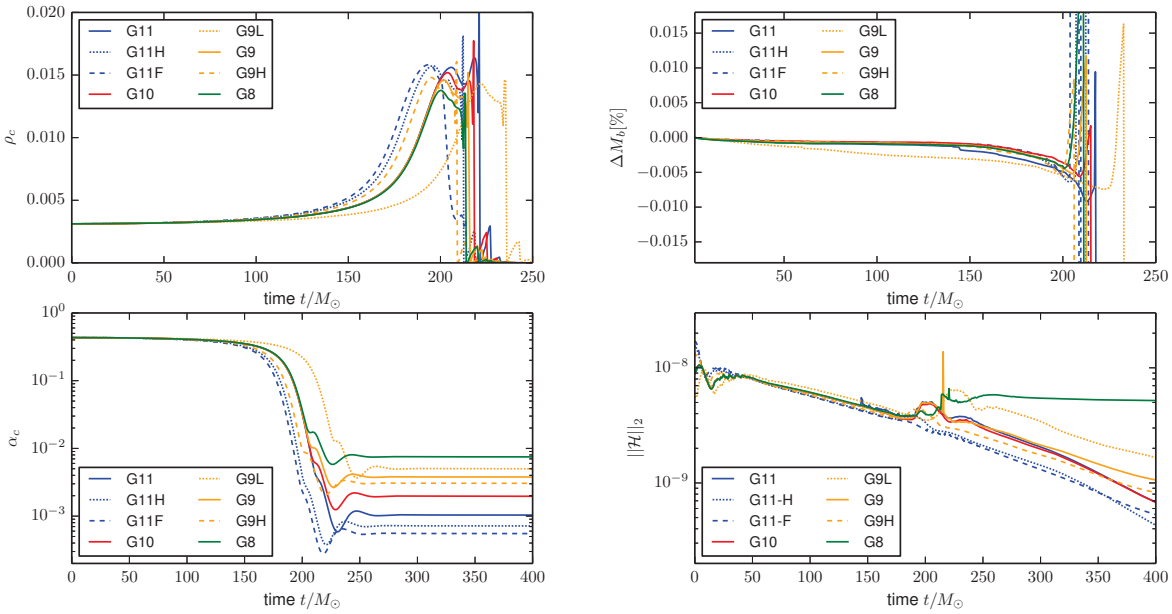

Figure 3.1: Rotating collapse dynamics. Central rest-mass density (top left) and central lapse (bottom left). Conservation of baryonic mass $\Delta M_b = 1 - M_b(t)/M_b(0)$ (top right), L_2 norm of the Hamiltonian constraint $||\mathcal{H}||_2$ (bottom right). The constraint violations are measured on level $l = 1$, i.e. the second coarsest level on which also the wave extraction takes place. We show results for various grid configurations, cf. Tab. 3.1. Plot adapted from [Die7].

points/refinement levels) the constraint violations decrease. Due to the Z4c formulation and its constraint damping properties the constraint violation remains below or at the level of the initial data.

In Fig. 3.2 we show a standard three-level self-convergence plot for the central lapse $\alpha_c(t)$ and the central density $\rho_c(t)$. Similar plots can be obtained also for other quantities. For higher resolutions, e.g. the G11 configurations, we observe second-order convergence almost up to horizon formation. In contrast, for lower resolutions, e.g. G9 setup, convergence is slower after $t \sim 100M_\odot$. Independent of the resolution the convergence drops after the horizon formation, and cannot be monitored at the origin.

3.2 Gravitational waveform

We compute the multipoles h_{lm} with a time domain integration of $\Psi_4 = \ddot{h}$ subtracting a quadratic polynomial as described in [Damour et al., 2008b; Baiotti et al., 2009]. We have experimented with the frequency domain integration of [Reisswig and Pollney, 2011], but had difficulties identifying a cutting frequency for the high-pass filter.

The dominant mode of the metric waveform is shown in Fig. 3.3. As pointed out in [Stark and Piran, 1985; Seidel and Moore, 1987; Seidel et al., 1988; Seidel, 1990], the quadrupole waveform is simple and shows the “precursor-burst-ringdown” pattern

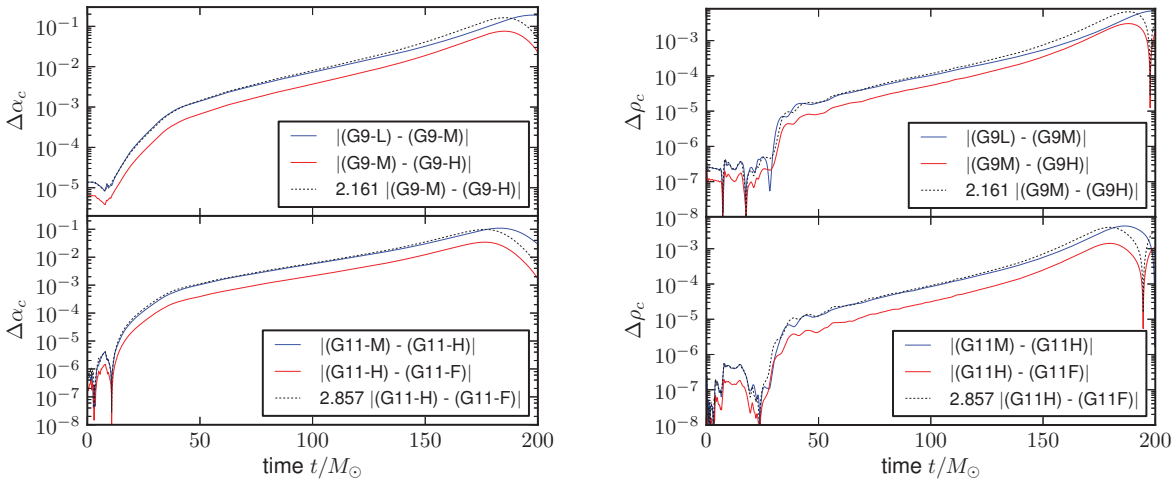

Figure 3.2: Convergence test for the central lapse α_c (left panels) and the central density ρ_c (right panels) for the G9 (upper panels) and G11 (lower panels) grid configurations. For comparison we have scaled the results assuming second order convergence (black dotted lines). Convergence is more robust and observed longer for the higher resolved G11 data.

known from black hole perturbation theory (either scattering [Vishveshwara, 1970; Bernuzzi et al., 2008] or radially infalling particles [Davis et al., 1971; Davis et al., 1972; Nakamura et al., 1987; Lousto and Price, 1997]). To prove this statement, we show together with our numerical relativity calculation the $(l, m) = (2, 0)$ waveform obtained by a perturbative Gaussian scattering onto a Kerr black hole with spin parameter $\chi = \chi_{\rm BH} \sim 0.544$ [Harms et al., 2014]. We scale the amplitude by an arbitrary factor. The similarity of the numerical and perturbative waveforms reflects the basic mechanism of the emission process.

It is interesting to connect the waveform features with the collapse dynamics. In perturbation theory this is done, for instance, analyzing the background potential that drives the particle motion [Davis et al., 1971; Davis et al., 1972]. For the collapse dynamics we use a simplified spacetime diagram (left panel of Fig. 3.3) and connect the dynamics to the emitted GW signal using the retarded time, Eq.(A.1), i.e. using null geodesics of Schwarzschild spacetime (right panel). The spacetime diagram shows the evolution of contour density lines and the apparent horizon radius. Most of the matter contracts in an almost homologous way, while at high densities ($r \lesssim 2$) the contour lines slightly expand before collapsing. An apparent horizon is first found at $t \sim 188 M_\odot$ for the G11H-setup. Soon after horizon formation all the matter is inside the horizon and actually leaves the grid due to gauge conditions [Thierfelder, 2011; Thierfelder et al., 2011b]. The events marked as red dots in the spacetime diagram with horizontal lines correspond to the waveform features marked in the waveform. The minimum in the precursor corresponds to a time $t \sim 80 M_\odot$, at which the collapse actually sets in. The first maximum is related to the moment of time at which fluid particles significantly accelerate, and is slightly antecedent apparent

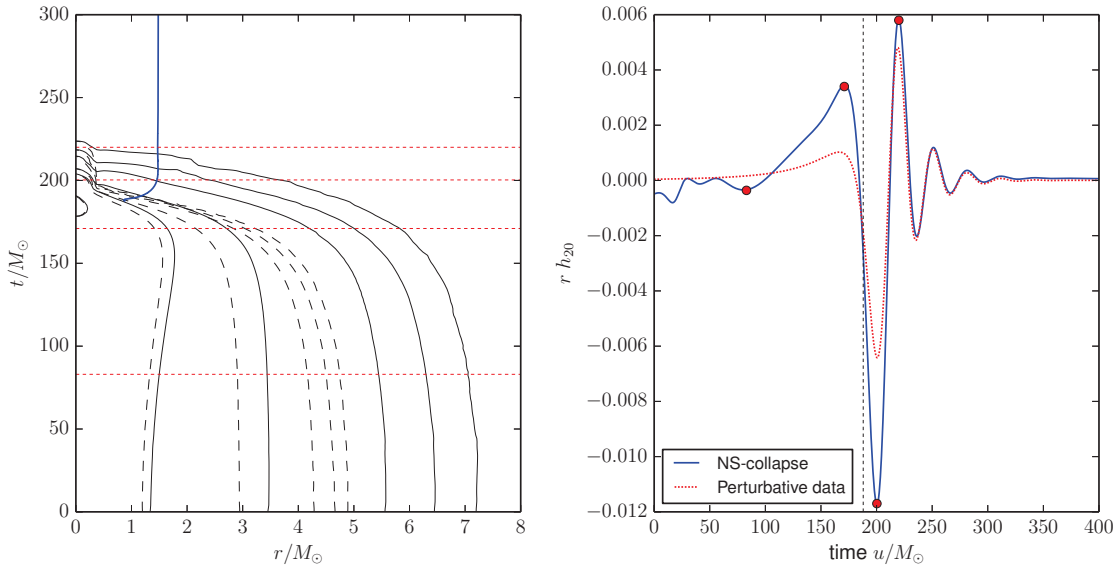

Figure 3.3: Spacetime diagram visualizing the collapse dynamics (left) and corresponding metric waveform rh_{20} for G11H in comparison with perturbation theory (right); cf. Tab. 3.1. Left panel: Contour lines in the equatorial plane (black solid) and perpendicular plane (black dashed) are shown for $\rho = 2.5 \times 10^{-5}, 10^{-4}, 2.5 \times 10^{-4}, 10^{-3}, 2.5 \times 10^{-3}, 10^{-2}$. The apparent horizon forms at $188M_\odot$ (blue line). Red dashed horizontal lines correspond to special marked features of the GW signal (right panel). Right panel: The $(2,0)$ mode compared with a perturbative Teukolsky simulation of black hole scattering [Harms et al., 2014], kindly provided by E. Harms. The horizon formation is marked with a vertical dashed line. Plot adapted from [Die7].

horizon formation.

We find that taking a worldline $r(t)$ of the spacetime diagram and employing the quadrupole waveform

$$Q_{20} \propto \ddot{I}_{20} \propto -2\dot{r}^2 - 2r\ddot{r}, \tag{3.1}$$

all qualitative features are captured up to horizon formation with I denoting the inertia tensor. The first maximum is determined by the competitive effect of the two terms: $-r\ddot{r} \geq 0$ and $-\dot{r}^2 \leq 0$. At $t < 150M_\odot$ the second term dominates, $-r\ddot{r} > \dot{r}^2$, but at later times $t > 150M_\odot$ the velocity term becomes comparable $\dot{r}^2 \sim -r\ddot{r}$. The maximum at $t \sim 175M_\odot$ results from the growth of $\dot{r}^2$ and the zero at $t \sim 180M_\odot$ comes from the instantaneous balance between the two terms. Shortly after black hole formation, when most mass is enclosed by the horizon and the horizon area stays approximately constant, the metric waveform has its absolute minimum followed by the maximum when all the matter is inside the horizon. Finally the black hole rings down to a stationary (unperturbed) state.

In addition to the metric waveform, we want to have a more detailed look at the curvature scalar $r\Psi_4$. The two dominant modes $(l,m) = (2,0)$ and $(l,m) = (4,0)$ are shown in Fig. 3.4 (left panels). The quadrupolar $l = 2$ mode, which is characterized by a burst of radiation peaking before black hole formation and followed by a ringdown

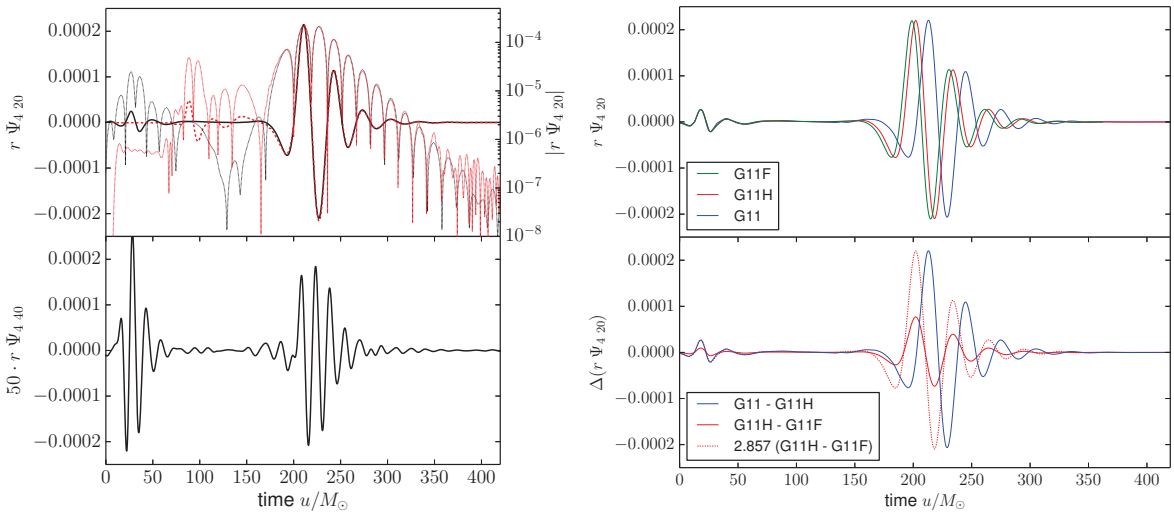

Figure 3.4: Rotating collapse curvature waveform $r\Psi_{4\,lm}$. Left: The $(l,m)=(2,0)$ mode (upper panel) in linear scale (solid lines) and its modulus in log scale (dotted lines). The waveform of [Reisswig et al., 2013a] is shown as a red dashed line for comparison. The $(l,m)=(4,0)$ mode is shown in the bottom panel. Right: Convergence study for $r\Psi_{4\,20}$. The results are scaled according to second order. Plot taken from [Die7].

pattern, carries most of the emitted GW energy $E_{GW}\sim 7.5\times 10^{-7}$.

The quasinormal ringing phase is more prominent on a log scale. We compare our results with [Reisswig et al., 2013a] (red line), extracted at future null infinity and kindly provided by the authors, and see good agreement between both data sets. Visually our results are also in agreement with [Giacomazzo and Perna, 2012].

According to the 10 local maxima between $u\in[225M_\odot, 380M_\odot]$, we calculate the fundamental complex frequencies $M\omega=(0.425,-0.0842)$ of the quasinormal ringing phase. These values agree within $(10\%,3\%)$ with perturbation theory [Berti et al., 2009] for a black hole with $\chi_{\rm BH}=0.544$.

The $(l,m)=(4,0)$-mode has an amplitude ~ 50 times smaller than the $(l,m)=(2,0)$ (Fig. 3.4). The amplitude is of the same order as the burst of radiation caused by the initial (constraint violating) perturbation, which shows that the data suffer from inaccuracies, and should be taken with caution in a physically meaningful analysis.

The right panels of Fig. 3.4 show a self-convergence test of the $(l,m)=(2,0)$ waveform. Approximately second-order convergence in the G11 data can be shown for the amplitude. However, pointwise convergence of the waveform is difficult to obtain due to the artificial pressure perturbation. Thus, simulations with different resolutions do not tend to the same continuum collapse time. Although the effect is rather small, it is visible in the convergence plot as a dephasing in the differences. For larger initial perturbations and lower resolutions the effect is larger. Probably, it can only be removed by using constraint satisfying initial data.

Additionally, we study uncertainties due to finite radius extraction. Waveforms of different radii $r=(100,150,200,250,300)M_\odot$ slightly differ in amplitude. The

amplitude uncertainty can be as large as 15% for $r = 100M_\odot$ and drops to below 5% for $r = 300M_\odot$, comparing to the linear extrapolated waveform at infinity. We want to emphasize that the use of the retarded time is essential in order to properly align the waveforms, i.e. the logarithmic term $2M \log(r/2M - 1)$ has a significant contribution at these radii; see Eq. A.1.

3.3 The end state: a spinning trumpet

For all resolutions an apparent horizon was found. The horizon mass and angular momentum, as measured by the apparent horizon finder [Lages, 2010], are $M_{\rm BH} \sim 1.859(1)M_\odot$ and $\chi_{\rm BH} \sim 0.543(7)$. The typical relative errors are at, or below, the $\sim 0.1\%$ level giving again evidence that our simulations can be seen as the most accurate simulations of the rotating neutron star collapse performed so far. In Fig. 3.5 (left panel) we show the differences between the horizon mass and spin with respect to the initial ADM quantities and those estimated by the apparent horizon.

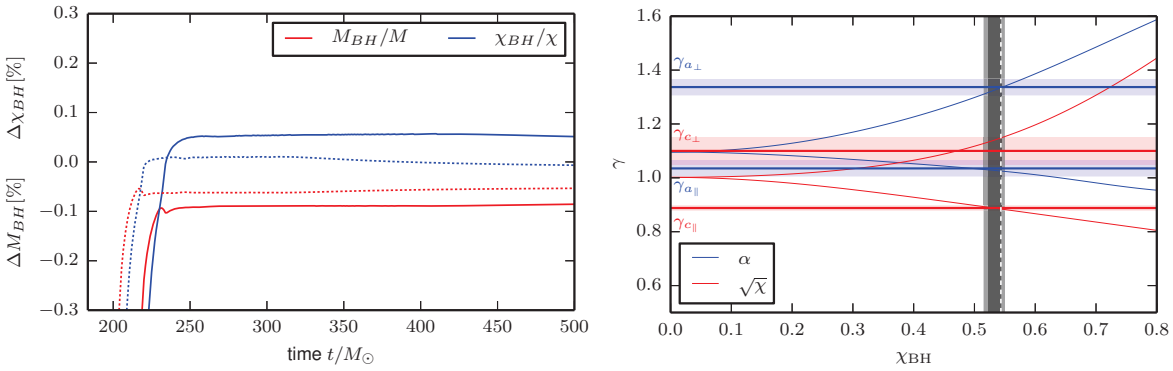

Figure 3.5: Left: Differences between the horizon mass (red) and dimensionless angular momentum (blue) of the final black hole with respect to the initial ADM quantities of the star. For both quantities the error is below 0.1%. G10 grid data are shown as solid lines; dashed lines are used for G11F data. Right: Characteristic behavior of metric variables $\sqrt{\chi}$ and α at $r = 0$. Exponents γ_c and $\gamma_{a,c}$ are extracted by fitting to Eq. (3.3) for G11H. The thin solid lines are spinning puncture data [Die9]. The thick lines are collapse data with error bars obtained from our simulations. Red (blue) color refers to $\sqrt{\chi}$ (α). The white dashed vertical line indicates the angular momentum from the apparent horizon finder. The dark shaded region represents the spin obtained from Eq. (3.5), the light shaded region the estimate according to $\gamma_{a,c}$. Plot adapted from [Die7].

When the moving puncture gauge is employed for spherical symmetric black holes, the spatial hypersurfaces approach an asymptotically cylindrical stationary solution, the *trumpet* [Hannam et al., 2007]. The end state of a spherical gravitational collapse asymptotically approaches the same trumpet solution found in vacuum simulations [Thierfelder et al., 2011b]. The spatial gauge conditions allow the matter to fall inwards into a region of spacetime that is not resolved by the numerical grid. Trumpet solutions are also found in dust (cf. [Staley et al., 2012]) and GWs collapse (cf. [Die5]).

According to the argumentation in spherical symmetry one can argue that puncture initial data evolve towards some stationary trumpet slices of Kerr [Hannam et al., 2009; Gabach Clement, 2010; Dain and Gabach Clement, 2009; Dennison et al., 2014] for rotating black holes. In [Die9] we presented a first numerical examination of spinning black holes in the moving puncture gauge. We will use these findings to show that the final state after the neutron star collapse is indeed described by a spinning puncture of mass M. In the following we present two arguments for this statement.

A first estimate is based on the leading order behavior of the (square root of the) conformal factor and the lapse function

$$\sqrt{\chi}(r \sim 0) \sim c_0 + c_1 r^{\gamma_c}, \text{ and } \alpha(r \sim 0) \sim a_0 + a_1 r^{\gamma_a} \ , \tag{3.2}$$

where γ_c and γ_a are characteristic exponents depending on the black hole spin (see the right panel of Fig. 3.5 and Fig. 2 of [Die9]). The exponents γ_c and γ_a are determined by the fitting functions

$$\sqrt{\chi}(r \sim 0) = c_0 + c_1 r^{\gamma_c}(1 + c_2 r + c_3 r^2), \tag{3.3}$$

$$\sqrt{\alpha}(r \sim 0) = a_0 + a_1 r^{\gamma_a}(1 + a_2 r + a_3 r^2). \tag{3.4}$$

The fit is calculated on the interval $r \in [0.01M_\odot, 0.3M_\odot]$ along the $x-$ and $z-$direction. The value parallel and perpendicular to the spin axis (z-axis) actually differ; cf. [Die9] and Fig. 3.5. We give error estimates based on different resolutions and different fitting intervals for r. The horizon spin (vertical white dashed line) lies within the uncertainties (light gray shaded region).

A second estimate is based on the fact that the trace of the extrinsic curvature differs for different spin magnitudes according to

$$\chi_{BH} \simeq \sqrt{1.41789 - 4.71218 \cdot \bar{K}(r=0)} \ , \tag{3.5}$$

when a stationary state is reached, where $\bar{K} = K/M \approx \hat{K}/M$; cf. again [Die9]. The value $\bar{K}(r=0) = K(r=0)/M$ can be extrapolated from a linear fit of K in the region $r \in [0.05M_\odot; 0.25M_\odot]$. We use an extrapolation parallel, orthogonal, and in an angle of 45° to the spin axis. For our slicing condition all these values coincide in principle and their differences can be used as an error estimate. We receive $K(r=0) = 0.1296$ along the x-axis, $K(r=0) = 0.1284$ along the z-axis, and $K(r=0) = 0.1293$ along the diagonal. Using Eq. (3.5) we get $\chi_{BH} = 0.533 \pm 0.011$ (dark gray shaded region), which agrees with the horizon spin within the measurement uncertainty.

Chapter 4

Spinning neutron stars in the CRV-approach

4.1 Construction of constant rotational velocity stars

To obtain constraint solved and consistent data, we have to solve the elliptic constraint equations together with the matter equations. Once these configurations are computed, they can be used as initial data for dynamical simulations. But also quasi-equilibrium configurations themselves contain important information about the system. In the following chapter we want to review important aspects of [Die6; Die13]. We discuss how to construct *constant rotational velocity* (CRV) data as first derived in [Tichy, 2011] and present results for single CRV stars (Sec. 4.2) and binary configurations (Sec. 4.3). For this purpose we will use the SGRID code, which is described in detail in [Die13] and briefly in Appendix D. Finally, we present the first dynamical evolutions of consistent and constraint solved spinning BNS configurations [Die6].

Basic equations and formalism

To construct quasi-equilibrium configurations, we have to solve the constraint Eqs. (2.28) together with the relativistic Euler (2.50) and the continuity equation (2.51) to ensure consistency of our data. For this purpose we will use the CTS approach explained in Sec. 2.1.3 including additional assumptions outlined below.

Assumptions for metric variables: The first assumption is the existence of an approximate symmetry vector

$$\boldsymbol{k} = \boldsymbol{\partial}_t + a_x \boldsymbol{\partial}_x + a_y \boldsymbol{\partial}_y, \tag{4.1}$$

where a_x, a_y can be specified depending on the particular problem. This vector is not necessarily a helical vector and can have a much more general form. Together with

the existence of $\boldsymbol{k}$ and the assumption that inside the stars

$$\mathcal{L}_{\boldsymbol{k}} g_{\mu\nu} = 0, \tag{4.2}$$

we assume conformal flatness and maximal slicing

$$\bar{\gamma}_{ij} = f_{ij}, \quad K := \gamma_{ij} K^{ij} = 0, \tag{4.3}$$

where f_{ij} describes the flat metric (δ_{ij} in Cartesian coordinates), which leads to ${}^{(3)}\bar{R} = 0$. These conditions are preserved infinitesimally in time, i.e., $\partial_t \bar{\gamma}_{ij} = \bar{u}_{ij} = \mathcal{L}_{\boldsymbol{k}} \bar{\gamma}_{\mu\nu} = 0$ and $\partial_t K = \mathcal{L}_{\boldsymbol{k}} K = 0$.

Finally, this leads to the following PDE system:

$$\bar{D}^2 \psi = -\frac{\psi^5}{32\alpha^2} (\bar{L}B)^{ij} (\bar{L}B)_{ij} - 2\pi\psi^5 E, \tag{4.4a}$$

$$(\bar{\Delta}\beta)^i = (\bar{L}B)^{ij} \bar{D}_j \ln(\alpha/\psi^6) + 16\pi\alpha\psi^4 S^i, \tag{4.4b}$$

$$\bar{D}^2(\alpha\psi) = \alpha\psi \left(\frac{7\psi^4}{32\alpha^2} (\bar{L}B)^{ij} (\bar{L}B)_{ij} + 2\pi\psi^4 (E + 2S) \right), \tag{4.4c}$$

with $\bar{D}_i = \partial_i$ in Cartesian coordinates and $B^i = \beta^i + k^i + \Omega\delta^{im}\epsilon_{mjl}(x^j - x^j_{\text{CM}})a^l$, where x^j_{CM} is the center of mass, Ω the orbital frequency, ϵ^{ijl} the Levi-Civita symbol, and a^l a unit vector pointing along the direction of the orbital angular momentum. Notice that also without Eq. (4.2) the same set of equations can be derived just assuming conformal flatness, maximal slicing and $\mathcal{L}_{\boldsymbol{t}} \bar{\gamma}_{ij} = 0$; see [Die13].

Assumptions for matter variables - the CRV approach: In addition to the considerations for the metric fields we have to make assumptions for the matter fields, most notably the fluid velocity; see [Tichy, 2011] and [Die13] for more details. As a first step, we split the four-velocity in a piece along k^μ, and one orthogonal to it (V^μ):

$$u^\mu = u^0 (k^\mu + V^\mu), \tag{4.5}$$

with $u^0 = -u^\nu n_\nu/\alpha$. While for irrotational binaries $\mathcal{L}_{\boldsymbol{k}} p_\mu = \mathcal{L}_{\boldsymbol{k}}(h u_\mu) = 0$ is correct, this statement does not hold for spinning neutron stars, which was shown in [Tichy, 2011]. To add spin to the individual neutron stars, we introduce the canonical momentum 1-form of a fluid element $p_i = P_i{}^\mu (h u_\mu)$ and split p_i in an irrotational part $D_i\phi$ and a rotational part w_i:

$$p_i = D_i \phi + w_i \tag{4.6}$$

or equivalently in four dimensions $p_\mu = \nabla_\mu \phi + w_\mu$. Although $\mathcal{L}_{\boldsymbol{k}} p_\mu \neq 0$ for spinning neutron stars, we assume

$$\mathcal{L}_{\boldsymbol{k}}(\rho u^0) = 0, \tag{4.7a}$$
$$\gamma_i{}^\mu \mathcal{L}_{\boldsymbol{k}}(\nabla_\mu \phi) = 0, \tag{4.7b}$$
$$\gamma_i{}^\mu \mathcal{L}_{\bar{\boldsymbol{k}}} w_\mu = 0, \tag{4.7c}$$

where $\bar{\boldsymbol{k}}$ points parallel to the worldline of the stars' center. Equation (4.7a)-(4.7c) can be interpreted in the following way: (i) the irrotational piece of the fluid velocity vanishes in corotating coordinates and (ii) the rotational piece is constant along the stars' center (which gives the method its name).

These assumptions also lead to

$$D_i \left(\rho \alpha u^0 V^i\right) = 0. \tag{4.8}$$

With the velocity field of the form

$$V^i = \frac{D^i \phi + w^i}{h u^0} - (\beta^i + k^i), \tag{4.9}$$

it is possible to write the continuity equation as

$$D_i \left[\frac{\rho\alpha}{h}(D^i\phi + w^i) - \rho\alpha u^0(\beta^i + k^i)\right] = 0. \tag{4.10}$$

Integrating and using $u^\mu u_\mu = -1$ leads to

$$h = \sqrt{L^2 - (D_i\phi + w_i)(D^i\phi + w^i)}, \tag{4.11}$$

with

$$L^2 = \frac{b + \sqrt{b^2 - 4\alpha^4 \left[(D_i\phi + w_i)w^i\right]^2}}{2\alpha^2}, \tag{4.12a}$$
$$b = \left[(k^i + \beta^i)D_i\phi - C\right]^2 + 2\alpha^2(D_i\phi + w_i)w^i, \tag{4.12b}$$

where the constant C is specified such that the baryonic mass of each star stays constant. Similarly, the Euler equation (2.50) can be simplified to

$$D_i \left[\frac{h}{u^0} + V^j D_j \phi\right] = 0, \tag{4.13}$$

or in an integrated form

$$\frac{h}{u^0} + V^j D_j \phi = -C = \text{const.}. \tag{4.14}$$

Throughout the thesis we specify

$$w^i = \delta^{il}\epsilon_{ljk}\omega^j(x^k - x^k_{C*}), \tag{4.15}$$

with the coordinate position of the stars center x^i_{C*} and the arbitrary angular velocity vector ω^i.

Specifying the symmetry vector: As described above the existence of an approximate symmetry vector k^α is a basic ingredient to derive the system of elliptic equations. In the past, helical Killing vectors were commonly used to construct quasi-circular configurations, see e.g. [Baumgarte and Shapiro, 2010] and references therein. For quasi-circular orbits with orbital frequency $\Omega_{\rm qc}$ and under the assumption of Cartesian coordinates the symmetry vector can be written as

$$k^\alpha_{\rm qc} = t^\alpha + \Omega_{\rm qc}\varphi^\alpha = t^\alpha + \Omega_{\rm qc}(xy^\alpha - yx^\alpha), \tag{4.16}$$

where the vectors $\boldsymbol{t} = \partial_t$, $\boldsymbol{x} = \partial_x$, $\boldsymbol{y} = \partial_y$, and $\boldsymbol{\varphi} = \partial_\varphi$ generate translations in the t, x, y, and φ directions. However, we can generalize this approach as outlined in [Die13][1].

Following [Moldenhauer et al., 2014] we assume for the symmetry vector k^α that:

(i) k^α approximately Lie-"drags" the flow;

(ii) k^α points along the motion of the star center;

(iii) each star center moves along a segment of an elliptic orbit at apoapsis, see Fig. 2 of [Moldenhauer et al., 2014].

The radii of the inscribed circles are $r_{\rm c_{1,2}} = (1-e)d_{1,2}$, where e is the input eccentricity parameter and $d_{1,2} = |x_{1,2} - x_{\rm CM}|$ are the distances of the stars from the center of mass assuming that apoapis occurs on the x-axis for simplicity. The two inscribed circles are centered around $x_{\rm c_{1,2}} = x_{1,2} \mp r_{\rm c_{1,2}} = x_{\rm CM} + e(x_{1,2} - x_{\rm CM})$. From (ii) it follows that

$$k^\alpha_{\rm ecc1,2} = t^\alpha + \Omega\,[(x - x_{\rm c_{1,2}})y^\alpha - y\,x^\alpha]. \tag{4.17}$$

Equation (4.17) can be generalized even more by adding a small radial component to the velocity field. This allows a slow inspiral of the orbit due to the emission of GWs. Assumption (ii) then tells us that assumption (iii) above needs to be modified to include a radial piece. Finally, the symmetry vector is given by:

$$k^\alpha_{1,2} = k^\alpha_{\rm ecc1,2} + \frac{v_r}{r_{12}}r^\alpha = t^\alpha + \Omega\,[(x - x_{\rm c_{1,2}})y^\alpha - y\,x^\alpha] + \frac{v_r}{r_{12}}r^\alpha \tag{4.18}$$

[1] Although no eccentric simulations were performed in this thesis, we want to present the principal idea how to construct the symmetry vector for completeness and refer the interested reader to the PhD-thesis of N. Moldenhauer.

where $r^\alpha = (0, x, y, z)$ points in the radial direction, $r_{12} = |x_1 - x_2|$ is the distance between the star centers and v_r is the radial velocity parameter. The parameter v_r can be obtained from an iterative procedure aimed at reducing the orbital eccentricity. In this case we also have to adjust the eccentricity parameter e that appears in $x_{c_{1,2}}$. The reason is that changing e amounts to changing the tangential orbital velocity, which is needed when we want non-eccentric inspiral orbits.

4.2 Single CRV-stars

The CRV approach also allows to construct single neutron stars for which we want to present results following the discussion in [Die13]. In case of a single neutron star x^i_{CM} coincides with the center of the star x^i_{C*} and $\Omega = 0$. The symmetry vector simply points along the time direction. If we specify the angular velocity ω^j as in the binary case, we can solve the CRV equations and obtain initial data for a single spinning star. Then, the individual spin χ can be defined by the ADM angular momentum and ADM mass.

Comparison with rigidly rotating stars

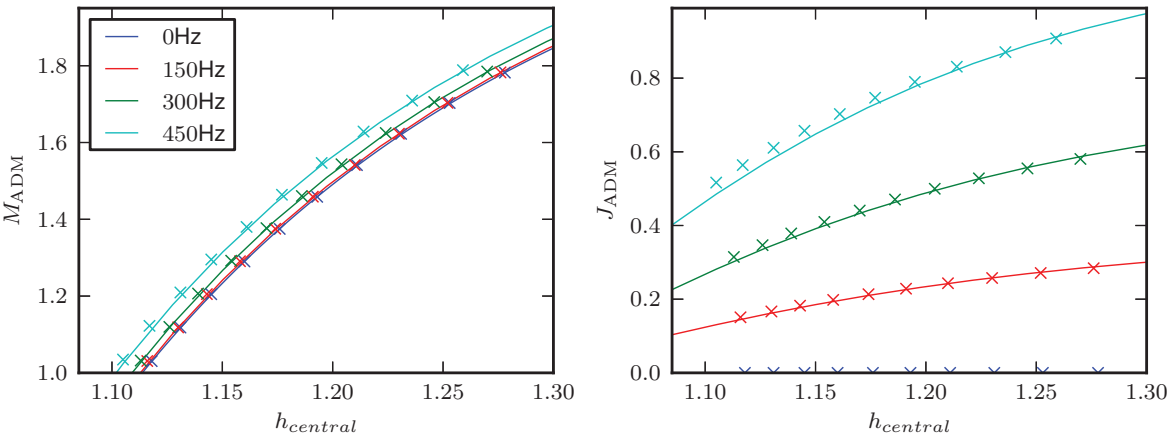

Figure 4.1: Comparison of single neutron stars with rigid rotation and CRV rotation using a simple polytropic EOS ($\Gamma 2.72$). ADM-mass (left) and ADM-angular momentum (right) as a function of the central enthalpy. The values for ω^z in the CRV-approach are 0.0, 0.005, 0.01, and 0.015 (crosses). The solid lines are computed for rigidly rotating stars with the LORENE library. Plot adapted from [Die13].

As a starting point of our investigation of single stars we want to compare single star CRV-results with rigidly rotating stars. In [Tichy, 2012] it is shown that the particular choice of the rotational velocity w^i, Eq. (4.15), leads to a negligible shear. Therefore, any substantial differential rotation can be neglected, which we want to verify in the following. For this purpose we construct single rotating neutron stars in the CRV approach and compare them with rigidly rotating stars. The rigidly rotating stars are computed with the module `Nrotstar` of the LORENE library [Gourgoulhon et al.].

Figure 4.1 summarizes our results for the $\Gamma 2.72$ simple polytrope. The left panel shows the ADM-mass, while the right panel refers to the ADM-angular momentum. Due to the fact that the angular velocity field ω^z does not agree with the frequency measured by an observer at infinity, we compute a sequence for constant ω^z and afterwards find a corresponding sequence of rigidly rotating stars by adjusting the frequency. The SGRID sequences are obtained for baryonic masses $M_b \in [1.1M_\odot, 2.0M_\odot]$ with $\Delta M_b = 0.1M_\odot$; cf. crosses in Fig. 4.1. We clearly see that for frequencies below 300Hz, rigidly rotating data and CRV data agree well once the frequency is adapted. For larger angular momentum discrepancies occur, caused by: (i) the reduced accuracy for faster rotating stars (see Fig. 4.2); (ii) the fact that the members of a sequence with different masses and the same ω^z may not all correspond to the same observable frequency.

Empirical ω-χ-relation

A fundamental problem of the CRV approach as implemented in SGRID is that although we can construct arbitrarily spinning neutron stars, we can not specify the ADM-mass and the ADM-spin *a priori*. To reduce computational costs, we want to investigate the dependence between the dimensionless spin of a single CRV-star and the input parameters of the SGRID code, namely the EOS, the baryonic mass M_b, and the angular velocity vector ω^i. For this reason we choose four different EOSs: SLy, ALF2, MS1b, and $\Gamma 2\kappa 124$ with baryonic masses $M_b \in [1.1, 1.7]$, spanning a range in the compactness of $\mathcal{C} \in (0.09, 0.20)$. The dimensionless angular momentum χ of a neutron star is given by

$$\chi = \frac{J_{\text{ADM}}}{M^2_{\text{ADM}}} = \frac{I\omega_{\text{obs}}}{M^2_{\text{ADM}}}, \tag{4.19}$$

with the moment of inertia I and $M_{\text{ADM}}, J_{\text{ADM}}$ denoting the ADM-mass and ADM-angular momentum. Unfortunately, ω_{obs}, the rotational frequency an observer at infinity would measure, is not known *a priori*. Therefore, we bring Eq. (4.19) in the form

$$\chi = f(\mathcal{C}, M_{\text{b}})\omega, \tag{4.20}$$

assuming a linear correlation between ω_{obs} and the angular velocity ω. Also, the gravitational mass of the single star (i.e. M_{ADM}) for this spacetime is not known in advance and, thus, needs to be absorbed in the function f. Via numerical experiments we find the phenomenological expression:

$$\chi = a_1(1 + m_1 M_{\text{b}})(1 + c_1\mathcal{C} + c_2\mathcal{C}^2 + c_3\mathcal{C}^3 + c_4\mathcal{C}^4)\omega, \tag{4.21}$$

where the parameters $a_1 = 88.8131$, $m_1 = 1.39522$, $c_1 = -19.003, c_2 = 152.99, c_3 = -570.678, c_4 = 806.896$ are obtained from a fit of the data presented in Fig. 4.2 (left panels) and where we use the compactness $\mathcal{C}$ of an irrotational star with the same

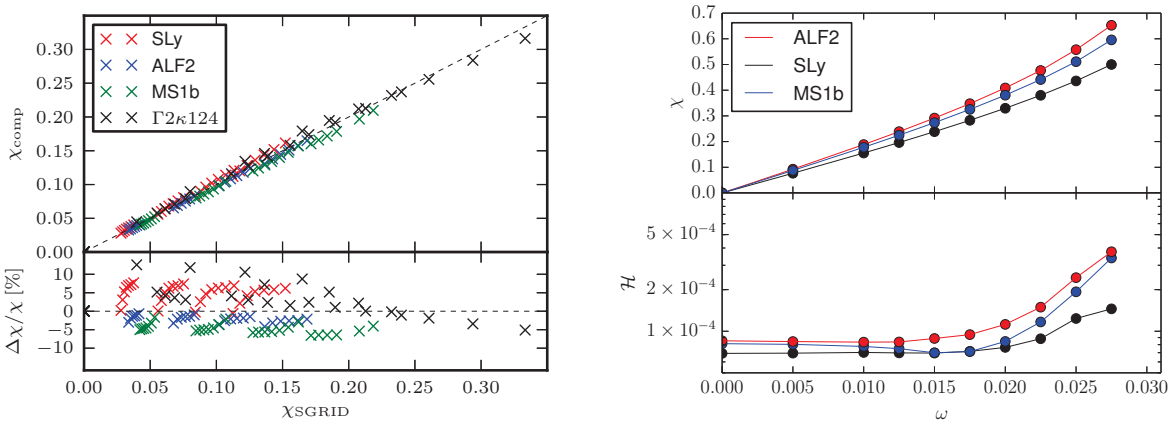

Figure 4.2: Left: Computed spin according to Eq. (4.21) (χ_{comp}) as a function of the spin obtained by SGRID for different EOSs. Absolute values (upper panel) and fractional residuals (bottom panel). Right: Dimensionless spin (top panel), and norm of the Hamiltonian constraint (bottom panel) versus the angular velocity ω for three EOSs (SLy, ALF2, and MS1b). Plot adapted from [Die13].

baryonic mass for simplicity. Specifically, we compute for four EOSs (SLy, ALF2, MS1b, $\Gamma 2\kappa 124$) and five different values of $|\boldsymbol{\omega}|$ ($\omega \in [0.000, 0.008]$ with $\Delta\omega = 0.002$), stars with baryonic masses of $M_b/M_\odot = (1.1, 1.2, 1.3, 1.4, 1.5, 1.6, 1.7)$. We want to stress that Eq. (4.21) is an empirical relation to reduce computational cost and might not represent underlying physical properties.

Fast rotating neutron stars

To date, the fastest spinning known neutron star is PSR J1748−2446ad, with a spin period of 1.4 ms, i.e. a frequency of 716 Hz [Hessels et al., 2006]. This corresponds most likely to a dimensionless spin of $\chi \in (0.3, 0.6)$. The large uncertainty results from our ignorance of the EOS and the mass of the star. We want to discuss in the following SGRID's capability of computing millisecond pulsars.

Considering such systems it is interesting to find the maximum spin value, which we can achieve with SGRID for different EOS, where we choose SLy, ALF2, and MS1b. The iteration process to achieve high spins is as follows: We start with $\omega = 0$ (zero spin) and increase the angular velocity in steps of $\Delta\omega = 0.005$ up to $\omega = 0.01$ and in smaller steps of $\Delta\omega = 0.0025$ up to $\omega = 0.0275$. We present the results in Fig. 4.2 (right panels). Depending on the EOS, maximum dimensionless spins of $0.5 \leq \chi_{\text{max}} \leq 0.7$ can be obtained (upper panel). The lower panel shows the L^2-norm of the Hamiltonian constraint in the domain covering the neutron star from the surface up to the inner Cartesian box; cf. Appendix D and [Die13]. We see that the Hamiltonian constraint is growing rapidly for angular velocities $\omega \geq 0.02$. We assume that this is related to the deformed shape of the neutron star for large spin magnitudes and the difficulties of the pseudo-spectral method handling corners; see Fig. 26 of [Die13].

4.3 Binaries within the CRV-approach

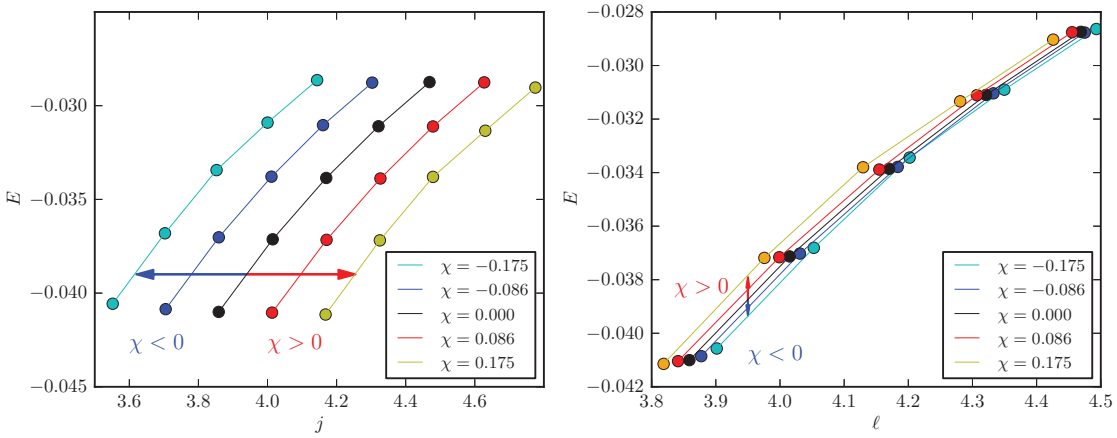

Figure 4.3: Reduced binding energy E vs. specific total momentum j (left) and reduced binding energy E vs. specific orbital angular momentum ℓ (right) for a binary system with $M_b^A = M_b^B = 1.4895$ and the SLy EOS. The influence of aligned and antialigned spin is shown with arrows.

To model spinning BNSs, a suitable ansatz for the fluid velocity field is necessary to incorporate spin and construct consistent quasi-equilibrium data. While spin is neglected completely in irrotational binaries or treated in an unphysical manner (assuming that the stars are tidally locked) in corotational binaries, the CRV approach [Tichy, 2011; Tichy, 2012] (see also [Die6; Die13]) offers the possibility to compute consistent and constraint solved data also for binary systems. Although alternative approaches have been proposed and employed in dynamical evolutions [Kastaun et al., 2013; Tsatsin and Marronetti, 2013; Kastaun and Galeazzi, 2015], they are based on non constraint-solved data and violate hydrodynamical stationarity conditions. Very recently also other groups started to use the CRV approach to construct BNS configurations [Tsokaros et al., 2015; Tacik et al., 2015] adapting the same framework employed in this thesis.

We present equilibrium sequences for SLy, $\Gamma 2\kappa 124$, MS1b, H4 (Table 2.2), the baryonic mass of the individual neutron stars for the piecewise polytropes is set to $M_b = 1.48945$, while the baryonic mass of the simple polytropes is $M_b = 1.62500$. For each of these EOSs we employ five different spin magnitudes, two spin configurations aligned with the orbital angular momentum ($\uparrow\uparrow$), one irrotational (00), and two antialigned ($\downarrow\downarrow$). While the baryonic mass is kept constant, the gravitational mass depends on the spin magnitude. Figure 4.3 shows the SLy sequence as a typical example. Each sequence essentially mimics an adiabatic evolution. We set $n_A = n_B = 24$, $n_\varphi = 8$, $n_{\text{Cart}} = 20$ for the $\Gamma 2\kappa 124$-sequence and increase the numbers to $n_A = n_B = 28$, $n_\varphi = 8$, $n_{\text{Cart}} = 24$ for the SLy, MS1b, and H4 EOSs to resolve the crust properly; cf. Appendix D.

While the natural quantity describing the spinning motion in the CRV framework is ω^i, cf. (4.15), no unambiguous definition of the stars' individual spins in a binary system exists. Therefore, we introduce two possible measurements of the spin magnitude[2].

The first estimate is given by comparing each spinning configuration with the irrotational setup. Under the assumption that the difference in the total angular momentum is due to the spins of the stars, we write

$$S \approx \frac{1}{2}\left(J_{\mathrm{ADM}}^{(\uparrow\uparrow,\downarrow\downarrow)} - J_{\mathrm{ADM}}^{(00)}\right) . \tag{4.22}$$

Finally, the dimensionless spin can by computed from $\chi = S/M_s^2$, where M_s is the gravitational mass of a single neutron star with the same ω^i.

Another method, first introduced in [Die6], uses single stars in isolation with the same rest mass and the same ω^i. For isolated stars it is possible to define properly the angular momentum $S_s = J_{\mathrm{ADM}}^s$ such that

$$S \approx S_s \quad \Rightarrow \quad \chi_s = S_s/M_s^2. \tag{4.23}$$

Both dimensionless spin values χ and χ_s agree within $\sim 10\%$ for the data we are considering, see e.g. Tab. 4.1 later. We observe that the spin value of χ_s gives generically results closer to post-Newtonian (PN) and effective-one-body (EOB) predictions, which is the reason why we consider in the following χ_s as the individual spin (e.g. Fig. 4.6).

We continue by investigating the constructed equilibrium sequences in terms of the reduced binding energy

$$E = \frac{1}{\nu}\left(\frac{M_{\mathrm{ADM}}}{M} - 1\right) \tag{4.24}$$

with $\nu = M^A M^B/M^2$ and $M = M^A + M^B$ and the specific total angular momentum

$$j = \frac{J}{\nu M^2}, \tag{4.25}$$

as well as the specific orbital momentum

$$\ell = \frac{L}{\nu M^2} = \frac{J - S^A - S^B}{\nu M^2}, \tag{4.26}$$

where $J = J_{\mathrm{ADM}}$.

Considering $E(j)$ and $E(\ell)$ is a gauge-invariant way to characterize the dynamics

[2]An alternative method was used recently in [Tacik et al., 2015] where the neutron star angular momentum is computed through quasi-local angular momentum integrals.

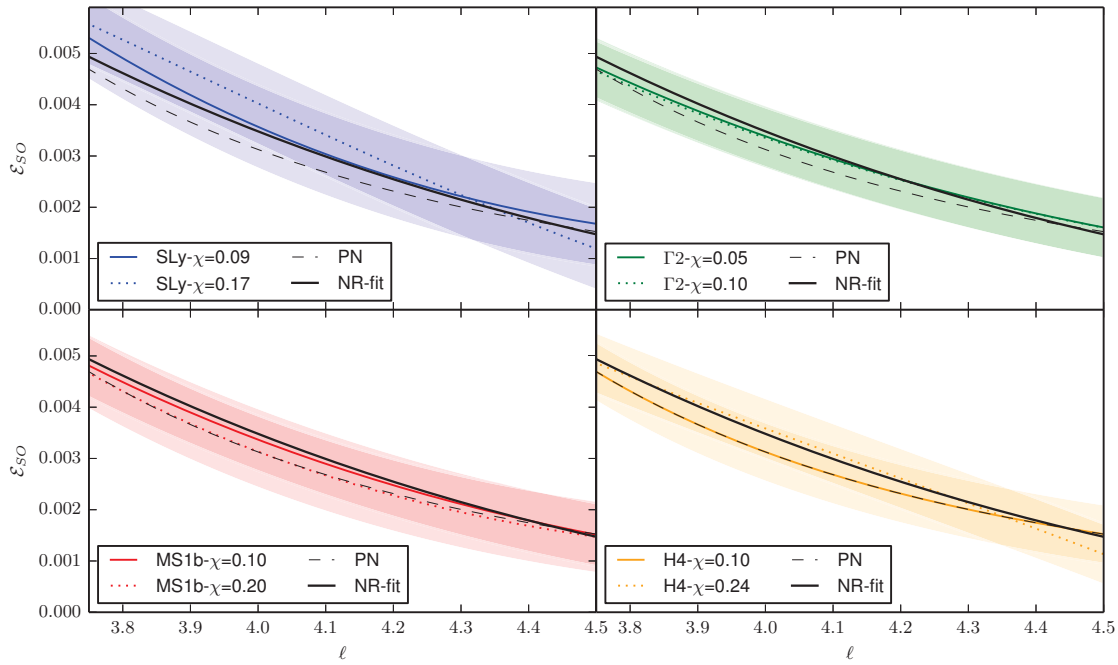

Figure 4.4: The spin-orbit coefficient $\mathcal{E}_{SO}$ of Eq. (4.30). We compare numerical results for the SLy (top left), $\Gamma 2\kappa 124$ (top right), MS1b (bottom left), and H4 (bottom right) EOSs with the predictions of the PN approximation Eq.(4.31) (black dashed lines). We also include an average line for our data in all panels (solid black lines). We estimate the numerical error bars from computations at different resolutions and show them as shaded regions.

of the binary [Damour et al., 2012a]. Regarding Fig. 4.3 it is noteworthy that the E-j-curves show a different ordering than the $E(\ell)$ curves. The subtraction of S^A, S^B in Eq. (4.26) compensates the horizontal shift of the curves, see arrows in the left panel. The E-j-relation does not make use of the assumption that S^A and S^B are the same as for isolated stars used in Eq. (4.26). Thus, they represent a more direct result of our numerical simulations[3]. However, the $E(\ell)$-curves (Fig. 4.3 right panel) allow to extract the dynamics of the system more easily. In fact, aligned configurations are less bound while antialigned configurations are more bound than the corresponding irrotational setup, which can be read off from the curves. This behavior follows from the fact that the spin-orbit interaction, which is the dominant spin-related effect, is repulsive for aligned spins and attractive for antialigned spins, e.g. [Damour, 2001].

To compute the spin-orbit contribution to the dynamics of the system, we write the binding energy as

$$E(\ell) = E_0 + E_{SO} + E_T + E_{SS} \ . \tag{4.27}$$

E_0 denotes the binding energy of a nonspinning binary (in the conformal flatness approximation), thus, it does not depend on the spin and matter effects; E_{SO} and E_{SS} represent the spin-orbit and spin-spin contributions, respectively; and E_T denotes the

[3]However, this method also assumes that M_s characterizes the mass of the neutron star in isolation and that it is a valid measure in the binary case.

tidal contribution. Assuming for simplicity that the dimensionless spins are identical $\boldsymbol{\chi} := \boldsymbol{\chi}^A = \mathbf{S}^A/(M^A)^2 = \boldsymbol{\chi}^B = \mathbf{S}^B/(M^B)^2$ the spin-orbit interaction is proportional to

$$E_{SO} \propto \boldsymbol{\chi} \cdot \mathbf{L} \propto |\boldsymbol{\chi}||\mathbf{L}| \cos(\angle(\boldsymbol{\chi}, \mathbf{L})). \tag{4.28}$$

Thus, the angle between $\boldsymbol{\chi}$ and the orbital angular momentum $\mathbf{L}$ defines whether E_{SO} acts repulsive or attractive. In our examples $\cos(\angle(\boldsymbol{\chi}, \mathbf{L}))$ is 1 for aligned and -1 for antialigned spins. Eq. (4.28) simplifies for these two possibilities and we can write

$$E_{SO} = \mathcal{E}_{SO}(\ell)\, \chi, \tag{4.29}$$

with $\chi = |\boldsymbol{\chi}|$. Notice that we impose that (i) the spin-orbit interaction does not depend on finite size effects; (ii) for the spins considered here ($\chi \lesssim 0.2$) the linear dependency of E_{SO} on χ captures the main dynamics.

According to our spin definition, Eq. (4.23), the spins are constant during the adiabatic evolution. This is a good approximation at these separations and also supported by binary black hole (BBH) [Lovelace et al., 2011; Scheel et al., 2015; Ossokine et al., 2015] and BNS simulations [Tacik et al., 2015]. We compute $\mathcal{E}_{SO}(\ell)$ by

$$\mathcal{E}_{SO}(\ell) = \frac{E_\chi^{(\uparrow\uparrow)}(\ell) - E_\chi^{(\downarrow\downarrow)}(\ell)}{2\chi}\,, \tag{4.30}$$

where for a given spin all the terms in Eq. (4.27) except E_{SO} cancel.

Figure 4.4 presents $\mathcal{E}_{SO}(\ell)$ for all four EOSs considered here: SLy, $\Gamma 2\kappa 124$, MS1b, and H4. We compute an average for all EOSs (solid line) and also include the linear in spin part of the 4 PN approximation from Eq. (8.23) in [Levi and Steinhoff, 2014]:

$$\begin{aligned} E_{SO} =& (\chi^A + \chi^B)\frac{\nu}{\ell^5}\left[2 + \frac{1}{\ell^2}\left(\frac{3\nu}{8} + 18\right) + \frac{1}{\ell}\left(\frac{5\nu^2}{16} - 27\nu + 162\right)\right] + \\ & \left(\frac{\chi^A}{q} + \chi^B q\right)\frac{\nu}{\ell^5}\left[\frac{3}{2} + \frac{99}{8\ell^2} - \frac{1}{\ell^4}\left(\frac{195\nu}{8} - \frac{1701}{16}\right)\right], \end{aligned} \tag{4.31}$$

with $q = 1, \nu = 1/4$, $\chi^A = \chi^B$ as a black dashed line.

We observe from the figure:

(i) $\mathcal{E}_{SO}(\ell)$ is always positive, therefore the SO-interaction is repulsive/attractive (positive/negative) according to the sign of $\angle(\boldsymbol{\chi}, \mathbf{L})$;

(ii) within the error bars no dependence on finite size effects is present;

(iii) the 4 PN and linear in spin expression, Eq. (4.31), given in [Levi and Steinhoff, 2014] captures the behavior of our conformally flat data.

Similar considerations as presented here for E_{SO} are also possible for E_{SS} and E_T. However, for the spin magnitudes and separations considered, E_{SS}, E_T lie within the uncertainty of our data. This is caused primarily by the large separation of the

two neutron stars, but dynamical evolutions can be used to extract the individual components. This is done in the following section.

4.4 Spinning neutron star evolutions

In this section we discuss the effect of the star's rotation on the binary dynamics. We start by describing the orbital motion, continue by investigating the merger remnant, and finalize with a discussion of the GW signal. Details about the investigated models are listed in Tab. 4.1. We employ the Einstein equations in the BSSN form (see Sec. 2.1.3) and use the 1+log and gamma-driver conditions (Sec. 2.1.2).

The numerical domain is made of 6 refinement levels, where the two outermost stay fixed and use 192 points, the 4 innermost are dynamically moved and also employ 192 points. The coarsest grid resolution is $h_0 = 4.80$ and the finest resolution is $h_5 = 0.15$. We test consistency using different resolutions; see Tab. II of [Die6]. The Berger-Oliger algorithm is employed for the time stepping [Berger and Oliger, 1984] on the inner levels. The prolongation and restriction operation is performed with the WENO4 algorithm, which will be the standard choice without conservative amr unless otherwise mentioned. Due to the fact that the Berger-Collela algorithm was not implemented in BAM at the time the simulations were performed, we decided to increase the number of points in the moving levels to cover the stars with larger boxes to reduce the systematic source of error by the non-conservative AMR.

Table 4.1: Equal mass configurations with baryonic mass of $M_b = 1.625$ with the $\Gamma 2\kappa 124$-EOS studied in this section. Spins are aligned ($\uparrow\uparrow$) or antialigned ($\downarrow\downarrow$) to the orbital angular momentum. The columns refer to: the name of the configuration, the rotational part of the fluid velocity ω^z, ADM mass $M_{\rm ADM}$, ADM angular momentum $J_{\rm ADM}$, the gravitational mass M_s of a single star in isolation, the spin S_s of an isolated star with the same ω^z and M_b, the corresponding dimensionless spin χ_s, the spin estimate S using the irrotational configuration as reference point Eq. (4.22), and the corresponding dimensionless spin χ. Γ configurations are evolved with a simple Γ-law EOS, P configurations with the corresponding polytrope (barotropic evolutions) for $\Gamma 2\kappa 124$. Table adopted from [Die6].

Name	ω^z	$M_{\rm ADM}$	$J_{\rm ADM}$	M_s	S_s	χ_s	S	χ
$\Gamma^{(\downarrow\downarrow)}_{050}$	-0.00230	2.99932	8.69761	1.51496	-0.11449	-0.0499	-0.10224	-0.0419
$\Gamma^{(\downarrow\downarrow)}_{025}$	-0.00115	2.99911	8.79949	1.51487	-0.05710	-0.0249	-0.05130	-0.0198
Γ_{000}	0.00000	2.99903	8.90209	1.51484	0.00000	0.0000	0.00000	0.0000
$\Gamma^{(\uparrow\uparrow)}_{025}$	0.00115	2.99907	9.00585	1.51487	0.05710	0.0249	0.05188	0.0252
$\Gamma^{(\uparrow\uparrow)}_{050}$	0.00230	2.99926	9.11092	1.51496	0.11449	0.0499	0.10442	0.0480
$P^{(\downarrow\downarrow)}_{100}$	-0.00460	3.00012	8.49472	1.51533	-0.23128	-0.1007	-0.20368	-0.0861
P_{000}	0.00000	2.99903	8.90209	1.51484	0.00000	0.0000	0.00000	0.0000
$P^{(\uparrow\uparrow)}_{100}$	0.00460	2.99993	9.32688	1.51533	0.23128	0.1007	0.21240	0.0950

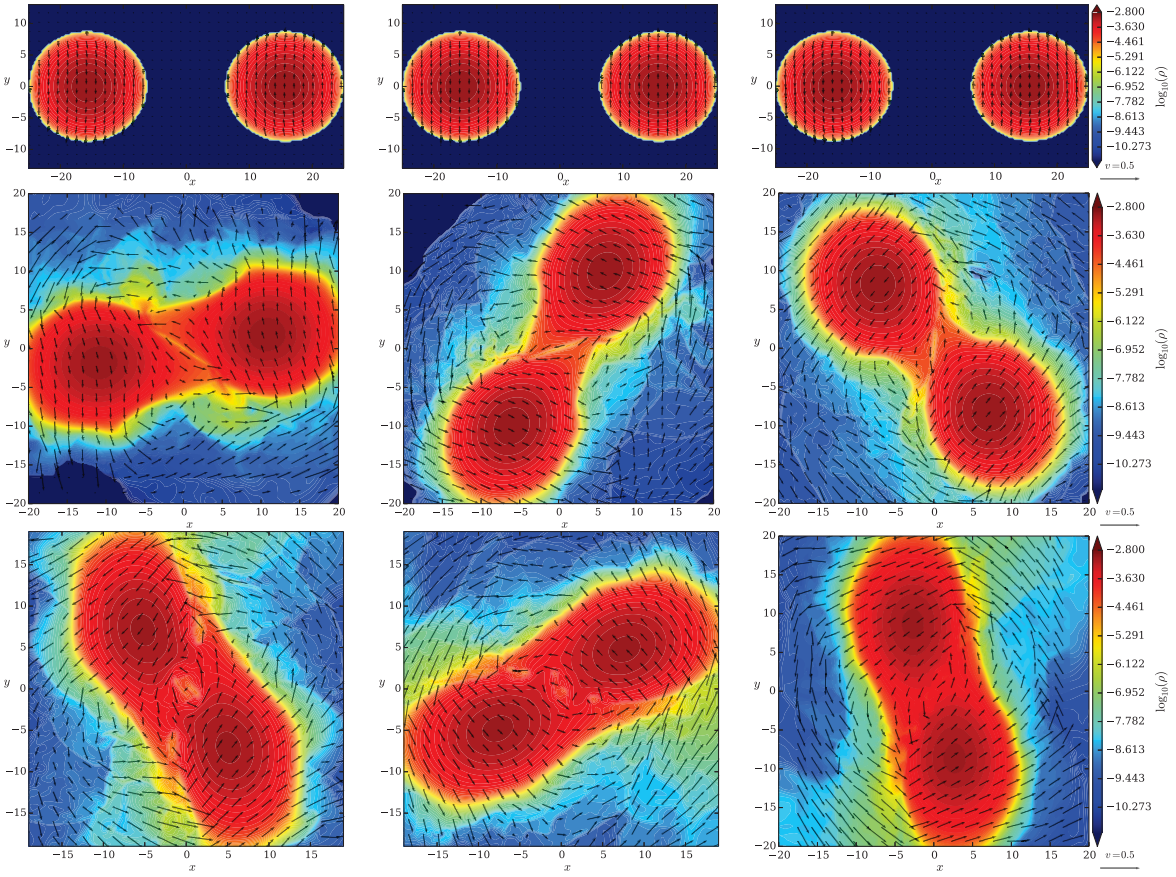

Figure 4.5: Snapshots of $\log_{10}\rho$ and (v^x, v^y) within the orbital plane. Rows from top to bottom refer to the initial configuration at $(0M, 0M, 0M)$, the moment of contact $(499M, 531M, 570M)$ and merger times $(543M, 587M, 628M)$. Columns from left to right: $\Gamma^{(\downarrow\downarrow)}_{050}$ Γ_{000} and $\Gamma^{(\uparrow\uparrow)}_{050}$.

4.4.1 Orbital motion

Figure 4.5 shows snapshots of the rest-mass density and fluid's velocity (v^x, v^y) on the orbital plane for $\Gamma^{(\downarrow\downarrow)}_{050}$ (left column), Γ_{000} (middle column), and $\Gamma^{(\uparrow\uparrow)}_{050}$ (right column). The top row shows results for the initial time slice. Only a very small difference in the velocity pattern due to the rotational state is visible. The central row represents the times when the two cores of the stars come in contact. The contact corresponds to the time when rest-mass density regions $\rho \sim 10^{-4} \sim 10^{14}$ g/cm^3 of the two stars touch each other and the shearing layer is formed, e.g. [Sekiguchi et al., 2011b]. The moment of contact happens at different times and different orbital phases for the three models shown in Fig. 4.5. This clearly shows that the moderate initial spins ($\chi \pm 0.05$) have a significant effect already after ~ 1.5 orbits. Finally, the last row represents snapshots at merger after ~ 3 orbits. We define throughout the thesis the merger as as the amplitude peak of the (2,2)-mode of the GW signal The remnants for all configurations are HMNSs with different angular momenta, see Sec. 4.4.2.

According to the merger times for spins aligned with the orbital angular momen-

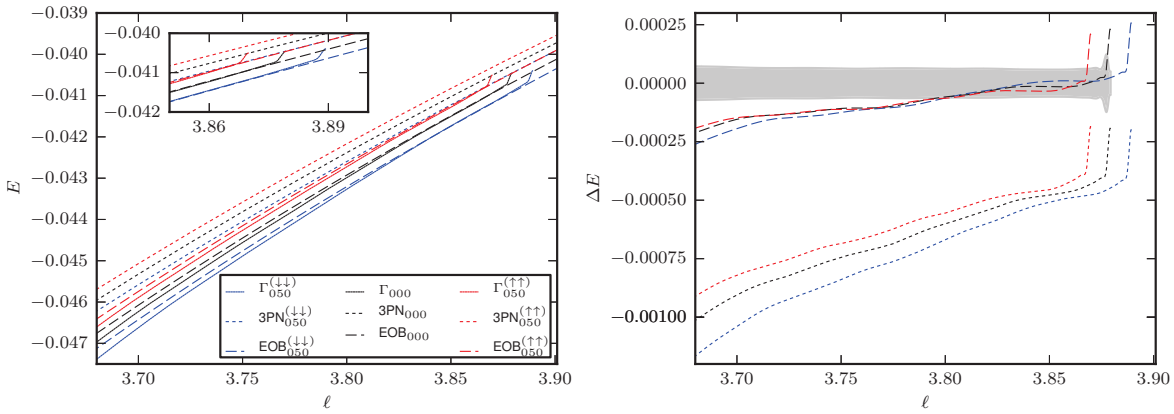

Figure 4.6: Binding energy E vs. orbital angular momentum ℓ curves for $\Gamma_{050}^{(\downarrow\downarrow)}$, $\Gamma_{050}^{(\uparrow\uparrow)}$, and Γ_{000}. Right: $E(\ell)$ curves for numerical data (solid lines), 3PN (dotted lines), and EOB (dashed lines). Left: Differences $\Delta E = E - E^X$ between numerical data and 3PN (dotted) and EOB curves (dashed). The uncertainty on the numerical data is shown in light gray. Plot adapted from [Die6].

tum the inspiral is longer for larger spin magnitudes, while for antialigned spins the inspiral is shorter for larger spin magnitudes. This effect can be understood in terms of spin-orbit interaction, cf. Sec. 4.3. As shown for quasi-equilibrium sequences, the spin-orbit interaction acts repulsive for aligned spins and attractive for antialigned spins. The analogous result in binary black hole simulations is sometimes called “hang-up” [Campanelli et al., 2006]. In BNS mergers it has been also found in [Kastaun et al., 2013; Tsatsin and Marronetti, 2013; Kastaun and Galeazzi, 2015] for constraint violating simulations. Spin-orbit interactions change quantitatively the binary dynamics already for moderate spins, which we want to show with gauge invariant binding energy vs. orbital angular momentum curves as for the quasi-equilibrium sequences. We compute the dimensionless binding energy and angular momentum per reduced mass as

$$E = \frac{(M_{\mathrm{ADM}}(t=0) - \mathcal{E}_{\mathrm{rad}})/M - 1}{\nu}, \tag{4.32}$$

$$\ell = \frac{L - \mathcal{J}_{\mathrm{rad}}}{M^2\nu}, \tag{4.33}$$

respectively, the isolation mass M refers to $M = 2M_s$ of Table 4.1. Equation (4.32) and (4.33) are the generalization of Eq. (4.24) and (4.26) to dynamical simulations including GW emission ($\mathcal{E}_{\mathrm{rad}}$ and $\mathcal{J}_{\mathrm{rad}}$). Equation (4.33) assumes (as for the quasi-equilibrium sequences) that the spin magnitude remains constant, see [Tacik et al., 2015].

We start our analysis by comparing the $E(\ell)$-curves of the early inspiral to *point-mass* analytical results, namely, a PN- and an EOB-curve. For the PN-curve, we employ the 3PN binding energy expression including next-to-next-to-leading order spin-orbit coupling given by Eq. (43) of [Nagar, 2011], and indicate it as $E^{\mathrm{3PN}}(\ell)$ (Fig. 4.6).

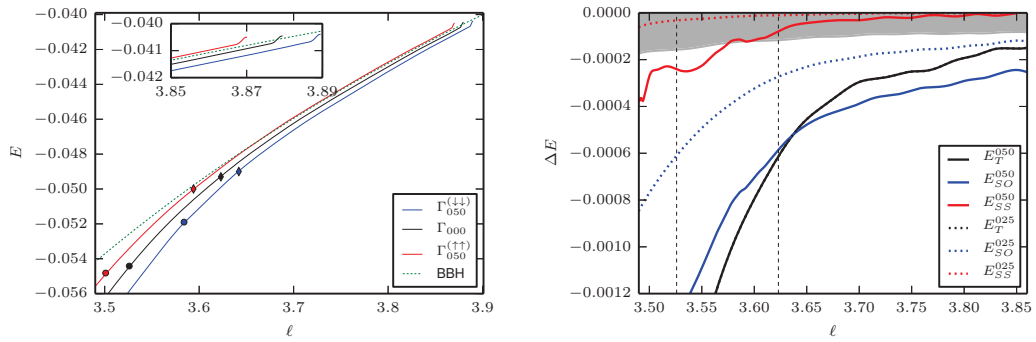

Figure 4.7: Binding energy E vs. reduced orbital angular momentum ℓ curves for Γ-models and a nonspinning BBH run. Left: $E(\ell)$ curves, diamonds indicate the approximate moment of contact and circles the moment of merger. Right: Different contributions to the binding energy in Eq. (4.34) –plotted all negative for easier comparison. The gray shaded region shows the uncertainty of the numerical data. The vertical dashed lines refer to the moment of contact and merger for Γ_{000}. E_T^{025} and E_T^{050} coincide in this plot. Doubling the spin approximately doubles the spin-orbit effect in the binding energy. For $\chi = 0.05$ the spin-orbit term is larger than the tidal term until $\ell \sim 3.65$. Plot adapted from [Die6].

Additionally, we consider the curve $E^{\rm EOB}(\ell)$, which is constructed within the EOB approach using the adiabatic limit[4]. More details about the EOB-model will be given in Sec. 6.1.

For a sufficiently large separation the conformally flat initial data sequences are close to the 3PN result, e.g. [Uryu et al., 2009]. But as mentioned in chapter 4.1 the conformally flat approximation introduces errors already at the 2PN level [Damour et al., 2000]. On the contrary the 3PN-EOB adiabatic curve has been found to correctly reproduce nonspinning numerical relativity data of different mass ratios up to $\ell \sim 3.55$ [Damour et al., 2012a].

The curves $E(\ell)$ are shown in Fig. 4.6 for $\Gamma_{050}^{(\downarrow\downarrow)}$, Γ_{000}, and $\Gamma_{050}^{(\uparrow\uparrow)}$, together with the PN and EOB curves. The right panel shows the differences $\Delta E = E - E^{\rm 3PN}$ and $\Delta E = E - E^{\rm EOB}$. As shown, the initial state, $\ell \sim 3.87$ (see inset), starts between the PN and EOB curves, but then the dynamics rapidly depart from the initial state. This variation is due to the emission of the artificial gravitational radiation related to the conformally flat assumption. The numerical evolution settles close to the EOB curve [Damour et al., 2012a; Bernuzzi et al., 2012a]. The difference between the EOB curves and the numerical data at early times is within the error-bars, which are estimated using different SGRID and BAM resolutions; see [Die6] for a more detailed explanation.

During the evolution the binaries binding energies depart systematically from the

[4] We use the spinning EOB model of [Damour, 2001]. The nonspinning part of the model is taken at 3PN [Damour et al., 2000] and it is resummed with a $(1,3)$ Padé approximant, e.g. [Bini and Damour, 2013; Pan et al., 2014]. The next-to-leading-order [Damour et al., 2008a] and next-to-next-to-leading-order [Nagar, 2011] spin-orbit couplings are included in the Hamiltonian. We restrict ourselves to the leading order spin-spin term for simplicity, which is sufficient for the spin magnitudes considered here.

Table 4.2: Dynamical quantities during orbital motion. Simulation time, GW frequency, angular momentum, and energy are reported at the moments of contact and merger. Note the contact time is not a well defined quantity, and just reported to give a rough estimate (see text). Table adapted from [Die6].[5]

Name	t_c/M	$M\omega_c$	ℓ_c	$E_c \times 10^2$	$t_{\rm mrg}/M$	$M\omega_{\rm mrg}$	$\ell_{\rm mrg}$	$E_{\rm mrg} \times 10^2$
$\Gamma_{050}^{(\downarrow\downarrow)}$	499	0.067	3.64	-4.89	543	0.124	3.58	-5.19
$\Gamma_{025}^{(\downarrow\downarrow)}$	514	0.065	3.63	-4.90	567	0.128	3.55	-5.36
Γ_{000}	531	0.069	3.62	-4.92	587	0.127	3.53	-5.44
$\Gamma_{025}^{(\uparrow\uparrow)}$	549	0.070	3.61	-4.95	610	0.125	3.51	-5.47
$\Gamma_{050}^{(\uparrow\uparrow)}$	570	0.071	3.60	-4.99	628	0.123	3.50	-5.48

EOB model, and the deviation becomes more and more significant. Note that the differences between EOB and numerical data are essentially independent of the spins (right panel of Fig. 4.6), which clearly suggests that the deviation is due to finite size effects, which are not included in the employed EOB model.

Figure 4.7 (left panel) shows the $E(\ell)$-curves for $\Gamma_{050}^{(\downarrow\downarrow)}$, Γ_{000}, and $\Gamma_{050}^{(\uparrow\uparrow)}$ together with a nonspinning BBH up to the merger. Around $\ell \sim 3.87$ (see inset) the BBH system is less bound than the irrotational configuration, but agrees within the data uncertainty. As observed in Fig. 4.6 tidal contributions become progressively more important and the systems become more bound, thus, deviating systematically from the BBH curve. At merger (Tab. 4.2), the aligned spin configurations are more bound than the antialigned ones.

In order to gain insight into the role of spin and tidal interactions during the merger phase we redo our analysis of the binding energy of Sec. 4.3 assuming

$$E \approx E_0 + E_{SO} + E_{SS} + E_T \ , \tag{4.34}$$

i.e. that the binding energy of a spinning BNS configuration can be approximated by the sum of four separate contributions: a nonspinning point-mass (black-hole) term E_0 (which is here not restricted to conformal flatness as in Sec. 4.3), a spin-orbit (SO) term E_{SO}, a spin-spin (SS) term E_{SS}, and a tidal (T) term E_T. The different terms have PN contributions starting from 1.5PN (SO), 2PN (SS) and 5PN (T). All terms can be calculated from our data, either the four runs Γ_{000}, $\Gamma_{050}^{(\uparrow\uparrow)}$, $\Gamma_{050}^{(\downarrow\downarrow)}$, BBH for $|\chi| = 0.05$ or Γ_{000}, $\Gamma_{025}^{(\uparrow\uparrow)}$, $\Gamma_{025}^{(\downarrow\downarrow)}$, BBH for $|\chi| = 0.025$. The SO term (cf. e.g. Eq. (2.7) of [Kidder, 1995]) has a structure of the form

$$E_{SO} = \frac{1}{r^3}\mathbf{L} \cdot \left[\mathbf{S}_A + \mathbf{S}_B + \frac{M_A - M_B}{M_A + M_B}\left(\frac{\mathbf{S}^B}{M^B} - \frac{\mathbf{S}^A}{M^A}\right)\right], \tag{4.35}$$

which simplifies in our case to $\propto \mathbf{L} \cdot \mathbf{S}$, so for aligned/antialigned spins $E_{SO} \propto$

[5] In contrast to the discussion in [Die6], we take the logarithmic term in Eq. (A.1) into account, which leads to minor differences in the results.

$\mathrm{sign}(S)|\mathbf{L}||\mathbf{S}|$. Similarly, the SS term has the structure

$$E_{SS} = \frac{1}{r^3}\left[3(\mathbf{n}\cdot\mathbf{S}^A)(\mathbf{n}\cdot\mathbf{S}^B) - (\mathbf{S}^A\cdot\mathbf{S}^B)\right] \tag{4.36}$$

with $\mathbf{n}$ denoting the unit vector pointing from one star to the other. The first term in Eq. (4.36) is exactly zero in our example and the remaining term $\propto \mathbf{S}^A\cdot\mathbf{S}^B$ does not change sign if both spins flip. A $(\uparrow\uparrow)$ binary configuration has a repulsive SO contribution ($E_{SO} > 0$), whereas a $(\downarrow\downarrow)$ configuration has an attractive SO contribution ($E_{SO} < 0$) to the binding energy.

The SO term is calculated by the combination of the aligned/antialigned spin runs with the same magnitude, i.e. $E_{SO} \approx (E^{(\uparrow\uparrow)} - E^{(\downarrow\downarrow)})/2$. Obviously, $E_0 \approx E_{\rm BBH}$ and $E_0 + E_T \approx E_{000}$. Thus, we calculate E_T from $E_{000} - E_{\rm BBH}$. Since the spins are parallel or anti-parallel to the orbital angular momentum, the SS term is estimated as $E_{SS} \approx (E^{(\uparrow\uparrow)} + E^{(\downarrow\downarrow)})/2 - E_{000}$. We present the different terms in the right panel of Fig. 4.7. The smallest contribution comes from the SS interaction, which is almost for the entire simulation within the uncertainty of our data. On the contrary the SO and tidal interactions are well resolved in our simulations even for moderate spins. For $\chi = 0.05$, the E_{SO} is the dominant contribution to the binding energy up to $\ell \sim 3.65$, then E_T becomes more dominant. This can be understood intuitively, because the dynamics reaches the hydrodynamical regime. Afterwards the differences between the E_{SO} and E_T become progressively larger. For $\chi = 0.025$ the E_T term is the largest negative term already at early simulation times. Thus, during the last three orbits the binding energy is "tidally dominated" as in the irrotational case.

Although the SS term is poorly resolved its presence is suggested by looking at the difference $E_{000} - E_{050}^{(\uparrow\uparrow)}$ and $E_{050}^{(\downarrow\downarrow)} - E_{000}$. These combinations are approximately $E_{SO} \pm E_{SS}$, where the SS contribution enters with a different sign. We can observe in our data that the former is less bound, while the latter is more bound by a small amount. Additionally, the inspection of $(E_{050}^{(\uparrow\uparrow)} - E_{050}^{(\downarrow\downarrow)})/2 - E_{BBH} \approx E_T + E_{SS}$ leads to a curve very close to E_T, but slightly more bound. Therefore, we conclude that no significant coupling between SO and tidal contributions is present.

4.4.2 Merger remnant

Due to the additional thermal support[6], all configurations evolved with the Γ-law EOS form a HMNS after merger. The angular momentum is radiated away in GWs on dynamical timescales, which leads to the collapse of the HMNS. In case of the irrotational configuration Γ_{000} this happens $\sim 1500M \sim 22$ ms after merger. The dimensionless angular momentum magnitude per reduced mass of the HMNS is approximately $j \approx \ell_{\rm mrg} \pm 2\chi/\nu$ (assuming again that the spin is constant during the

[6]Notice that we do not include magnetic fields nor cooling mechanisms and focus uniquely on thermal and centrifugal support.

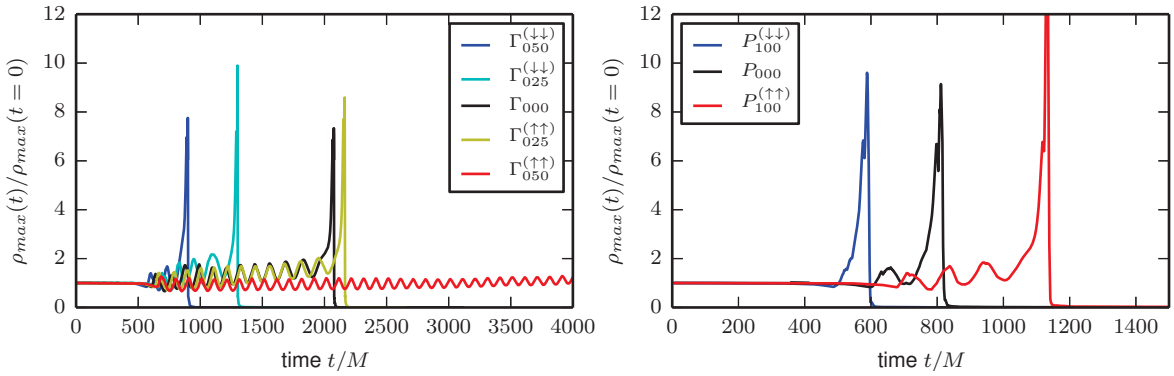

Figure 4.8: Evolution of the maximum mass-density $\rho_{max}(t)$ (normalized by its initial value) for the configurations $\Gamma_{050}^{(\uparrow\uparrow)}$, $\Gamma_{025}^{(\uparrow\uparrow)}$, Γ_{000}, $\Gamma_{025}^{(\downarrow\downarrow)}$, $\Gamma_{050}^{(\downarrow\downarrow)}$ (left panel) and for the configurations $P_{100}^{(\uparrow\uparrow)}$, P_{000}, $P_{100}^{(\downarrow\downarrow)}$ (right panel). Plot adapted from [Die6].

inspiral). We obtain $j \sim 3.18, 3.53, 3.9$ for $\Gamma_{050}^{(\downarrow\downarrow)}$, Γ_{000}, and $\Gamma_{050}^{(\uparrow\uparrow)}$. Therefore, it is clear that antialigned configurations will collapse earlier, whereas aligned configurations collapse later.

Figure 4.8 (left panel) shows the evolution of the maximum rest mass density, $\rho_{max}(t)$, for the configurations evolved with the Γ-law EOS. The main oscillations visible in the plot are caused by quasiradial modes. The averaged rest-mass density increases almost linearly over time to a critical density, $\rho_c \sim 2\rho_{max}(t=0)$ ($\rho_c \sim 1.2 \times 10^{15}$ g/cm^3), at which the collapse sets in. As motivated by the discussion above, we observe that antialigned configurations collapse earlier than the corresponding aligned setups. $\Gamma_{050}^{(\uparrow\uparrow)}$ survives even for several dynamical timescales and does not collapse until the end of the simulation ($t \sim 4000M$). We have not evolved this setup longer since other physical effects like magnetic fields and neutrino cooling play an important role after such a long simulation time, e.g. [Sekiguchi et al., 2011a; Paschalidis et al., 2012; Hotokezaka et al., 2013a; Deaton et al., 2013], and long-term simulations of the HMNSs can become inaccurate, in particular if no refluxing algorithm of a conservative mesh refinement is applied (see next chapter). However, assuming a linear trend in $\rho_{max}(t)$, the collapse should happen $\sim 167000M$ (~ 272 ms) after merger.

Regarding the barotropic evolution (right panel of Fig. 4.8) we observe a similar behavior as for the Γ-law EOS, although the collapse happens earlier, since no thermal support is included. Notably the $P_{100}^{(\downarrow\downarrow)}$ collapses promptly to a BH without forming a HMNS first.

During its evolution the HMNS oscillates and becomes progressively more compact. The most dominant modes are the quasiradial mode F, the $m = 2$ f-mode, and nonlinear combinations of them, e.g. [Shibata and Uryu, 2000; Stergioulas et al., 2011]. We project the rest-mass density onto spherical harmonics and consider for

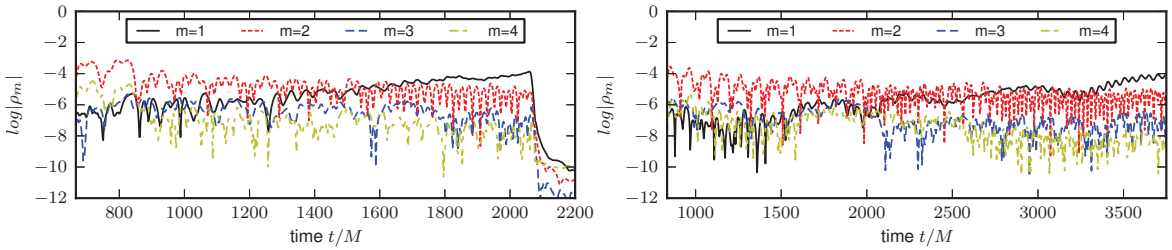

Figure 4.9: Evolution of projections $\rho_m(t)$ for $m = 1, 2, 3, 4$ and different models for Γ_{000} (left) and $\Gamma^{(\uparrow\uparrow)}_{050}$ (right). Plot adapted from [Die6].

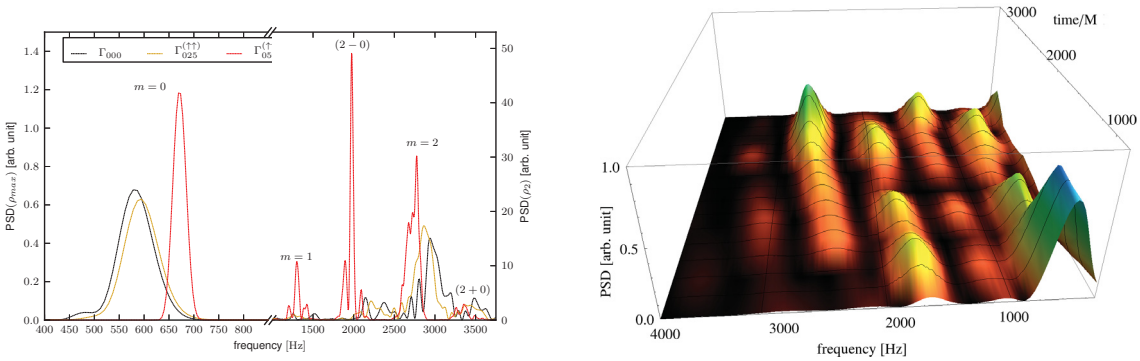

Figure 4.10: Fourier analysis of the rest mass projections ρ_m. Left: Power spectral density (PSD) of $\rho_{max}(t)$ and $\rho_2(t)$ for Γ_{000}, $\Gamma^{(\uparrow\uparrow)}_{025}$, $\Gamma^{(\uparrow\uparrow)}_{050}$ in arbitrary units. Right: Spectrogram of the quantity $\rho_{12}(t) \equiv \rho_1(t) + \rho_2(t)$ in the model $\Gamma^{(\uparrow\uparrow)}_{050}$. Plots taken from [Die6].

simplicity only $\rho(x, y, z = 0, t)$, i.e. restrict our analysis to the orbital plane $z = 0$:

$$\rho_m(t) = \int \rho(x, y, z = 0, t) e^{im\phi(x,y)} \mathrm{d}x\mathrm{d}y \ , \tag{4.37}$$

see e.g. [Baiotti et al., 2009]. The evolution of the first four modes $m = 1, 2, 3, 4$ is shown in Fig. 4.9 for Γ_{000} (left) and $\Gamma^{(\uparrow\uparrow)}_{050}$ (right). Dominant in the plot is the $m = 2$ mode, while actually, the projection with larger amplitude is the quasiradial ($m = 0$), cf. Fig. 4.8. But this frequency of the radial mode is too low to be seen in the GW spectrum. Regarding Fig. 4.9 the time evolution of $\rho_m(t)$ is qualitatively similar for different configurations. In all cases a growing $m = 1$ mode appears. We can not exclude the possibility that the growing $m = 1$ mode is triggered by numerical effects, but we think that it is a physical hydrodynamical effect due to mode couplings.

The frequencies of the modes can be extracted with a Fourier analysis of the ρ_m projections and ρ_{max}. We restrict the Fourier transform to the signal after merger. In Fig. 4.10 we show on the left the spectra of ρ_{max} and ρ_2 for $\Gamma_{000}, \Gamma^{(\uparrow\uparrow)}_{025}, \Gamma^{(\uparrow\uparrow)}_{050}$ and on the right the spectrogram of $\Gamma^{(\uparrow\uparrow)}_{050}$. We see clearly that the spectrum is built of few frequencies. An identification of the $m = 0, 1, 2$-modes together with nonlinear couplings "2 ± 0" [Stergioulas et al., 2011; Dimmelmeier et al., 2006; Baiotti et al., 2009] is possible.

Tab. 4.3 summarizes the peak frequencies for the different configurations. The

Table 4.3: Peak frequencies of the PSD of ρ_m and ρ_{max}. They are estimated by fitting a Gaussian of standard deviation σ. The value of the latter is reported in parenthesis. Table adapted from [Die6].

	$m=0$	$m=1$	$m=2$
Γ_{000}	584 (34)	1543 (38)	2974 (114)
$\Gamma_{025}^{(\uparrow\uparrow)}$	594 (34)	1482 (38)	2871 (103)
$\Gamma_{050}^{(\uparrow\uparrow)}$	671 (13)	1341 (13)	2738 (76)

frequency peak of the $m = 2$ mode shifts to higher frequencies in case of aligned configurations. This is because the HMNS with more angular momentum support is less compact, and the proper frequencies decrease if the compactness decreases[7]. For $\Gamma_{050}^{(\uparrow\uparrow)}$ the observed shift with respect to the irrotational configuration Γ_{000} is 236 Hz. The value is significant at the 1-σ level. On the contrary, the frequency of the quasiradial mode ($m = 0$) decreases for HMNS with larger angular momentum. As outlined in [Stergioulas et al., 2011], the quasiradial mode frequency depends on the compactness and also on how close the star model is to the collapse-instability threshold. The frequency is larger for larger compactness, but close to the instability threshold the frequencies can decrease since the instability threshold is a neutral point. This allows the interpretation of our data, where HMNSs with larger angular momentum support are further from collapse threshold and thus have higher frequencies.

Investigating the dynamical excitation of the modes by the spectrogram of the $\Gamma_{050}^{(\uparrow\uparrow)}$ (right panel) for the quantity $\rho_{12}(t) \equiv \rho_1(t) + \rho_2(t)$, we see that at early times the $m = 0$ (quasiradial) mode dominates, but after $t \sim 2000M$ the $m = 2$ becomes the main oscillation mode. A "drift" of the $m = 2$ mode towards higher frequencies is visible, which corresponds to the fact that the HMNS becomes more compact. The "$2 - 0$" coupling remains the secondary peak during the whole simulation and also the $m = 3$ and "$2 + 0$" modes are visible. At the end of the evolution the $m = 1$ mode has the largest power (cf. corresponding panel in Fig. 4.9). Thus, we can conclude from the spectrogram that (i) the modes are "instantaneously" characterized by relatively narrow peaks; (ii) different parts of the signal are dominated by different modes; (iii) a frequency drift is visible when the HMNS becomes more compact.

All configurations except $\Gamma_{050}^{(\uparrow\uparrow)}$ end with a black hole surrounded by a nonmassive accretion disk. We summarize important properties of the BH and disk systems in Tab. 4.4. We observe for antialigned spin configurations larger BH masses and higher spin magnitudes. The contrary effect is visible for aligned spin configurations. The spin of the black hole is larger for aligned configurations in barotropic evolutions. This does not hold for the Γ-law simulations, where the more massive disk carries more angular momentum. The maximum spin obtained in our simulations is $\chi_{\rm BH} \sim 0.84$,

[7] See [Dimmelmeier et al., 2006] for a similar discussion about sequences for single rotating stars with the same rest mass.

Table 4.4: Important quantities for the merger remnant. Stated are the black hole mass, the dimensionless spin of the black hole, and the absolute disk mass of the surrounding disk as well as the percentage with respect to the total baryonic mass. Table taken from [Die6].

	$\Gamma_{050}^{(\downarrow\downarrow)}$	$\Gamma_{025}^{(\downarrow\downarrow)}$	Γ_{000}	$\Gamma_{025}^{(\uparrow\uparrow)}$	$\mathrm{P}_{100}^{(\downarrow\downarrow)}$	P_{000}	$\mathrm{P}_{100}^{(\uparrow\uparrow)}$
M_{BH}	2.92	2.88	2.85	2.86	2.95	2.94	2.89
χ_{BH}	0.80	0.79	0.78	0.79	0.81	0.83	0.84
$M_{\mathrm{b,\ disk}}$	0.039	0.068	0.081	0.082	0.006	0.021	0.065
$M_{\mathrm{b,\ disk}}/M_b$	1.2%	2.1%	2.5%	2.5%	0.2%	0.6%	2.0%

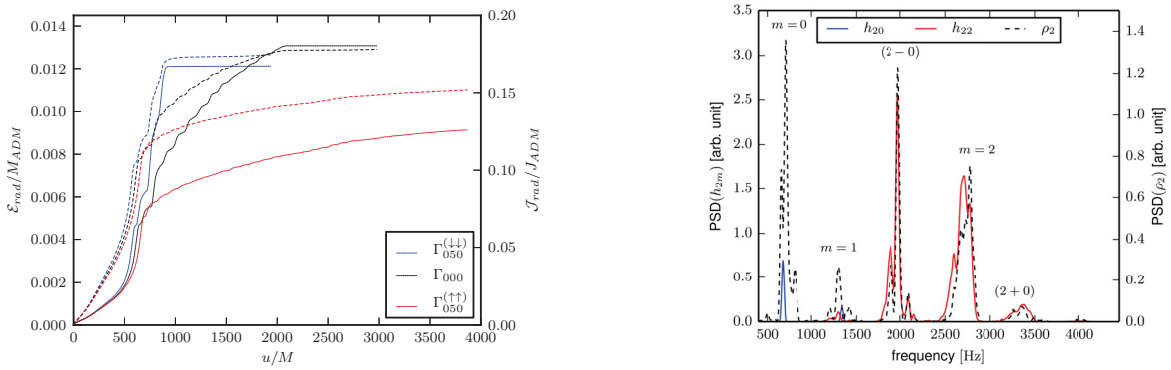

Figure 4.11: Left: Energy (solid lines) and angular momentum (dashed lines) radiated in GWs for models $\Gamma_{050}^{(\downarrow\downarrow)}$,$\Gamma_{000}$, and $\Gamma_{050}^{(\uparrow\uparrow)}$. Right: Fourier analysis of the $l = 2$ postmerger waveform multipoles and matter projection ρ_2 for model $\Gamma_{050}^{(\uparrow\uparrow)}$. The waveform frequencies strongly correlate with the fluid's modes. Plots taken from [Die6].

which is consistent with the findings of [Kastaun et al., 2013; Kastaun and Galeazzi, 2015]. The uncertainty on the black hole mass calculated from different resolutions is ~ 0.01, and even larger for the angular momentum.

4.4.3 Gravitational radiation

Due to the different angular velocities of the neutron stars, the total energy and angular momentum emitted in GWs differs for the investigated models (Fig. 4.11-left panel). The irrotational configuration emits about 1.2% of the initial ADM mass and 18% of the initial angular momentum. The $\Gamma_{050}^{(\downarrow\downarrow)}$ emits the same amount in half the time. The $\Gamma_{050}^{(\uparrow\uparrow)}$ emits 0.8% of the initial mass and about 15% of the initial angular momentum until the end of the simulation. The largest amount, $\sim 97\%$, of the energy is radiated in the $(l, m) = (2, 2)$ multipole, which is the main emission channel. But as discussed above, in the postmerger phase also other channels are clearly excited; the largest amplitudes are observed in the $(2, 0), (3, 3), (3, 2)$, and the $(4, 4)$ modes (in descending order).

Figure 4.12 (left panel) shows the $l = m = 2$ inspiral waveforms for $\Gamma_{050}^{(\downarrow\downarrow)}$, Γ_{000} and $\Gamma_{050}^{(\uparrow\uparrow)}$ plotted over the retarded time u. In the upper-left panel the real part and amplitude of the $l = m = 2$ mode and in the lower-left panel the GW frequency $M\omega_{22} = -\Im(\dot{h}_{22}/h_{22})$ is shown. The merger happens at $t_{\mathrm{mrg}}/M \sim 543,\ 587,\ 628$

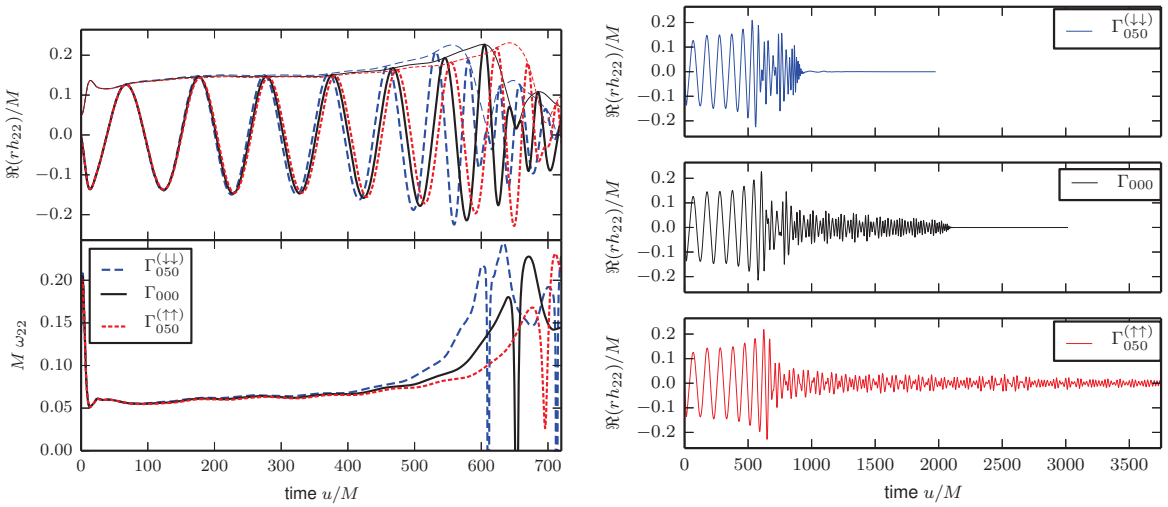

Figure 4.12: GW signal for models $\Gamma_{050}^{(\downarrow\downarrow)}$, Γ_{000}, and $\Gamma_{050}^{(\uparrow\uparrow)}$. Left: Inspiral waveforms $\Re(r\,h_{22})$ and $r|h_{22}|$, and frequency $M\omega_{22}$. Right: Full signal $\Re(r\,h_{22})$. Plots taken from [Die6].

for $\Gamma_{050}^{(\downarrow\downarrow)}$, Γ_{000}, and $\Gamma_{050}^{(\uparrow\uparrow)}$, respectively (see also Fig. 4.5). From Tab. 4.2 a linear dependency of the merger frequencies from the angular momentum of the initial configuration is visible; the only exception is the $\Gamma_{050}^{(\downarrow\downarrow)}$ model, where the GW signal seems to be corrupted around merger. This linear trend is also visible in the binding energy, and will be discussed in Sec. 6.2.2 (see Fig. 6.6). In a less quantitative form, we can make similar statements for the moment of contact, although the moment of contact has no strict definition. Comparing the accumulated phase of the GW, the irrotational configuration emits 7.0 GW cycles to merger, $\Gamma_{050}^{(\downarrow\downarrow)}$ 6.3 cycles, and $\Gamma_{050}^{(\uparrow\uparrow)}$ 7.3 cycles. This phase difference results mainly from the spin-orbit interactions described in Sec. 4.4.1.

Figure 4.12 (right panel) shows the complete waveform of the $(2,2)$ mode. The amplitude of the waves and Fig. 4.11 show that for an earlier collapse more energy and angular momentum is emitted in a shorter time. Similar to the discussion in Sec. 4.4.2 we perform a Fourier analysis of the $(2,2)$ and $(2,0)$ multipoles, and compare with the mode analysis of the matter fields. Figure 4.11 (right panel) shows the spectrum for $\Gamma_{050}^{(\uparrow\uparrow)}$ after the merger. Regarding only the postmerger signal, a strong correlation between the spectra of the waves and matter modes exists. The first part of the signal with frequencies up to $\sim 1.2-1.3$ kHz will be dominated by the inspiral. Therefore, no observation of the quasiradial mode frequency of the HMNS is possible.

As discussed in the next chapters and shown e.g. in [Oechslin and Janka, 2007; Bauswein and Janka, 2012; Stergioulas et al., 2011; Hotokezaka et al., 2013a; Bauswein et al., 2014; Takami et al., 2014; Takami et al., 2015a] the frequencies of the peaks of the GW postmerger spectrum depend strongly on the chosen EOS. Recent studies suggest that this dependencies can give constraints on the EOS for supranuclear densities. The long wave train of model $\Gamma_{050}^{(\uparrow\uparrow)}$ shows a similar frequency shift

caused by the rotational state, which implies that even moderate spin magnitudes may be important[8]. In fact, a shift towards lower frequencies for antialigned configurations can be in favor of a possible GW detection by advanced interferometers.

[8]Very recently [Bauswein et al., 2015] studied the influence of the rotational state in smooth particle hydrodynamics simulations under the assumption of conformal flatness and no noticeable frequency shift was present for the DD2 EOS. However, we also found a frequency shift in [Die13] of $\sim 60\mathrm{Hz}$ for the SLy EOS and larger spin magnitudes and also [Kastaun and Galeazzi, 2015] report a frequency shift. This shows that the magnitude of the shift probably depends on the employed EOS, which has to be quantified with further studies.

Chapter 5

Binary neutron star mergers for different EOSs and mass-ratios

After the intense discussion about the influence of the individual spin on the dynamics and GW signal in BNS systems, we want to focus in this chapter on the EOS and the mass ratio. We combine this study with the investigation of the performance of the conservative mesh refinement algorithm introduced in Sec. 2.2.4.

As outlined, a systematic source of error is the mass violation caused by material, which crosses refinement boundaries when the standard BO algorithm is applied and no additional refluxing algorithm is employed. We have tried to reduce this effect by increasing the box size covering the neutron stars in the previous chapter. However, this procedure (i) increases the computational costs significantly[1] and (ii) still does not solve the problem completely. Instead, the BC algorithm (Sec. 2.2.4) corrects the flux across refinement boundaries and improves the accuracy and mass conservation dramatically. We tested the new algorithm in single neutron star spacetimes, see Appendix B, and found an overall better performance for the considered examples. Now we are following [Die8] and show the improvements obtained in BNS simulations when an additional correction step is employed.

Important properties and details of the configurations are stated in Tab. 5.1. Most initial data used in the subsequent part are calculated with the LORENE code [Gourgoulhon et al.], while one configuration (MS1b-094194-c) is computed with SGRID. We evolve models with and without the correction step of the BC algorithm. In addition to binaries with mass ratios of $q = 1.0$ and $q = 1.16$, we present a $q = 1.5$ binary with total mass of $M = 2.50 M_\odot$ using the stiff MS1b EOS (MS1b-100150) and a $q = 2.06$ binary with total mass of $2.89 M_\odot$ (MS1b-094194-c). Although the last two configurations might be seen as extreme, there is no reason to exclude them. In fact population synthesis models even suggest a possible channel for producing such binaries and the absence of these in observational data might only be a selection

[1] Notice that the overall algorithm scales cubically with the number of grid points.

Table 5.1: BNS configurations and grid setups. The first column defines the configuration name. Next 11 columns describe the physical properties: EOS, gravitational mass of the individual stars $M^{A,B}$, baryonic mass of the individual stars $M_b^{A,B}$, stars' compactnesses $\mathcal{C}^{A,B}$, tidal coupling constant κ_2^T (Eq. (6.12)), initial GW frequency $M\omega_{22}^0$, ADM-Mass $M_{\rm ADM}$, ADM-angular momentum $J_{\rm ADM}$. Next 8 columns describe the grid configuration: finest grid spacing h_{L-1}, radial resolution inside the shells h_r, number of points n (n^{mv}) in the fix (moving) levels, radial point number n_r and azimuthal number of points n_θ in the shells, inradius up to which GRHD equations are solved r_1, and the outer boundary r_b. Notice that we divide most configurations in 3 different grid setups R1, R2, R3 (compare simulation name). The configurations are evolved with and without the C step, which we denote with a "c" or "n" in the configuration name. Table adapted from [Die8].

Name	EOS	M^A	M^B	M_b^A	M_b^B	$\mathcal{C}^A$	$\mathcal{C}^B$	κ_2^T	$M\omega_{22}^0$	M_{ADM}	J_{ADM}	h_{L-1}	h_r	n	n^{mv}	n_r	n_θ	r_1	r_b
MS1-135135-R2c	MS1	1.35	1.35	1.46	1.46	0.139	0.139	325	0.052	2.676	7.16	0.240	7.68	160	80	160	70	614	1870
MS1-135135-R2n	MS1	1.35	1.35	1.46	1.46	0.139	0.139	325	0.052	2.676	7.16	0.240	7.68	160	80	160	70	614	1870
MS1-125145-R2c	MS1	1.45	1.25	1.61	1.38	0.148	0.129	331	0.052	2.673	7.10	0.240	7.38	160	80	160	70	590	1870
MS1-125145-R2n	MS1	1.45	1.25	1.61	1.38	0.148	0.129	331	0.052	2.673	7.10	0.240	7.38	160	80	160	70	590	1870
H4-135135-R2c	H4	1.35	1.35	1.47	1.47	0.147	0.147	210	0.052	2.674	7.13	0.2232	7.1424	160	80	160	70	571	1739
H4-135135-R2n	H4	1.35	1.35	1.47	1.47	0.147	0.147	210	0.052	2.674	7.13	0.2232	7.1424	160	80	160	70	571	1739
H4-125145-R2c	H4	1.45	1.25	1.59	1.35	0.158	0.136	212	0.052	2.674	7.10	0.230	7.36	160	80	160	70	589	1792
H4-125145-R2n	H4	1.45	1.25	1.59	1.35	0.158	0.136	212	0.052	2.674	7.10	0.230	7.36	160	80	160	70	589	1792
ALF2-135135-R2c	ALF2	1.35	1.35	1.49	1.49	0.161	0.161	138	0.052	2.675	7.15	0.202	6.464	160	80	160	70	517	1574
ALF2-135135-R2n	ALF2	1.35	1.35	1.49	1.49	0.161	0.161	138	0.052	2.675	7.15	0.202	6.464	160	80	160	70	517	1574
ALF2-125145-R2c	ALF2	1.45	1.25	1.61	1.37	0.172	0.150	140	0.052	2.673	7.08	0.200	6.4	160	80	160	70	512	1558
ALF2-125145-R2n	ALF2	1.45	1.25	1.64	1.37	0.172	0.150	140	0.052	2.673	7.08	0.200	6.4	160	80	160	70	512	1558
SLy-135135-R2c	SLy	1.35	1.35	1.49	1.49	0.174	0.174	74	0.052	2.675	7.15	0.1824	5.8368	160	80	160	70	467	1421
SLy-135135-R2n	SLy	1.35	1.35	1.49	1.49	0.174	0.174	74	0.052	2.675	7.15	0.1824	5.8368	160	80	160	70	467	1421
SLy-125145-R2c1	SLy	1.45	1.25	1.62	1.38	0.187	0.161	75	0.052	2.673	7.07	0.1824	5.8368	160	80	160	70	467	1421
SLy-125145-R2n1	SLy	1.45	1.25	1.62	1.37	0.187	0.161	75	0.052	2.673	7.07	0.1824	5.8368	160	80	160	70	467	1421
SLy-125145-R2c2	SLy	1.45	1.25	1.62	1.37	0.187	0.161	75	0.052	2.673	7.07	0.188	6.106	160	80	160	70	488	1464
SLy-125145-R2n2	SLy	1.45	1.25	1.62	1.37	0.187	0.161	75	0.052	2.673	7.07	0.188	6.106	160	80	160	70	488	1464
MS1b-100150-R1c	MS1b	1.50	1.00	1.64	1.06	0.157	0.109	461	0.042	2.479	6.16	0.291	9.312	128	64	128	56	596	1820
MS1b-100150-R1n	MS1b	1.50	1.00	1.64	1.06	0.157	0.109	461	0.042	2.479	6.16	0.291	9.312	128	64	128	56	596	1820
MS1b-100150-R2c	MS1b	1.50	1.00	1.64	1.06	0.157	0.109	461	0.042	2.479	6.16	0.2328	7.4496	160	80	160	70	596	1814
MS1b-100150-R2n	MS1b	1.50	1.00	1.64	1.06	0.157	0.109	461	0.042	2.479	6.16	0.2328	7.4496	160	80	160	70	596	1814
MS1b-100150-R3c	MS1b	1.50	1.00	1.64	1.06	0.157	0.109	461	0.042	2.479	6.16	0.194	6.208	192	96	192	84	596	1810
MS1b-100150-R3n	MS1b	1.50	1.00	1.64	1.06	0.157	0.109	461	0.042	2.479	6.16	0.194	6.208	192	96	192	84	596	1810
MS1b-094194-c	MS1b	1.94	0.94	2.20	1.00	0.199	0.103	253	0.036	2.868	7.85	0.250	8.000	128	72	144	63	572	1692

effect, see Appendix A of [Die13] for a detailed discussion.

In this section we employ the Z4c scheme (Sec. 2.1.3) with constraint preserving boundary conditions [Ruiz et al., 2011; Hilditch et al., 2013]. For all our runs the grid consists of $L = 7$ refinement levels, $l > l^{\rm mv} = 4$ levels move dynamically and $l = 0$ is substituted by spherical patches. Specific grid information are given in Tab. 5.1. An average restriction operation and a second order (essentially non-oscillatory) ENO scheme is used for prolongation (a2e2[n]); cf. Tab. B.2. Regarding the single star tests in Appendix B the a2e2 scheme performs best, which is the reason why we use it here. To evaluate the influence of the correction step, we use the a2e2n scheme for comparison. All runs are performed with an atmosphere setting of $f_{atm} = 10^{-11}$ and $f_{thr} = 10^2$.

5.1 Influence of the EOS and the mass ratio

We start our discussion focusing on mass ratios $q = 1.00$ and $q = 1.16$ and a total binary mass of $M = 2.70 M_\odot$. These configurations start with the same GW frequency

of $M\omega_{22}^0 = 0.052$, i.e., 3 to 5 orbits before merger, depending on the EOS and mass ratio q. In general, we observe that stiffer (softer) EOSs give shorter (longer) inspirals and lower (higher) dimensionless GW frequencies at merger. Unequal-mass systems are characterized by slightly shorter inspirals than equal-mass ones and smaller merger frequencies of about $\sim 3\%$. For the same mass, stars with stiff EOS have larger radii than those with soft EOS and the attractive tidal interactions are stronger. This leads to a shorter inspiral and lower frequency at merger. The opposite holds for soft EOSs. A detailed description of the inspiral dynamics for irrotational binaries is given in Sec. 6.1.3 and Sec. 6.2.1. Therefore, we focus at this point on the postmerger.

In fact, the postmerger dynamics has a rich phenomenology depending on the main binary properties: total mass, mass-ratio, EOS and the stars' spins; cf. e.g. [Shibata and Taniguchi, 2006; Shibata et al., 2011; Hotokezaka et al., 2013a; Hotokezaka et al., 2013b; Kastaun and Galeazzi, 2015].

Most neutron star mergers result in an oscillating massive, differentially rotating compact object; see the $\rho_{max} = \max(\rho)$ evolution in Fig. 5.1. The compact object's angular momentum is redistributed from the inner region to outer ones by torque and nonlinear hydrodynamical interaction. The stability of the object depends on the mass, EOS and dissipative processes. We characterize the merger remnant as a *hypermassive neutron star* (HMNS), in case its rest mass is larger than the maximum rest mass of a stable uniformly rotating star with the same EOS, or a *supramassive neutron star* (SMNS), in case its rest mass is smaller; see [Baumgarte et al., 2000]. If the rest mass is below the maximal supported rest mass of a stable TOV-solution, we simply define it as a *massive neutron star* (MNS). The definitions refer in principle to equilibrium configurations for cold EOSs and axisymmetry, thus, they cannot be rigorously applied to the merger remnants; see also [Hotokezaka et al., 2013a].

HMNSs are dynamically unstable objects, which collapse to black holes on timescales of $\sim 2000 - 10000 M_\odot \sim 10 - 50$ ms; SMNSs appear stable on those timescales, but eventually collapse later due to dissipative processes, e.g. emission of angular momentum by GWs. The density distribution and velocity fields in the orbital plane are presented in Fig. 5.3. The chosen simulation time for the snapshots is close to the moment of merger.

Equal-mass merger

Three of our four $q = 1$ configurations (H4-135135,ALF2-135135,SLy-135135) merge in a HMNS which collapses to a black hole within $\tau_{\rm HMNS} \sim 2000 - 5000 M_\odot \sim 700 - 2000 M \sim 10 - 25$ ms. All of these setups employ EOSs supporting approximately the same maximum mass for single nonrotating stars. We observe that for stiffer EOSs $\tau_{\rm HMNS}$ is larger. In principle, stiff EOS binaries are gravitationally less bound compared to soft EOS binaries, so their binding energy and angular momentum at merger is larger; cf. Eqs. (6.15b) and (6.15c). As a result, the HMNS has more

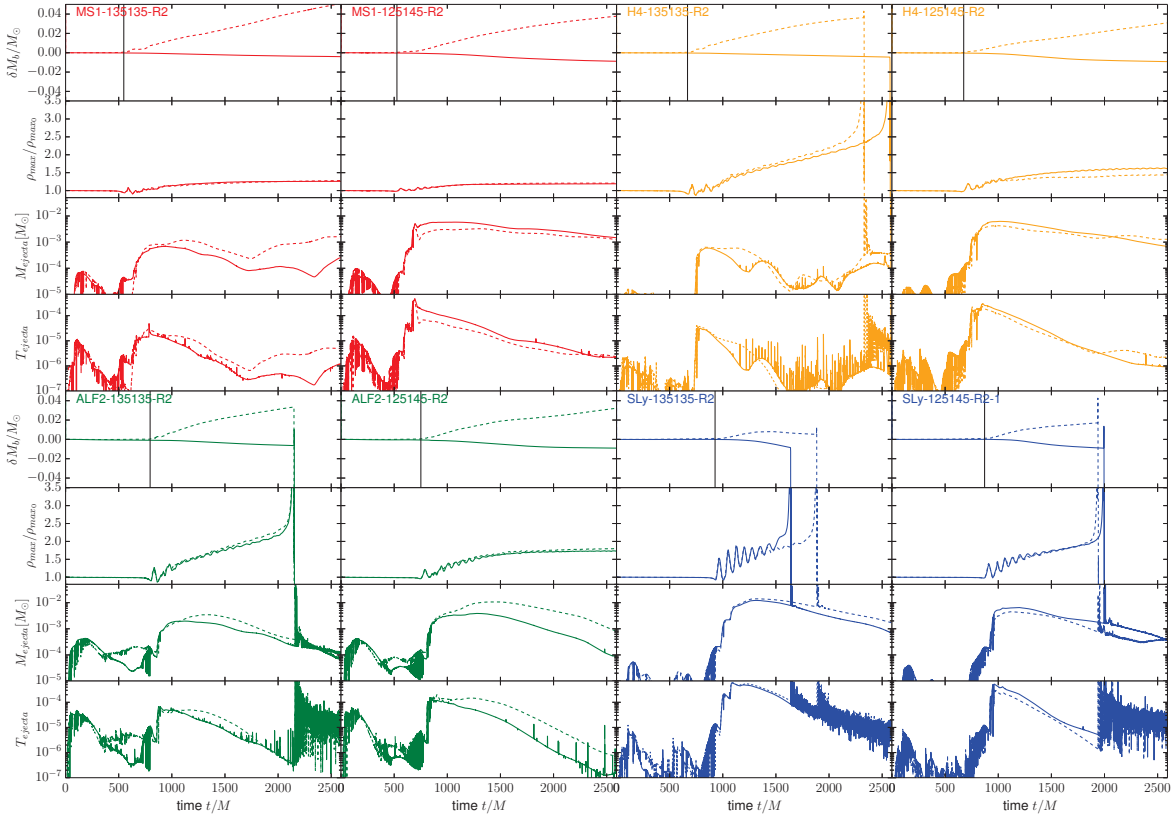

Figure 5.1: Evolution of several dynamical quantities for $M = 2.70M_\odot$ with $q = 1.00, 1.16$ configurations. Results for different EOSs are colored differently. For each configuration, the panel contains four plots. From top to bottom: rest-mass violation $\delta M_b = M_b(t) - M_b(t = 0)$ on level $l = 1$; maximum density $\rho_{max} = \max(\rho)$ on the grid scaled to its initial value $\rho_{max}(t)/\rho_{max}(t = 0)$; rest mass of the ejected material M_{ejecta}; kinetic energy of the ejecta T_{ejecta}. Results for the conservative AMR are presented with solid lines, while the corresponding results for the nonconservative AMR are shown dashed. Vertical lines represent the moment of merger; adapted from [Die8].

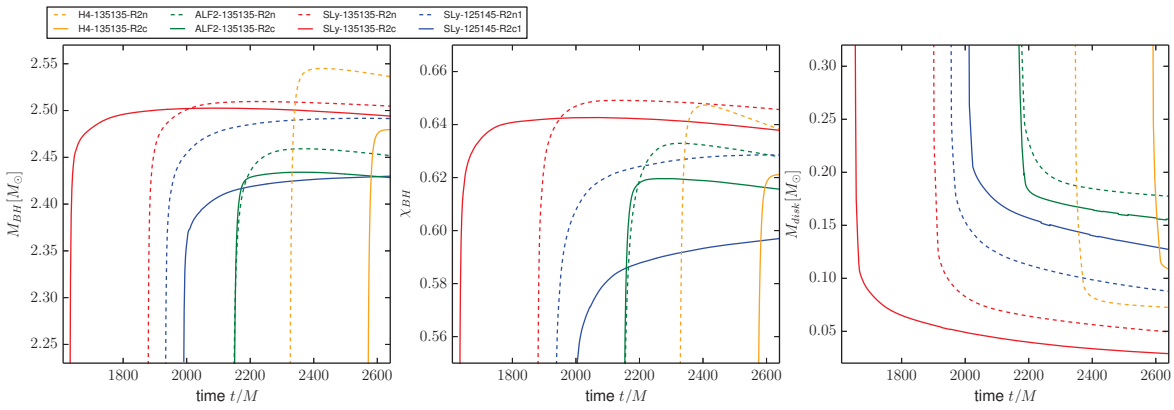

Figure 5.2: Black hole and disk evolution for simulations with and without conservative AMR. Left: Horizon mass of the black hole. Middle: Black hole dimensionless angular momentum. Right: Rest mass of the final disk. Plot adapted from [Die8].

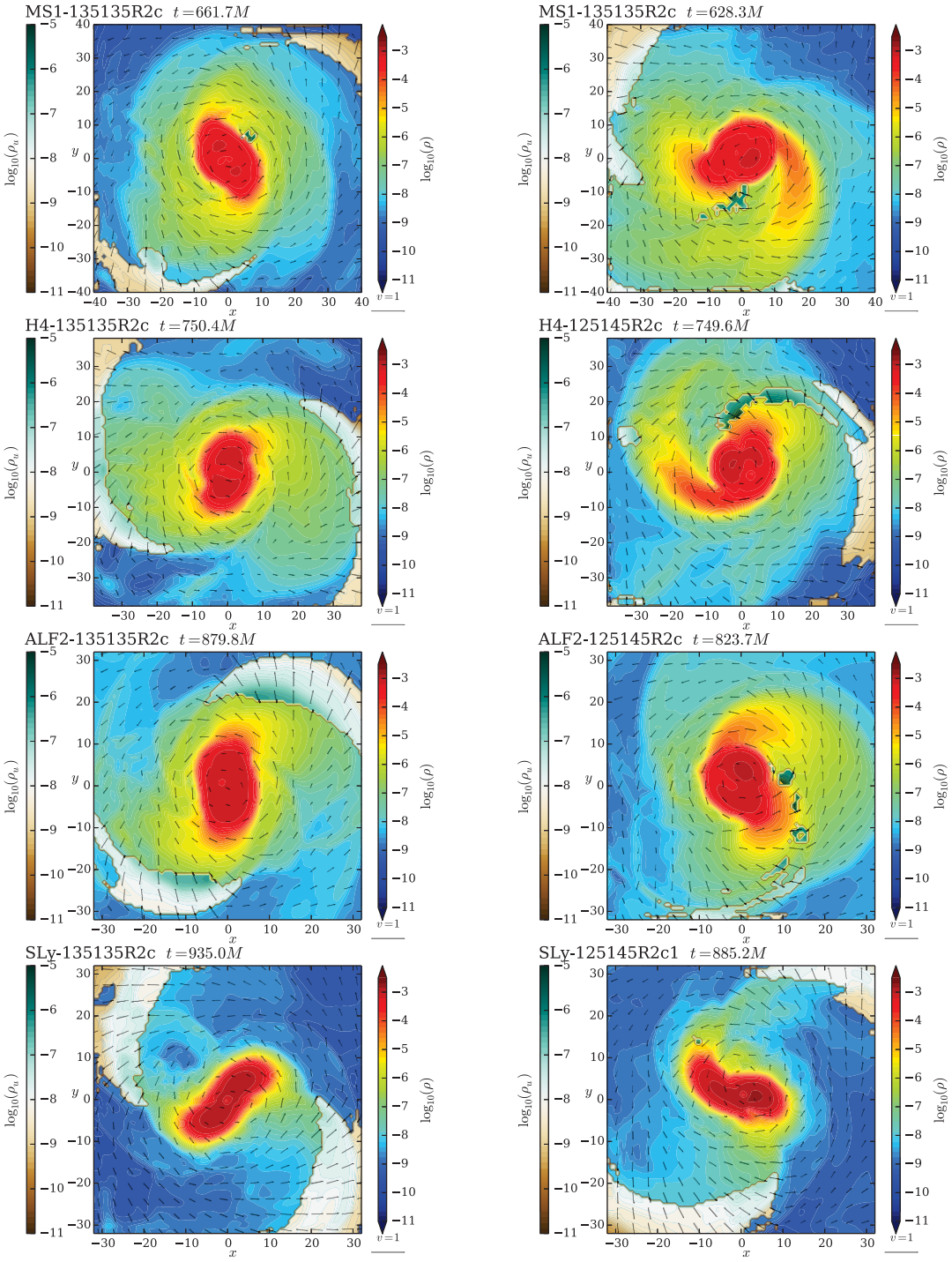

Figure 5.3: 2D snapshots of bound rest-mass density (ρ), the unbound rest-mass density (ρ_u) and the velocity in the orbital plane for all configurations around the merger. Left (from top to bottom): MS1-135135-R2c, H4-135135-R2c, ALF2-135135-R2c, SLy-135135-R2c. Right (from top to bottom): MS1-125145-R2c, H4-125145-R2c, ALF2-125145-R2c, SLy-125145-R2c1.

Table 5.2: Summary of the numerical results for the $M = 2.70M_\odot$-simulations. Columns: Simulation name, merger time, merger frequency, final remnant, the lifetime of the HMNS $\tau_{\rm HMNS}$, 2nd peak f_s- and f_2-mode frequency, mass and kinetic energy of the ejected material $M_{\rm ejecta}$ (see Fig. 5.1), the mass of the disk surrounding the central object $M_{\rm disk}$ measured $\sim 200M_\odot$ after BH formation, the black hole mass $M_{\rm BH}$ and its dimensionless angular momentum $\chi_{\rm BH}$, cf. Eqs. (A.2). Table adapted from [Die8].

Name	$t_{\rm mrg}$ $[M_\odot]$ (M)	$M\omega_{22}^{\rm mrg}$	$f_{\rm mrg}$ [kHz]	Remnant	$\tau_{\rm HMNS}$ $[M_\odot]$ (ms)	$M\omega_{22}^{s}$	f_s [kHz]	$M\omega_{22}^{2}$	f_2 [kHz]	$M_{\rm ejecta}$ $[10^{-3}]$	$T_{\rm ejecta}$ $[10^{-4}]$ $(10^{50}$ erg)	$M_{\rm disk}$ $[10^{-2}]$	$M_{\rm BH}$	$\chi_{\rm BH}$
MS1-135135-R2c	1479 (547.8)	0.112	1.38	MNS	–	0.134	1.60	0.166	1.99	0.7	0.1 (0.2)	–	–	–
MS1-135135-R2n	1476 (546.7)	0.114	1.36	MNS	–	0.135	1.61	0.170	2.04	1.2	0.1 (0.2)	–	–	–
MS1-125145-R2c	1420 (525.9)	0.110	1.32	MNS	–	0.130	1.56	0.172	2.06	5.8	0.7 (1.2)	–	–	–
MS1-125145-R2n	1419 (525.6)	0.111	1.33	MNS	–	0.125	1.50	0.157	1.88	3.2	0.2 (0.4)	–	–	–
H4-135135-R2c	1804 (668.1)	0.129	1.54	HMNS→BH	5130 (25)	0.146	1.75	0.214	2.57	0.6	0.3 (0.5)	10.8	2.48	0.62
H4-135135-R2n	1803 (667.8)	0.130	1.55	HMNS→BH	4470 (22)	0.145	1.73	0.216	2.58	0.6	0.3 (0.6)	8.5	2.54	0.65
H4-125145-R2c	1822 (674.8)	0.120	1.44	HMNS	–	0.140	1.68	0.197	2.36	6.0	1.6 (2.8)	–	–	–
H4-125145-R2n	1820 (674.1)	0.120	1.44	HMNS	–	0.146	1.75	0.194	2.32	4.0	1.2 (2.3)	–	–	–
ALF2-135135-R2c	2148 (795.6)	0.142	1.71	HMNS→BH	3760 (19)	0.168	2.01	0.235	2.81	3.5	0.4 (0.7)	17.8	2.43	0.62
ALF2-135135-R2n	2145 (794.4)	0.142	1.71	HMNS→BH	3770 (19)	0.165	1.98	0.230	2.75	2.0	0.4 (0.7)	21.1	2.44	0.63
ALF2-125145-R2c	2028 (751.1)	0.138	1.65	HMNS	–	0.157	1.88	0.222	2.66	3.9	0.4 (0.8)	–	–	–
ALF2-125145-R2n	2027 (750.7)	0.139	1.66	HMNS	–	0.160	1.91	0.225	2.69	10.6	1.0 (1.9)	–	–	–
SLy-135135-R2c	2504 (927.5)	0.168	2.01	HMNS→BH	2159 (11)	0.206	2.46	0.292	3.49	12.2	4.0 (7.1)	8.4	2.48	0.64
SLy-135135-R2n	2495 (924.1)	0.168	2.01	HMNS→BH	2577 (13)	0.207	2.48	0.290	3.47	14.2	5.9 (10.5)	9.6	2.49	0.64
SLy-125145-R2c1	2353 (871.5)	0.162	1.93	HMNS→BH	3020 (15)	0.184	2.20	0.286	3.42	6.5	2.8 (5.1)	17.9	2.40	0.58
SLy-125145-R2n1	2350 (870.4)	0.161	1.93	HMNS→BH	2870 (14)	0.187	2.24	0.283	3.39	4.5	1.7 (3.0)	14.5	2.46	0.61
SLy-125145-R2c2	2350 (870.4)	0.161	1.92	HMNS→BH	3310 (16)	0.186	2.23	0.285	3.41	6.2	2.1 (3.7)	18.4	2.40	0.58
SLy-125145-R2n2	2348 (869.6)	0.160	1.91	HMNS→BH	2180 (11)	0.184	2.20	0.283	3.39	5.4	2.5 (4.5)	11.1	2.49	0.62

angular momentum support at formation and, thus, a longer lifetime. But, the initial angular momentum is not the only factor that determines the lifetime of the HMNS. At formation of the HMNS, the density inside the star increases and the pressure response depends on the adiabatic index of the fluid which is different for each EOS; see Eq. (2.55). Therefore, the nonlinear oscillations and the efficiency of the angular momentum redistribution depend also on the EOS [Hotokezaka et al., 2013a]. In general, stiffer EOSs have larger pressure support, especially at high densities.

Finally, in a more realistic situation than the one considered here (and on longer timescales), thermal support and angular momentum transport driven by cooling mechanisms (neutrinos) and magnetic fields[2] are expected to play a role.

We state the lifetimes of the HMNSs in Tab. 5.2 and find that our results agree within ± 5 ms with results presented in the literature [Hotokezaka et al., 2013a].

In contrast to the other $q = 1$-simulations, MS1-135135 produces a differentially rotating object stable over the whole simulation time, i.e. $\sim 6000M_\odot \approx 2200M \approx 30$ ms after merger. We classify the merger remnant as a MNS, because non-rotating stars described by MS1 support a maximum rest mass of $\sim 2.767M_\odot > 2.70M_\odot$. We expect that the merger remnant will stabilize via GW emission reaching a uniformly rotating and cold configuration on the characteristic timescale, $\tau_{\rm GW} \sim J/\dot{J} \sim \langle R\rangle^4/\langle M\rangle^3 \sim 40000M_\odot \approx 15000M \approx 200$ ms.

[2]Note that even the highest resolved simulations with present techniques have not properly resolved magnetic field amplification effects [Kiuchi et al., 2014a].

Unequal-mass merger

The unequal-mass $q = 1.16$ configurations H4-125145 and ALF2-125145 have a different merger remnant than the corresponding $q = 1$ configurations. We find an object, which is stable over $5000M_\odot \approx 1850M \approx 25$ ms. However, due to the fact that the mass is still larger than the supported mass of the uniform rotating model, we characterize the remnants as HMNSs. It is most likely that they will collapse within $t < \tau_{\rm GW}$. This statement is supported by [Hotokezaka et al., 2013b; Hotokezaka et al., 2013a], where similar configurations with a slightly different thermal component $\Gamma_{th} = 1.8$ form BHs. The two other unequal-mass setups behave similarly as their equal-mass counterpart. The MS1-125145 setup forms a stable MNS and the SLy-125145 collapses to a black hole, but, following the general trend, the HMNS lifetime is longer.

For unequal-mass mergers the merger remnant is in general more deformed than the corresponding $q = 1$ configuration and strongly non-axisymmetric at formation; see Fig. 5.3. Additionally, we conclude that unequal-mass binaries have more stable merger remnants (larger $\tau_{\rm HMNS}$), slightly larger radii and a different central density than the corresponding $q = 1$ configurations; cf. Fig. 5.1.

Independently of the mass-ratio all the remnants oscillate violently after formation, which is visible in the evolution of ρ_{max} in Fig. 5.1. The softer the EOS, the larger are the oscillations (e.g. SLy), because of the different pressure response of the EOS for densities around $\rho \gtrsim \rho_2$ (Tab. 2.2); cf. discussion above and [Hotokezaka et al., 2013a]. The oscillations have a quasi-radial character, and relax either within a few radial periods or before the onset of collapse.

In cases where a black hole forms, the masses are $M_{\rm BH} = 2.4 - 2.5\,M_\odot$, and the dimensionless black hole spin is $\chi_{\rm BH} = 0.58 - 0.64$, see Appendix A for details about the computation of $M_{\rm BH}$ and $\chi_{\rm BH}$. The evolution of the black hole mass and spin are presented in Fig. 5.2 (left and middle panels). These results suggest that the black hole properties mostly depend on the total mass of the system and only weakly on other details (mass-ratio and EOS). However, the uncertainties are of the order of $\sim 2\% - 5\%$, and therefore it is difficult to draw precise conclusions.

In all cases where a black hole forms, it is surrounded by an accretion disk of rest mass $M_{\rm disk} \sim (0.05 - 0.2)M_\odot$; see Tab. 5.2 and the right panel of Fig. 5.2. Independent of the mass-ratio and EOS the disk geometry is essentially axisymmetric. The maximum density inside the disk decreases from $\sim 10^{-5}$ to $\sim 10^{-7}$. When the black hole masses and spins reach their plateaus (Fig. 5.2), the dense regions of the disk extend up to distances $\lesssim 30M_\odot \approx 45$ km. Lower density material, which is still gravitationally bound to the system extends up to $\sim (100 - 130)M_\odot \approx (150 - 200)$km. We observe an accretion rate of the order $\dot{M}_{\rm disk} \sim 10^{-8}$.

5.1.1 Assessment of conservative AMR

Before continuing our investigation of the physical properties we want to present and evaluate the improvements due to the additional correction/refluxing step in the BC - algorithm described in Sec. 2.2.4. We show the results obtained with the C step (solid lines) and without the C step (dashed lines) in the AMR algorithm in Fig. 5.1. Quantitative results are given in Tab. 5.2. We observe that for all configurations the correction step is important for the simulation accuracy after merger.

As discussed already, the rest mass in BNS simulations does not stay perfectly constant. Two main and competing causes for the mass violation in our simulations exist: (i) when fluid crosses refinement boundaries rest mass tends to increase; (ii) the artificial atmosphere treatment tends to decrease the rest mass. The introduced correction step can only improve violations of type (i).

The use of the C step leads for most of the configurations to an improvement by a factor of ~ 5, except for the MS1-135135-R2 configuration where an improvement by more than a factor of ~ 10 is observed. No significant improvement is observed for SLy-125145-R2, where the violation is $\lesssim 20\%$ from merger to the end of the run.

Small imprints of the EOS are visible in the rest-mass conservation. Without the C step mass conservation is in general better for softer EOSs; probably related to the smaller star deformations. The opposite is true with the C step, where slightly larger errors are observed for softer EOSs. We suggest that this is caused by the influence of numerical viscosity, which seems to be more significant in those setups than in the runs without correction step due to a better overall conservation.

Figure 5.1 characterizes the influence of the mass violations on the properties and lifetime of the merger remnant. We observe systematic shifts in the collapse time for several configurations, although no qualitative differences due to the sufficiently high grid resolutions are present. But we expect that for lower resolutions and masses closer to the threshold of black hole formation, qualitative differences will occur when no correction step is employed. This statement is supported by different maximal central densities ρ_{max} for simulations with and without C step.

Regarding the ejecta masses, we observe maximal differences of a factor of ~ 3 between the runs with and without the C step. Bottom panels of Figure 5.1 show that no clear trend is identifiable when the differences are largest. The simulation of the low density material and the ejecta remains challenging even with conservative AMR. A local AMR strategy tracking the ejecta would be the best way for accurate simulations. Additionally to the resolution effects, we expect that the influence of the artificial atmosphere is significant. Firstly, we observe spurious ejecta due to atmosphere fluctuations during the inspiral and, secondly, when ejecta have expanded into larger radii (coarser resolutions) we expect an effect as the one discussed in Appendix B for the $\mathrm{TOV}_{\mathrm{MIG}}$-test, where rest mass violation is caused by too low

resolution.

The introduced C step also influences the final black hole and the remnant disk; cf. Tab. 5.2 and Fig. 5.2. Without the C step the estimated disk mass $M_{\rm disk}$ changes up to $\sim 0.06 M_\odot$. For all EOSs and mass ratios the final black hole mass and spin are overestimated without C step, which is related to the increase of the rest mass (upper panels of Fig. 5.1).

We observe that the extracted GW signal during the inspiral is not influenced by the use of the C step. We expect that this behavior would change, when additional refinement levels are added inside the star during the inspiral. Since the stars stay compact during the orbital motion and only a negligible amount of matter crosses refinement boundaries at this stage, i.e. there is no need of further improving mass conservation. However, GWs emitted in the post merger phase reflect the slightly different dynamics, but the characteristic frequencies are essentially unaffected; cf. Tab. 5.2.

5.1.2 Ejecta

In the following we will discuss shortly the effect of the EOS and mass-ratio on the dynamical ejecta and focus exclusively on the simulations with C step. A detailed analysis of the dynamical formation of the ejecta will be presented in Sec. 5.2 for the $q = 1.5$-configuration.

The main results can be found in Fig. 5.1, which shows the evolution of the ejecta mass and kinetic energy, and Tab. 5.2, which reports the maximum values. The maximum ejecta masses are present shortly after the merger moment. At this time the ejecta rest masses lie within $M_{\rm ejecta} \sim 10^{-3}\, M_\odot - 10^{-2}\, M_\odot$.

For a mass ratio of $q = 1$ we observe larger ejecta for softer EOSs, whereas stiffer EOSs produce smaller ejecta. For a fixed EOS (except for SLy), $q = 1.16$ configurations have larger ejecta than the corresponding $q = 1$ configurations. The same statement holds for the kinetic energy, which is larger for softer EOSs and larger q. Most of our results (MS1, H4, and ALF2 configurations) agree with the work of [Hotokezaka et al., 2013b; Bauswein et al., 2013]. This proves the robustness of our simulations, keeping in mind that ejecta computations are still challenging and that mass conservation, artificial atmosphere, and finite resolution are the main limiting factors. This becomes most clear for the SLy configurations. The relative mass violations (see Sec. 5.1.1) suggest that the evolution of soft EOSs is less accurate than the others; cf. [Hotokezaka et al., 2013b]. We assume that these uncertainties are reasons why SLy-135135 produces larger ejecta than the corresponding unequal mass setup[3].

[3]Notice, a similar setup as SLy-135135 has been evolved in [Bauswein et al., 2013], where the ejecta mass was estimated within $(4\times10^{-2}, 6.4\times10^{-2})$ for a smooth particle hydrodynamics simulation with conformal flatness assumption.

5.1.3 Gravitational waves

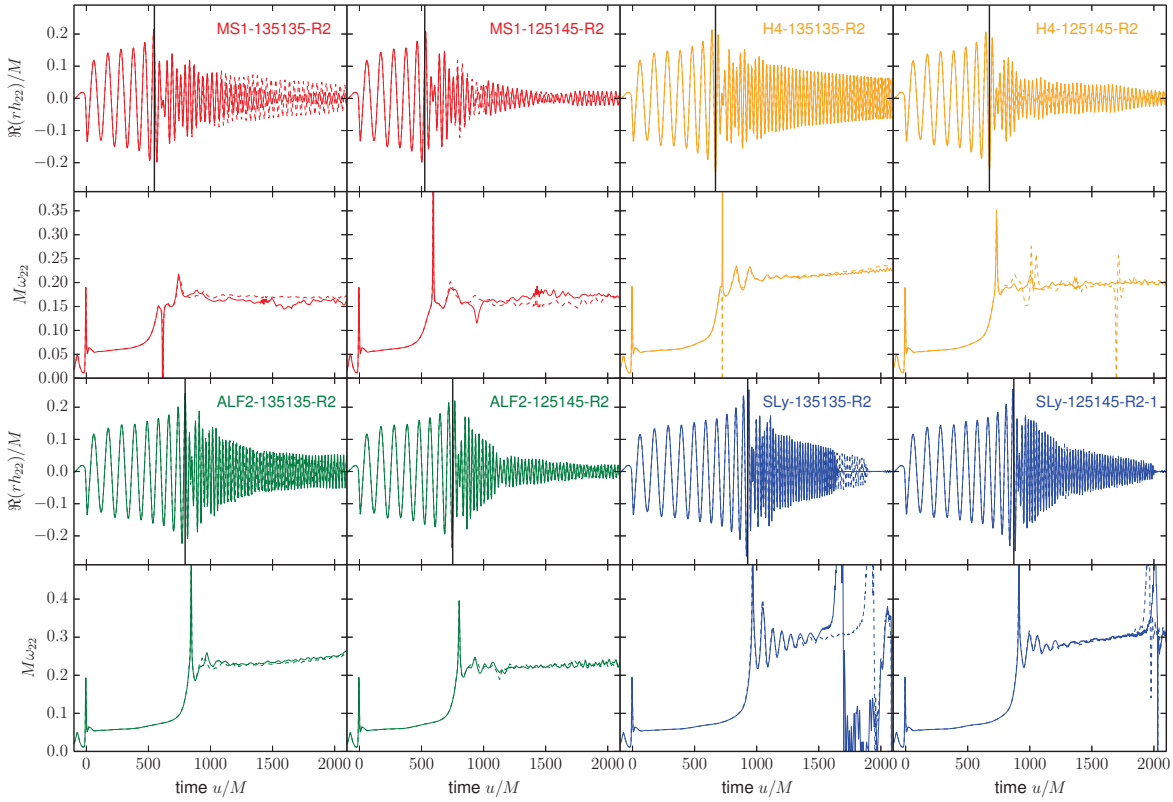

Figure 5.4: GW signals for $M = 2.70M_\odot$ with $q = 1.00, 1.16$ configurations. For each configuration, the panel contains two plots. Top: $\Re(rh_{22})$; Bottom: $M\omega_{22}$. Results for the conservative AMR are presented in solid lines, while the corresponding results for the nonconservative AMR are shown dashed. Vertical lines mark the moment of merger. Plot adapted from [Die8].

We present the $l = m = 2$ multipoles of the GWs in Fig. 5.4. For each setup the upper panel shows the real part of the wave and the instantaneous GW frequency is shown in the bottom panel. The vertical line marks the moment of merger. During the inspiral motion, the characteristic chirping signal, in which frequency and amplitude monotonically increase, is present. At small separations the dynamics is strongly affected by tidal interactions and the GWs phase carries information about the EOS. We will discuss this aspect in more detail in Sec. 6.1 and 6.2; here we focus on the post-merger dynamics.

After the merger the amplitude of the GW drops down since the two stars merge in a single body which has, for one instant, a quasi-spherical geometry [Thierfelder et al., 2011a]; cf. also the frequency spikes in the bottom panels of Fig. 5.4. As discussed in the previous section, the merger remnant can be approximated by a compact star oscillating nonlinearly at its proper frequencies. The $m = 2$ f-mode with frequency f_2 is the most efficient emitter of GWs. Therefore, the GW spectra of the HMNS/MNS are dominated by this frequency; see Fig. 5.5. The figure includes the spectrum of the entire signal (thick line) and the spectrum considering only the signal for $t > t_{\rm mrg}$ (thin

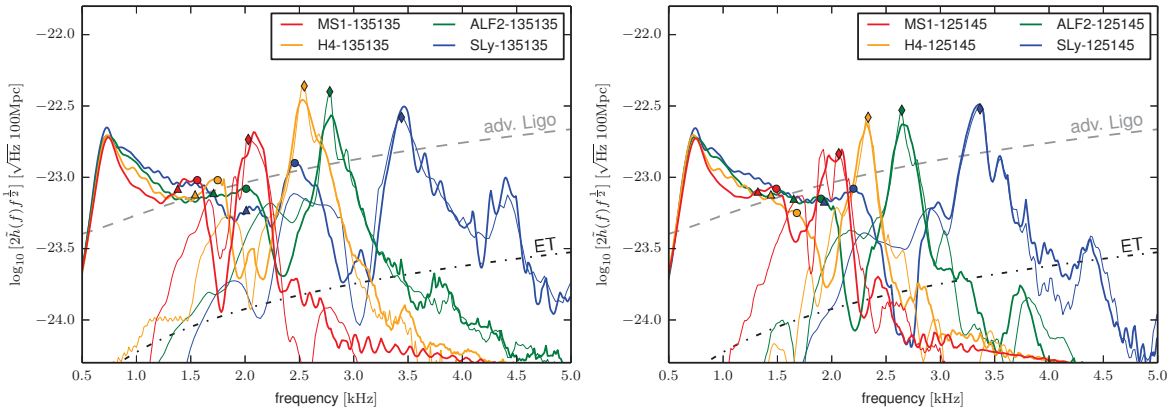

Figure 5.5: PSD for $M = 2.70 M_\odot$, $q = 1$ (left) and $q = 1.16$ (right) configurations. The thick lines refer to the entire GW-signal, while the thin lines include only the GWs emitted after the moment of merger $t > t_{\rm mrg}$. We assume the binary at an effective distance of $100\mathrm{Mpc}$ and consider the radiation emitted orthogonal to the orbital plane; see [Bernuzzi et al., 2012b] Additionally, we add the expected sensitivity of advanced LIGO [advLIGO] and the Einstein Telescope [Punturo et al., 2010b; Punturo et al., 2010a]. The markers refer to $f_{\rm mrg}$ (triangles), f_s (circles), and f_2 (diamonds). In contrast to [Die8] no Hanning-window is used for the Fourier transformation.

line). We mark the relevant frequencies: the merger frequency $f_{\rm mrg}$ with triangles, a secondary peak frequency f_s with circles, and the main post merger peak, the f_2 frequency, with diamonds. There has been intense research about the identification and characterization of this postmerger GW spectrum frequencies, e.g. [Bauswein and Janka, 2012; Stergioulas et al., 2011; Hotokezaka et al., 2013b; Hotokezaka et al., 2013a; Bauswein et al., 2014; Takami et al., 2014; Bauswein and Stergioulas, 2015; Takami et al., 2015a; Bauswein et al., 2015]. For most configurations, the f_2 frequency is clearly identifiable, although a double peak is present for the MS1 models. Our measured f_2-frequencies agree with the results of [Bauswein et al., 2013; Hotokezaka et al., 2013b; Takami et al., 2015b]. We see that the f_2 frequency is smaller for stiffer EOSs and for fixed EOS, $q = 1.16$ configurations have slightly smaller f_2 than $q = 1$. We will discuss the origin of these phenomena in detail in Sec. 6.2.2.

Regarding the lower panels of Fig. 5.4 we observe relatively large oscillations right after the merger, which correspond to the very nonlinear phase described in Sec. 5.1. At this time different modes are excited, compare e.g. the spectrogram (right panel) in Fig. 4.10. Due to the nonlinearity of the underlying equations, mode coupling is present, most notably between the quasiradial mode F and the f_2 [Stergioulas et al., 2011], i.e. $f_\pm = F \pm f_2$. When a MNS is formed, e.g. for MS1, the frequency oscillations relax quickly; the power in the $f_\pm$ channels decreases, and the frequency settles to the f_2 mode. When a HMNS is formed, the frequency increases monotonically because of the stars contraction prior to collapse.

As mentioned above, a secondary peak f_s is present in Fig. 5.5 [4]. Its origin is not entirely understood, but appears to be related to the very late inspiral phase. This can be confirmed by restricting the PSD to times $t > t_{\rm mrg}$, for which several f_s peaks are not present or strongly suppressed. Other configurations, e.g. SLy135135 and H4135135, show a secondary peak also in the PSD at times $t > t_{\rm mrg}$. Our values of f_s agree with the frequencies called f_1 in [Takami et al., 2015b], while the interpretation of our results might also be compatible with the interpretation of [Bauswein and Stergioulas, 2015]. Bauswein et al. suggest that two different effects lead to the f_s-frequency: (i) the nonlinear mode coupling $f_- = F - f_2$; (ii) the motion of spiral arms during the last stage of the merger process, mostly at times $t \lesssim t_{\rm mrg}$.

5.2 A stiff $1.0M_\odot - 1.5M_\odot$ binary

Table 5.3: Summary of the numerical results for the MS1b-100150 simulation. Columns: Simulation name, merger time $t_{\rm mrg}$, GW frequency at merger, peak frequency of the GW spectrum during the HMNS phase f_2, and maximum mass of the ejected material $M_{\rm ejecta}$. Table adapted from [Die8].

Resolution	$t_{\rm mrg}$ $[M_\odot]$ (M)	$M\omega_{22}^{\rm mrg}$	$f_{\rm mrg}$ [kHz]	$M\omega_{22}^{2}$	f_2 [kHz]	$M_{\rm ejecta}$ $[10^{-3}M_\odot]$
MS1b-100150-R1c	2675 (1070)	0.086	1.11	0.137	1.77	32.6
MS1b-100150-R1n	2640 (1056)	0.085	1.10	0.139	1.79	27.8
MS1b-100150-R2c	2710 (1084)	0.086	1.11	0.141	1.82	27.7
MS1b-100150-R2n	2701 (1080)	0.085	1.10	0.140	1.81	29.4
MS1b-100150-R3c	2754 (1101)	0.088	1.13	0.145	1.87	29.9
MS1b-100150-R3n	2757 (1102)	0.088	1.14	0.142	1.83	28.3

As a particular testbed we consider the evolution of a $q = 1.5$ configuration employing the MS1b EOS [Müller and Serot, 1996; Lattimer and Prakash, 2001]. The total binary mass is $M = 2.5M_\odot$. The individual masses are $M^A = 1.5\,M_\odot$ and $M^B = 1.0\,M_\odot$. A $q = 1.5$ has been simulated in [Shibata and Taniguchi, 2006] for the soft EOS APR, but no GW signal was computed. We use this case study to discuss the mechanisms which generate the ejecta in the strong field region and the ejecta geometry at their formation.

Dynamics and Merger remnant

A 3D rendering of the density ρ during the merger process at selected times $t/M \sim 1024, 1183, 1280, 2176$ is shown in Fig. 5.6. We visualize the bound and unbound material; from yellow to light blue (bound density ρ) and from blue to red (unbound density ρ_u)[5]. About 1.5 orbits before the moment of merger the two stars

[4] Notice that we do not see a secondary peak for the high-mass ratio simulations of Sec. 5.2 and Sec. 5.3; cf. also Fig. 13 of [Die8].

[5] Note the different scales for the bound and unbound material.

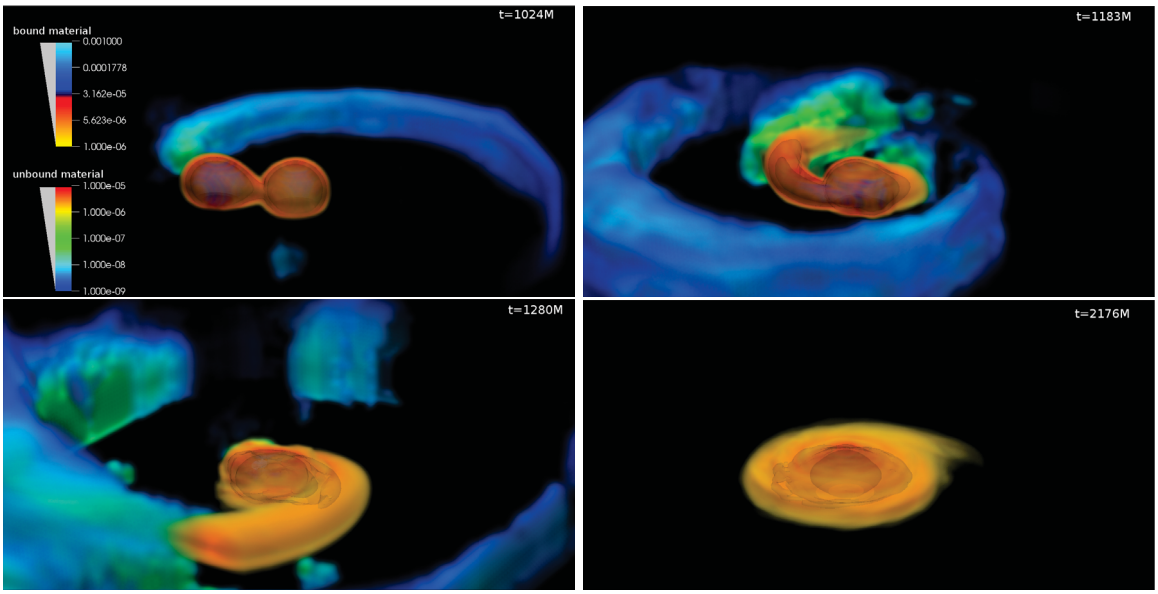

Figure 5.6: The strong-field merger dynamics of MS1b-100150. The figure shows four snapshots of the bound and unbound density ρ at $t \sim 1024M$ (top-left), $t \sim 1183M$ (top-right), $t \sim 1280M$ (bottom-left), and $t \sim 2176M$ (bottom-right). All subplots contain the same contour range and the same part of the computational domain. The bound density ρ is shown on a logarithmic scale from 10^{-6} (yellow) to 10^{-3} (blue), and highlighted with contours for $\rho = (10^{-5}, 10^{-4}, 10^{-3})$. The unbound material is shown on a logarithmic scale from 10^{-9} (blue) to 10^{-5} (red). Top-left: About 1.5 orbits before the moment of merger the stars come in contact. At $t \sim 1024M$ the companion ($M_B = 1.0\,M_\odot$, left) is deformed by the tidal field of the primary ($M_A = 1.5\,M_\odot$, right). Ejecta originate from the tidal tail of the companion, and are emitted around the orbital plane. Top-right: At $t \sim 1183M$, shortly after the moment of merger, the companion is already partially disrupted and most of the ejecta is emitted around this time. Bottom-left: At $t \sim 1280M$ material is also ejected by the shock-heating–driven mechanism (as described in the text). On larger scales (not shown in the plot) ejecta appear anisotropically distributed around the orbital plane with an opening angle $\sim 10°$. Bottom-right: The merger remnant is composed of a MNS with a high density core surrounded by an accretion disk of rest mass $\sim 0.3M_\odot$. The entire disk has a radius of $\sim 35M_\odot \approx 55$km. Plot adapted from [Die8].

come in contact. At this time the companion ($M_B = 1\,M_\odot$) is very deformed and the mass ejection from the low-density outer layers of the companion, $\rho \sim 10^{-8/-9} \sim 10^9$ g cm^{-3} takes place; see the green and blue tail in the top left panel. Shortly after this time, the companion is partially disrupted. Material is captured into the primary star and a hot and differentially rotating core is produced. Other material forms a tidal tail, see the top-right and bottom-left panels, and low density material $\rho \lesssim 10^{-7}$ in the outer part of the tidal tail becomes unbound. The higher density material of the tidal tail closer to the primary star expands by centrifugal forces but remains mostly bound.

The merger remnant is composed of a high density hot core surrounded by a thick accretion disk of rest mass $\sim 0.3\,M_\odot$ and of radius $\sim 35M_\odot \approx 55$km shown in the bottom-right panel of Fig. 5.6. Due to the chosen EOS, which supports stable stars with masses up to $M = 2.76$, we do not expect that the remnant will collapse.

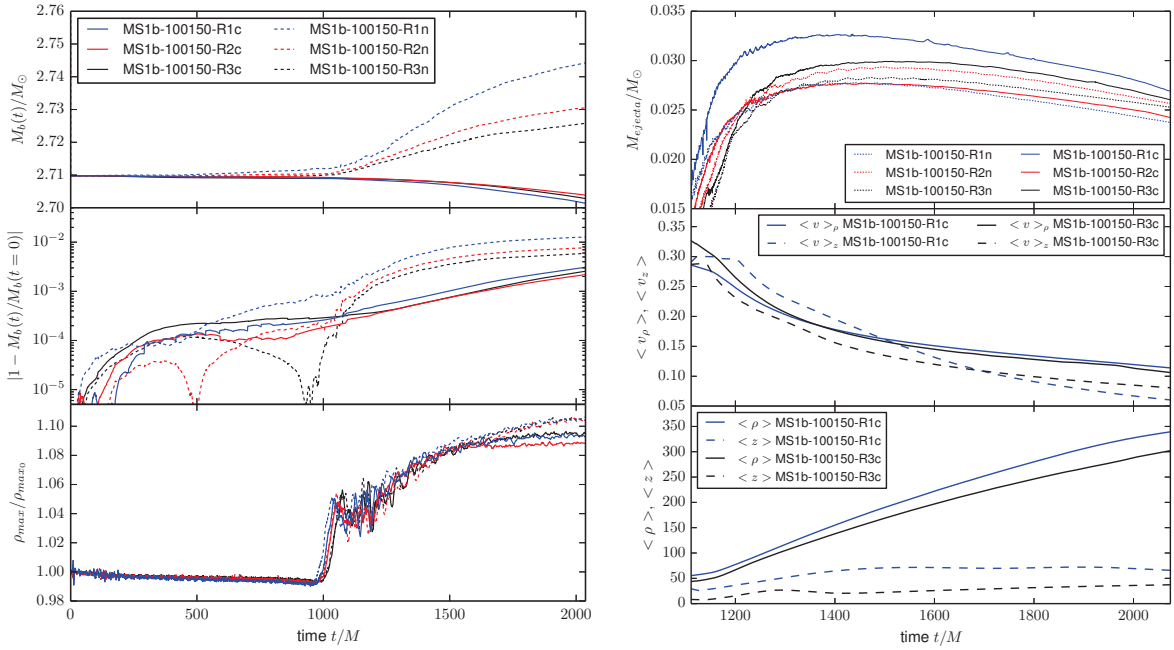

Figure 5.7: Left: Rest-mass conservation for MS1b-100150 and resolution study. The plot shows results for R1 (blue), R2 (red), R3 (black), and runs with (solid lines) and without (dashed lines) the C step: rest mass (top panel), error of the rest-mass conservation (middle panel), maximum density $\rho_{max}(t)$ normalized by the initial maximum density $\rho_{max}(t=0)$ (bottom panel) Right: Mass, average velocities and geometry of the ejected mass MS1b-100150: Ejecta mass for all resolutions (top panel), $\langle v \rangle_\rho$ in the (x, y) plane and $\langle v \rangle_z$ in the (x, z) plane (middle panel), $\langle \rho \rangle, \langle z \rangle$ (bottom panel); cf. Appendix A. (The middle and bottom panels are restricted to highest and lowest resolution for better readability.) Plot adapted from [Die8].

We observe ejecta with a total rest mass of $M_{\text{ejecta}} \sim 0.03\, M_\odot$. The large amount of ejected mass offers the possibility to study with enough accuracy the ejecta formation process. As listed in Tab. 5.1 we checked the consistency of our results against resolution (considering three different grid setups) and against the influence of the C step. Mass conservation and the maximum density are shown in Fig. 5.7 (left panels). The conservative AMR improves the results significantly. For the lowest resolution the rest mass is conserved up to 0.3% with the C step and 1.7% without the C step. Larger differences in the rest mass are present for the nonconservative AMR runs regarding different resolutions than for the conservative AMR. Additionally, the central density of the remnant is denser without the C step, which is again caused by the mass-violation and increasing mass without C step. We observe an absolute uncertainty in the rest-mass conservation of $\sim 2.5 \times 10^{-3}\, M_\odot$ at the end of the simulation, and an uncertainty of the ejecta mass M_{ejecta} of $\sim 2.5 \times 10^{-4}\, M_\odot$.

Ejecta formation

Finally, we want to discuss the dynamical process at the origin of mass ejection. We can identify two hydrodynamical mechanisms in our simulation:

(i) the torque exerted by the central two-cores structure on the tidal tail,

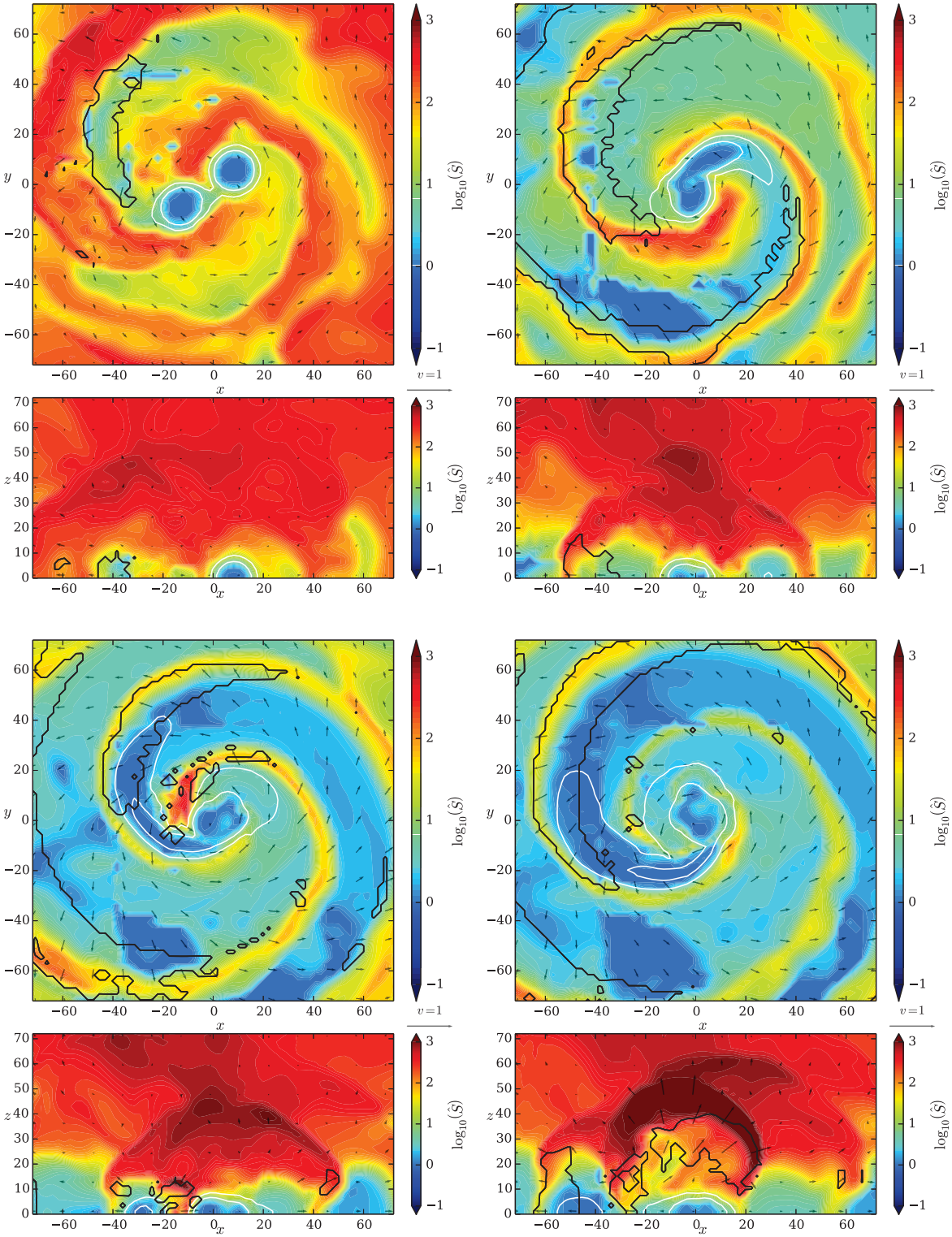

Figure 5.8: Snapshots of the MS1b-100150-R1c evolution on the $(x, y, z = 0)$ and $(x, y = 0, z)$ planes for $t = 806.4M, 1117.6M$ (upper panels) and $t = 1184.4M, 1212.4M_\odot$ (bottom panels). White contour lines are plotted for the density of $\rho = (10^{-5}, 10^{-4})$, and black lines refer to unbound material with $\rho_u = 10^{-8}$, the velocity v^i is visualized by black arrows. The logarithm of the entropy indicator $\log_{10} \hat{S}$ (Eq. (A.10)) is presented according to the color bar.

(ii) shock heating/waves generated in the region between the two cores.

Most of the unbound mass is ejected at times close to the moment of merger $t_{\rm mrg} \sim 1060M$ and in the orbital plane with a small opening angle of $\lesssim 15^\circ$. The first three panels of Fig. 5.6 clearly show that mass is ejected mostly from the tidal tails of the companion star. Thus, the torque mechanism (i) is the most dominant effect for this configuration.

For a more detailed study of mechanism (ii), we consider 2D plots of the x-y- and x-z-plane for the rest-mass density ρ, velocity v^i, and entropy indicator $\hat{S}$, Eq. (A.10), in Fig. 5.8. The color map refers to $\log_{10} \hat{S}$, white contour lines to densities $\rho = (10^{-6}, 10^{-5})$, arrows to the velocity pattern, and regions delimited by black solid lines highlight unbound material ρ_u with $\rho_u > 10^{-8}$.

Around $t \sim 1900 \approx 760M$, the rotation of the cores exerts torque on the slow-density outer layers of the companion star. Due to this process, the material gains enough energy, becomes unbound and is ejected from the system. The average velocity of the ejected material is $\langle v \rangle_\rho \sim 0.3$. At this time also minor ejecta due to shock heating occur, see top left panel of Fig. 5.8.

Within $t \sim t_{\rm mrg} \sim 2650 \approx 1060M$ and $t \sim 2900 \approx 1160M$ we observe also mass ejection from the tidal tail of the primary star. The entropy indicator $\hat{S}$ shows a spiral-like pattern in Fig. 5.8 which proves that the influence of the thermal pressure component P_{th}, as expected, is larger in less dense regions.

At $t \sim 3000 \approx 1200M$ a large amount of material is ejected by shock heating generated between the two density maxima of the HMNS; shown in the bottom panels of Fig. 5.8. The fluid is heated up and driven outward by the thermal pressure in high entropy regions. Although the mass is initially ejected in a direction almost perpendicular to the orbital plane, it falls back on the orbital plane and acquires angular momentum.

We present the rest mass, the kinetic energy and measures of the ejecta geometry in Fig. 5.7 (right panels). The rest mass of the total ejected material is about $M_{\rm ejecta} \sim 0.03\, M_\odot$ for all employed resolutions. The mass decrease present in the figure is mostly a numerical effect caused by resolution and the atmosphere setup. The kinetic energy of the ejecta is $T_{\rm ejecta} \sim 3.2 \times 10^{-4} \approx 2.9 \times 10^{50}$erg. The lower right panel of Fig. 5.7 presents measures for the geometry of the ejecta. Most of the material expands more rapidly inside the orbital plane than perpendicular to it. Additionally, $\langle \rho \rangle$ and $\langle z \rangle$, Eq. (A.7a) and (A.7b), suggest that the ejecta extends mainly around the equatorial plane with a small opening angle of $\theta \sim \arctan[z/\rho] \sim 10^\circ$. Due to the high mass ratio, the ejecta is anisotropic distributed on large scales.

The mechanisms (i) and (ii), which we described in detail for this configuration, are rather general and also present in our other setups. Therefore, the geometrical and kinematic properties of dynamical ejecta are expected to be representative at

least on a qualitative level, cf. [Hotokezaka et al., 2013b; Sekiguchi et al., 2015], although different mass ratios and EOSs lead to quantitative differences. A possible inclusion of more realistic microphysical aspects, e.g. neutrinos and magnetic fields[6], may change the picture; see [Sekiguchi et al., 2015] for the discussion of possible ejecta caused by neutrino heating.

5.3 A $q = 2.06$ configuration

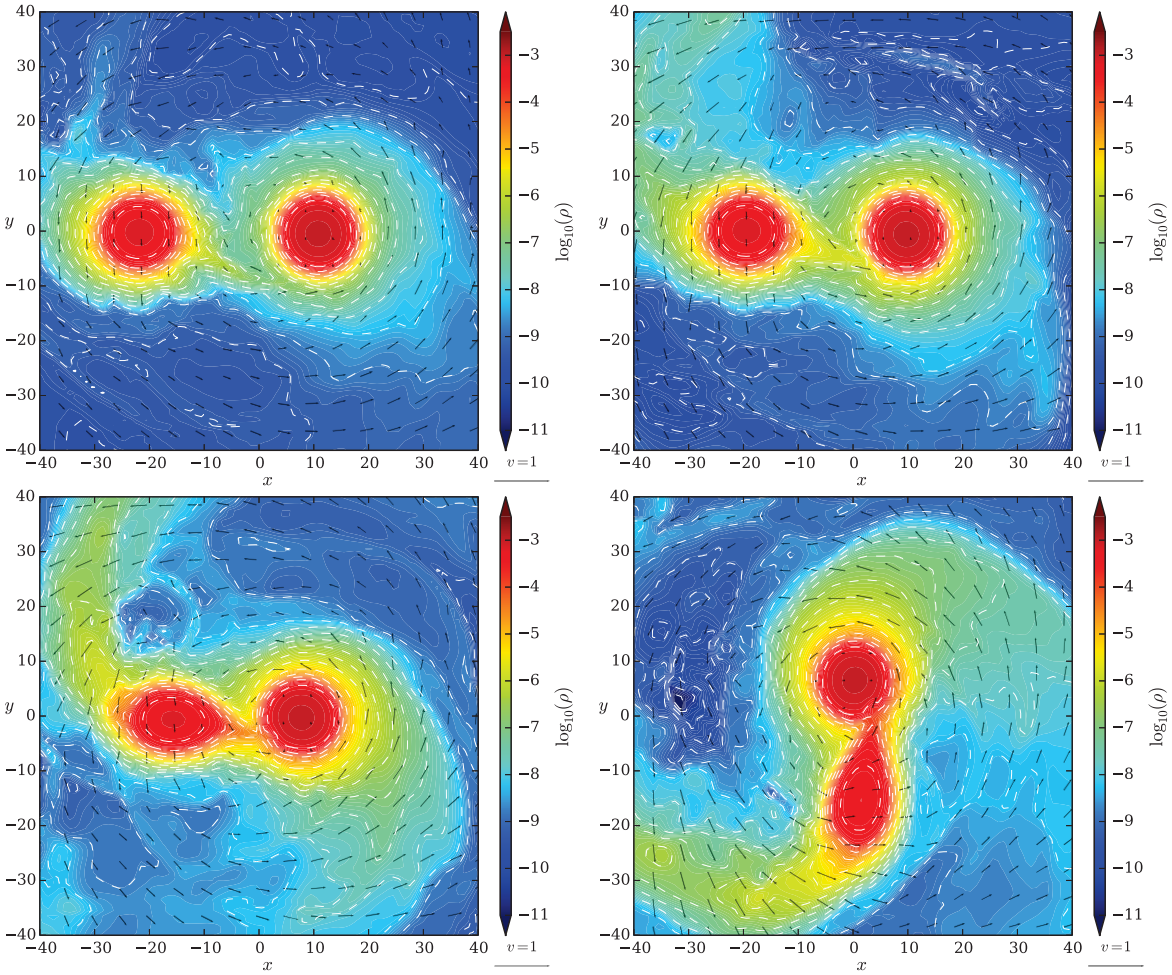

Figure 5.9: Plot of the matter density ρ and the velocity v^i in the orbital plane for $t = 1726M; t = 2227M; t = 2644M; t = 2692M$ (from top left to bottom right). During the four revolutions between the upper left and lower left panel, one can see a clear mass transfer between the two stars. The last plot refers to the moment of merger, where the companion star shows large tidal deformation.

Finally, we want to show results for a binary configuration with a mass-ratio of $q = 2.06$, which is the highest mass-ratio simulated in full general relativity to date. Notice that although the setup has a high mass-ratio, the initial linear ADM momentum is rather small: $\boldsymbol{P}_{\rm ADM} = (4.23 \times 10^{-7}, -1.10 \times 10^{-5}, -1.96 \times 10^{-6})$.

[6]Because the mechanisms producing mass ejection described here operate on very short timescales (a few milliseconds), we expect differences only on longer timescales when magnetic fields are included.

The computation of such systems became possible due to the improvements in the SGRID code, which is used to construct the quasi-equilibrium initial data for this section; cf. [Die13] and Appendix D. The two stars are characterized by rest masses of $M_b^A = 2.200$ and $M_b^B = 1.000$, corresponding to the gravitational masses $M^A = 1.944$ and $M^B = 0.944$. We employ the MS1b EOS. The initial GW frequency is $M\omega_{22}^0 = 0.0359$, see Tab. 5.1 for further details.

Mass transfer

We present snapshots of the density and velocity field during the inspiral in Fig. 5.9. The upper left panel shows the binary at $t = 1726M$, where the two stars are clearly separated, but mass transfer between the two stars becomes visible. The upper right panel shows the system at $t = 2227M$, two revolutions later. The lower left panel shows the setup another two revolutions later at $t = 2644M$. Finally, the system merges at $t = 2692M$ (lower right panel). At this time, the companion star is disrupted due to the tidal interaction with the primary star. Between $t = 1726M$ and $t = 2644M$ material with a rest mass of $\sim (2\text{–}3) \times 10^{-2} M_\odot$ was transferred between the two stars. This is roughly $(2\text{–}3)\%$ of the total rest mass of the less massive star. The mass transfer happens continuously in our simulation until the companion is tidally disrupted. We estimate the mass-transfer by measuring the rest-mass inside the finest refinement levels around star A and star B. The high uncertainty is caused by the artificial atmosphere treatment and the length of the simulation.

Assuming an average mass transfer rate of $\dot{M}_{AB} \sim 10^{-5} \approx 1 M_\odot \text{ s}^{-1}$ we can estimate the accretion power of the process. However, due to the uncertainty of the numerical data and the fact that no electromagnetic fields or neutrino emission are included in our simulation, we can just present a simple order-of-magnitude estimate. Consider the change in energy of the transfered matter going down from the less massive to the more massive star's Newtonian potential well, we have an average accretion power of $\sim \dot{M}_{AB}(\mathcal{C}^A - \mathcal{C}^B) \sim 10^{-6} \approx 10^{53}$ erg s^{-1}, which is comparable to the neutrino luminosities found in simulations of BNS mergers [Sekiguchi et al., 2011a; Sekiguchi et al., 2015; Palenzuela et al., 2015]. Since the process takes place over $\sim 10^{-2}$ s, the total accretion energy is $\sim 10^{51}$ ergs. As mentioned above, the released energy in photons or neutrinos can not be estimated from our simulations with the current version of the BAM code and has to be postponed to the future. We also do not see a noticeable imprint of the mass transfer on the phase of the GWs. Note that in Newtonian SPH simulations [Fryer et al., 2015] for a BNS configuration with $q = 2$ no mass transfer is mentioned, while in [Dan et al., 2011] the authors found mass transfer for a white dwarf binary simulations with $q = 2$.

After merger ($t = 2692M$) a SMNS is formed. We do not expect that the SMNS collapses on dynamical timescales and forms a stable configuration, since the final SMNS mass is close to the maximum supported mass of a stable TOV star with the

same EOS. Furthermore, no indication for a collapse is present in the simulation at $t = 6500M \simeq 0.09$s, where the central density reaches a constant value of $\rho_c \simeq 9.8 \times 10^{-4} \simeq 6 \times 10^{14}$ g cm^{-3}.

Ejecta and kick

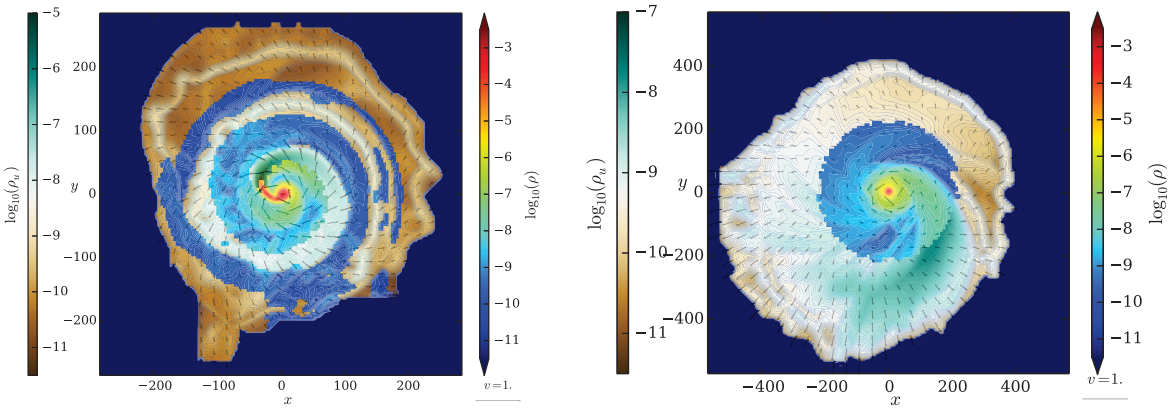

Figure 5.10: Contour plot of the matter density ρ, the density of unbound material ρ_u, and the velocity field v^i. A clear spiral like pattern in the ejecta is visible at $t = 2798M$ (left panel). At $3421M$ material is anisotropically ejected over the entire grid (right panel). Plot adapted from [Die13].

Because of the high mass ratio, a significant amount of material is ejected, where the rest mass of the ejected material is $M_{\text{ejecta}} \simeq 7.6 \times 10^{-2} M_\odot$. This is among the largest ejecta found in full general relativistic simulations of binary neutron star mergers on quasi-circular orbits, e.g. [Hotokezaka et al., 2013b] and [Die8], and is even slightly larger than the ejecta found in eccentric binary simulations [East and Pretorius, 2012].

Figure 5.10 visualizes the ejected material. As for the detailed case study in Sec. 5.2, most of the material is ejected by torque on the tidal tail of the companion star (left panel). The right panel shows clearly that matter is ejected anisotropically, since the density inside the ejected material differs for different directions by several orders of magnitude.

The anisotropic mass ejection causes a recoil of the merger remnant. One possible way of approximating the linear momentum of the ejecta is $\boldsymbol{P}_{\text{ej}} = M_{\text{ej}} \langle \boldsymbol{v}_{\text{plane}} \rangle = M_{\text{ej}} (\int D\, \boldsymbol{v}_{\text{plane}} \mathrm{d}x\mathrm{d}y)/(\int D \mathrm{d}x\mathrm{d}y)$, where the integrals and $\boldsymbol{v}_{\text{plane}}$ are restricted to the orbital plane, but M_{ej} refers to the rest mass of the unbound matter over the entire domain. For our setup, we obtain $v^{\text{ej}}_{\text{kick}} = \|\boldsymbol{P}_{\text{ej}}\|/M \sim 100 - 1000$ km s^{-1}, which is consistent with the coordinate speed of the position of the SMNS. Nevertheless, the value is just an order of magnitude estimate, because of the difficulties computing the ejecta, the long simulation time, and the gauge dependence of the measurement. Additionally, we see some contribution to the kick from anisotropic GW emission caused by the unequal masses of the constituents. The kick velocity related to the GW-emission is $\boldsymbol{v}^{\text{GW}}_{\text{kick}} = -\int \dot{\boldsymbol{P}}_{\text{GW}} \mathrm{d}t \,/M$ where the linear momentum flux $\dot{\boldsymbol{P}}_{\text{GW}}$ is computed

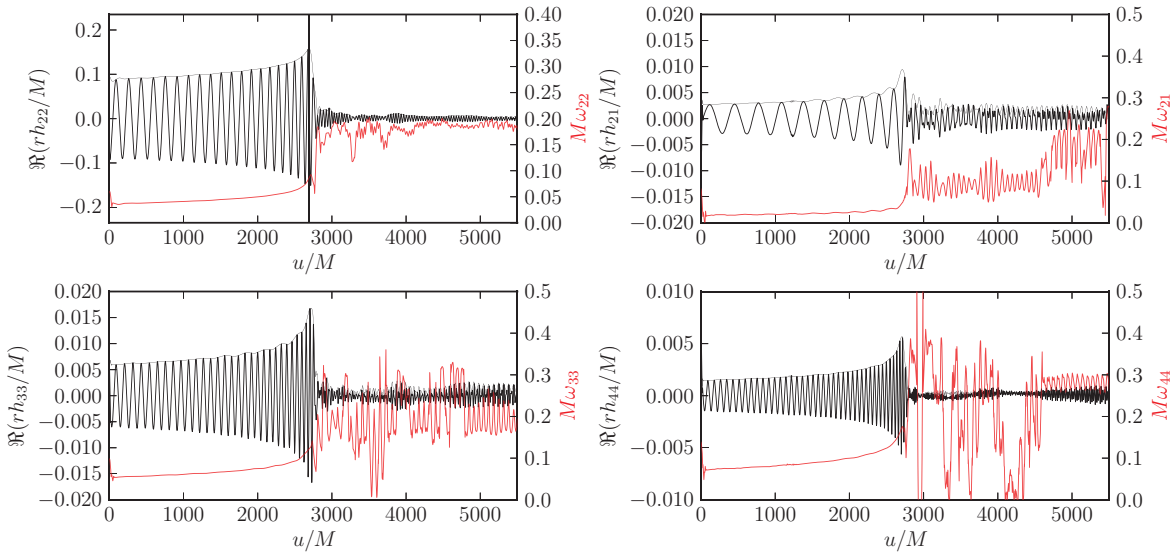

Figure 5.11: The four multipoles $(l, m) = (2, 2)$, $(2, 1)$, $(3, 3)$, and $(4, 4)$, which are the most dominant GW emitter during inspiral. The real part (black) and the dimensionless GW frequency (red). The vertical line marks the moment of merger (only shown in the upper left panel). The frequency oscillations correspond to artifacts caused by the outer boundary and by zeros of the amplitude. Plot taken from [Die13].

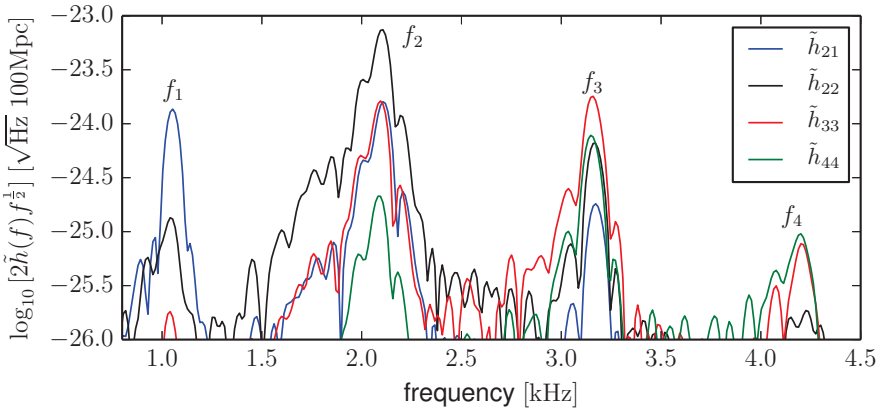

Figure 5.12: PSD for the time interval $u \in [3800M, 5700M]$, i.e. restricted to the SMNS spectrum. Clearly visible is the harmonicity of the frequencies f_1, f_2, f_3, f_4. The spectra are filtered with a Hanning-window. Plot adapted from [Die13].

as in [Brügmann et al., 2008]. For our setup, $v^{\text{GW}}_{\text{kick}} \simeq 100$ km s^{-1} at merger, which is smaller than the ejecta kick, cf. [Kyutoku et al., 2015; Kawaguchi et al., 2015].

Waveforms

Figure 5.11 presents the four modes $(l, m) = (2, 2)$, $(2, 1)$, $(3, 3)$, and $(4, 4)$, which are the main GW emitter during the inspiral. The inspiral-merger signal ends at $u_{\text{mrg}} = 2692M$. Because of the high mass ratio more energy is released in subdominant modes, for a quantitative analysis, we compare our simulation with an equal mass setup used in chapter 6. While for the $q = 1$ simulation $\sim 99.6\%$ of the energy is released in the $(2, 2)$-mode, only $\sim 98\%$ is released for MS1b-094194-c. Furthermore, because of symmetry the $(2, 1)$ and the $(3, 3)$ modes are zero for $q = 1$, but for

$q = 2.06$ the $(2,1)$-mode releases about $\sim 0.08\%$ and the $(3,3) \sim 1.4\%$. The $(4,4)$ mode contributes to $\sim 0.19\%$ of the total energy for $q = 1$ and 0.22% for $q = 2.06$.

During the post-merger phase several modes are excited and contribute to the GW emission. As done before, we compute the PSD for the SMNS restricted to the interval $u \in [3800M, 5700M]$. The result is shown in Fig. 5.12. The $f_2 = 2.09\text{kHz}$ ($Mf_2 = 0.0298$) frequency is clearly visible in all modes. The peaks of the other modes reveal that the f_k frequencies are harmonic to a very high accuracy, i.e., $f_1 = f_2/2 = f_3/3 = f_4/4$. We find: $f_1 = 1.05\text{kHz}$ ($Mf_1 = 0.0150$), $f_3 = 3.16\text{kHz}$ ($Mf_3 = 0.0449$), $f_4 = 4.20\text{kHz}$ ($Mf_4 = 0.0598$). For this setup the agreement is better than 1%, although the uncertainty, $\sim 0.15\text{kHz}$, is even larger. A similar harmonicity was also found in [Stergioulas et al., 2011], using the conformal flatness approximation and performing a Fourier transformation of the pressure. However, Fig. 5.12 verifies for the first time that the harmonicity holds in full-general relativistic simulations and that it is present in the emitted GW signal.

Chapter 6

Gravitational waveform modeling

In this chapter we perform a more detailed investigation of the gravitational waveform produced in a BNS merger simulation. We compare the numerical data with a recently improved semi-analytical, resummed tidal EOB model in Sec. 6.1. The EOB model also allows us to draw conclusions about quasi-universal properties present during the inspiral and in the post-merger phase, which will be discussed in Sec. 6.2.

6.1 The Effective-One-Body model

Probably the most intuitive, analytical approach for the description of compact binaries with comparable masses is post-Newtonian (PN) theory, where relativistic corrections proportional to $\sim (v/c)^2$ or $\sim (GM)/(c^2 r)$ are added to the Newtonian equations (see [Blanchet, 2014] for a review). In addition, also gravitational self-force (GSF) calculations taking into account self-field effects modifying the leading-order geodesic motion of small masses can give valuable information about the orbital dynamics of binary systems (cf. [Barack, 2009] and references therein).

The *Effective-One-Body* formalism [Buonanno and Damour, 1999; Buonanno and Damour, 2000; Damour et al., 2000; Damour, 2001] allows to combine PN, GSF, and NR results. Thus, it is an alternative to the direct combination of PN and NR waveforms; see e.g. [Hannam et al., 2008b; Hannam et al., 2008a; MacDonald et al., 2013; Read et al., 2013]. We are going to review briefly important properties of the EOB model in Sec. 6.1.1 and describe the recently improved tidal EOB model, proposed in [Die2] and mainly developed by S. Bernuzzi and A. Nagar, in more detail in Sec. 6.1.2. Finally, we compare it with NR simulations in Sec. 6.1.3.

6.1.1 Basics of the EOB model

The EOB formalism maps the relativistic 2-body problem, with masses M^A and M^B into the motion of an effective particle of mass $\mu = M^A M^B/(M^A + M^B)$ moving in an effective metric $g^{\rm eff}_{\mu\nu}$. It consists of three building blocks:

(i) a Hamiltonian $H_{\rm EOB}$ describing the conservative dynamics,

(ii) a radiation reaction force $\mathcal{F}$,

(iii) a factorized gravitational waveform h_{lm}.

In all these parts standard PN results are employed in a resummed form, i.e. some non-polynomial functions to incorporate non-perturbative features of the exact solution. This makes the model robust and predictive even in the strong-field and fast-motion regime.

EOB Hamiltonian

Within the usual PN formalism, the conservative dynamics of a two-body system is described by the Hamiltonian. In the center of mass system ($\mathbf{p_1} + \mathbf{p_2} = \mathbf{0}$) the rescaled Hamiltonian $\hat{H} = H/\mu$ for the relative motion of the rescaled variables, $\mathbf{q} = (\mathbf{q}_1 - \mathbf{q}_2)/(GM)$ and $\mathbf{p} = (\mathbf{p}_1 - \mathbf{p}_2)/\mu$, is given by

$$H^{\text{relative}}_{4PN}(\mathbf{q}, \mathbf{p}) = \hat{H}_{\text{N}} + \frac{1}{c^2}\hat{H}_{\text{1PN}} + \frac{1}{c^4}\hat{H}_{\text{2PN}} + \frac{1}{c^6}\hat{H}_{\text{3PN}} + \frac{1}{c^8}\hat{H}_{\text{4PN}}. \tag{6.1}$$

Equation (6.1) includes corrections up to 4PN, where $\mathbf{q}$ denotes the coordinates and $\mathbf{p}$ the conjugate momenta.

In Newtonian theory $\hat{H}_{\text{N}}$ determines the motion of a particle with mass μ around an object with mass M. The EOB formalism generalizes this approach, where the effective external spacetime is described in such a way that the geodesic motion of a particle with mass μ in the effective metric $g^{\text{eff}}_{\mu\nu}$ is equivalent to the PN-expanded dynamics, Eq. (6.1). The effective metric is of the form

$$g^{\text{eff}}_{\mu\nu}dx^\mu dx^\nu = -A(r;\nu)c^2dT^2 + B(r;\nu)dr^2 + r^2(d\theta + \sin^2(\theta)d\varphi^2). \tag{6.2}$$

The metric functions/potentials $A(r;\nu)$ and $B(r;\nu)$ can be constructed in a Taylor expanded form in $(GM)/(c^2r)$. Some of the expansion coefficients can be determined by, e.g., taking the Newtonian limit, requiring that the effective metric tends to the Schwarzschild metric for $\nu \to 0$, specifying a particular effective mass-shell condition, imposing that the linearized effective metric corresponds to the linearized Schwarzschild metric. We refer the reader to [Damour, 2012] for more details and references therein.

Finally, we have to correlate the effective Hamiltonian $\hat{H}_{\text{eff}}$, which in the non-spinning case is given by

$$\hat{H}_{\text{eff}}(u, p_{r_*}, p_\varphi) = \sqrt{A(u;\nu)\,(1 + p^2_\varphi u^2 + 2\nu(4-3\nu)u^2p^4_{r*}) + p^2_{r*}}, \tag{6.3}$$

and the real EOB-Hamiltonian H_{EOB}. This can be done with the map

$$H_{\text{EOB}} = \mu\hat{H}_{\text{EOB}} = M\sqrt{1 + 2\nu(\hat{H}_{\text{eff}} - 1)}, \tag{6.4}$$

where $u \equiv 1/R \equiv GM/(rc^2)$, $p_\varphi \equiv P_\varphi/(M\mu)$ is the dimensionless orbital angular momentum, and $p_{r_*} \equiv \sqrt{A/B}p_r = P_r/\mu$ denotes the dimensionless radial momentum.

Factorized Gravitational Waveform

We follow in our description of the GW signal [Damour and Nagar, 2008; Damour and Nagar, 2009a; Damour et al., 2009], where the multipolar waveform was presented as a product of several factors:

$$h_{lm} = h_{lm}^{(N)}(v_\varphi)\; S_{\rm eff}\; \hat{h}_{lm}^{\rm tail}(y)\;\; \left[\rho_{lm}(v_\varphi^2)\right]^l\;\; \hat{h}_{lm}^{\rm NQC}, \tag{6.5}$$

with $y = (GH_{\rm EOB}\Omega)^{2/3}$. $h_{lm}^{(N)}(v_\varphi)$ describes the Newtonian contribution, $S_{\rm eff}$ a source factor, $\hat{h}_{lm}^{\rm tail} = T_{lm}e^{i\delta_{lm}}$ the tail factor, ρ_{lm} the resummed modulus corrections, and $\hat{h}_{lm}^{\rm NQC}$ possible next-to-quasi-circular corrections with v_φ being the azimuthal velocity, see e.g. [Damour et al., 2013] for a detailed description of the individual terms.

Equations of Motion and Radiation Reaction

From Eq. (6.4) we can derive the equations of motion:

$$\frac{dR}{dt} = \left(\frac{A}{B}\right)^{1/2}\frac{\partial \hat{H}_{\rm EOB}}{\partial p_{r*}}\,, \tag{6.6a}$$

$$\frac{d\varphi}{dt} = \frac{\partial \hat{H}_{\rm EOB}}{\partial p_\varphi} = \Omega\,, \tag{6.6b}$$

$$\frac{dp_{r*}}{dt} = -\left(\frac{A}{B}\right)^{1/2}\frac{\partial \hat{H}_{\rm EOB}}{\partial R} + \hat{\mathcal{F}}_{r*}\,, \tag{6.6c}$$

$$\frac{dp_\varphi}{dt} = \hat{\mathcal{F}}_\varphi\,. \tag{6.6d}$$

To solve this system of equations, we have to specify the μ-rescaled radiation reaction forces $\hat{\mathcal{F}}_{r*,\varphi} = \mathcal{F}_{r*,\varphi}/\mu$. In our analysis $\hat{\mathcal{F}}_{r*}$ will be set to zero, but also other choices are possible, see e.g. [Damour et al., 2013; Damour and Nagar, 2014]. We set the azimuthal part of the radiation reaction force to

$$\mathcal{F}_\varphi = -\frac{1}{8\pi\nu\Omega}\sum_{l=2}^{l_{\rm max}}\sum_{m=1}^{l}(m\Omega)^2|rh_{lm}|^2. \tag{6.7}$$

Thus, the radiation reaction force depends on the emitted GW signal given by Eq. (6.5) and itself influences the orbital dynamics, which changes again the GW signal. Iterating over this process leads finally to a self-consistent solution describing the dynamics of the system.

6.1.2 Tidal EOB models

Beyond the test-mass limit, the potential $A(R)$ describing the effective metric of a BNS system is a deformation of the Schwarzschild potential $A_{\rm Schw}$, which is

governed by two different physical effects: (i) finite-mass ratio effects, parametrized by $\nu \equiv \mu/M$; and (ii) tidal effects, parametrized by relativistic tidal polarizability parameters κ^l_A [Hinderer, 2008; Damour and Nagar, 2009b; Binnington and Poisson, 2009; Hinderer et al., 2010].

Figure 6.1 contrasts the deformations of $A(R;\, \nu;\, \kappa^l_A)$ induced by finite-mass-ratio effects, which make $A(R)$ more repulsive, and by tidal effects, which make $A(R)$ more attractive in the strong-field regime where they dominate over the repulsive finite-mass-ratio effects. Figure 6.1 also compares the new resummed tidal EOB model (incorporating recent advances in the relativistic theory of tidal interactions [Bini and Damour, 2014c; Dolan et al., 2014; Bini and Damour, 2014b]) with another tidal EOB model that incorporates a tidal potential treating tidal interactions in a nonressummed way, up to next-to-next-to-leading order (NNLO, fractional 2PN) [Vines and Flanagan, 2010; Bini et al., 2012]. The resummed tidal EOB model is significantly more attractive than the NNLO one at small separations. The marker in the figure indicates the radial location corresponding to the merger for the resummed EOB model ($R_{\rm mrg} = 6.093$).

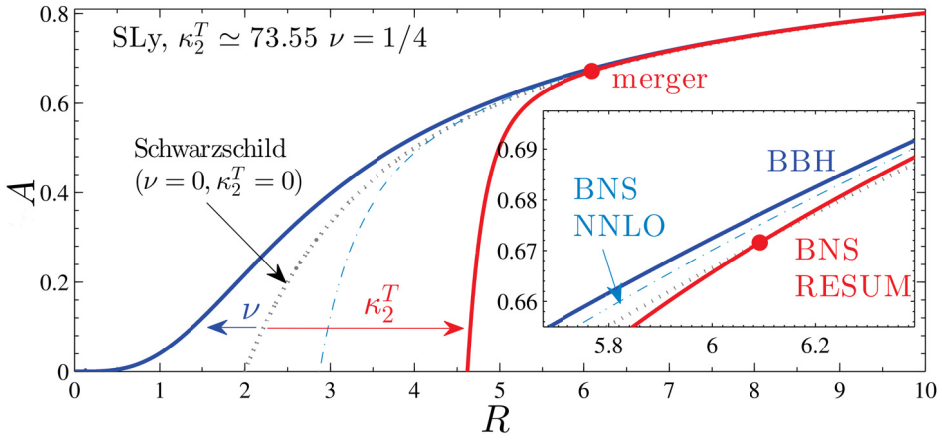

Figure 6.1: The main radial gravitational potential $A(R)$ in various EOB models. Finite-mass ratio effects, modeled by ν, make the gravitational interaction more repulsive than the Schwarzschild potential $A_{\rm Schw} = 1 - 2M/r$, while tidal effects, modeled by κ^T_2, make it more attractive. In the TEOB$_{\rm Resum}$ model tidal effects are stronger than in the TEOB$_{\rm NNLO}$ model and change the A-potential even at the moment of merger at $R_{\rm mrg} = 6.093$ (see inset). The tidal EOB models are shown for an equal-mass ($1.35M_\odot - 1.35M_\odot$) – configuration for the SLy EOS. Plot adapted from [Die2] and authored by S. Bernuzzi.

As outlined in [Damour and Nagar, 2010; Damour et al., 2012b], tidal interactions can be incorporated in the EOB formalism by a radial potential of the form

$$A(R;\, \nu;\, \kappa^l_A;\, \kappa^l_B) = A^0(R;\, \nu) + A^T(R; \kappa^l_A) + A^T(R; \kappa^l_B), \tag{6.8}$$

where $A^0(R)$ is the point-particle contribution and $A^T(R)$ incorporates additional tidal interaction. The point-particle contribution up to 5PN [Bini and Damour,

2013; Barausse et al., 2012] can be given explicitly:

$$A^0_{5\mathrm{PN}}(u;\nu) = 1 - 2u + \nu(a_3 u^3 + a_4 u^4 + (a^c_5(\nu) + a^{\ln}_5 \ln u)u^5 + (a^c_6(\nu) + a^{\ln}_6 \ln u)u^6). \quad (6.9)$$

In practice we use the Taylor-expanded function $A^0_{5\mathrm{PN}}$ in a resummed form employing a $(1,5)$ Padé approximant, i.e. $A^0(u;\nu) \equiv P^1_5[A^0_{5\mathrm{PN}}(u;\nu)] = \frac{1+n_1 u}{1+d_1 u+d_2 u^2+d_3 u^3+d_4 u^4+d_5 u^5}$, where the logarithmic terms are treated as constants. The individual terms in Eq. (6.9) are $a_4 = \frac{94}{3} - \frac{41}{32}\pi^2, a^c_5 = -\frac{4237}{60} + \frac{2275}{512}\pi^2 + \frac{256}{5}\ln 2 + \frac{128}{5}\gamma + \left(-\frac{211}{6} + \frac{41}{32}\pi^2\right)\nu, a^{\ln}_5 = \frac{64}{5}, a^{\ln}_6 = -\frac{7004}{105} - \frac{144}{5}\nu, a^c_6 = 3097.3\nu^2 - 1330.6\nu + 81.38$ with the Euler constant γ.

Although at 5PN both $a^{\ln}_6$ and the linear-in-ν part of $a^c_6(\nu)$ are analytically known [Barausse et al., 2012; Bini and Damour, 2014c; Bini and Damour, 2014a], we use the effective value deduced from a comparison between the EOB model and BBH simulations [Mroue et al., 2013]. In addition, no flexibility parameter calibrated to our NR data is added to the model.

The tidal contribution to $A(u)$ (omitting the negligible gravitomagnetic part [Damour and Nagar, 2009b]) is

$$A^{(+)}_T(u;\nu) \equiv -\sum_{l=2}^{4}\left[\kappa^{(l)}_A u^{2l+2}\hat{A}^{(l^+)}_A + \kappa^{(l)}_B u^{2l+2}\hat{A}^{(l^+)}_B\right], \quad (6.10)$$

with

$$\kappa^{(l)}_A = 2k^l_A\left(X_A/\mathcal{C}_A\right)^{2l+1} M_B/M_A, \quad \kappa^{(l)}_B = 2k^l_B\left(X_B/\mathcal{C}_B\right)^{2l+1} M_B/M_A, \quad (6.11)$$

where $X_{A,B} \equiv M_{A,B}/M$ and $k^{(l)}_{A,B}$ are the dimensionless Love numbers [Hinderer, 2008; Damour and Nagar, 2009b; Binnington and Poisson, 2009; Hinderer et al., 2010]. The EOS information is essentially encoded in the total dimensionless quadrupolar tidal coupling constant defined as

$$\kappa^T_2 \equiv \kappa^{(2)}_A + \kappa^{(2)}_B. \quad (6.12)$$

The relativistic correction factors $\hat{A}^{(l^+)}_A$ formally include all the higher PN corrections after the leading-order. We want to present two possible approaches for the description of the tidal interactions: The NNLO tidal EOB model ($\mathrm{TEOB_{NNLO}}$) and the resummed tidal EOB model ($\mathrm{TEOB_{Resum}}$).

The $\mathrm{TEOB_{NNLO}}$ model uses the PN-expanded, fractionally 2PN accurate, expression

$$\hat{A}^{(l^+)\mathrm{NNLO}}_A = 1 + \alpha^{(l)}_1 u + \alpha^{(l)}_2 u^2, \quad (6.13)$$

with $\alpha^{(2),(3)}_{1,2} \neq 0$ and $\alpha^{(4)}_{1,2} = 0$ [Bini et al., 2012].

In our resummed tidal EOB model ($\mathrm{TEOB_{Resum}}$) we use for the $l = 2$ term in

Eq. (6.10) the expression

$$\hat{A}_A^{(2^+)}(u) = 1 + \frac{3u^2}{1 - R_{\rm LR}u} + \frac{X_A \tilde{A}_1^{(2^+)1{\rm SF}}}{(1 - R_{\rm LR}u)^{7/2}} + \frac{X_A^2 \tilde{A}_2^{(2^+)2{\rm SF}}}{(1 - R_{\rm LR}u)^{p}}, \tag{6.14}$$

where the functions $\tilde{A}_1^{(2^+)1{\rm SF}}(u)$ and $\tilde{A}_2^{(2^+)2{\rm SF}}(u)$ are defined as in [Bini and Damour, 2014b]. The exponent p in the last term of Eq. (6.14) is set to $p = 4$. In the TEOB$_{\rm Resum}$ approach the $l = 3, 4$ contributions of the resummed model are taken from the TEOB$_{\rm NNLO}$ model. An important aspect of the resummed model is to use as the pole location in Eq. (6.14) the light ring $R_{\rm LR}(\nu; \kappa_A^{(l)})$ of the NNLO tidal EOB model [Bini et al., 2012], i.e. the location of the maximum of $A^{\rm NNLO}(R; \nu; \kappa_A^{(l)})/R^2$.

Finally, we set the radial part of the radiation reaction, $\hat{\mathcal{F}}_{r*}$, to zero [Damour and Nagar, 2014]; and complete the non-zero tidal part of radiation reaction with the next-to-leading-order tidal contribution [Damour and Nagar, 2010; Vines and Flanagan, 2010; Damour et al., 2012b].

6.1.3 Comparison of the Tidal EOB model and numerical results

Table 6.1: BNS configurations. Columns refer to: configuration name, EOS, the tidal coupling constants κ_2^T, TEOB$_{\rm NNLO}$ light-ring location, star compactnesses $\mathcal{C}_{A,B}$ and gravitational masses in isolation, initial ADM mass $M^0_{\rm ADM}$, and ADM angular momentum, $J^0_{\rm ADM}$ and the initial circular GW frequency $M\omega^0_{22}$. The next columns describe the grid configuration with: number of refinement levels L, finest grid spacing h_{L-1}, radial resolution inside the shells h_r, number of points n (n^{mv}) in the fixed (moving) levels, radial point number n_r and angular point number n_θ in the shells, and the location of the outer boundary r_b.

Name	EOS	κ_2^T	$R_{\rm LR}$	$\mathcal{C}_{A,B}$	$M_{A,B}$	$M^0_{\rm ADM}$	$J^0_{\rm ADM}$	$M\omega^0_{22}$	L	h_{L-1}	h_r	n	n^{mv}	n_r	n_θ	r_b
2B$_{135}$	2B	23.912	3.253	0.205	1.34997	2.67762	7.66256	0.038	7	0.186	5.952	128	64	128	56	1163
									7	0.124	3.968	192	96	192	84	1157
									7	0.093	2.976	256	128	256	112	1153
SLy$_{135}$	SLy	73.545	3.701	0.174	1.35000	2.67760	7.65780	0.038	7	0.228	7.296	128	64	128	56	1426
									7	0.152	4.864	192	96	192	84	1418
									7	0.114	3.648	256	128	256	112	1414
$\Gamma 2_{164}$	$\Gamma 2\kappa 124$	75.067	3.728	0.160	1.64388	3.25902	11.11313	0.0414	5	0.3	2.4	96	64	682	32	1760
									5	0.2	1.6	144	96	1023	48	1759
									5	0.15	1.2	192	128	1364	64	1757
$\Gamma 2_{151}$	$\Gamma 2\kappa 124$	183.39	4.160	0.140	1.51484	3.00497	9.71561	0.0367	5	0.3	2.4	96	64	682	32	1760
									5	0.2	1.6	144	96	1023	48	1759
H4$_{135}$	H4	210.59	4.211	0.147	1.35003	2.67768	7.66315	0.038	7	0.279	8.928	128	64	128	56	1745
									7	0.186	5.952	192	96	192	84	1735
									7	0.1395	4.464	256	128	256	112	1730
MS1b$_{135}$	MS1b	289.80	4.381	0.142	1.35001	2.67769	7.66517	0.038	7	0.291	9.312	128	80	128	56	1820
									7	0.194	6.208	192	120	192	84	1809
									7	0.1455	4.656	256	160	256	112	1804

We compare the two tidal EOB models (TEOB$_{\rm NNLO}$ and TEOB$_{\rm Resum}$) and the Taylor T4 (with NLO tides and 3PN waveforms [Flanagan and Hinderer, 2008; Hinderer et al., 2010]) with equal-mass BNS simulations, where we employ the Z4c formulation of Einstein's equations (Sec. 2.1.3). All configurations are computed with the LORENE library and their main properties are summarized in Tab. 6.1. We employ multiple resolutions. The simulations of (2B$_{135}$, SLy$_{135}$, $\Gamma 2_{151}$, H4$_{135}$, MS1b$_{135}$) use three resolutions with $(64, 96, 128)$ grid points resolving the stars diameter. For ($\Gamma 2_{164}$) only the $(64, 96)$ resolutions are available. For all simulations level $l = 0$ employed

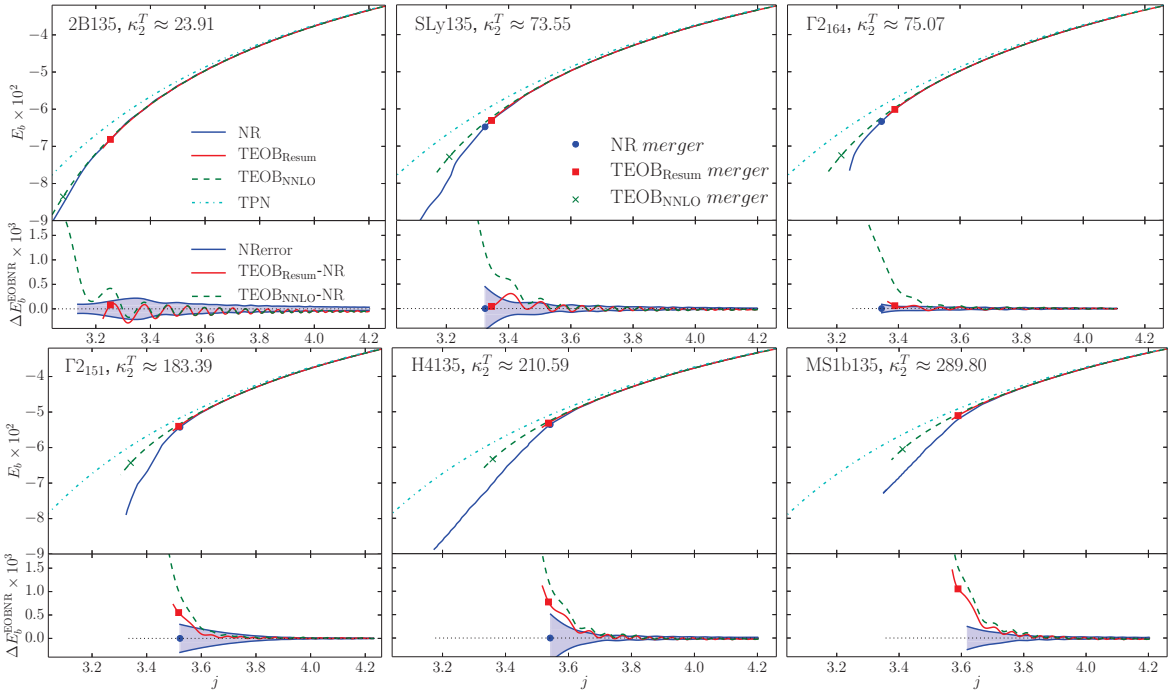

Figure 6.2: Energetics comparison between NR data, $\text{TEOB}_{\text{Resum}}$, $\text{TEOB}_{\text{NNLO}}$ and TPN. Each bottom panel shows the two EOB-NR differences. The filled circles locate the merger points (top) and the corresponding differences (bottom). The shaded area indicates the NR uncertainty. The $\text{TEOB}_{\text{Resum}}$ model displays, globally, the smallest discrepancy with NR data (most notably close to merger), supporting the theoretical, light-ring driven, amplification of the relativistic tidal factor. Plot adapted from [Die2].

the technique of “cubed spheres" and no additional Berger-Collela refluxing algorithm was used. The grid specifications are also stated in Tab. 6.1[1].

Numerical uncertainties are conservatively estimated as the difference between the highest and the second highest available resolutions, cf. [Bernuzzi et al., 2012a] and Appendix C.

Our comparison of the energetics is again based on the gauge-invariant relation between the binding energy and the orbital angular momentum, see Sec. 4.3 and Sec. 4.4.1.

The top panels of Fig. 6.2 compare for all EOSs and all models the energetics. The TPN model is a 2PN accurate expansion of the function $E(\ell)$ in powers of $1/c^2$. The markers identify the corresponding merger points. In the bottom panels the differences $\Delta E^{\text{EOBNR}}(\ell) = E^{\text{EOB}}(\ell) - E^{\text{NR}}(\ell)$ for $\text{TEOB}_{\text{Resum}}$ and $\text{TEOB}_{\text{NNLO}}$ are presented. The shaded area indicates the NR uncertainty. The main findings of this comparison are:

[1]We want to point out that for MS1b_{135} we performed tests with a smaller moving box first, but as shown in the previous chapter especially for stiff EOS mass enters the mesh refinement buffer region and causes mass violation. This can be solved with a conservative amr, which was not finally implemented when the simulations were performed. To overcome this issue we increased the box size as in Sec. 4.4. Furthermore, some simulations use higher resolution and different extraction radii compared to [Die2], which explains small differences.

(i) TPN is always above the NR curve with an unacceptably large difference towards merger;

(ii) the location of the $\mathrm{TEOB_{NNLO}}$ merger point in the (E, ℓ) plane is, in all cases, significantly away from the corresponding NR merger point;

(iii) by contrast, the $\mathrm{TEOB_{Resum}}$ merger point is, in most cases, close to the NR merger point;

(iv) the $\mathrm{TEOB_{Resum}}$–NR differences oscillate around zero during most of the simulated ~ 10 orbits;

(v) the $\mathrm{TEOB_{Resum}}$–NR differences are in most cases within or slightly above the NR uncertainty essentially up the merger.

Table 6.2: BNS phasing results. Columns refer to: the dimensionless merger frequency $M\omega_{22}^{\mathrm{mrg}}$ and the phase differences at the moment of merger $\Delta\phi^{\mathrm{X}} \equiv \phi^{\mathrm{X}} - \phi^{\mathrm{NR}}$, with $X = \mathrm{TT4}, \mathrm{TEOB_{NNLO}}, \mathrm{TEOB_{Resum}}$. The NR uncertainty $\delta\phi^{\mathrm{NR}}_{\mathrm{NRmrg}}$ is given in addition. The resummed $\mathrm{TEOB_{Resum}}$ model displays the best agreement with NR data. The phase differences, in radians, are obtained by aligning all waveforms in the frequency interval $I_\omega \approx (0.04, 0.06)$, except $\Gamma 2_{164}$ where we chose $I_\omega \approx (0.0428, 0.06)$.

Name	$M\omega_{22}^{\mathrm{mrg}}$	$\Delta\phi^{\mathrm{TT4}}_{\mathrm{NRmrg}}$	$\Delta\phi^{\mathrm{TEOB_{NNLO}}}_{\mathrm{NRmrg}}$	$\Delta\phi^{\mathrm{TEOB_{Resum}}}_{\mathrm{NRmrg}}$	$\delta\phi^{\mathrm{NR}}_{\mathrm{NRmrg}}$
$\mathrm{2B_{135}}$	0.213	-1.33	-0.28	$+0.51$	$\pm$ 2.13
$\mathrm{SLy_{135}}$	0.164	-2.71	-1.74	-0.75	$\pm$ 0.81
$\Gamma 2_{164}$	0.157	-2.29	-1.36	-0.31	$\pm$ 0.90
$\Gamma 2_{151}$	0.125	-2.60	-1.92	-1.27	$\pm$ 1.20
$\mathrm{H4_{135}}$	0.127	-3.24	-2.35	-1.88	$\pm$ 2.06
$\mathrm{MS1b_{135}}$	0.120	-2.87	-2.40	-2.45	$\pm$ 3.91

The EOB resummed tidal waveform is obtained following [Damour et al., 2009; Damour et al., 2012b]. We compare the EOB and NR quadrupole waveforms rh_{22}, with $r(h_+ - \mathrm{i}h_\times) = \sum_{lm} rh_{lm}\,{}_{-2}Y_{lm}$, by using a standard (time and phase) alignment procedure in the time domain. Relative time and phase shifts are determined by minimizing the L^2 distance between the EOB and NR phases integrated on a time interval corresponding to the dimensionless frequency interval $I_\omega = M(\omega_L, \omega_R) = (0.04, 0.06)$ for all EOSs, except $\Gamma 2_{164}$, for which $I_\omega = (0.0428, 0.06)$ because the simulation starts at higher GW frequency (see markers in Fig. 6.3). This choice for I_ω allows to average out the phase oscillations linked to the residual eccentricity (~ 0.01) of the NR simulations; see also Sec. V C in [Die13] for a discussion about the influence of the artificial eccentricity.

A sample of time-domain comparisons for six representative κ_2^T's is shown in Fig. 6.3. Top panels compare the real part and modulus of rh_{22} for $\mathrm{TEOB_{Resum}}$ and NR waveforms. The bottom panels compare: (i) phase and relative amplitude differences between $\mathrm{TEOB_{Resum}}$ and NR; (ii) phase differences between the tidal Taylor T4 with NLO tides and 3PN waveform (TT4) and NR; and (iii) NR phase uncertainty (shaded

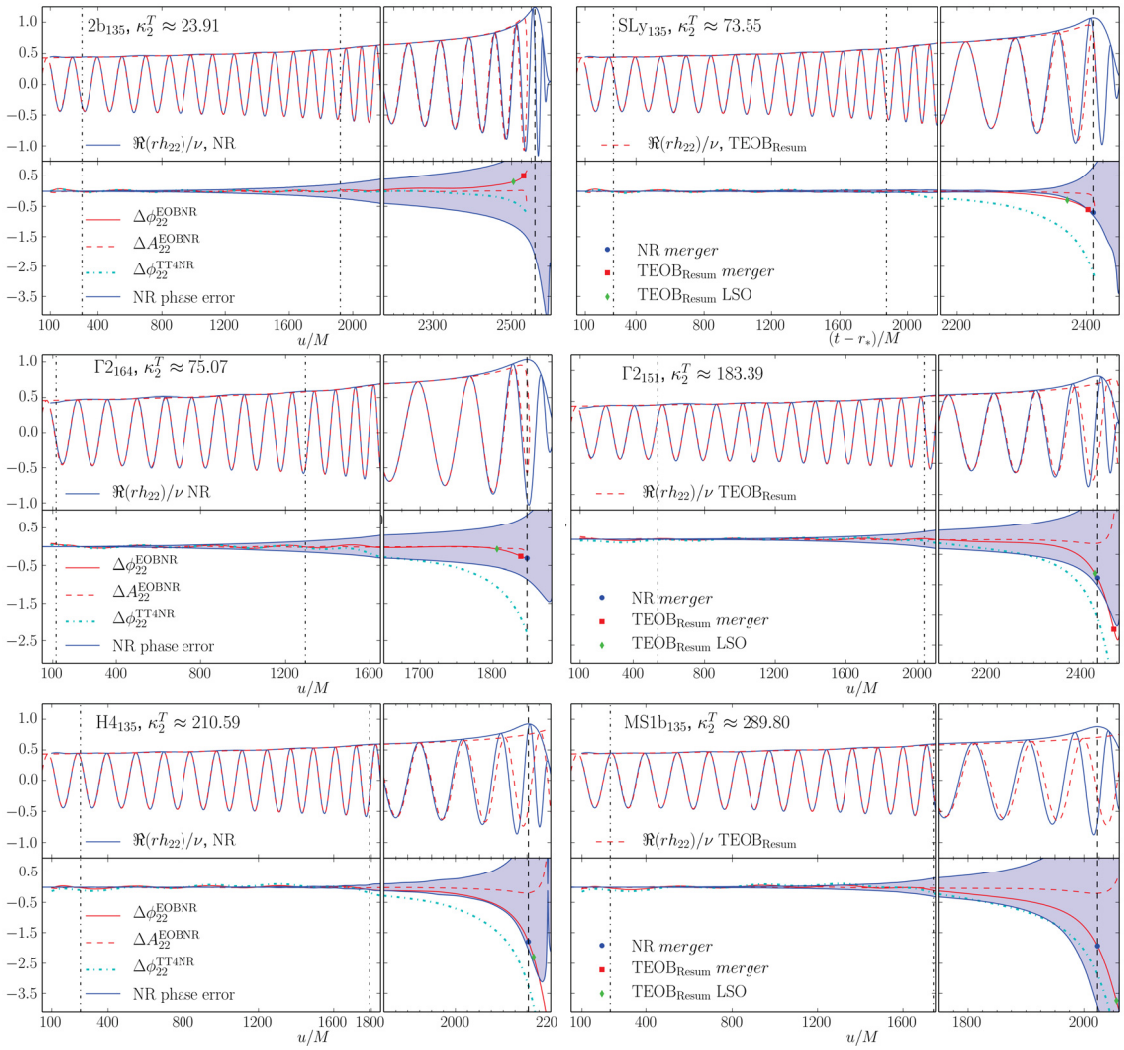

Figure 6.3: Phasing and amplitude comparison between $\mathrm{TEOB_{Resum}}$, NR and the phasing of TT4. Waves are aligned on a time window marked with vertical dot-dashed lines. The markers indicate: the crossing of the $\mathrm{TEOB_{Resum}}$ LSO radius; NR (dashed vertical line) and EOB merger moments. Plot adapted from [Die2].

region). The two vertical (dot-dashed) lines indicate the alignment interval; as in Fig. 6.2, the markers indicate the EOB (red) and NR (blue) mergers. The crossing of the radius of the $\mathrm{TEOB_{Resum}}$ last stable orbit (LSO) is indicated by a green marker. The time-domain comparisons shows that for all κ_2^T the $\mathrm{TEOB_{Resum}}$ model is compatible with NR data up to merger within NR uncertainties. Note that the TT4 phasing performs systematically worse than $\mathrm{TEOB_{Resum}}$.

Figure 6.3 is quantitatively completed by Table 6.1, which compares the phase differences $\Delta\phi^X \equiv \phi^X - \phi^{\rm NR}$ with $X = \mathrm{TT4}$, $\mathrm{TEOB_{NNLO}}$, $\mathrm{TEOB_{Resum}}$ evaluated (after time-alignment) at the moment of NR merger. The NR uncertainty at merger $\delta\phi^{\rm NR}_{\rm NRmrg}$ is also listed in the table. These numbers indicate how the disagreement with NR systematically decreases when successively considering the analytical models TT4, $\mathrm{TEOB_{NNLO}}$ and $\mathrm{TEOB_{Resum}}$. Such hierarchy of qualities among analytical models can

also be confirmed by the phasing diagnostic $Q_\omega(\omega) \equiv \omega^2/\dot{\omega}$ [Baiotti et al., 2010; Bernuzzi et al., 2012a]; see in particular Fig. 4 in [Die2], where one obtains $Q_\omega^{\rm NR} \approx Q_\omega^{\rm TEOB_{Resum}} < Q_\omega^{\rm TEOB_{NNLO}} < Q_\omega^{\rm TT4}$.

6.2 Quasi-universal relations in BNS simulations

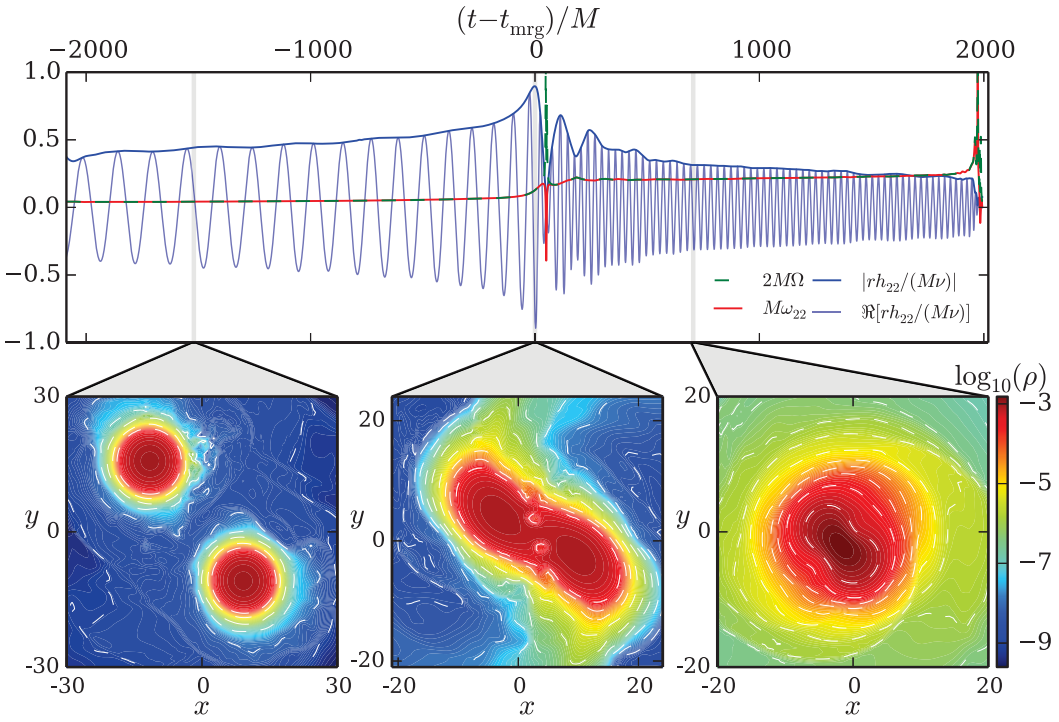

Figure 6.4: A typical equal-mass BNS simulation ($1.35M_\odot - 1.35M_\odot$ with the H4 EOS). Top panel: Real part and amplitude of the GW mode $\Re(rh_{22})/(\nu M)$ (blue) and the corresponding frequency $M\omega_{22}$ (red) plotted against the retarded time u shifted to the moment of merger. Also included is twice the dynamical frequency $2M\Omega = 2\frac{\partial E}{\partial \ell} \sim M\omega_{22}$. Bottom panels show snapshots of the density ρ inside the orbital plane during the late inspiral (left), at merger (middle), during the postmerger (right). Adapted from [Die3].

As discussed in the previous section, the EOB model can predict the dynamics and the emitted GW signal of BNS systems even up to the moment of merger; cf. [Die2]. In contrast to full-general relativistic simulations it allows an easier understanding of the underlying physical principles in the range of the validity of the model. In Sec. 6.2.1 we use the EOB model to make predictions about existing quasi-universal relations of the merger frequency, binding energy, reduced orbital angular momentum, and the wave's amplitude in the late inspiral of NS binaries [Die1; Die10]. We verify the predictions with numerical simulations and show in Sec. 6.2.2 that similar quasi-universal relations hold in the post-merger phase. This might allow the development of a single model for the construction of GW templates for the inspiral-merger-postmerger. A first glimpse towards a combined description of pre- and post-merger is presented in Fig. 6.4, where a typical GW signal is shown. It is clearly visible that the dynamical frequency obtained from $2M\Omega = 2\partial E/\partial \ell$ characterizes the emitted

GW frequency over the entire simulation not only during the inspiral, which will be of importance later.

6.2.1 The late inspiral and merger

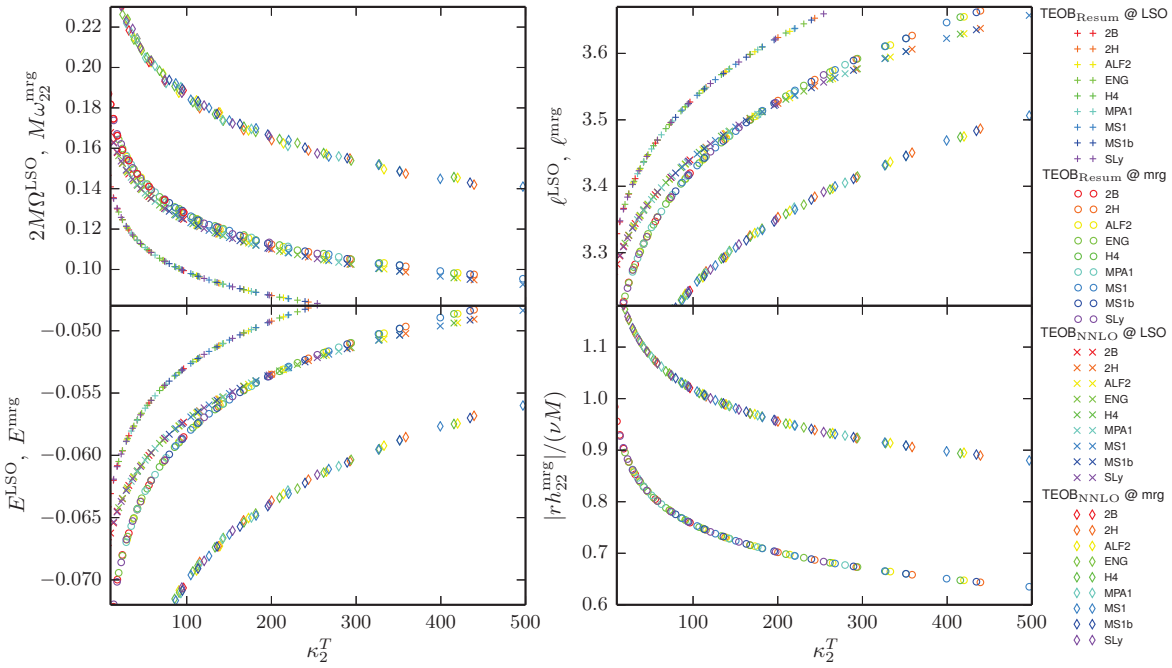

Figure 6.5: Orbital frequency at LSO, GW frequency at merger (upper left), binding energy (lower left), reduced orbital angular momentum (upper right), and GW amplitude (lower right). Results are shown at the LSO or at the peak of the GW amplitude for equal-masses, irrotational mergers. The employed EOB models are the adiabatic and nonadiabatic TEOB$_{\rm NNLO}$ and TEOB$_{\rm Resum}$ models discussed before. Different colors refer to different EOSs.

For simplicity we start our investigation about the existence of quasi-universal relations with adiabatic EOB-models corresponding to the adiabatic version of the TEOB$_{\rm NNLO}$ and TEOB$_{\rm Resum}$ models discussed before. We focus for these models on the dimensionless gravitational frequency $M\omega_{22}^{\rm LSO} = 2M\Omega^{\rm LSO}$, the binding energy $E^{\rm LSO} = (H_{\rm EOB} - M)/\mu$, as well as the dimensionless angular momentum per reduced mass $\ell^{\rm LSO}$ at the last stable orbit (LSO).

Stable circular orbits at u are minima of $\hat{H}_{\rm eff}$ for a fixed value of the momentum p_φ. From Eq. (6.6b) follows that $M\Omega(u;\nu) = \mu^{-1}\partial H_{\rm EOB}/\partial\ell$, with $\ell \equiv p_\varphi$. The end of the adiabatic circular dynamics is the LSO, the inflection point of $\hat{H}_{\rm eff}$. As shown in Fig. 6.1 the ν-corrections to the potential A act globally repulsive, while the tidal contribution A^T is attractive. The LSO frequency results as a balance between repulsive and attractive effects.

Writing $2M\Omega^{\rm LSO}$, $E^{\rm LSO}$, $\ell^{\rm LSO}$ as a function of the tidal coupling constant κ_l^T introduced in Eq. (6.12), these quantities become essentially independent of the choice of the EOS. Figure 6.5 displays this property for irrotational binaries. Although, the functional dependence $2M\Omega^{\rm LSO}(\kappa_2^T)$, $E^{\rm LSO}(\kappa_2^T)$, and $\ell^{\rm LSO}(\kappa_2^T)$ is complicated and

cannot be made explicit, we can fit the data with a (2,1)-Padé approximant and obtain percentual residuals $\lesssim 1\%$ as done in Fig. 1 of [Die1].

A similar observation can be made for the nonadiabatic EOB model ($\mathcal{F}_\varphi \neq 0$), which goes beyond the adiabatic-circular-LSO analysis. As shown in Fig. 6.5, the wave frequency $M\omega_{22}^{\rm mrg}$, the binding energy $E^{\rm mrg}$, the dimensionless orbital momentum $\ell^{\rm mrg}$, and the rescaled GW amplitude $|rh_{22}^{\rm mrg}|/(\nu M)$ at the moment of merger are also characterized by a κ_l^T-universality.

For all these different EOB models, the underlying principle for the universal behavior is the same. As discussed in Sec. 6.1.1 the EOB framework incorporates tidal interactions by an additive correction A^T to the radial, Schwarzschild-like metric potential A of the EOB Hamiltonian and the tidal correction A^T is parametrized by the relativistic tidal coupling constants $\kappa_{A,B}^{(l)}$ [Damour and Nagar, 2010; Damour et al., 2012b]. Thus, the leading order finite size effect on the dynamics is determined solely by the value of κ_2^T, Eq. (6.12).

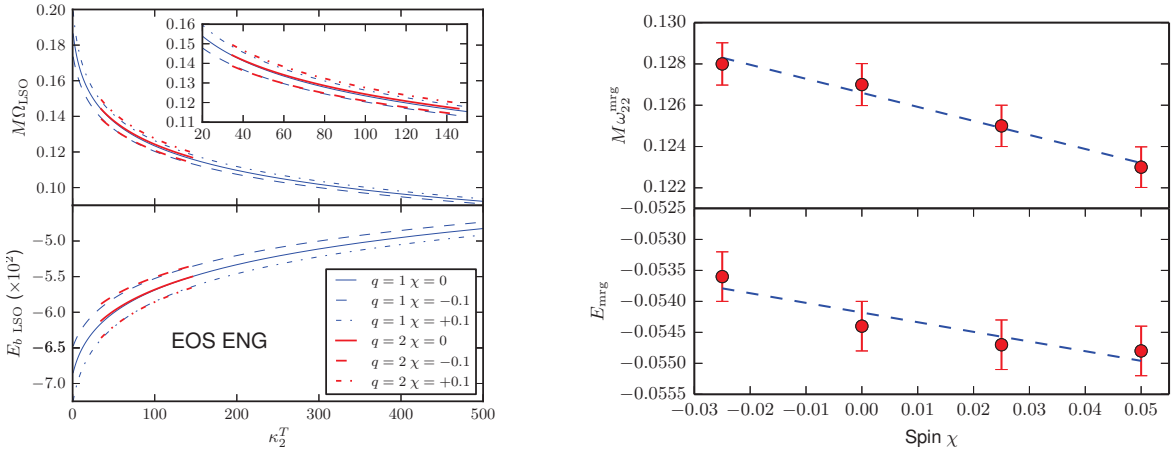

Figure 6.6: Left: GW frequency (top) and binding energy (bottom) versus the coupling constant κ_2^T at the EOB LSO for the ENG EOS. The effect of the mass ratio is almost negligible. The effect of the spin is dominated by spin-orbit coupling. (Plot adapted from [Die1].) Right: Merger frequency $M\omega_{22}^{\rm mrg}$ (top panel) and reduced binding energy at merger $E_{\rm mrg}$ for the configurations of Γ-models of Tab. 4.1 except $\Gamma_{050}^{(\downarrow\downarrow)}$, where the waveform seems to be corrupted around the moment of merger; cf. Sec. 4.4.3.

The left panel of Fig. 6.6 shows that the same quasi-universal behavior is also present for unequal-mass binaries. As an example we show the ENG EOS and vary the mass ratio $q \in [1, 2]$, where the difference in q leads to a difference of $\lesssim 0.5\%$. A similar statement for spinning binaries[2] is not true, in fact, the spin-orbit interaction changes the EOB LSO frequency and binding energy already for astrophysical reasonable spins

[2]We include spin effects following [Damour, 2001], which is robust enough for realistic spin values ($\chi_{A,B} \lesssim 0.1$). The spin-orbit interaction is taken at NNLO [Nagar, 2011], the spin-spin at leading-order [Balmelli and Jetzer, 2013]. The gauge freedom is fixed as in [Damour et al., 2008a; Nagar, 2011]. We only consider spins parallel and antiparallel to the orbital angular momentum to avoid precession effects.

$\chi \sim 0.01 - 0.1$. As suggested for the spin-orbit interaction, the spin dependence is linear for spins $\chi \lesssim 0.1$; cf. Sec. 4.3 and Sec. 4.4.

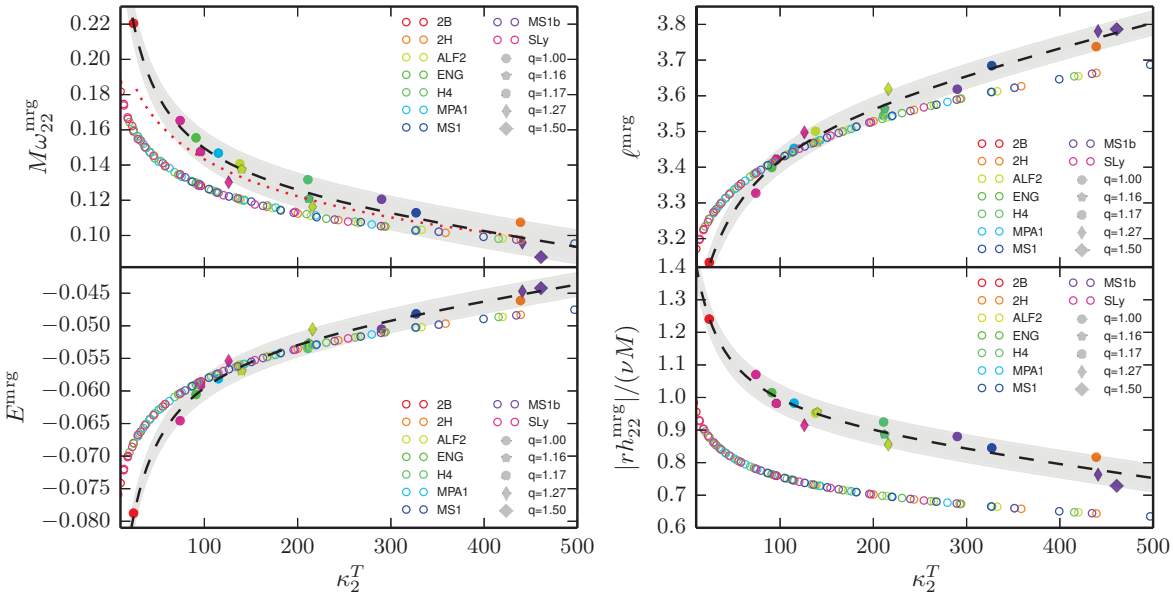

Figure 6.7: Orbital frequency, GW frequency (upper left), binding energy (lower left), reduced orbital angular momentum (upper right), and GW wave amplitude at the moment of merger. Shown are numerical results (filled markers) for different mass ratios q denoted by different markers and the nonadiabatic TEOB$_{\rm Resum}$. Different colors refer to different EOSs. The dashed black lines refer to Eqs. (6.15). The red dotted line refers to the fit of [Read et al., 2013].

While the adiabatic and nonadiabatic tidal EOB analyses capture the relevant qualitative features of the merger dynamics, also full general relativistic NR simulations show the same behavior and can be fitted similarly with a Padé approximant; cf. Fig. 6.7. The figure represents data for nine different EOSs (different colors) and five different mass-ratios (different markers). We constrain the fit to the black-hole limit by factoring out $E^{\rm mrg}(\kappa_l^T = 0) \approx -0.1201$, $M\omega_{22}^{\rm mrg}(\kappa_l^T = 0) \approx 0.3596$ and $\ell^{\rm mrg}(\kappa_l^T = 0) \approx 2.8077$ given by equal-mass BBH simulations [Damour et al., 2012a]. Finally, we achieve:

$$M\omega_{22}^{\rm mrg}(\kappa_2^T) \approx 0.3596 \frac{1 + 2.4384 \cdot 10^{-2}\kappa_2^T - 1.7167 \cdot 10^{-5}(\kappa_2^T)^2}{1 + 6.8865 \cdot 10^{-2}\kappa_2^T}, \quad (6.15a)$$

$$E^{\rm mrg}(\kappa_2^T) \approx -0.1201 \frac{1 + 2.9905 \cdot 10^{-2}\kappa_2^T - 1.3665 \cdot 10^{-5}(\kappa_2^T)^2}{1 + 6.7484 \cdot 10^{-2}\kappa_2^T}, \quad (6.15b)$$

$$\ell^{\rm mrg}(\kappa_2^T) \approx 2.8077 \frac{1 + 4.0302 \cdot 10^{-2}\kappa_2^T + 7.538 \cdot 10^{-6}(\kappa_2^T)^2}{1 + 3.1956 \cdot 10^{-2}\kappa_2^T}, \quad (6.15c)$$

$$|rh_{22}^{\rm mrg}|/(\nu M) \approx 1.6498 \frac{1 + 2.5603 \cdot 10^{-2}\kappa_2^T - 1.024 \cdot 10^{-5}(\kappa_2^T)^2}{1 + 4.7278 \cdot 10^{-2}\kappa_2^T}, \quad (6.15d)$$

shown as black dashed lines with 95% confidence interval plotted as gray shaded areas in Fig. 6.7. It is interesting that from Eq. (6.15a) and Eq. (6.15b) one obtains

an essentially linear relation between the binding energy and the frequency at the moment of merger:

$$E^{\rm mrg} \approx -0.281\, M\omega_{22}^{\rm mrg} - 0.0178. \tag{6.16}$$

We also include the fit of [Read et al., 2013] in Fig. 6.7 as a red dotted line in the upper left panel, which represents a phenomenological relation between the logarithm of $M\omega_{22}^{\rm mrg}$ and $\Lambda^{1/5} = (\frac{2}{3}k_2)^{1/5}C^{-1} = (\frac{16}{3}\kappa_2^T(q=1))^{1/5}$ for equal-mass, irrotational NR waveforms. We suspect that the good performance of the fit is also caused by the κ_2^T-universality.

Finally, we can use the simulations of Sec. 4.4 to show the linear in χ-dependence of the merger frequency and binding energy at merger. Figure 6.6 (right panel) shows our results, where a linear shift is present in $M\omega_{22}^{\rm mrg}$ and $E^{\rm mrg}$ within the numerical uncertainties.

6.2.2 The post-merger spectrum

After the discussion of quasi-universal relations at the moment of merger, we want to investigate the influence of the EOS on the post-merger GW spectrum. Figure 6.8 represents a subset of the possible parameter space. We mark the merger frequency $f_{\rm mrg}$ with triangles and the main peak frequencies f_2 with diamonds (cf. Fig. 5.5). We want to summarize the following details, which were in part already mentioned in the previous chapter:

(i) the low frequency cut-off is artificial due to the fact that the simulations start a few orbits before merger;

(ii) other peaks, mostly related to nonlinear mode coupling or other hydrodynamical interactions, exist [Shibata et al., 2005; Stergioulas et al., 2011; Bauswein and Stergioulas, 2015];

(iii) the broad peaks indicate that the frequencies change in time (cf. Fig. 4.10) and that probably more than one phenomenon, e.g. mode coupling and the motion of spiral arms, is the origin of the peaks [Bauswein and Stergioulas, 2015].

In the following we focus uniquely on the interpretation of the f_2 peak, which is the most robust and best understood feature of the GW spectrum.

Regarding the merger as a reference point, we have shown that the binaries' reduced binding energy E, reduced angular momentum ℓ, and GW frequency/amplitude show quasi-universal behavior at the LSO or the moment of merger. Therefore, it appears natural to investigate the dependency of the postmerger spectrum on κ_2^T.

Figure 6.9 shows the dependency of f_2 on κ_T. To enlarge the sample, we show our data [Die3; Die13] together with those tabulated in [Hotokezaka et al., 2013b; Takami et al., 2015b], given a total of more than 100 simulations. The combined dataset spans the ranges $M \in [2.45M_\odot, 2.9M_\odot]$, $q \in [1.0, 2.06]$, and eleven different EOSs. The

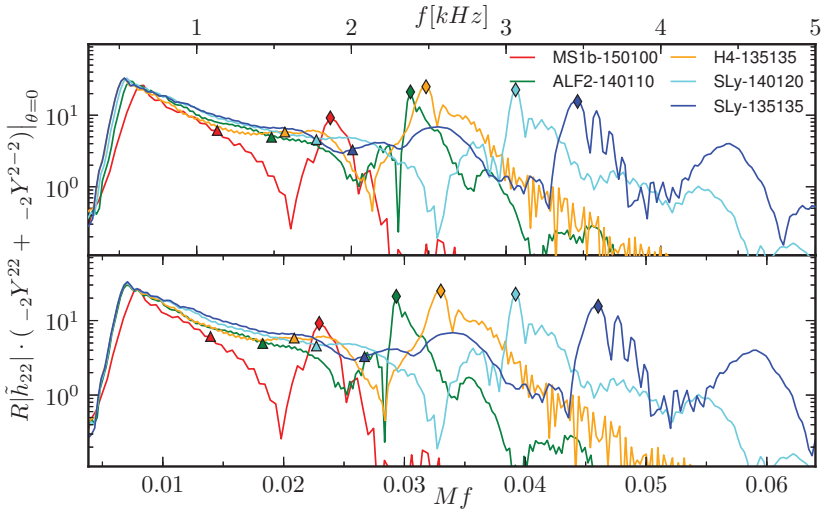

Figure 6.8: GWs spectra from neutron star mergers in kHz (top panel) and dimensionless (bottom panel). The plot shows a small subset of the parameter space, where names refer to EOS-$M^A M^B$, see also [Die3]. Triangles mark frequencies $f_{\rm mrg}$ corresponding to $t_{\rm mrg}$, diamonds mark f_2 frequencies.

same dataset is plotted in all panels. We label the total mass M (top left), the EOS (top right), the mass-ratio q (bottom left), and $\Gamma_{\rm th}$ (bottom right) with different colors. We see a clear correlation with κ_2^T, but due to the scattering of the data no strong correlation with M, EOS, q, and Γ_{th} is present. Each data point is typically determined within an accuracy of $\delta f \gtrsim \pm(0.15\text{–}0.20)$ kHz or dimensionless $\delta f \gtrsim \pm(1.8\text{–}2.8)\times 10^{-3}$, cf. [Bauswein et al., 2012]. We fit all data with a Padé approximant of the form

$$M f_2(\kappa_2^T) \approx 0.053850 \frac{1 + 8.7434 \cdot 10^{-4} \kappa_2^T}{1 + 4.55 \cdot 10^{-3} \kappa_2^T}, \tag{6.17}$$

for $\kappa_2^T \in [45, 500]$, see black line. Additionally, we include the 95% confidence interval as a gray shaded region similar to Fig. 6.7.

Although Eq. (6.17) is just a empirical fit, there is strong evidence for an underlying theoretical explanation supported by two main arguments.

First, from Eqs. (6.15a)-(6.15b) we see that the angular momentum and binding energy of the system at merger depend solely on κ_2^T. Large κ_2^T can be obtained with stiff EOS, small compactnesses, and/or large mass-ratio Eq. (6.12). The remnants of larger κ_2^T (stiffer EOS) binaries have larger angular momentum support at formation and are less bound. The values $(E^{\rm mrg}(\kappa_2^T), \ell^{\rm mrg}(\kappa_2^T))$ provide initial conditions for the dynamics of the MNS/HMNS and, thus, it is plausible to assume that the postmerger correlations also depend on κ_2^T and other physical effects: the total mass, the mass ratio, the EOS, and thermal effects play a subdominat role. In particular, the data indicate that thermal effects lead to a frequency shift of at most $\Delta f_2 \lesssim (0.1\text{–}0.2)$ kHz; cf. [Bauswein et al., 2012; Hotokezaka et al., 2013a; Takami et al., 2015b; Kaplan et al., 2014]. We suggest that magnetic field effects and instabilities [Ciolfi et al.,

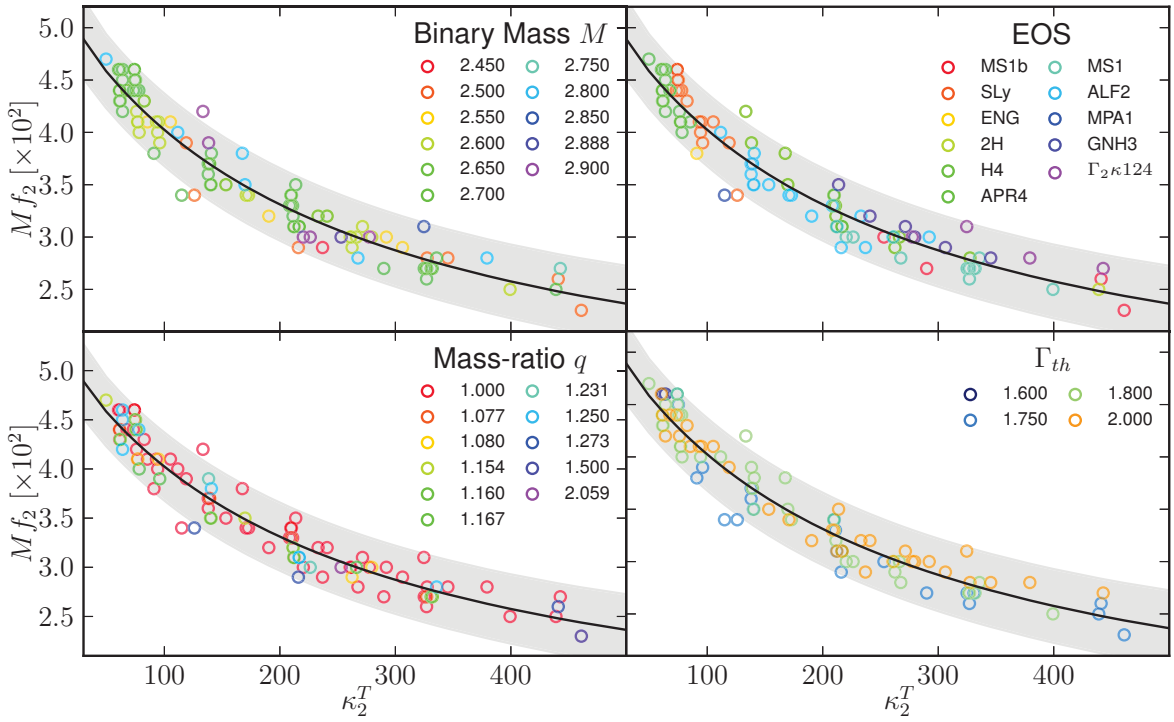

Figure 6.9: f_2 frequency as a function of the tidal coupling constant κ_2^T. Each panel shows the same dataset. The color code in each panel indicates the different values of binary mass (top left), EOS (top right), mass-ratio (bottom left), and $\Gamma_{\rm th}$ (bottom right). The black solid line is the fit (6.17) and the gray area marks the 95% confidence interval.

2011; Zink et al., 2012; Kiuchi et al., 2014a] and cooling or other dissipative mechanisms, e.g. [Giacomazzo et al., 2011a; Kiuchi et al., 2012], act on longer timescales than those simulated here or have not sufficient energy to produce a significant GW frequency shift. However, even higher frequency shifts can be observed for dimensionless spins $\chi \gtrsim 0.05 - 0.1$, see Sec. 4.4.3. Thus, for a detailed analysis of the post-merger quasi-universal relations also binary pulsars have to be considered in the future.

Second, assuming that $E(\ell)$ is generated by a Hamiltonian flow that continuously connects merger and postmerger, one can use the frequency

$$M\Omega = \frac{\partial E}{\partial \ell} \tag{6.18}$$

and sees that Ω is the relevant dynamical frequency for both inspiral-merger and postmerger. Keeping in mind that the standard quadrupole formula predicts that a source with $m = 2$ geometry rotating with a frequency Ω emits GWs at a frequency 2Ω, we have plotted ω_{22} and 2Ω in Fig. 6.4. Therefore, we interpret the gauge-invariant Ω as the orbital frequency during the inspiral, and the angular frequency of the MNS/HMNS during postmerger.

Chapter 7

Conclusion

Summary

The scope of this thesis was to perform numerical simulations of neutron star spacetimes in full general relativity to enlarge our knowledge about the physical processes during these events.
We discussed single and binary neutron stars within the constant rotational velocity approach under the assumption of conformal flatness. Our investigation showed that, as predicted by post-Newtonian theory, the spin-orbit interaction of aligned (antialigned) spins acts repulsive (attractive). Although we were restricted to conformal flatness, we have seen that the spin-orbit interaction obtained from our data agrees within the uncertainties of the numerical data with the post-Newtonian results for sufficiently large separations. We were also able to compute single constant rotational velocity stars with high spins showing SGRID's capability to construct millisecond pulsars.

Using the conformally flat configurations as initial data, we performed the first realistic spinning binary neutron star simulations employing consistent and constraint satisfying data. We computed the spin-orbit, spin-spin, and tidal contribution to the binding energy. Although the analysis was restricted to astrophysical reasonable spin magnitudes $\chi \lesssim 0.1$, we found that the spin-orbit effects dominate over finite size effects up to the contact of the two neutron stars. Imprints of the individual spins were also found during the hypermassive neutron star phase. While the lifetime of the merger remnant was reduced for antialigned spins, we found that for aligned spins the collapse could be delayed by several milliseconds. On top of this, a frequency shift of the main emission modes of the post-merger GW signal towards higher (lower) frequencies for aligned (antialigned) setups was present.

While our first simulations where affected by systematic errors due to the refinement strategy, which we tried to resolve with larger box sizes, we improved the BAM code by introducing an additional refluxing algorithm, which ensures mass conservation for material crossing refinement boundaries. We validated the new

implementation with a number of different single star tests (see also Appendix B) and applied it for the study of the rotating neutron star collapse. Because of the improvements, we were able to add refinement levels inside the collapsing neutron star. This allowed us to resolve the central regions with sufficiently high resolution to (i) compute the emitted GW signal properly, showing the simple "precursor-burst-ringdown" structure; (ii) perform a local analysis of the final black hole, showing that the final spacetime agrees with the spacetime of a spinning trumpet.

Our newly implemented algorithm was also tested in binary neutron star simulations employing different mass ratios and EOSs. We have seen that in the post-merger phase the mass conservation could be improved by a factor of ~ 5 compared to the standard Berger-Oliger approach. The results obtained from our simulations were in agreement with the data published with other numerical relativity codes showing the robustness of BAM. With the performed simulations we could study the influence of the mass ratio and the EOS. We found that larger ejecta are present for higher-mass ratios and that softer EOSs lead to larger ejecta for the same mass-ratio. We also showed that HMNSs formed with softer EOSs collapse earlier than for stiff EOSs (in cases where the same maximum mass was supported). On the basis of a $q = 1.5$-simulation we discussed the two main mechanisms for dynamical ejecta: torque present in the tidal tail and shock heating. We also evolved the highest mass ratio ever considered in a full general relativistic binary neutron star configuration: a $q = 2.06$ setup with the MS1b EOS. Due to the high mass ratio and the rather stiff EOS, we observed mass transfer between the two stars several revolutions before merger releasing accretion energy of $\sim 10^{51}$ ergs. Additionally, due to the anisotropic mass ejection and the GW emission, the merger remnant received a kick larger than the escape velocity of globular clusters.

We used several of our simulations at different resolutions to compute the GW signal and validated a recently improved tidal effective-one-body model, which incorporates an enhanced attractive tidal potential motivated by recent analytical advances in the post-Newtonian and gravitational self-force description of relativistic tidal interactions. The analytical model allows to compute the gravitational waveform accurately up to the moment of merger within the uncertainty of the numerical simulations. The development and verification of the EOB model represents a significant improvement in the description and computation of GW templates.

Motivated by the EOB model and on the basis of the large number of simulations, which were performed during the thesis, we were able to show that quasi-universal relations exist in binary neutron star merger simulations. Strictly speaking: the frequency, the binding energy, the reduced orbital angular momentum, and the amplitude of the GW signal at particular points of the evolution (e.g. LSO or merger) depend strongly on the tidal coupling constants κ_2^T, which characterize tidal con-

tributions. The particular EOS, the mass-ratio, and the total mass do not seem to play a noticeable role. While the EOB model predicts such relations only up to the moment of merger, where the analytical description breaks down, we were able to show quasi-universal behavior also for the peak frequency of the post-merger GW signal. Although the mass-ratio and the EOS do not affect the quasi-universal relations, the spin has a significant influence. As outlined, the spin-orbit interaction shifts the merger quantities ($M\omega_{22}^{\rm mrg}, \ell^{\rm mrg}, E^{\rm mrg}$,$rh_{22}^{\rm mrg}/(\nu M)$) and also influences the f_2-frequency of the HMNS.

Future work

Beyond the improvements in the simulation of binary neutron star systems made in this thesis, we want to propose next consequent steps for the near future:

- While the first dynamical evolutions of CRV data showed that the binary neutron star parameter space can be explored also for binary pulsars, one should continue this investigation by considering spinning neutron stars with more realistic EOSs. A first step towards this goal was made in [Die13], but more work has to be done.
- Still pending is an improved version of the NR-tidal EOB comparison of [Die2] with higher resolutions, more accurate numerical methods [Die15], and eccentricity reduced initial data [Die13]. This allows to place stronger constraints on the resummed tidal EOB model and to calibrate additional parameters (NQC-corrections) to improve the performance of the models.
- Since the first study of binary neutron star simulations showed that even moderate spin has an influence on the merger dynamics and the emitted GW signal, it is useful for future GW modeling to develop a tidal EOB model including spin contributions.
- Based on the large number of simulations already performed, a detailed discussion of the GW spectrum shortly after merger is important to understand the origin of the secondary peak f_s observed in Fig. 5.5, since its origin is under debate and described differently in [Takami et al., 2015b] and [Bauswein and Stergioulas, 2015].

On a longer perspective also more microphysical aspects should be included in the code. Still pending is the implementation of magnetic fields and a neutrino transport scheme in BAM. While as a part of the thesis an approximate scheme modeling energy loss due to neutrinos [Paschalidis et al., 2012] was implemented, an accurate and more realistic algorithm is preferred.

Appendix A

Simulation analysis

In this appendix we describe important aspects of the gravitational wave extraction and the black hole and ejecta computation as done in the BAM code.

A.1 Gravitational wave extraction

Gravitational waves are extracted using the Newman-Penrose formalism [Newman and Penrose, 1962] with the curvature scalar Ψ_4. Individual modes can be obtained by a multipole decomposition on extraction spheres using spherical harmonics with spin weight -2: Y^{-2}_{lm}. The algorithm and implementations used in this thesis are described in detail in [Brügmann et al., 2008]. In all binary neutron star simulations, we reconstruct the metric multipoles rh_{lm} from the curvature multipoles $r\Psi_{4\ lm}$ using the frequency domain integration of [Reisswig and Pollney, 2011] with a cutting frequency of $m\omega^0_{22}/2$. In the case of the rotating neutron star collapse presented in chapter 3, we computed the multipoles rh_{lm} with a time domain integration of $\Psi_4 = \ddot{h}$ subtracting a quadratic polynomial [Damour et al., 2008b; Baiotti et al., 2009].

It is important for all our analysis to plot the waveform against the retarded time,

$$u = t - r_* = t - r_{\rm extr} - 2M \ln\left(r_{\rm extr}/2M - 1\right), \tag{A.1}$$

with the extraction radius $r_{\rm extr}$, especially when features of the GW signal are connected to events of the dynamics.

A.2 Merger and post-merger analysis

Black hole computation

The merger remnant of several BNS configurations considered here is a HMNS, which collapses to a black hole on a dynamical timescale. The lifetime of the remnant τ is the time between the moment of merger to the time an apparent horizon forms. The black hole is then characterized by its horizon mass $M_{\rm BH}$ and spin $J_{\rm BH}$ computed

from the apparent horizon

$$J_{BH} = \frac{1}{8\pi}\oint \varphi^l R^m K_{lm} \mathrm{d}A, \tag{A.2a}$$

$$M_{BH} = \sqrt{\frac{A_{BH}}{16\pi} + \frac{4\pi J_{BH}^2}{A_{BH}}}, \tag{A.2b}$$

with A_{BH} being the surface area of the horizon, $\mathrm{d}A$ the area element of the surface, φ^α a vector field tangential to the surface satisfying $\mathcal{L}_\varphi q_{ij} = 0$, where q_{ij} is the induced metric on the horizon; cf. [Thornburg, 2006; Lages, 2010] for more details.

The average radius of the black hole is r_{AH}. This allows to estimate the rest-mass of the accretion disk formed after collapse as,

$$M_{\text{disk}} = \int_{r>r_{\mathrm{AH}}} \mathrm{d}^3x \; q^{(D)} \; , \tag{A.3}$$

where the almost spherical region inside the apparent horizon is excluded.

Ejecta computation

We characterize material as ejected, when it fulfills the two conditions:

$$u_t < -1, \tag{A.4a}$$

$$\bar{v}_r = v^i x_i > 0 \; , \tag{A.4b}$$

with $u_t = -W(\alpha - \beta_i v^i)$ being the first lower component of the fluid 4-velocity, and $x^i = (x, y, z)$ in Cartesian coordinates. The first condition in (A.4) assumes that fluid elements follow geodesics and that the orbit is unbound, which is in agreement with previous work, e.g. [East and Pretorius, 2012; Hotokezaka et al., 2013b], and captures the correct order of magnitude. The condition $\bar{v}_r > 0$ requires that the material has an outward pointing radial velocity. This condition was also used in [East and Pretorius, 2012], but not in e.g. [Hotokezaka et al., 2013b]. The total ejecta mass is computed as,

$$M_{\text{ejecta}} = \int_{\mathcal{U}} \mathrm{d}^3x \; q^{(D)} \; , \tag{A.5}$$

with $\mathcal{U} = \{x^i = (x, y, z) \; : \; u_t < -1 \;\text{ and }\; \bar{v}_r > 0\}$.

The kinetic energy of the ejecta can be approximated as the difference between the total energy E_{ejecta}, the rest mass M_{ejecta} and the total internal energy U_{ejecta} [Hotokezaka et al., 2013b],

$$\begin{aligned} T_{\text{ejecta}} &= E_{\text{ejecta}} - (M_{\text{ejecta}} + U_{\text{ejecta}}) \\ &= \int_{\mathcal{U}} \mathrm{d}^3x \; D(e - 1 - \epsilon) \; , \end{aligned} \tag{A.6}$$

where $e = \alpha u^t h - p/(\rho \alpha u^t)$.

Additionally, we compute integrals monitoring the geometry of the ejecta in the x-y and x-z-plane:

$$\langle \rho \rangle = \left(\frac{\int_{\mathcal{U}} \mathrm{d}x\mathrm{d}y \; D \; (x^2 + y^2)}{\int_{\mathcal{U}} \mathrm{d}x\mathrm{d}y \; D} \right)^{1/2} , \tag{A.7a}$$

$$\langle z \rangle = \left(\frac{\int_{\mathcal{U}} \mathrm{d}x\mathrm{d}z \; D \; z^2}{\int_{\mathcal{U}} \mathrm{d}x\mathrm{d}z \; D} \right)^{1/2} , \tag{A.7b}$$

similar integrals in three dimensions have been proposed already in [Hotokezaka et al., 2013b]. The energy/speed of the ejecta can be estimated by

$$\langle v \rangle_\rho = \left(\frac{\int_{\mathcal{U}} \mathrm{d}x\mathrm{d}y \; D v^2}{\int_{\mathcal{U}} \mathrm{d}x\mathrm{d}y \; D} \right)^{1/2} , \tag{A.8}$$

$$\langle v \rangle_z = \left(\frac{\int_{\mathcal{U}} \mathrm{d}x\mathrm{d}z \; D v^2}{\int_{\mathcal{U}} \mathrm{d}x\mathrm{d}z \; D} \right)^{1/2} . \tag{A.9}$$

Furthermore, we compute an entropy "indicator",

$$\hat{S} = \frac{p}{\kappa \rho^\Gamma}, \tag{A.10}$$

first introduced in [Die8], where Γ and κ are defined locally by the density ρ and the chosen EOS, Eq. (2.55). In cases where the additional thermal contribution to the pressure P_{th} is small $\hat{S} \sim 1$, while in presence of shock heating $\hat{S} \gg 1$.

Appendix B

Testbeds for the conservative mesh refinement

As discussed in Sec. 2.2.4 the implementation of a flux-correction step can in principle lead to mass conservation up to round off errors. However, in addition to the truncation errors occurring at refinement boundaries, also the atmosphere treatment and finite resolution in the outer regions of the numerical domain can cause mass violations. In the following, we investigate single star spacetimes to test the improvements and limits of the newly implemented algorithms in the BAM code. We give the specific grid configurations and atmosphere settings in Tab. B.1. All tests were performed for different combinations of the restriction (R), prolongation (P), and correction (C) step, see Tab. B.2. We tested both: the BSSN and the Z4c evolution system, but have not seen major differences regarding the mass conservation. However, the Z4c evolution scheme leads in general to smaller Hamiltonian and momentum constraints violations.

TOV$_{static}$

As the simplest possible test, we consider a spherical star with a gravitational mass of $1.40M_{\odot}$. The initial configuration is modeled with the $\Gamma 2\kappa 100$ EOS assuming zero temperature, while the evolution is performed with an ideal gas EOS allowing temperature effects. The finest refinement level $l = 4$ is fully contained in the star covering half of the diameter and level $l = 3$ ends at the star surface (top panel of Fig. B.1a).

Although the solution is trivial and static at the continuum, we observe some dynamics in numerical simulations due to truncation errors mostly triggered by (i) the artificial atmosphere treatment close to the star surface; (ii) truncation errors on the refinement levels $l = 2, 3$; (iii) a gauge change from maximal to $1 + \log$ slicing; (iv) boundary effects caused by the finite size of the computational domain.

The middle and bottom panel of Fig. B.1a show the relative error in the rest mass

Table B.1: Grid and parameter configurations for single star spacetimes. L denotes the total number of boxes, l^{mv} is the finest non-moving level, n (n^{mv}) is the number of points in the fixed (moving) boxes, h_0, h_{L-1} are the grid spacing in level $l = 0, L-1$. f_{atm} defines the atmosphere level, and f_{thr} the atmosphere threshold factor. The resolution in level l is $h_l = h_0/2^l$.

Single star test	L	l^{mv}	n	n^{mv}	h_0	h_{L-1}	f_{atm}	f_{thr}
TOV_{static}	5	–	56	56	2.0	0.125	10^{-9}	10^{2}
TOV_{static}	5	–	56	56	2.0	0.125	10^{-11}	10^{2}
TOV_{boost}	5	–	128	128	2.0	0.125	10^{-9}	10^{2}
TOV_{boost}	5	–	128	128	2.0	0.125	10^{-11}	10^{2}
TOV_{mig}	7	–	128	128	9.6	0.150	10^{-10}	10^{2}
TOV_{mig}	7	–	128	128	9.6	0.150	10^{-11}	10^{2}
TOV_{mig}	7	–	128	128	9.6	0.150	10^{-12}	10^{2}
TOV_{mig}	7	–	128	128	9.6	0.150	10^{-13}	10^{2}
TOV_{mig}	7	–	128	128	9.6	0.150	10^{-10}	10^{1}
TOV_{mig}	7	–	128	128	9.6	0.150	10^{-11}	10^{1}
TOV_{mig}	7	–	128	128	9.6	0.150	10^{-11}	10^{3}
TOV_{mig}	7	–	128	128	9.6	0.150	10^{-11}	10^{4}
RNS_{BU7}	6	1	128	64	2.0	0.0625	10^{-9}	10^{2}
RNS_{Kep}	7	2	144	96	4.0	0.0625	10^{-9}	10^{2}

Table B.2: Restriction (R), prolongation (P), and mass correction (C) used for the single star tests. Averages (AVG), Lagrangian interpolation (LAG) and WENO, WENOZ interpolation of [Jiang, 1996; Borges et al., 2008]. The expected convergence order for smooth problems is reported in columns named "Order".

Name	R	Order	P	Order	C
a2e2	AVG	2	ENO	2	✓
a2e2n	AVG	2	ENO	2	✗
a2wz6	AVG	2	WENOZ	6	✓
a2wz6n	AVG	2	WENOZ	6	✗
l4l4	LAG	4	LAG	4	✓
l4l4n	LAG	4	LAG	4	✗
w4w4	WENO	4	WENO	4	✓
w4w4n	WENO	4	WENO	4	✗

and its time derivative. Clearly visible is an improvement in the mass conservation due to the C step for all RP choices. The improvement is ~ 2 orders of magnitude. Even using a correction step, the 4th order WENO and Lagrangian RP introduce spurious oscillations in the rest-mass derivative (green and orange solid lines). In general, using the average R leads to the smallest errors.

The influence of the atmosphere treatment is investigated by lowering f_{atm} from 10^{-9} to 10^{-11} (black dashed line). A lower atmosphere significantly improves the mass conservation. In this test the error in the rest-mass derivative related to the C step is about $|dM_b/dt| \sim 10^{-5}$, while the one related to the atmosphere treatment is about $|dM_b/dt| \sim 10^{-f_{thr}\, f_{atm}}$. Optimal results can only be obtained with a proper

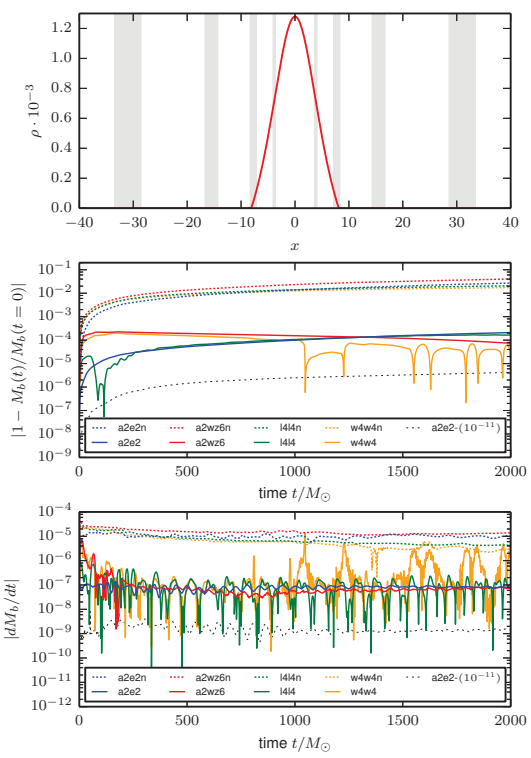

(a) Top: Initial density profile of the TOV$_{static}$ test along the x-axis, gray regions indicate buffer zones. Middle: The relative rest-mass change $|1 - \frac{M_b(t)}{M_b(t=0)}|$ for different RPC combinations. Bottom: The time derivative of the rest mass.

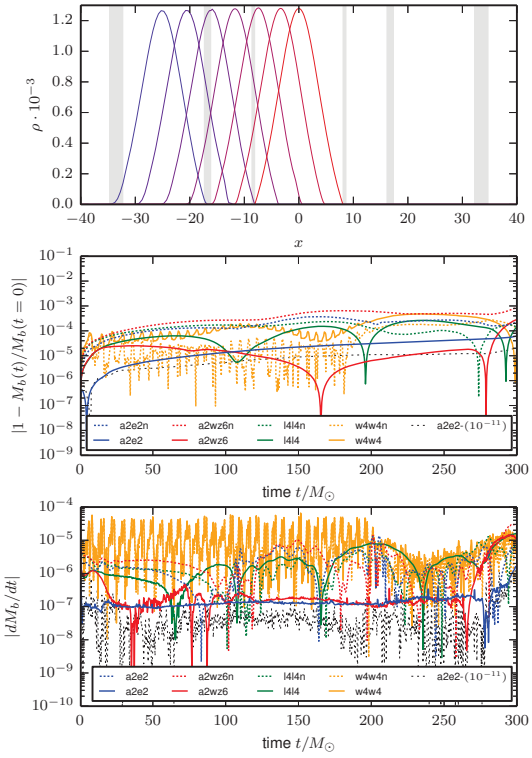

(b) Top: Evolution of the density profile along the x-axis; the profiles correspond to times $t/M_\odot = 0, 50, 100, 150, 200, 250, 300M$. The star is boosted in the negative x direction. The buffer zones of the refinement levels are shaded in gray. Middle: The relative rest-mass change for different RPC combinations. Bottom: The time derivative of the rest mass.

Figure B.1: Results of the TOV$_{static}$ test (left) and the TOV$_{boost}$ test (right). Plots adapted from [Die8].

combination of RPC and $(f_{thr},\ f_{atm})$.

TOV$_{boost}$

The same star model as in the TOV$_{static}$ test is used, but now boosted in the negative x-direction. We have further tested our implementation by boosting the star in $+x, \pm y, \pm z$-direction with and without bitant symmetry to find possible implementation errors in the correction algorithm, but no noticeable difference occurred.

At $t = 0$ the star is entirely covered by the finest refinement level $l = 4$. During the evolution, the star crosses completely the two finest refinement levels, as shown in Fig. B.1b (top panel). Again the C step improves mass conservation for almost all RP choices (middle and bottom panels). But the effectiveness depends also on the RP choice. In particular, the C step is not effective with WENO RP. The a2e2 and a2wz6

schemes perform best, indicating the importance of a conservative R. Similarly to the previous test, we test the role of the atmosphere parameters on the optimal a2e2 setup. Lowering the atmosphere by a factor 100 improves mass conservation by a factor 10 (see dotted black line).

TOV$_{mig}$

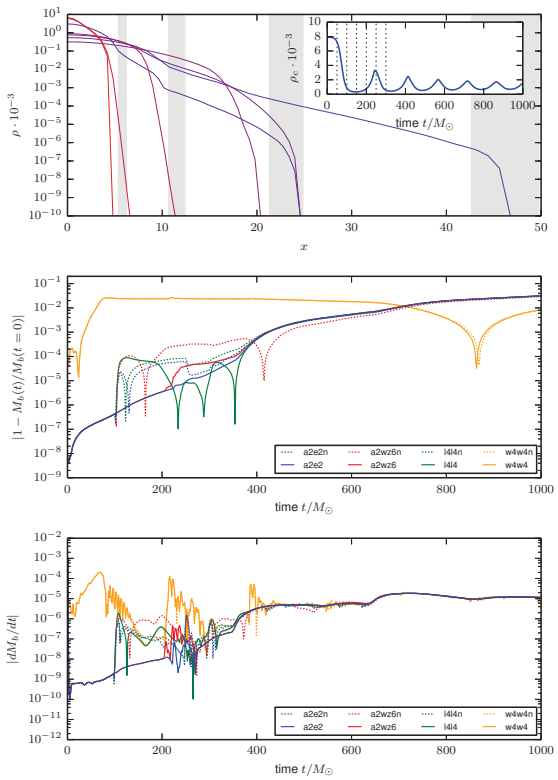

(a) Results of the TOV$_{mig}$ test. Top: Evolution of the density profile along the x-axis; the profiles correspond to times $t/M_\odot = 0, 50, 100, 150, 200, 250, 300$. The buffer zones of the refinement levels are shaded in gray. The inset shows the time evolution of the central density, vertical dashed lines refer to the times shown in the top panel. Middle: The relative rest-mass change for different RPC combinations. Bottom: The time derivative of the rest mass.

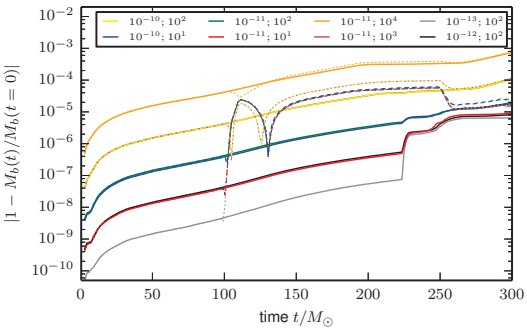

(b) TOV$_{mig}$ test for different atmosphere parameters. First number represents f_{atm}, second number f_{thr}; a2e2 RPC (solid); a2e2n RPC (dotted).

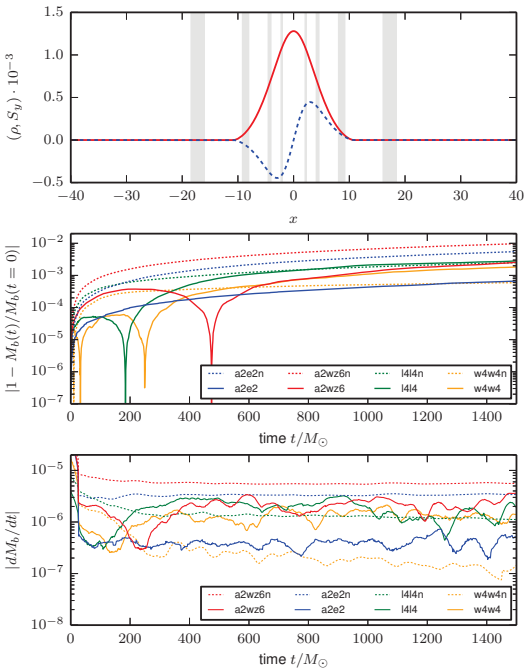

(c) RNS$_{\mathrm{BU7}}$ test. Top: Density profile (red) and momentum density (blue) along the x-axis. Middle: Relative rest-mass change for different RPC combinations. Bottom: The time derivative of the rest mass.

Figure B.2: Results for the TOV$_{mig}$ test (a), investigation of the atmosphere influence for the TOV$_{mig}$ test (b), and results for the RNS$_{\mathrm{BU7}}$ test (c). Plots adapted from [Die8].

As a third test we investigate an unstable single neutron star configuration. The initial central density is $\rho_c = 7.9934 \times 10^{-3}$ and the gravitational mass $1.4476 M_\odot$

(e.g. [Baiotti et al., 2005; Cordero-Carrion et al., 2009; Thierfelder et al., 2011a]). The configuration is in an unstable equilibrium and truncation errors trigger a migration to a stable configuration. This involves violent nonlinear oscillations. During these expansions and contractions, matter crosses the grid refinement levels.

We observe (Fig. B.2a) that the conservative AMR is effective up to times $t \lesssim 400M_\odot$ corresponding to approximately two bounces of the star core (see inset in the upper panel); up to the first bounce the rest-mass conservation improves by ~ 2 orders of magnitude if a C step is applied. At times $t \gtrsim 400M_\odot$ matter densities $\rho \sim 10^{-5}$ reach outer regions, where the resolution is dropped by a factor of ~ 16 and interactions with the atmosphere become significant.

Our experiments with various atmosphere parameters are shown in Fig. B.2b. A reduction of ρ_{thr} by an order of magnitude improves the mass-conservation by approximately one order for the beginning of the simulation. For different ρ_{atm} but the same ρ_{thr} the error stays the same. We can minimize the relative rest-mass violation up to 10^{-9} with $f_{atm} = 10^{-13}$ and $f_{thr} = 10^2$. If no C step is applied and the atmosphere is small enough ($\rho_{atm} \lesssim 10^{-10}$), a dramatic mass violation happens as soon as matter crosses the first refinement boundary at $t \sim 100M_\odot$ (dotted lines). The C step solves this issue. However, as time advances, rest-mass conservation is progressively corrupted in all the cases due to the drop in resolutions in the outer region reached by the low-density star's outer layers bouncing back and forth.

RNS$_{\mathrm{BU7}}$

In the following we discuss a stable uniformly rotating neutron star described by the polytropic EOS $\Gamma 2\kappa 100$, and with $\rho_c = 1.28 \times 10^{-3}$, axes ratio 0.65, and gravitational mass $1.6655M_\odot$, cf. [Dimmelmeier et al., 2006]. The initial data are computed with the RNS code [Stergioulas and Friedman, 1995; Nozawa et al., 1998]. The star is evolved with the Γ-law EOS for about six rotation periods. Fig. B.2c summarizes our results, namely that the C step improves the accuracy in many cases and that the best RP setup is again a2e2. The l4l4 and l4l4n RP perform equally good at late times. Surprisingly, the nonconservative w4w4n RP is here observed to give good results, and at the end of the simulation, it is comparable to a2e2, but shows spurious oscillations in $(1 - M_b(t))/M_b(t = 0)$.

RNS$_{\mathrm{Kep}}$

Finally, we want to study a new test, first introduced in [Die8]. Here, a rotating neutron star at the Kepler limit is modeled with the $\Gamma 2\kappa 100$ EOS, and with $\rho_c = 1.444 \times 10^{-3}$, axes ratio 0.58, and gravitational mass $1.7498M_\odot$. The star is evolved with the Γ-law EOS with $\Gamma = 1.9$ instead of $\Gamma = 2$. The lower polytropic exponent triggers an expansion and disruption of the star. Finally, matter crosses several refinement levels and is spread over the entire grid.

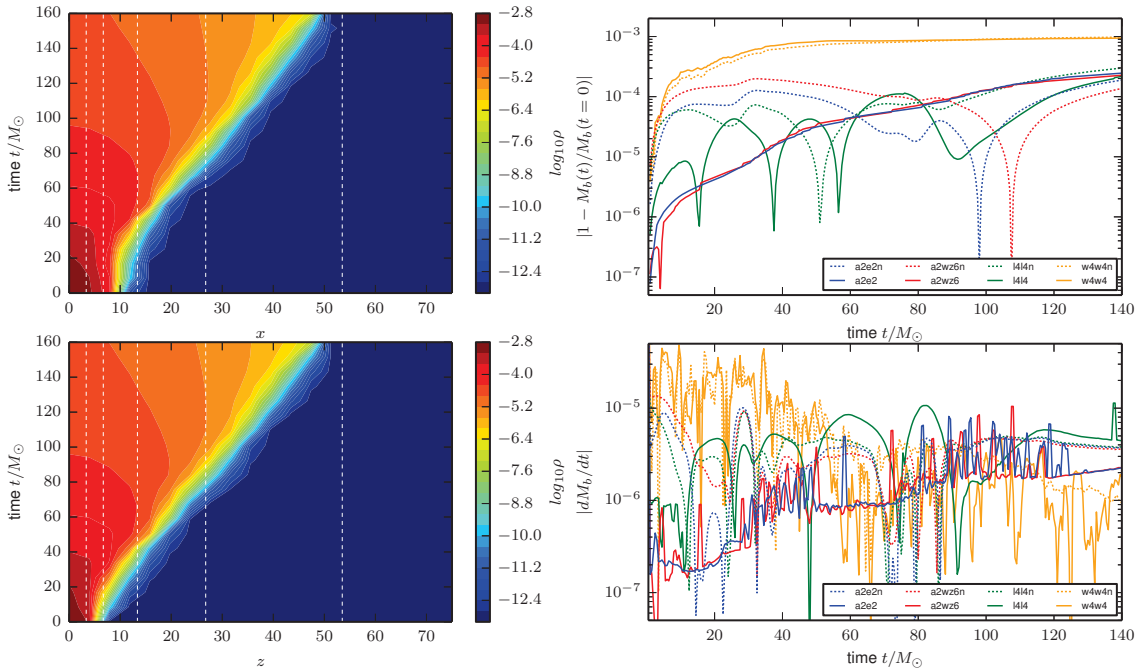

Figure B.3: Results of the RNS_{Kep} test. Left: Density evolution along directions x (top) and z (bottom). Right: The relative rest-mass change (top) and rest-mass time-derivative (bottom) for different RPC combinations. Plot adapted from [Die8].

The left panels of Fig. B.3 show how the matter expands along the x-axis and the z-axis over time, i.e. perpendicular and along the symmetry axis. The right panels of the figure show the mass conservation. The best RPC combinations are again a2wz6 and a2e2.

Summary of single star tests

The best mass conservation could be achieved with the a2e2-scheme for the single star tests. The a2e2 simulations show in most cases the smallest dM_b/dt and no artificial oscillations in $1 - M_b(t)/M_b(t=0)$. The artificial oscillations are present in at least one test for all other RPC-setups. Furthermore, we have found for the TOV_{static}, TOV_{boost}, and TOV_{mig} tests that also the artificial atmosphere treatment leads to mass violations (a similar behavior is expected for the other tests as well). The stability of the simulation improves with higher atmosphere values, but lower atmosphere thresholds improve mass conservation. Therefore, it is necessary to find a compromise between these two effects. In addition large violations of rest-mass conservations are observed in the lowest resolved regions; where the violations become independent on the C step and the atmosphere values and are mostly triggered by low resolution.

Appendix C

Numerical flux computation tests in single and binary neutron star systems

While the main part of the thesis has focused on the physical properties of BNS merger simulations, except the discussion about the conservative mesh refinement, we want to present here the influence of the numerical flux computation.

In the first part we will discuss an algorithm which allows higher than second order convergence for smooth problems, and describe different reconstruction schemes. We continue with single star tests and a detailed convergence analysis of BNS configurations. The discussion is based on the results of [Die15] and will be published in the near future.

Most numerical relativity codes employ a second order numerical flux in which truncation errors of the GRHD scheme are the main source of uncertainty in high-quality waveform production runs [Bernuzzi et al., 2012a; Hotokezaka et al., 2013c]. While in vacuum simulations high-order finite differencing stencils can effectively reduce the phase errors, e.g. [Husa et al., 2008], the situation is more complicated in BNS merger simulations due to shocks and discontinuities. The first BNS simulations with a higher than second order LLF flux were presented by [Radice et al., 2014a; Radice et al., 2014b; Radice et al., 2015], where an algorithm similar to our implementation was employed. In their simulation the simple polytropic $\Gamma 2 \kappa 124$ EOS is used and a convergence order of 3.2 is obtained for the phase and amplitude of the curvature waveform.

C.1 Flux computation and reconstruction algorithms

C.1.1 Higher-order LLF scheme

While throughout the thesis we used the flux computation according to the second order central LLF flux, which was tested in detail in [Thierfelder, 2011; Thierfelder et al., 2011a; Bernuzzi et al., 2012a], knowledge about the characteristic variables allows a construction not restricted to second order convergence. One possible flux-splitting approach based on the LLF flux and reconstruction of the characteristic fields [Jiang, 1996; Suresh, 1997; Mignone et al., 2010] is summarized below[1]:

(i) Primitive recovery **w** from the conservative variables **q** (Sec. 2.2.3);

(ii) Projection of the positive and negative part of the flux onto the left eigenvector matrix of the Jacobian $\frac{\partial \hat{\mathbf{F}}}{\partial \mathbf{q}}$

$$\hat{\mathbf{F}}^{\pm}_{i+1/2,\mathcal{S}} = \frac{1}{2}\mathbf{L}_{i+1/2} \cdot \left(\mathbf{F}_{\mathcal{S}} \pm a^{(k)}\mathbf{q}_s\right), \tag{C.1}$$

with $\mathbf{L}_{i+1/2}$ being the left eigenvector matrix, and $\pm$ indicating the positive and negative flux, $\mathcal{S}$ is the stencil size of the reconstruction (Rec[.]) and $a^{(k)} = \max_{\mathcal{S}}(|\lambda^{(k)}|)$ denoting the maximum of the local characteristic speeds of the k-th characteristic field variable.

(iii) Reconstruction of the flux with a high resolution shock capturing scheme

$$\mathrm{Rec}[\hat{\mathbf{F}}^{\pm}_{(i+1/2),\mathcal{S}}] \mapsto \hat{\mathbf{F}}^{\pm}_{i+1/2}. \tag{C.2}$$

(iv) Finally the numerical flux is obtained by

$$\hat{\mathbf{F}}_{i+1/2} = \left(\hat{\mathbf{F}}^{+}_{i+1/2} + \hat{\mathbf{F}}^{-}_{i-1/2}\right) \cdot \mathbf{R}_{i+1/2}. \tag{C.3}$$

In our implementation the right (left) eigenvector matrices **R** (**L**) are computed from arithmetic averages at the interface. Their explicit expressions can be found in [Font, 2007]. Most notable is that due to divisions by the density ρ the transformation to the characteristic system for low-density regions is problematic or even impossible. To solve this problem two approaches can be made:

- A hybrid method, which uses the second-order LLF scheme for $\rho < \rho_{hyb} = f_{hyb} \cdot \rho_{thr}$ and the higher order scheme above ρ_{hyb}, can be employed.
- The artificial atmosphere (Sec. 2.2.3) can be used with a higher cutoff (larger f_{atm} or f_{thr}).

[1] For simplicity we restrict ourselves again to one dimension.

C.1.2 Reconstruction algorithm

Improved fifth-order weighted essentially non-oscillatory - scheme : WENOZ

The principle idea of a WENO algorithm is to add k Lagrangian interpolation polynomials Lag of small stencil sizes to a larger stencil, where each individual polynomial obtains a particular weight ω_l according to its smoothness. With this approach high order convergence for smooth problems can be obtained, but also shock capturing properties are present in case of discontinuous problems. The general WENO-reconstruction formula is

$$\mathrm{Rec}[f_{\mathcal{S}}] = \sum_{l=0}^{k-1} \omega_l \, \mathrm{Lag}_l(f). \tag{C.4}$$

The particular WENOZ-implementation in BAM follows [Borges et al., 2008] and uses a stencil of size five divided in three substencils ($k = 3$) each of size three. The smoothness of the individual substencils, i.e. of Lag_l, is determined by the smoothness indicator

$$\beta_l = \sum_{j=1}^{2} \int_{x_{i-1/2}}^{x_{i+1/2}} (\Delta x)^{2j-1} \left(\frac{\mathrm{d}^j}{\mathrm{d}x^j} \mathrm{Lag}_l(x) \right)^2 \mathrm{d}x. \tag{C.5}$$

The WENO-weights are computed according to

$$\omega_l = \frac{\alpha_l}{\sum_{j=0}^{2} \alpha_j}, \tag{C.6a}$$

$$\alpha_l = d_l \left(1 + \frac{|\beta_2 - \beta_0|}{(\beta_l + \epsilon)^2} \right), \tag{C.6b}$$

with $d_0 = 3/10, d_1 = 3/5, d_2 = 1/10$ being the ideal weights generating the central upstream fifth-order scheme and ϵ is set to 10^{-40}.

Fifth-order monotonicity preserving scheme: MP5

The MP5 scheme of [Suresh, 1997] achieves higher-order convergence by providing an accurate polynomial interpolation and limiting the result to ensure monotonicity near discontinuities. The particular implementation in BAM follows [Mignone et al., 2010]. The algorithm is based on the 5-th order accurate representation

$$f_{i+1/2} = \frac{2f_{i-2} - 13f_{i-1} + 47f_i + 27f_{i+1} - 3f_{i+2}}{60} \tag{C.7}$$

and defines the monotonicity-preserving bound as

$$f^{MP} = f_i + \mathrm{Minmod}\left[f_{i+1} - f_i, \alpha(f_i - f_{i-1}) \right], \tag{C.8}$$

with $\text{Minmod}[a,b] = 0.5\ (\text{sgn}(a) + \text{sgn}(b))\ \min[|a|,|b|]$. The free parameter α defines the maximum steepness and gives a restriction to the CFL number $c \leq 1/(1+\alpha)$. We tested the algorithm for $\alpha = 2$ and $\alpha = 4$. The final reconstructed result is

$$\text{Rec}[f_{\mathcal{S}}] = \begin{cases} f_{i+1/2} & \text{, if}(f_{i+1/2} - f_i)(f_{i+1/2} - f^{MP}) < 0, \\ \text{Median}(f^{min}, f_{i+1/2}, f^{max}) & \text{, else,} \end{cases} \tag{C.9}$$

with

$$f^{min} = \max\left(\min\left(f_i, f_{i+1}, f^{MD}\right), \min\left(f_i, f^{UL}, f^{LC}\right)\right), \tag{C.10a}$$
$$f^{max} = \min\left(\max\left(f_i, f_{i+1}, f^{MD}\right), \min\left(f_i, f^{UL}, f^{LC}\right)\right). \tag{C.10b}$$

Where we have used the following abbreviations:

$$f^{UL}_{i+1/2} = f_i + \alpha(f_i - f_{i-1}), \tag{C.11a}$$
$$f^{MD}_{i+1/2} = \frac{f_{i+1} + f_i}{2} - \frac{1}{2} d^{M4}_{i+1/2}, \tag{C.11b}$$
$$f^{LC}_{i+1/2} = f_i + \frac{1}{2}(f_i - f_{i-1}) + \frac{4}{3} d^{M4}_{i-1/2}, \tag{C.11c}$$
$$d^{M4}_{i+1/2} = \text{Minmod}\left(-f_{i+2} + 6f_{i+1} - 9f_i + 4f_{i-1}, 4f_{i+2} - 9f_{i+1} + 6f_i - f_{i-1}, f_{i+1} - 2f_i + f_{i-1}, f_{i+2} - 2f_{i+1} + f_i\right), \tag{C.11d}$$
$$\text{Median}(a,b,c) = a + \text{Minmod}(b-a, c-a). \tag{C.11e}$$

The MP5-reconstruction method is heuristic, it preserves monotonicity and does not degenerate to first-order at smooth extrema.

C.2 Single star tests

In the following, we compare the standard second order central LLF flux with primitive reconstruction as discussed (Sec. 2.2.3) and the LLF flux based on the reconstruction of the characteristic variables (outlined above)[2].

Barotropic evolutions

Starting with barotropic evolutions, we employ a single polytropic EOS ($\Gamma 2 \kappa 100$), i.e. a zero temperature EOS without any thermal component. The employed initial data are similar to the TOV_{static} test of Appendix B. In general barotropic evolutions are simpler, because only four of the five evolution equations in Eq. (2.53) have to be evolved. The τ-equation is redundant and can be discarded. This reduces computational costs and minimizes the influence of the artificial atmosphere on the neutron star.

[2] For both algorithms, the expected convergence order can be shown in special-relativistic tests [Die15].

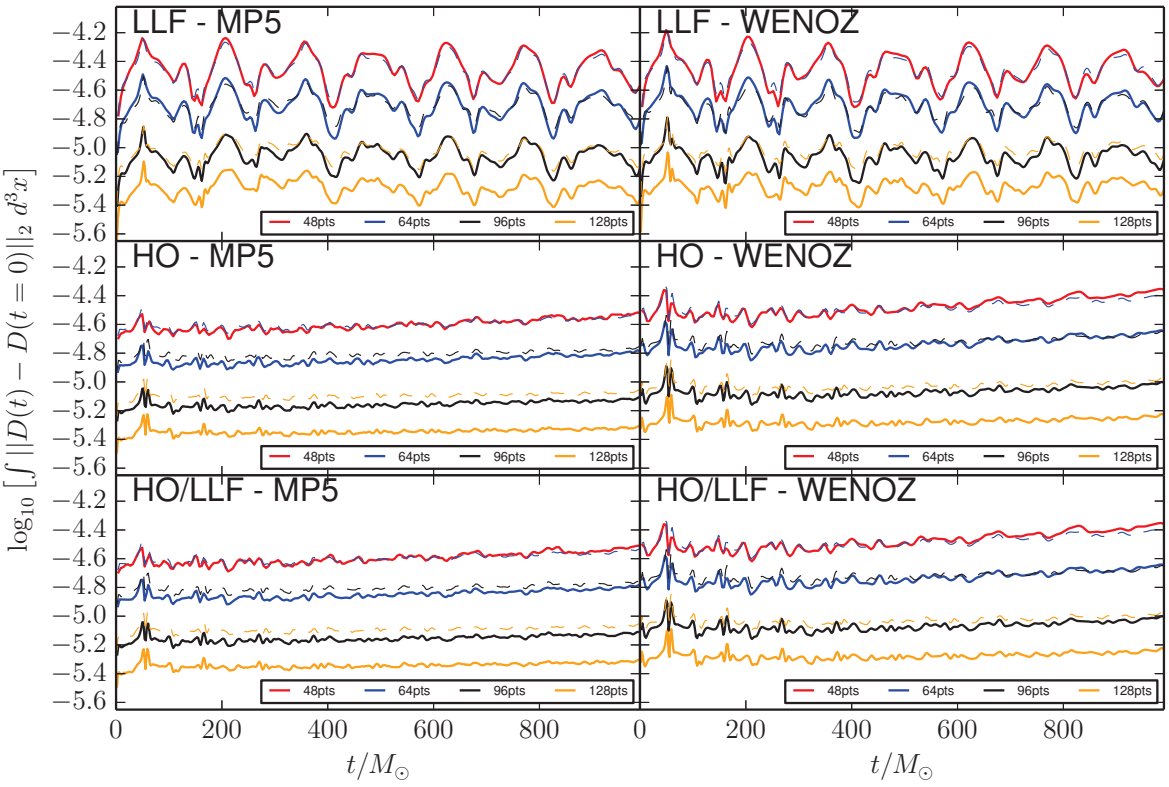

Figure C.1: L_2-error of the rest-mass density: $\log_{10}\left(\int ||D(t) - D(t=0)||_2 \mathrm{d}^3x\right)$ for a single TOV-star with barotropic evolution. In all tests a convergence order around ~ 2 is obtained.

The BSSN evolution scheme (Sec. 2.1.3) is used for the spacetime evolution. For all simulations a total of 3 refinement levels are used and we study in total four different grid resolutions covering the diameter of the star with $48, 64, 96, 128$ points (represented by red, blue, black, orange lines, respectively), where octant symmetry is used for all simulations. We set the atmosphere parameters to $f_{thr} = 100$ and f_{atm} to 10^{-11} for the second order LLF and the hybrid scheme and to 10^{-9} for the pure higher order scheme. For the hybrid scheme we use $f_{hyb} = 5$. Figure C.1 shows the L_2-error of the rest mass for a single neutron star with a barotropic EOS. The L_2-error is computed as $\log_{10}\left(\int ||D(t) - D(t=0)||_2 \mathrm{d}^3x\right)$. We employ the 2nd order LLF scheme (LLF), the characteristic reconstruction (HO), and a mixture of both methods (HO/LLF) for the WENOZ and the MP5 reconstruction. For all schemes a convergence order of ~ 2 (dashed lines) is obtained. We find that for the 2nd order LLF-scheme large oscillations are present. For HO and HO/LLF the L_2-norm is less oscillatory. In most cases the MP5 reconstruction scheme performs slightly better than the WENOZ scheme. Furthermore, we do not see differences between the HO and HO/LLF reconstruction, which is related to the small value of f_{hyb}.

Ideal gas evolutions

As a second test, we consider an evolution including temperature effects by employing an ideal gas EOS. Due to the additional thermal pressure, the surface of

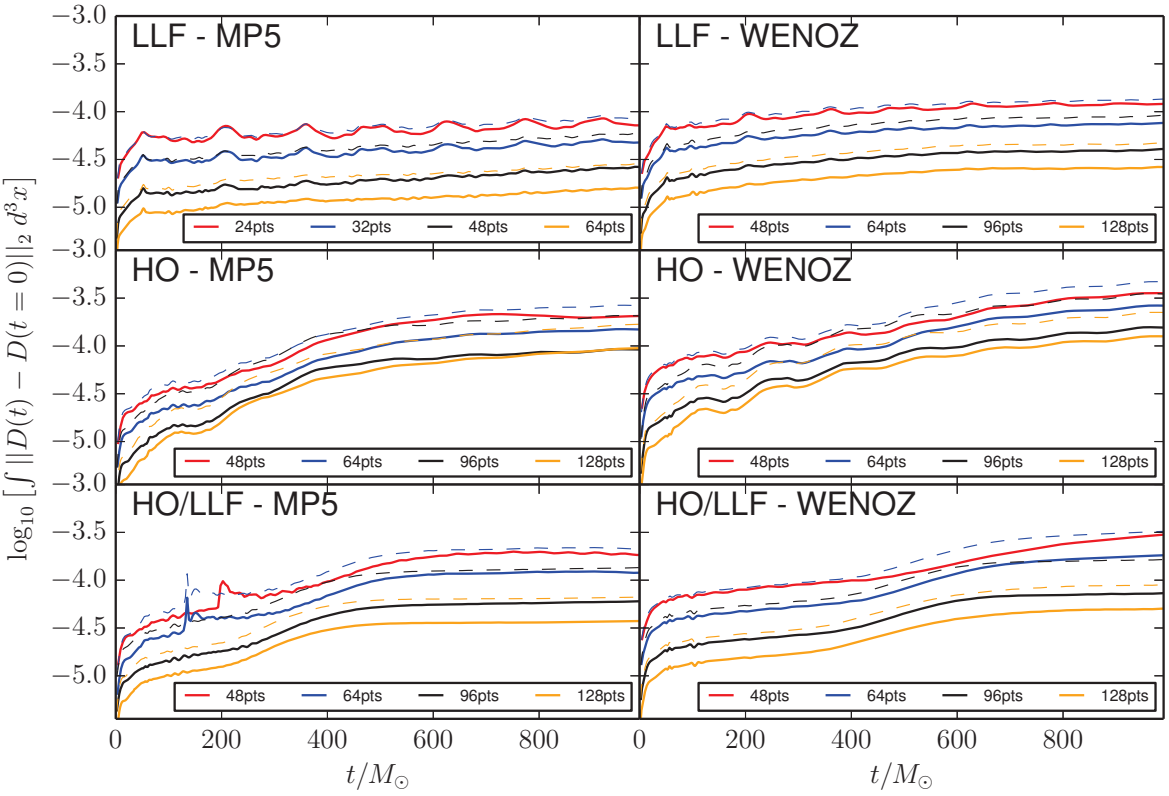

Figure C.2: L_2-error of the rest-mass density: $\log_{10}\left(\int ||D(t) - D(t=0)||_2 \mathrm{d}^3x\right)$ for a single TOV-star with ideal gas EOS.

the star does not stay as sharp as in the barotropic evolution. This is problematic in case of the higher order characteristic reconstruction. In fact, we have to use $f_{atm} = 5 \times 10^{-8}$ for the HO-WENOZ scheme and $f_{atm} = 10^{-7}$ for the HO-MP5 scheme. The hybrid method employs $f_{hyb} = 10^4$ combined with WENOZ and $f_{hyb} = 2 \times 10^4$ combined with MP5[3]. The simple 2nd order LLF-flux based on primitive reconstruction uses, as in the barotropic case, $f_{atm} = 10^{-11}$. For all simulations $f_{thr} = 100$ is set.

Figure C.2 summarizes our main findings. In all cases we obtain results less accurate than the zero-temperature evolutions. The 2nd order LLF-scheme performs best and shows the smallest errors. For LLF and HO/LLF (especially for late times) we observe approximately second order convergence. The pure HO-scheme performs independent of the reconstruction worst. This behavior can be explained with the high value of f_{atm} suggesting that the atmosphere is the main source of error. Therefore, the hybrid scheme performs better than the pure HO-method.

We want to emphasize that although the test seems to be trivial, the high value of $\Gamma = 2$ in the ideal gas EOS is a strong test of the numerical method. In fact, we expect effectively smaller values for Γ_{th} for realistic EOSs [Bauswein et al., 2010], which allows smaller values of f_{hyb} and f_{atm} as we will see in the next subsection.

Furthermore, we want to discuss briefly why we expect to see only second order

[3]We find in general that higher atmosphere thresholds have to be used when the MP5 reconstruction is employed.

convergence for neutron star spacetimes when the WENOZ reconstruction is used. For this purpose we have to remember the special construction used for WENO-schemes, where high order convergence is obtained for smooth solutions, when the WENO-weights Eq. (C.6) are close to the ideal weights. In fact, we see that this is not the case in our simulations, in particular at the stars surface the weights differ significantly from the ideal weights and practically only a second order polynomial is used for the WENO-reconstruction. Thus, no high order convergence can be expected for neutron stars simulations at the employed resolutions. Furthermore, our investigations in [Die14] suggest that errors from the star's surface propagate through the star and convergence will be reduced to second order after a finite amount of time. We expect that a similar argumentation holds also for the MP5-reconstruction regarding the fact that, e.g. $f^{UL}_{i+1/2}$ (Eq. (C.11a)) is only second order accurate.

C.3 Binary neutron stars

Due to the high computational costs of convergence tests, we restrict our analysis to one equal mass binary with $1.35M_\odot - 1.35M_\odot$ constituents modeled with the soft EOS SLy, see Tab. 2.2. The initial GW frequency is $M\omega^0_{22} = 0.060$, which results in ~ 3 orbits, i.e. ~ 6 GW cycles. We use the Z4c scheme with constraint preserving boundary conditions. Our convergence analysis is based on four different resolutions, where the specific grid configurations are given in Tab. C.1. All configurations use a total of 7 refinement levels, where all levels $l > l^{mv} = 4$ are dynamically moved, the $l = 0$-box is substituted by spherical patches.

Table C.1: Grid configuration for the convergence tests of an equal mass $1.35M_\odot - 1.35M_\odot$ binary. The columns refer to: the resolution name, the number of points in the non-moving boxes n, the number of points in the moving boxes n^{mv}, the grid spacing in the finest level h_6, the radial grid spacing in the shells $(l = 0)$ h_r, the number of radial grid points n_r, the number of azimuthal grid points n_θ, the outer boundary position r_b.

Name	n	n^{mv}	h_6	h_r	n_r	n_θ	r_b
Low	128	64	0.228	7.296	128	56	1426
Med	192	96	0.152	4.864	192	84	1418
High	256	128	0.114	3.648	256	112	1414
Fine	320	160	0.0912	2.9184	320	140	1411

Figure C.3 shows a convergence test for the curvature scalar Ψ_4 investigating the amplitude differences (upper panels) and the phase differences (lower panels). The differences Low-Med, Med-High, High-Fine are shown as solid red, blue, black lines, respectively. Additionally, we scale Med-High and High-Fine according to second order, so that they should match Low-Med, Med-High (dashed and dot-dashed lines).

For almost all simulations, we find that, as expected, the amplitude and phase differences become smaller for higher resolutions. But not all of our simulations show a clear convergence order.

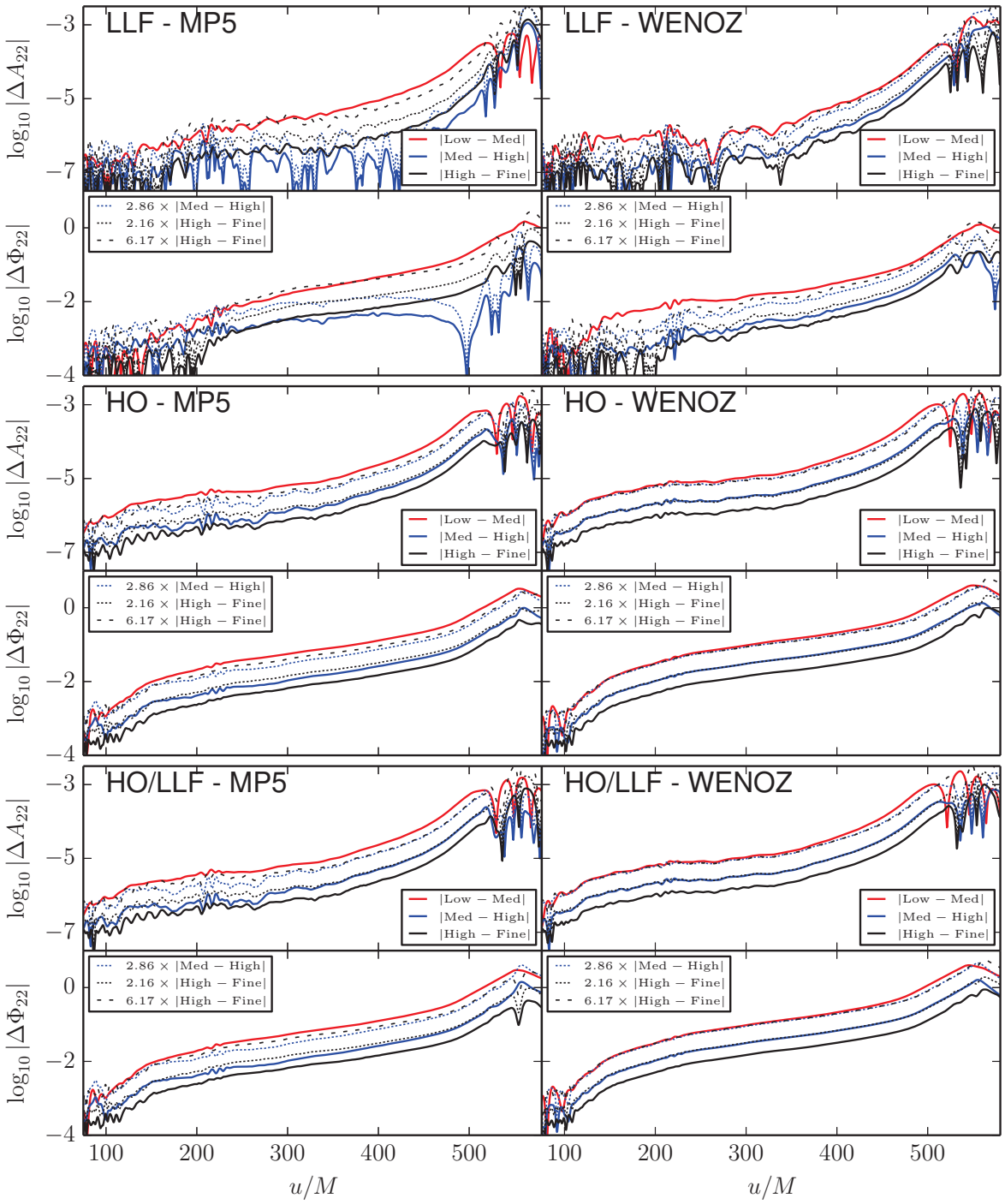

Figure C.3: Convergence analysis of the dominant $(2, 2)$ curvature GW signal for an equal mass binary. The upper panels represent a convergence analysis of the amplitude $|\Delta A_{22}|$ the lower panels refer to the phase difference $|\Delta\Phi_{22}|$. We present results for a second order LLF (LLF), a higher order LLF (HO), and a hybrid scheme (HO/LLF) for MP5 and WENOZ reconstruction. Solid lines refer to: Low-Med (red), Med-High (blue),High-Fine (black) differences. Dashed lines are scaled according to second order convergence.

Most notably, for the 2nd order LLF scheme (upper panels) with MP5 reconstruction no clear order of convergence is visible. It is unclear why the results for the Med and High resolution are almost identical. Nevertheless, our analysis shows that the conservative error estimate used throughout the thesis for the LLF-WENOZ method, i.e. the difference between the highest and the second highest available resolutions, is reasonable [Bernuzzi et al., 2012a].

The results for the higher order LLF-method (Fig. C.3-middle panels) and the hybrid method (Fig. C.3-lower panels) are quite similar, which is the reason why we discuss them simultaneously. For the MP5 reconstruction method, we observe for low resolutions a convergence faster than second order, in fact the order seems to be ~ 3.2. Unfortunately, the convergence becomes slower for high resolutions, where a convergence order of $\lesssim 2$ is present. On the contrary, for the WENOZ reconstruction method, we observe clear second order convergence in amplitude and phase for all combinations. This allows to use a Richardson extrapolation to compute the GW signal accurately. Therefore, the HO-WENOZ or HO/LLF-WENOZ scheme seems to be the preferred choice for numerical simulations performed in the future.

Additionally, we present the rest-mass conservation as a consistency check for the accuracy of our simulation. It is important to notice that we do not use the conservative mesh refinement implementation, since the implementation was not completely tested when the first experiments with higher-order convergence methods started. However, we have seen in Sec. 5.1 that there is only minor influence of the correction step during the inspiral of the two neutron stars and that the artificial atmosphere is the main source of error (especially for a soft EOS as SLy).

In Fig. C.4 we present the rest mass (baryonic mass) in the upper panels, where Low, Med, High, Fine refer to solid red, blue, black, orange lines, respectively. The lower panels show $\log_{10}|M_b(t)/M_b(t=0)-1|$. As for the investigation of the gravitational waveform, we see that overall the results converge with increasing resolution, where the mass change $M_b(t)/M_b(t=0)-1$ goes to zero in the limit of infinite resolution. We want to summarize the most important observations:

(i) Better results are obtained for lower atmosphere thresholds.

(ii) For all MP5 simulations the Low-resolution does not seem to be in the convergent regime, but higher resolved MP5 runs give smaller absolute errors than the corresponding WENOZ simulations.

(iii) The combination of a pure higher order scheme with WENOZ, does not seem to converge with a clear convergence order, probably due to the high atmosphere values.

(iv) The best performance is obtained with the hybrid HO/LLF-scheme, where the HO/LLF-WENOZ simulation shows for all resolutions an almost perfect 4th order

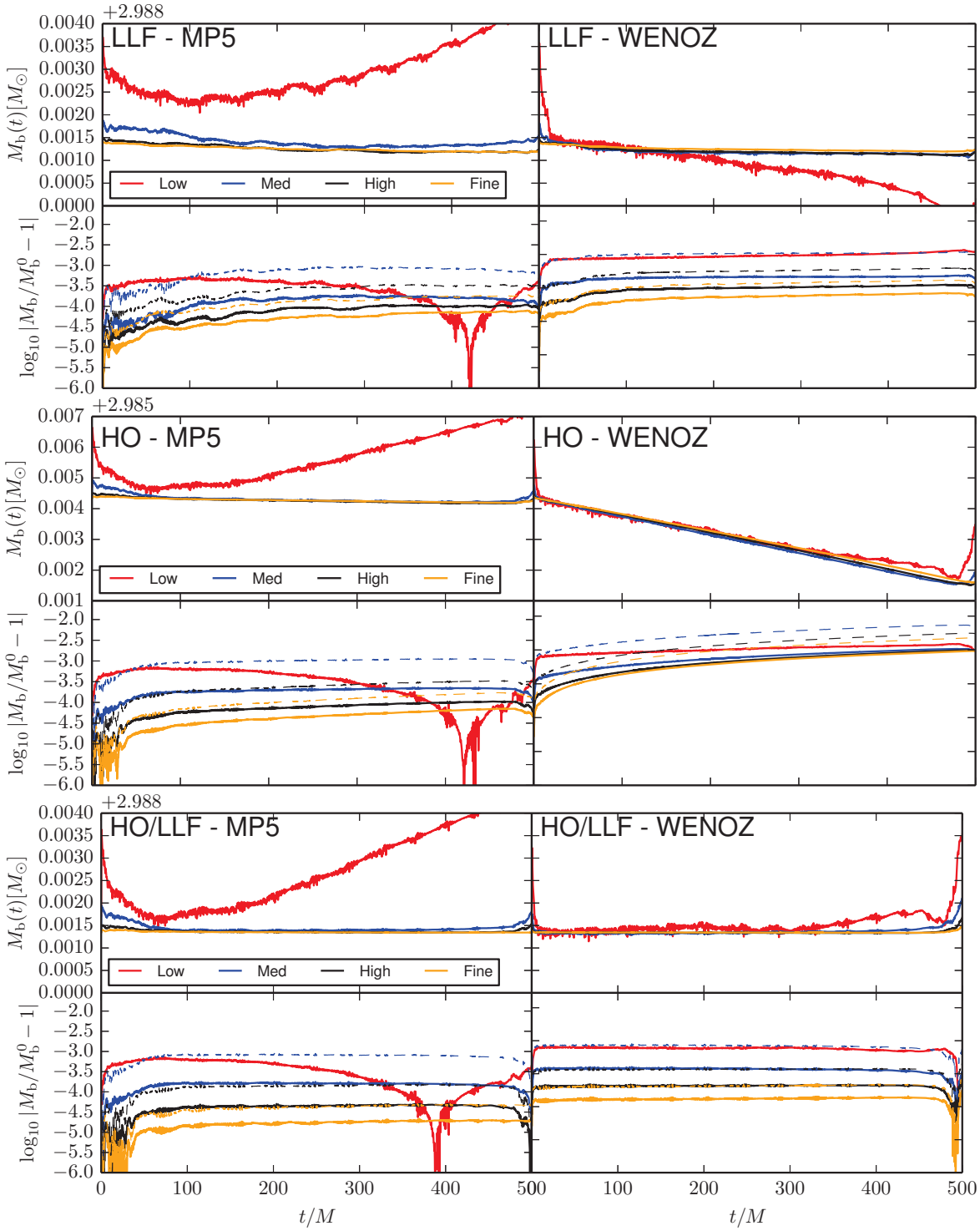

Figure C.4: Convergence study of the rest mass for an equal mass binary configuration. Upper panels present rest mass during the inspiral $M_b(t)$, lower panels show $\log_{10}|M_b(t)/M_b(t = 0) - 1|$, i.e. the error of the rest-mass conservation. The colors refer to: Low (red), Med (blue), High (black), Fine (orange). We scale the results according to fourth order convergence.

convergence [4] over the entire inspiral.

Concluding our investigation, we find that overall the hybrid HO/LLF numerical flux algorithm and a WENOZ reconstruction is the method of choice. We observe clear fourth order convergence of the rest-mass conservation and we observe a clear second order convergence of the GW. The convergence is present for all employed resolutions and therefore the GW signal allows Richardson extrapolation to obtain accurate waveform templates.

[4]Notice, it is not surprising that the convergence order for the mass conservation is higher than the one for the GW signal since in principle mass conservation should be obtained up to round-off error (except the artificial atmosphere treatment and the mesh refinement boundaries). Obtaining 4th order convergence suggests that especially the atmosphere effects are surface effects which do not influence the mass conservation significantly iff the atmosphere threshold is low enough.

Appendix D

SGRID

We construct our quasi-equilibrium data with the SGRID and the LORENE codes. While the public available LORENE code [Gourgoulhon et al.] was used for the thesis without major modifications[1], the SGRID code was improved by the implementation of piecewise polytropic EOSs. Therefore, we present important aspects of the SGRID code in this appendix following [Die13].

D.1 Grid configuration

To construct quasi-equilibrium data with the SGRID code, we place the two neutron stars along the x axis, see Fig. D.1 for an illustration of the grid structure for $y > 0$ and $z = 0$. The particular coordinate transformations from Cartesian coordinates to the employed A, B, φ coordinates can be found in [Ansorg, 2007; Tichy, 2009] and [Die13]. In total the numerical domain consists of six subgrids, three for $x < 0$ and three for $x > 0$. One on each side is covering the exterior of the star running from the stars surface ($A = 0$) to spatial infinity, a second running from the star's surface ($A = 0$) to a value A_{max}, and the last is a Cartesian box taking care of the coordinate singularity for $A = 1$ and covering $A > A_{\text{max}}$; see Fig. D.1.

Due to the fact that spatial infinity is part of our numerical domain, we can impose Dirichlet boundary conditions:

$$\lim_{r\to\infty} \psi = 1, \qquad \lim_{r\to\infty} B^i = 0, \qquad \lim_{r\to\infty} \alpha\psi = 1. \tag{D.1a}$$

The inner domain boundary ($A = 0$) is the star's surface, where Eq. (4.10) is subject to the boundary condition

$$\left[(D^i + w^i\phi) - hu^0(\beta^i + k^i)\right] D_i\rho = 0. \tag{D.2}$$

In the A, B-directions and in the Cartesian boxes Chebychev polynomials are

[1] Small modifications, the correction of a wrong label in the piecewise polytropic implementation and the computation of the mass-shedding parameter, were implemented by M. Ujevic.

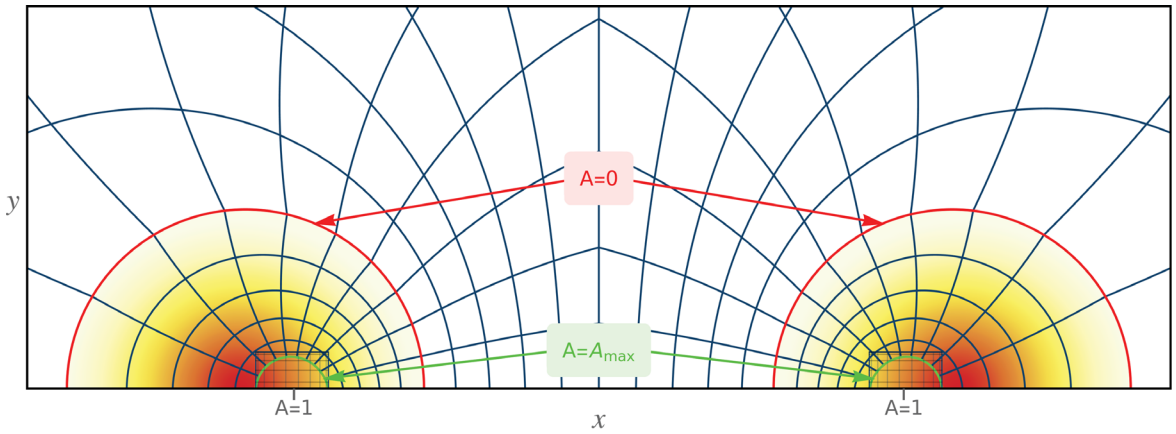

Figure D.1: The grid structure in the x-y-plane for an equal-mass configuration. Lines of constant A and B are shown with straight lines together with an overlay of the density profile. Moreover one can see the Cartesian boxes with Chebychev grids inside the stars. Plot taken from [Die13] and authored by N. Moldenhauer.

employed, while for the φ-direction a Fourier expansion is used. Furthermore, we impose along the x-axis the following regularity conditions:

$$\partial_\varphi F = 0, \qquad \partial_s F + \partial_s \partial_\varphi \partial_\varphi F = 0, \tag{D.3}$$

where F represents ψ, B^i, α, ϕ and $s = \sqrt{y^2 + z^2}$.

For a typical configuration, we employ between 16 and 28 points in A, B and 8 points in the φ-direction. For the Cartesian box we choose normally $n_x = n_y = n_z = n_{\text{Cart}} = n_A - 4$ points. Figure D.2 shows the convergence of the code.

D.2 Iteration procedure

A specific iteration procedure as described in [Tichy, 2012] and [Die13] is used to solve the coupled system of partial differential equations. The main points are summarized in the following:

(i) Define an initial configuration (e.g. a TOV-star [Tolman, 1939; Oppenheimer and Volkoff, 1939] or previously constructed configurations). Set the velocity potential ϕ in each star to $\phi = \Omega(x_{C*} - x_{\text{CM}})y$, where x_{C*} is the x-coordinate of the star's center.

(ii) Evaluate the residuals of all elliptic equations; stop if the residuals are below the prescribed tolerance.

(iii) Solve (4.10) if the residuum of Eq. (4.10) is bigger than combined residuals of Eqs. (4.4). Notice that we always employ a softening procedure, i.e. $\phi = \zeta\phi_{\text{solved}} + (1-\zeta)\phi_{\text{old}}$, typically $\zeta = 0.2$ is used.

(iv) Solve the elliptic equations for ψ, B^i, α (typically with a softening of $\zeta = 0.4$).

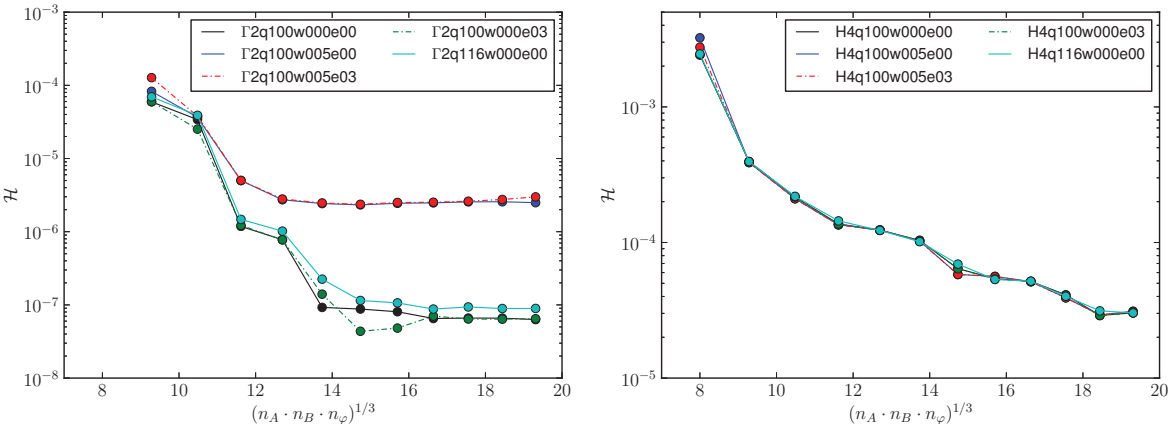

Figure D.2: Convergence analysis. Results for the simple polytropic $\Gamma 2\kappa 124$ EOS (left) and the piecewise polytrope H4 (right) are shown. We consider mass ratios of $q = 1.00$ and $q = 1.16$ (denoted by q100 and q116), angular velocities of $\omega^i = (0, 0, 0)$ and $\omega^i = (0, 0, 0.005)$ (denoted by w000 and w005), and eccentricities of $e = 0$ and $e = 0.3$ (denoted by e00 and e03). Exponential convergence up to saturation is obtained for simple polytropes, the level of saturation depends mostly on the angular velocity field. For piecewise polytropes the results are less accurate and a polynomial convergence with 3rd-4th order is obtained. Eccentricity and different mass ratios do not seem to affect the accuracy. The Hamiltonian constraint is computed inside the two stars in the region $A \in [0, A_{\max}]$ including the star's surface. We have fixed $n_\varphi = 8, n_{\text{Cart}} = n_A - 4$. Plot taken from [Die13].

(v) The positions of the stars' centers, $x_{C*,\pm}$, are determined by the maximum of h along the x-axis and Ω and x_{CM} are computed in such a way that the stars' centers remain at $x_{C*\pm}$ when h is updated.

(vi) Compute h and choose $C_\pm$ such that the rest mass of each star remains constant and adjust the domain boundaries $\sigma_\pm$ accordingly[2].

(vii) Go back to step (ii).

D.3 Code novelties

We want to highlight some novelties of the SGRID code presented in [Die13]. In particular these changes allow the computation of piecewise-polytropic EOSs, larger mass ratios, and elliptic orbits[3]; cf. [Die13].

While for simple polytropic EOSs the matter quantities, most notably the pressure p and the density ρ are C^∞ and only the star's surface needs special attention. The same is not true for piecewise-polytropes. Considering a single, piecewise-polytropic TOV star, $q = \frac{p}{\rho} \in C^0$ (cf. [Tichy, 2009; Tichy, 2012]), while $q = h - 1 \in C^1$, which is the reason why we switched to the latter definition of q. We can compute the other

[2]Typically we filter out high frequencies in $\sigma_\pm$ for overall stability and apply $\partial_B \sigma_\pm(B, \varphi)|_{B=0,1} = 0$ to keep the stars on the x-axis.

[3]Elliptic BNS simulations and the computation of the corresponding quasi-equilibrium configurations will be discussed in the PhD thesis of N. Moldenhauer in detail.

matter variables in terms of the new q-variable with

$$\rho = \left[\frac{q+1-K_i}{\kappa_i(n_i+1)}\right]^{n_i}, \tag{D.4a}$$

$$p = \rho\frac{q+1-K_i}{n_i+1}, \tag{D.4b}$$

$$\rho_E = n_i p + K_i \rho, \tag{D.4c}$$

with $K_i = \frac{\epsilon(\rho_{i-1})}{\rho_{i-1}} - n_i\kappa_i\rho_{i-1}^{1/n_i}$ and $n_i = 1/(\Gamma_i - 1)$. The subscript i refers to the specific interval of the piecewise-polytropic EOS; cf. Eq.(2.55).

Another important novelty, also implemented in collaboration with W. Tichy, is a new algorithm to update Ω and x^1_{CM}. This allows to construct high-mass ratios as used in Sec. 5.3. While in the past the force balance equation

$$\partial_1 \ln\left[\alpha^2 - \left(\beta^i + k^i + \frac{w^i}{hu^0}\right)\left(\beta_i + k_i + \frac{w_i}{hu^0}\right)\right]\Bigg|_{x^1_{C*\pm}} = -2\partial_1 \ln\Gamma\big|_{x^1_{C*\pm}}, \tag{D.5}$$

was used to compute Ω and x^1_{CM}. We noticed that for large mass ratios, this leads to a large magnitude of the ADM momentum

$$P^i_{ADM} = \int S^i \psi^{10} d^3x, \tag{D.6}$$

mainly in the y-component P^y_{ADM}. We adopt a similar algorithm as in [Taniguchi and Shibata, 2010] to solve this problem. Ω and x^1_{CM} enter in the matter flux

$$S^i = \alpha(\rho_E + p)(u^0)^2(V^i + k^i + \beta^i) \tag{D.7}$$

due to the symmetry vector k^i. Using Ω of a previous iteration step, we solve $P^y_{ADM} = 0$ for x^1_{CM} and update the star centers. Afterwards we compute Ω from Eq. (D.5) for each star center obtaining a new value. The final Ω is obtained by softening with $\zeta = 0.5$.

These code improvements allowed the simulation of the $q = 2.06$-simulation in Sec. 5.3 and more realistic EOSs as just simple polytropes; cf. [Die13].

Bibliography

[advLIGO] "Advanced LIGO Anticipated Sensitivity Curves", LIGO Document Report No. T0900288-v3.

[ET] Einstein Telescope - http://www.et-gw.eu/.

[IND] INDIGO - Indian Initiative in Gravitational-wave Observations, http://www.gw-indigo.org.

[KAGRA] KAGRA - Kamioka Gravitational Wave Detector, http://gwcenter.icrr.u-tokyo.ac.jp/en/.

[LIGO] LIGO - Laser Interferometer Gravitational Wave Observatory, http://www.ligo.caltech.edu/.

[LISA] LISA (laser interferometer space antenna), proposal for a gravitational wave detector in space. Preprint, Max-Planck-Institut für Quantenoptik, MPQ 177, May 1993.

[SpEC] SpEC - Spectral Einstein Code, http://www.black-holes.org/SpEC.html.

[VIRGO] Virgo/EGO - European Gravitational Observatory, http://www.ego-gw.it/.

[Aasi et al., 2013] Aasi, J. et al. (2013). Prospects for Localization of Gravitational Wave Transients by the Advanced LIGO and Advanced Virgo Observatories.

[Abadie et al., 2010] Abadie, J. et al. (2010). Predictions for the Rates of Compact Binary Coalescences Observable by Ground-based Gravitational-wave Detectors. *Class.Quant.Grav.*, 27:173001.

[Abdikamalov et al., 2014] Abdikamalov, E., Ott, C., Radice, D., Roberts, L., Haas, R., et al. (2014). Neutrino-driven Turbulent Convection and Standing Accretion Shock Instability in Three-Dimensional Core-Collapse Supernovae.

[Alcubierre, 1997] Alcubierre, M. (1997). The appearance of coordinate shocks in hyperbolic formulations of general relativity. *Phys. Rev. D*, 55:5981–5991.

[Alcubierre, 2003] Alcubierre, M. (2003). Hyperbolic slicings of spacetime: singularity avoidance and gauge shocks. *Class. Quantum Grav.*, 20(4):607–624.

[Alcubierre, 2008] Alcubierre, M. (2008). *Introduction to 3+1 Numerical Relativity*. Oxford University Press, Oxford.

[Alcubierre et al., 2003] Alcubierre, M., Brügmann, B., Diener, P., Koppitz, M., Pollney, D., et al. (2003). Gauge conditions for long term numerical black hole evolutions without excision. *Phys.Rev.*, D67:084023.

[Alic et al., 2012] Alic, D., Bona-Casas, C., Bona, C., Rezzolla, L., and Palenzuela, C. (2012). Conformal and covariant formulation of the Z4 system with constraint-violation damping. *Phys.Rev.*, D85:064040.

[Amaro-Seoane et al., 2012] Amaro-Seoane, P., Aoudia, S., Babak, S., Binétruy, P., Berti, E., Bohé, A., Caprini, C., Colpi, M., Cornish, N., Danzmann, K., Dufaux, J.-F., Gair, J.,

Jennrich, O., Jetzer, P., Klein, A., Lang, R., Lobo, A., Littenberg, T., McWilliams, S., Nelemans, G., Petiteau, A., Porter, E., Schutz, B., Sesana, A., Stebbins, R., Sumner, T., Vallisneri, M., Vitale, S., Volonteri, M., and Ward, H. (2012). Low-frequency gravitational-wave science with elisa/ngo. *Class. Quantum Grav.*, 29:124016.

[Anderson et al., 2008] Anderson, M., Hirschmann, E. W., Lehner, L., Liebling, S. L., Motl, P. M., Neilsen, D., Palenzuela, C., and Tohline, J. E. (2008). Magnetized Neutron Star Mergers and Gravitational Wave Signals. *Phys. Rev. Lett.*, 100:191101.

[Andersson et al., 2013] Andersson, N., Baker, J., Belczynski, K., Bernuzzi, S., Berti, E., et al. (2013). The Transient Gravitational-Wave Sky. *Class.Quant.Grav.*, 30:193002.

[Ansorg, 2007] Ansorg, M. (2007). Multi-Domain Spectral Method for Initial Data of Arbitrary Binaries in General Relativity. *Classical Quantum Gravity*, 24:S1–S14.

[Arnowitt et al., 1962] Arnowitt, R., Deser, S., and Misner, C. W. (1962). The dynamics of general relativity. In Witten, L., editor, *Gravitation: An Introduction to Current Research*, pages 227–265. Wiley, New York.

[Bahcall and Meszaros, 2000] Bahcall, J. N. and Meszaros, P. (2000). 5-GeV to 10-GeV neutrinos from gamma-ray burst fireballs. *Phys.Rev.Lett.*, 85:1362–1365.

[Baiotti et al., 2009] Baiotti, L., Bernuzzi, S., Corvino, G., De Pietri, R., and Nagar, A. (2009). Gravitational-Wave Extraction from Neutron Stars Oscillations: comparing linear and nonlinear techniques. *Phys. Rev.*, D79:024002.

[Baiotti et al., 2010] Baiotti, L., Damour, T., Giacomazzo, B., Nagar, A., and Rezzolla, L. (2010). Analytic modelling of tidal effects in the relativistic inspiral of binary neutron stars. *Phys. Rev. Lett.*, 105:261101.

[Baiotti et al., 2008] Baiotti, L., Giacomazzo, B., and Rezzolla, L. (2008). Accurate evolutions of inspiralling neutron-star binaries: prompt and delayed collapse to black hole. *Phys. Rev.*, D78:084033.

[Baiotti et al., 2005] Baiotti, L., Hawke, I., Montero, P. J., Loffler, F., Rezzolla, L., et al. (2005). Three-dimensional relativistic simulations of rotating neutron star collapse to a Kerr black hole. *Phys.Rev.*, D71:024035.

[Baiotti et al., 2007] Baiotti, L., Hawke, I., and Rezzolla, L. (2007). On the gravitational radiation from the collapse of neutron stars to rotating black holes. *Class. Quant. Grav.*, 24:S187–S206.

[Balmelli and Jetzer, 2013] Balmelli, S. and Jetzer, P. (2013). An Effective-One-Body Hamiltonian with next-to-leading order spin-spin coupling for two nonprecessing black holes with aligned spins.

[Banyuls et al., 1997] Banyuls, F., Font, J. A., Ibáñez, J. M., Martí, J. M., and Miralles, J. A. (1997). Numerical 3+1 general-relativistic hydrodynamics: A local characteristic approach. *Astrophys. J.*, 476:221.

[Barack, 2009] Barack, L. (2009). Gravitational self force in extreme mass-ratio inspirals. *Class.Quant.Grav.*, 26:213001.

[Barausse et al., 2012] Barausse, E., Buonanno, A., and Le Tiec, A. (2012). The complete non-spinning effective-one-body metric at linear order in the mass ratio. *Phys.Rev.*, D85:064010.

[Baumgarte and Shapiro, 1998] Baumgarte, T. W. and Shapiro, S. L. (1998). On the Numerical integration of Einstein's field equations. *Phys. Rev. D*, 59:024007.

[Baumgarte and Shapiro, 2010] Baumgarte, T. W. and Shapiro, S. L. (2010). *Numerical Relativity: Solving Einstein's Equations on the Computer*. Cambridge University Press, Cambridge.

[Baumgarte et al., 2000] Baumgarte, T. W., Shapiro, S. L., and Shibata, M. (2000). On the Maximum Mass of Differentially Rotating Neutron Stars. *Astrophys. J.*, 528:L29.

[Bauswein et al., 2013] Bauswein, A., Goriely, S., and Janka, H.-T. (2013). Systematics of dynamical mass ejection, nucleosynthesis, and radioactively powered electromagnetic signals from neutron-star mergers. *Astrophys.J.*, 773:78.

[Bauswein et al., 2012] Bauswein, A., Janka, H., Hebeler, K., and Schwenk, A. (2012). Equation-of-state dependence of the gravitational-wave signal from the ring-down phase of neutron-star mergers. *Phys.Rev.*, D86:063001.

[Bauswein and Janka, 2012] Bauswein, A. and Janka, H.-T. (2012). Measuring neutron-star properties via gravitational waves from binary mergers. *Phys.Rev.Lett.*, 108:011101.

[Bauswein et al., 2010] Bauswein, A., Janka, H.-T., and Oechslin, R. (2010). Testing Approximations of Thermal Effects in Neutron Star Merger Simulations. *Phys.Rev.*, D82:084043.

[Bauswein and Stergioulas, 2015] Bauswein, A. and Stergioulas, N. (2015). Unified picture of the post-merger dynamics and gravitational wave emission in neutron star mergers. *Phys. Rev.*, D91(12):124056.

[Bauswein et al., 2014] Bauswein, A., Stergioulas, N., and Janka, H.-T. (2014). Revealing the high-density equation of state through binary neutron star mergers. *Phys.Rev.*, D90(2):023002.

[Bauswein et al., 2015] Bauswein, A., Stergioulas, N., and Janka, H.-T. (2015). Exploring properties of high-density matter through remnants of neutron-star mergers.

[Bauswein et al., 2015] Bauswein, A., Stergioulas, N., and Janka, H.-T. (2015). Inferring neutron-star properties from gravitational-wave signals of binary mergers. *ArXiv e-prints*.

[Berger and Colella, 1989] Berger, M. J. and Colella, P. (1989). Local adaptive mesh refinement for shock hydrodynamics. *Journal of Computational Physics*, 82:64–84.

[Berger and Oliger, 1984] Berger, M. J. and Oliger, J. (1984). Adaptive Mesh Refinement for Hyperbolic Partial Differential Equations. *J.Comput.Phys.*, 53:484.

[Bernuzzi and Hilditch, 2010] Bernuzzi, S. and Hilditch, D. (2010). Constraint violation in free evolution schemes: comparing BSSNOK with a conformal decomposition of Z4. *Phys. Rev.*, D81:084003.

[Bernuzzi et al., 2008] Bernuzzi, S., Nagar, A., and De Pietri, R. (2008). Dynamical excitation of space-time modes of compact objects. *Phys. Rev.*, D77:044042.

[Bernuzzi et al., 2012a] Bernuzzi, S., Nagar, A., Thierfelder, M., and Brügmann, B. (2012a). Tidal effects in binary neutron star coalescence. *Phys.Rev.*, D86:044030.

[Bernuzzi et al., 2012b] Bernuzzi, S., Thierfelder, M., and Brügmann, B. (2012b). Accuracy of numerical relativity waveforms from binary neutron star mergers and their comparison with post-Newtonian waveforms. *Phys.Rev.*, D85:104030.

[Berti et al., 2009] Berti, E., Cardoso, V., and Starinets, A. O. (2009). Quasinormal modes of black holes and black branes. *Class. Quant. Grav.*, 26:163001.

[Beyer and Sarbach, 2004] Beyer, H. and Sarbach, O. (2004). On the well posedness of the Baumgarte-Shapiro- Shibata-Nakamura formulation of Einstein's field equations. *Phys. Rev. D*, 70:104004.

[Bini and Damour, 2013] Bini, D. and Damour, T. (2013). Analytical determination of the two-body gravitational interaction potential at the fourth post-Newtonian approximation. *Phys.Rev.*, D87(12):121501.

[Bini and Damour, 2014a] Bini, D. and Damour, T. (2014a). Analytic determination of the eight-and-a-half post-Newtonian self-force contributions to the two-body gravitational interaction potential. *Phys.Rev.*, D89(10):104047.

[Bini and Damour, 2014b] Bini, D. and Damour, T. (2014b). Gravitational self-force corrections to two-body tidal interactions and the effective one-body formalism. *Phys.Rev.*, D90(12):124037.

[Bini and Damour, 2014c] Bini, D. and Damour, T. (2014c). High-order post-Newtonian contributions to the two-body gravitational interaction potential from analytical gravitational self-force calculations. *Phys.Rev.*, D89(6):064063.

[Bini et al., 2012] Bini, D., Damour, T., and Faye, G. (2012). Effective action approach to higher-order relativistic tidal interactions in binary systems and their effective one body description. *Phys.Rev.*, D85:124034.

[Binnington and Poisson, 2009] Binnington, T. and Poisson, E. (2009). Relativistic theory of tidal Love numbers. *Phys. Rev.*, D80:084018.

[Blanchet, 2014] Blanchet, L. (2014). Gravitational Radiation from Post-Newtonian Sources and Inspiralling Compact Binaries. *Living Rev. Relativity*, 17:2.

[Bona et al., 1995] Bona, C., Massó, J., Seidel, E., and Stela, J. (1995). A New Formalism for Numerical Relativity. *Phys. Rev. Lett.*, 75:600–603.

[Bona et al., 1997] Bona, C., Massó, J., Seidel, E., and Stela, J. (1997). First order hyperbolic formalism for numerical relativity. *Phys. Rev. D*, 56:3405–3415. gr-qc/9709016.

[Borges et al., 2008] Borges, R., Carmona, M., Costa, B., and Don, W. S. (2008). An improved weighted essentially non-oscillatory scheme for hyperbolic conservation laws. *Journal of Computational Physics*, 227(6):3191–3211.

[Boyd, 2001] Boyd, J. P. (2001). *Chebyshev and Fourier Spectral Methods (Second Edition, Revised)*. Dover Publications, New York.

[Brügmann et al., 2008] Brügmann, B., González, J. A., Hannam, M., Husa, S., Sperhake, U., and Tichy, W. (2008). Calibration of Moving Puncture Simulations. *Phys. Rev. D*, 77:024027.

[Buonanno and Damour, 1999] Buonanno, A. and Damour, T. (1999). Effective one-body approach to general relativistic two- body dynamics. *Phys. Rev.*, D59:084006.

[Buonanno and Damour, 2000] Buonanno, A. and Damour, T. (2000). Transition from inspiral to plunge in binary black hole coalescences. *Phys. Rev.*, D62:064015.

[Burgay et al., 2003] Burgay, M., D'Amico, N., Possenti, A., Manchester, R., Lyne, A., et al. (2003). An Increased estimate of the merger rate of double neutron stars from observations of a highly relativistic system. *Nature*, 426:531–533.

[Campanelli et al., 2006] Campanelli, M., Lousto, C., and Zlochower, Y. (2006). Spinning-black-hole binaries: The orbital hang up. *Phys.Rev.*, D74:041501.

[Carroll, 2003] Carroll, S. M. (2003). *Spacetime and Geometry: An Introduction to General Relativity*. Benjamin Cummings.

[Ciolfi et al., 2011] Ciolfi, R., Lander, S. K., Manca, G. M., and Rezzolla, L. (2011). Instability-driven evolution of poloidal magnetic fields in relativistic stars. *Astrophys.J.*, 736:L6.

[Cordero-Carrion et al., 2009] Cordero-Carrion, I. et al. (2009). An improved constrained scheme for the Einstein equations: an approach to the uniqueness issue. *Phys. Rev.*, D79:024017.

[Dain and Gabach Clement, 2009] Dain, S. and Gabach Clement, M. E. (2009). Extreme Bowen-York initial data. *Class.Quant.Grav.*, 26:035020.

[Damour, 2001] Damour, T. (2001). Coalescence of two spinning black holes: An effective one- body approach. *Phys. Rev.*, D64:124013.

[Damour, 2012] Damour, T. (2012). The General Relativistic Two Body Problem and the Effective One Body Formalism.

[Damour et al., 2009] Damour, T., Iyer, B. R., and Nagar, A. (2009). Improved resummation of post-Newtonian multipolar waveforms from circularized compact binaries. *Phys. Rev.*, D79:064004.

[Damour et al., 2000] Damour, T., Jaranowski, P., and Schäfer, G. (2000). On the determination of the last stable orbit for circular general relativistic binaries at the third post-Newtonian approximation. *Phys. Rev.*, D62:084011.

[Damour et al., 2008a] Damour, T., Jaranowski, P., and Schäfer, G. (2008a). Effective one body approach to the dynamics of two spinning black holes with next-to-leading order spin-orbit coupling. *Phys.Rev.*, D78:024009.

[Damour and Nagar, 2008] Damour, T. and Nagar, A. (2008). Comparing Effective-One-Body gravitational waveforms to accurate numerical data. *Phys. Rev.*, D77:024043.

[Damour and Nagar, 2009a] Damour, T. and Nagar, A. (2009a). Improved analytical description of inspiralling and coalescing black-hole binaries. *Phys. Rev. D*, 79(8):081503.

[Damour and Nagar, 2009b] Damour, T. and Nagar, A. (2009b). Relativistic tidal properties of neutron stars. *Phys. Rev.*, D80:084035.

[Damour and Nagar, 2010] Damour, T. and Nagar, A. (2010). Effective One Body description of tidal effects in inspiralling compact binaries. *Phys. Rev.*, D81:084016.

[Damour and Nagar, 2014] Damour, T. and Nagar, A. (2014). New effective-one-body description of coalescing nonprecessing spinning black-hole binaries. *Phys.Rev.*, D90(4):044018.

[Damour et al., 2013] Damour, T., Nagar, A., and Bernuzzi, S. (2013). Improved effective-one-body description of coalescing nonspinning black-hole binaries and its numerical-relativity completion. *Phys.Rev.*, D87:084035.

[Damour et al., 2008b] Damour, T., Nagar, A., Hannam, M., Husa, S., and Brügmann, B. (2008b). Accurate Effective-One-Body waveforms of inspiralling and coalescing black-hole binaries. *Phys. Rev.*, D78:044039.

[Damour et al., 2012a] Damour, T., Nagar, A., Pollney, D., and Reisswig, C. (2012a). Energy versus Angular Momentum in Black Hole Binaries. *Phys.Rev.Lett.*, 108:131101.

[Damour et al., 2012b] Damour, T., Nagar, A., and Villain, L. (2012b). Measurability of the tidal polarizability of neutron stars in late-inspiral gravitational-wave signals. *Phys.Rev.*, D85:123007.

[Dan et al., 2011] Dan, M., Rosswog, S., Guillochon, J., and Ramirez-Ruiz, E. (2011). Prelude to a double degenerate merger: the onset of mass transfer and its impact on gravitational waves and surface detonations. *Astrophys. J.*, 737:89.

[Davis et al., 1971] Davis, M., Ruffini, R., Press, W., and Price, R. (1971). Gravitational radiation from a particle falling radially into a schwarzschild black hole. *Phys.Rev.Lett.*, 27:1466–1469.

[Davis et al., 1972] Davis, M., Ruffini, R., and Tiomno, J. (1972). Pulses of gravitational radiation of a particle falling radially into a schwarzschild black hole. *Phys. Rev.*, D5:2932–2935.

[Deaton et al., 2013] Deaton, M. B., Duez, M. D., Foucart, F., O'Connor, E., Ott, C. D., Kidder, Lawrence, E., Muhlberger, C. D., Scheel, M. A., and Szilágyi, B. (2013). Black Hole-Neutron Star Mergers with a Hot Nuclear Equation of State: Outflow and Neutrino-Cooled Disk for a Low-Mass, High-Spin Case. *Astrophys. J.*, 776:47.

[Del Pozzo et al., 2013] Del Pozzo, W., Li, T. G. F., Agathos, M., Broeck, C. V. D., and Vitale, S. (2013). Demonstrating the feasibility of probing the neutron star equation of state with second-generation gravitational wave detectors. *Phys. Rev. Lett.*, 111:071101.

[Dennison et al., 2014] Dennison, K. A., Baumgarte, T. W., and Montero, P. J. (2014). Trumpet Slices in Kerr Spacetimes. *Phys.Rev.Lett.*, 113(26):261101.

[Dermer and Holmes, 2005] Dermer, C. D. and Holmes, J. M. (2005). Cosmic rays from gamma ray bursts in the Galaxy. *Astrophys.J.*, 628:L21–L24.

[Dessart et al., 2009] Dessart, L., Ott, C., Burrows, A., Rosswog, S., and Livne, E. (2009). Neutrino signatures and the neutrino-driven wind in Binary Neutron Star Mergers. *Astrophys.J.*, 690:1681.

[Dimmelmeier et al., 2006] Dimmelmeier, H., Stergioulas, N., and Font, J. A. (2006). Nonlinear axisymmetric pulsations of rotating relativistic stars in the conformal flatness approximation. *Mon. Not. Roy. Astron. Soc.*, 368:1609–1630.

[d'Inverno, 1992] d'Inverno, R. (1992). *Introducing Einstein's Relativity*. Oxford University Press, Oxford (UK). ++good, introductory but still covers a lot of material.

[Dionysopoulou et al., 2015] Dionysopoulou, K., Alic, D., and Rezzolla, L. (2015). General-relativistic resistive-magnetohydrodynamic simulations of binary neutron stars.

[Dolan et al., 2014] Dolan, S. R., Nolan, P., Ottewill, A. C., Warburton, N., and Wardell, B. (2014). Tidal invariants for compact binaries on quasi-circular orbits.

[Duez et al., 2006] Duez, M. D., Liu, Y. T., Shapiro, S. L., Shibata, M., and Stephens, B. C. (2006). Collapse of magnetized hypermassive neutron stars in general relativity. *Phys. Rev. Lett.*, 96:031101.

[Duez et al., 2004] Duez, M. D., Shapiro, S. L., and Yo, H.-J. (2004). Relativistic hydrodynamic evolutions with black hole excision. *Phys.Rev.*, D69:104016.

[East and Pretorius, 2012] East, W. E. and Pretorius, F. (2012). Dynamical Capture Binary Neutron Star Mergers. *Astrophys. J. Lett.*, 760:L4.

[East et al., 2012] East, W. E., Pretorius, F., and Stephens, B. C. (2012). Hydrodynamics in full general relativity with conservative AMR. *Phys.Rev.*, D85:124010.

[Eichler et al., 1989] Eichler, D., Livio, M., Piran, T., and Schramm, D. N. (1989). Nucleosynthesis, Neutrino Bursts and Gamma-Rays from Coalescing Neutron Stars. *Nature*, 340:126–128.

[Faber and Rasio, 2012] Faber, J. A. and Rasio, F. A. (2012). Binary Neutron Star Mergers. *Living Rev.Rel.*, 15:8.

[Flanagan and Hinderer, 2008] Flanagan, E. E. and Hinderer, T. (2008). Constraining neutron star tidal Love numbers with gravitational wave detectors. *Phys.Rev.*, D77:021502.

[Font, 2007] Font, J. A. (2007). Numerical hydrodynamics and magnetohydrodynamics in general relativity. *Living Rev. Relativity*, 11:7.

[Fornberg, 1998] Fornberg, B. (1998). *A Practical Guide to Pseudospectral Methods*. Cambridge University Press, Cambridge, UK.

[Fryer et al., 2015] Fryer, C. L., Belczynski, K., Ramirez-Ruiz, E., Rosswog, S., Shen, G., and Steiner, A. W. (2015). The Fate of the Compact Remnant in Neutron Star Mergers.

[Gabach Clement, 2010] Gabach Clement, M. E. (2010). Conformally flat black hole initial data, with one cylindrical end. *Class.Quant.Grav.*, 27:125010.

[Galeazzi et al., 2013] Galeazzi, F., Kastaun, W., Rezzolla, L., and Font, J. A. (2013). Implementation of a simplified approach to radiative transfer in general relativity. *Phys. Rev. D*, 88:064009.

[Giacomazzo and Perna, 2012] Giacomazzo, B. and Perna, R. (2012). General Relativistic Simulations of Accretion Induced Collapse of Neutron Stars to Black Holes. *Astrophys.J.*, 758:L8.

[Giacomazzo et al., 2009] Giacomazzo, B., Rezzolla, L., and Baiotti, L. (2009). Can magnetic fields be detected during the inspiral of binary neutron stars? *Mon. Not. R. Astron. Soc. Lett.*, 399:L164–L168.

[Giacomazzo et al., 2011a] Giacomazzo, B., Rezzolla, L., and Baiotti, L. (2011a). Accurate evolutions of inspiralling and magnetized neutron-stars: equal-mass binaries. *Phys. Rev.*, D83:044014.

[Giacomazzo et al., 2011b] Giacomazzo, B., Rezzolla, L., and Stergioulas, N. (2011b). Collapse of differentially rotating neutron stars and cosmic censorship. *Phys.Rev.*, D84:024022.

[Goriely et al., 2011] Goriely, S., Bauswein, A., and Janka, H.-T. (2011). R-Process Nucleosynthesis in Dynamically Ejected Matter of Neutron Star Mergers. *Astrophys.J.*, 738:L32.

[Gourgoulhon, 2012] Gourgoulhon, E. (2012). *3+1 Formalism in General Relativity*. Springer, Berlin.

[Gourgoulhon et al.] Gourgoulhon, E., Grandclément, P., Marck, J.-A., Novak, J., and Taniguchi, K. `http://www.lorene.obspm.fr`.

[Gundlach and Martin-Garcia, 2006] Gundlach, C. and Martin-Garcia, J. M. (2006). Well-posedness of formulations of the Einstein equations with dynamical lapse and shift conditions. *Phys. Rev. D*, 74:024016.

[Hannam et al., 2008a] Hannam, M., Husa, S., Brügmann, B., and Gopakumar, A. (2008a). Comparison between numerical-relativity and post-Newtonian waveforms from spinning binaries: the orbital hang-up case. *Phys. Rev.*, D78:104007.

[Hannam et al., 2009] Hannam, M., Husa, S., and Murchadha, N. O. (2009). Bowen-York trumpet data and black-hole simulations. *Phys.Rev.*, D80:124007.

[Hannam et al., 2007] Hannam, M., Husa, S., Pollney, D., Brügmann, B., and O'Murchadha, N. (2007). Geometry and Regularity of Moving Punctures. *Phys. Rev. Lett.*, 99:241102.

[Hannam et al., 2008b] Hannam, M., Husa, S., Sperhake, U., Brügmann, B., and González, J. A. (2008b). Where post-Newtonian and numerical-relativity waveforms meet. *Phys. Rev.*, D77:044020.

[Harms et al., 2014] Harms, E., Bernuzzi, S., Nagar, A., and Zenginoglu, A. (2014). A new gravitational wave generation algorithm for particle perturbations of the Kerr spacetime. *Class.Quant.Grav.*, 31:245004.

[Hemberger et al., 2013] Hemberger, D. A., Lovelace, G., Loredo, T. J., Kidder, L. E., Scheel, M. A., Szilágyi, B., Taylor, N. W., and Teukolsky, S. A. (2013). Final spin and radiated energy in numerical simulations of binary black holes with equal masses and equal, aligned or anti-aligned spins. *Phys. Rev. D*, 88:064014.

[Hessels et al., 2006] Hessels, J. W. T., Ransom, S. M., Stairs, I. H., Freire, P. C. C., Kaspi, V. M., and Camilo, F. (2006). A radio pulsar spinning at 716-hz. *Science*, 311:1901–1904.

[Hilditch et al., 2013] Hilditch, D., Bernuzzi, S., Thierfelder, M., Cao, Z., Tichy, W., et al. (2013). Compact binary evolutions with the Z4c formulation. *Phys. Rev.*, D88:084057.

[Hinderer, 2008] Hinderer, T. (2008). Tidal Love numbers of neutron stars. *Astrophys.J.*, 677:1216–1220.

[Hinderer et al., 2010] Hinderer, T., Lackey, B. D., Lang, R. N., and Read, J. S. (2010). Tidal deformability of neutron stars with realistic equations of state and their gravitational wave signatures in binary inspiral. *Phys. Rev.*, D81:123016.

[Hotokezaka et al., 2013a] Hotokezaka, K., Kiuchi, K., Kyutoku, K., Muranushi, T., Sekiguchi, Y.-i., et al. (2013a). Remnant massive neutron stars of binary neutron star mergers: Evolution process and gravitational waveform. *Phys.Rev.*, D88(4):044026.

[Hotokezaka et al., 2013b] Hotokezaka, K., Kiuchi, K., Kyutoku, K., Okawa, H., Sekiguchi, Y.-i., Shibata, M., and Taniguchi, K. (2013b). The mass ejection from the merger of binary neutron stars. *Phys. Rev. D*, 87:024001.

[Hotokezaka et al., 2013c] Hotokezaka, K., Kyutoku, K., and Shibata, M. (2013c). Exploring tidal effects of coalescing binary neutron stars in numerical relativity. *Phys.Rev.*, D87(4):044001.

[Hulse and Taylor, 1975] Hulse, R. and Taylor, J. (1975). Discovery of a pulsar in a binary system. *Astrophys.J.*, 195:L51–L53.

[Husa et al., 2008] Husa, S., González, J. A., Hannam, M., Brügmann, B., and Sperhake, U. (2008). Reducing phase error in long numerical binary black hole evolutions with sixth order finite differencing. *Class. Quant. Grav.*, 25:105006.

[Jiang, 1996] Jiang, G. (1996). Efficient Implementation of Weighted ENO Schemes. *J. Comp. Phys.*, 126:202–228.

[Kaplan et al., 2014] Kaplan, J., Ott, C., O'Connor, E., Kiuchi, K., Roberts, L., et al. (2014). The Influence of Thermal Pressure on Equilibrium Models of Hypermassive Neutron Star Merger Remnants. *Astrophys.J.*, 790:19.

[Kastaun and Galeazzi, 2015] Kastaun, W. and Galeazzi, F. (2015). Properties of Hypermassive Neutron Stars Formed in Mergers of Spinning Binaries. *Phys. Rev. D*, 91(6):064027.

[Kastaun et al., 2013] Kastaun, W., Galeazzi, F., Alic, D., Rezzolla, L., and Font, J. A. (2013). On the black hole from merging binary neutron stars: how fast can it spin? *Phys. Rev. D*, 88:021501(R).

[Kawaguchi et al., 2015] Kawaguchi, K., Kyutoku, K., Nakano, H., Okawa, H., Shibata, M., and Taniguchi, K. (2015). Black hole-neutron star binary merger: Dependence on black hole spin orientation and equations of state. *Phys. Rev. D*, 92(2):024014.

[Kidder, 1995] Kidder, L. E. (1995). Coalescing binary systems of compact objects to post$^{5/2}$-Newtonian order. V. Spin effects. *Phys. Rev. D*, 52:821–847.

[Kidder et al., 2001] Kidder, L. E., Scheel, M. A., and Teukolsky, S. A. (2001). Extending the lifetime of 3D black hole computations with a new hyperbolic system of evolution equations. *Phys. Rev. D*, 64:064017.

[Kiuchi et al., 2014a] Kiuchi, K., Kyutoku, K., Sekiguchi, Y., Shibata, M., and Wada, T. (2014a). High resolution numerical-relativity simulations for the merger of binary magnetized neutron stars. *Phys. Rev. D*, 90(4):041502(R).

[Kiuchi et al., 2012] Kiuchi, K., Sekiguchi, Y., Kyutoku, K., and Shibata, M. (2012). Gravitational waves, neutrino emissions, and effects of hyperons in binary neutron star mergers. *Class.Quant.Grav.*, 29:124003.

[Kramer et al., 2006] Kramer, M., Stairs, I. H., Manchester, R., McLaughlin, M., Lyne, A., et al. (2006). Tests of general relativity from timing the double pulsar. *Science*, 314:97–102.

[Kyutoku et al., 2015] Kyutoku, K., Ioka, K., Okawa, H., Shibata, M., and Taniguchi, K. (2015). Dynamical mass ejection from black hole-neutron star binaries. *Phys. Rev. D*, 92(4):044028.

[Lages, 2010] Lages, N. (2010). *Apparent Horizons and Marginally Trapped Surfaces in Numerical General Relativity*. PhD thesis, University of Jena.

[Lattimer and Prakash, 2001] Lattimer, J. and Prakash, M. (2001). Neutron star structure and the equation of state. *Astrophys.J.*, 550:426.

[Lattimer and Schramm, 1974] Lattimer, J. M. and Schramm, D. N. (1974). Black-hole-neutron-star collisions. *apjl*, 192:L145–L147.

[Levi and Steinhoff, 2014] Levi, M. and Steinhoff, J. (2014). Equivalence of ADM Hamiltonian and Effective Field Theory approaches at next-to-next-to-leading order spin1-spin2 coupling of binary inspirals. *J. Cosmol. Astropart. Phys.*, 1412(12):003.

[Li and Paczynski, 1998] Li, L.-X. and Paczynski, B. (1998). Transient events from neutron star mergers. *Astrophys.J.*, 507:L59.

[Liu et al., 2008] Liu, Y. T., Shapiro, S. L., Etienne, Z. B., and Taniguchi, K. (2008). General relativistic simulations of magnetized binary neutron star mergers. *Phys. Rev. D*, 78:024012.

[Lousto and Price, 1997] Lousto, C. O. and Price, R. H. (1997). Headon collisions of black holes: The Particle limit. *Phys.Rev.*, D55:2124–2138.

[Lovelace et al., 2011] Lovelace, G., Scheel, M. A., and Szilágyi, B. (2011). Simulating merging binary black holes with nearly extremal spins. *Phys. Rev. D*, 83:024010.

[Lyne et al., 2004] Lyne, A., Burgay, M., Kramer, M., Possenti, A., Manchester, R., et al. (2004). A Double - pulsar system - A Rare laboratory for relativistic gravity and plasma physics. *Science*, 303:1153–1157.

[MacDonald et al., 2013] MacDonald, I., Mroue, A. H., Pfeiffer, H. P., Boyle, M., Kidder, L. E., et al. (2013). Suitability of hybrid gravitational waveforms for unequal-mass binaries. *Phys.Rev.*, D87(2):024009.

[Metzger and Berger, 2012] Metzger, B. and Berger, E. (2012). What is the Most Promising Electromagnetic Counterpart of a Neutron Star Binary Merger? *Astrophys.J.*, 746:48.

[Metzger et al., 2010] Metzger, B., Martinez-Pinedo, G., Darbha, S., Quataert, E., Arcones, A., et al. (2010). Electromagnetic Counterparts of Compact Object Mergers Powered by the Radioactive Decay of R-process Nuclei. *Mon.Not.Roy.Astron.Soc.*, 406:2650.

[Mignone et al., 2010] Mignone, A., Tzeferacos, P., and Bodo, G. (2010). High-order conservative finite difference GLM-MHD schemes for cell-centered MHD. *J.Comput.Phys.*, 229:5896–5920.

[Misner et al., 1973] Misner, C. W., Thorne, K. S., and Wheeler, J. A. (1973). *Gravitation*. W. H. Freeman, New York.

[Moldenhauer et al., 2014] Moldenhauer, N., Markakis, C. M., Johnson-McDaniel, N. K., Tichy, W., and Brügmann, B. (2014). Initial data for binary neutron stars with adjustable eccentricity. *Phys. Rev. D*, 90(8):084043.

[Mroue et al., 2013] Mroue, A. H., Scheel, M. A., Szilagyi, B., Pfeiffer, H. P., Boyle, M., et al. (2013). A catalog of 174 binary black-hole simulations for gravitational-wave astronomy. *Phys.Rev.Lett.*, 111:241104.

[Müller and Serot, 1996] Müller, H. and Serot, B. D. (1996). Relativistic mean field theory and the high density nuclear equation of state. *Nucl. Phys.*, A606:508–537.

[Nagar, 2011] Nagar, A. (2011). Effective one body Hamiltonian of two spinning black-holes with next-to-next-to-leading order spin-orbit coupling. *Phys.Rev.*, D84:084028.

[Nakamura et al., 1987] Nakamura, T., Oohara, K., and Kojima, Y. (1987). General relativistic collapse to black holes and gravitational waves from black holes. *Prog. Theor. Phys. Suppl.*, 90:1–218.

[Neilsen et al., 2014] Neilsen, D., Liebling, S. L., Anderson, M., Lehner, L., O'Connor, E., et al. (2014). Magnetized Neutron Stars With Realistic Equations of State and Neutrino Cooling. *Phys.Rev.*, D89(10):104029.

[Newman and Penrose, 1962] Newman, E. T. and Penrose, R. (1962). An approach to gravitational radiation by a method of spin coefficients. *J. Math. Phys.*, 3(3):566–578. erratum in J. Math. Phys. 4, 998 (1963).

[Nozawa et al., 1998] Nozawa, T., Stergioulas, N., Gourgoulhon, E., and Eriguchi, Y. (1998). Construction of highly accurate models of rotating neutron stars - comparison of three different numerical schemes. *Astron. Astrophys. Suppl. Ser.*, 132:431.

[Oechslin and Janka, 2007] Oechslin, R. and Janka, H. T. (2007). Gravitational waves from relativistic neutron star mergers with nonzero-temperature equations of state. *Phys. Rev. Lett.*, 99:121102.

[Oppenheimer and Volkoff, 1939] Oppenheimer, J. R. and Volkoff, G. (1939). On massive neutron cores. *Phys. Rev.*, 55:374.

[Ossokine et al., 2015] Ossokine, S., Boyle, M., Kidder, L. E., Pfeiffer, H. P., Scheel, M. A., and Szilágyi, B. (2015). Comparing Post-Newtonian and Numerical-Relativity Precession Dynamics.

[Ott et al., 2011] Ott, C., Reisswig, C., Schnetter, E., O'Connor, E., Sperhake, U., et al. (2011). Dynamics and Gravitational Wave Signature of Collapsar Formation. *Phys.Rev.Lett.*, 106:161103.

[Ott et al., 2013] Ott, C. D., Abdikamalov, E., Mösta, P., Haas, R., Drasco, S., et al. (2013). General-Relativistic Simulations of Three-Dimensional Core-Collapse Supernovae. *Astrophys.J.*, 768:115.

[Paczynski, 1986] Paczynski, B. (1986). Gamma-ray bursters at cosmological distances. *Astrophys. J.*, 308:L43–L46.

[Palenzuela et al., 2015] Palenzuela, C., Liebling, S. L., Neilsen, D., Lehner, L., Caballero, O. L., O'Connor, E., and Anderson, M. (2015). Effects of the microphysical Equation of State in the mergers of magnetized Neutron Stars With Neutrino Cooling. *Phys. Rev. D*, 92(4):044045.

[Pan et al., 2014] Pan, Y., Buonanno, A., Taracchini, A., Kidder, L. E., Mroue, A. H., et al. (2014). Inspiral-merger-ringdown waveforms of spinning, precessing black-hole binaries in the effective-one-body formalism. *Phys.Rev.*, D89:084006.

[Paschalidis et al., 2012] Paschalidis, V., Etienne, Z. B., and Shapiro, S. L. (2012). Importance of cooling in triggering the collapse of hypermassive neutron stars. *Phys.Rev.*, D86:064032.

[Perego et al., 2014] Perego, A., Rosswog, S., Cabezon, R., Korobkin, O., Kaeppeli, R., et al. (2014). Neutrino-driven winds from neutron star merger remnants. *Mon.Not.Roy.Astron.Soc.*, 443:3134.

[Pollney et al., 2011] Pollney, D., Reisswig, C., Schnetter, E., Dorband, N., and Diener, P. (2011). High accuracy binary black hole simulations with an extended wave zone. *Phys. Rev.*, D83:044045.

[Punturo et al., 2010a] Punturo, M. et al. (2010a). The Einstein Telescope: A third-generation gravitational wave observatory. *Class. Quant. Grav.*, 27:194002.

[Punturo et al., 2010b] Punturo, M. et al. (2010b). The third generation of gravitational wave observatories and their science reach. *Class. Quant. Grav.*, 27:084007.

[Radice and Rezzolla, 2011] Radice, D. and Rezzolla, L. (2011). Discontinuous Galerkin methods for general-relativistic hydrodynamics: formulation and application to spherically symmetric spacetimes. *Phys.Rev.*, D84:024010.

[Radice et al., 2014a] Radice, D., Rezzolla, L., and Galeazzi, F. (2014a). Beyond second-order convergence in simulations of binary neutron stars in full general-relativity. *Mon.Not.Roy.Astron.Soc.*, 437:L46–L50.

[Radice et al., 2014b] Radice, D., Rezzolla, L., and Galeazzi, F. (2014b). High-Order Fully General-Relativistic Hydrodynamics: new Approaches and Tests. *Class.Quant.Grav.*, 31:075012.

[Radice et al., 2015] Radice, D., Rezzolla, L., and Galeazzi, F. (2015). High-Order Numerical-Relativity Simulations of Binary Neutron Stars.

[Read et al., 2013] Read, J. S., Baiotti, L., Creighton, J. D. E., Friedman, J. L., Giacomazzo, B., et al. (2013). Matter effects on binary neutron star waveforms. *Phys.Rev.*, D88:044042.

[Read et al., 2009a] Read, J. S., Lackey, B. D., Owen, B. J., and Friedman, J. L. (2009a). Constraints on a phenomenologically parameterized neutron- star equation of state. *Phys. Rev.*, D79:124032.

[Read et al., 2009b] Read, J. S., Markakis, C., Shibata, M., Uryu, K., Creighton, J. D., et al. (2009b). Measuring the neutron star equation of state with gravitational wave observations. *Phys.Rev.*, D79:124033.

[Reimann, 2004] Reimann, B. (2004). Slice stretching at the event horizon when geodesically slicing the Schwarzschild spacetime with excision. *Class. Quantum Grav.*, 21:4297–4304.

[Reimann, 2005] Reimann, B. (2005). How slice stretching arises when maximally slicing the Schwarzschild spacetime with vanishing shift. *Class. Quantum Grav.*, 22:4563–4587.

[Reisswig et al., 2013a] Reisswig, C., Haas, R., Ott, C., Abdikamalov, E., Mösta, P., et al. (2013a). Three-Dimensional General-Relativistic Hydrodynamic Simulations of Binary Neutron Star Coalescence and Stellar Collapse with Multipatch Grids. *Phys.Rev.*, D87:064023.

[Reisswig et al., 2013b] Reisswig, C., Ott, C., Abdikamalov, E., Haas, R., Moesta, P., et al. (2013b). Formation and Coalescence of Cosmological Supermassive Black Hole Binaries in Supermassive Star Collapse. *Phys.Rev.Lett.*, 111:151101.

[Reisswig and Pollney, 2011] Reisswig, C. and Pollney, D. (2011). Notes on the integration of numerical relativity waveforms. *Class.Quant.Grav.*, 28:195015.

[Rezzolla and Zanotti, 2013] Rezzolla, L. and Zanotti, O. (2013). *Relativistic hydrodynamics*. Oxford University Press.

[Ronchi et al., 1996] Ronchi, C., Iacono, R., and Paolucci, P. (1996). The cubed sphere: A new method for the solution of partial differential equations in spherical geometry. *Journal of Computational Physics*, 124(1):93 – 114.

[Rosswog, 2015] Rosswog, S. (2015). The multi-messenger picture of compact binary mergers. *Int.J.Mod.Phys.*, D24(05):1530012.

[Rosswog et al., 1999] Rosswog, S., Liebendoerfer, M., Thielemann, F., Davies, M., Benz, W., et al. (1999). Mass ejection in neutron star mergers. *Astron.Astrophys.*, 341:499–526.

[Ruiz et al., 2011] Ruiz, M., Hilditch, D., and Bernuzzi, S. (2011). Constraint preserving boundary conditions for the Z4c formulation of general relativity. *Phys. Rev.*, D83:024025.

[Scheel et al., 2015] Scheel, M. A., Giesler, M., Hemberger, D. A., Lovelace, G., Kuper, K., Boyle, M., Szilágyi, B., and Kidder, L. E. (2015). Improved methods for simulating nearly extremal binary black holes. *Classical Quantum Gravity*, 32(10):105009.

[Schutz, 1985] Schutz, B. F. (1985). *A first course in general relativity*. Cambridge University Press.

[Seidel, 1990] Seidel, E. (1990). Gravitational radiation from even parity perturbations of stellar collapse: Mathematical formalism and numerical methods. *Phys. Rev.*, D42:1884–1907.

[Seidel and Moore, 1987] Seidel, E. and Moore, T. (1987). Gravitational Radiation From Realistic Relativistic Stars: Odd Parity Fluid Perturbations. *Phys.Rev.*, D35:2287–2296.

[Seidel et al., 1988] Seidel, E., Myra, E., and Moore, T. (1988). Gravitational Radiation From Type II Supernovae: The Effect of the High Density Equation of State. *Phys.Rev.*, D38:2349–2356.

[Sekiguchi et al., 2011a] Sekiguchi, Y., Kiuchi, K., Kyutoku, K., and Shibata, M. (2011a). Effects of hyperons in binary neutron star mergers. *Phys. Rev. Lett.*, 107:211101.

[Sekiguchi et al., 2011b] Sekiguchi, Y., Kiuchi, K., Kyutoku, K., and Shibata, M. (2011b). Gravitational waves and neutrino emission from the merger of binary neutron stars. *Phys. Rev. Lett.*, 107:051102.

[Sekiguchi et al., 2015] Sekiguchi, Y., Kiuchi, K., Kyutoku, K., and Shibata, M. (2015). Dynamical mass ejection from binary neutron star mergers: Radiation-hydrodynamics study in general relativity. *Phys.Rev.*, D91(6):064059.

[Shibata, 2003] Shibata, M. (2003). Axisymmetric general relativistic hydrodynamics: Long-term evolution of neutron stars and stellar collapse to neutron stars and black holes. *Phys. Rev.*, D67:024033.

[Shibata et al., 2000] Shibata, M., Baumgarte, T. W., and Shapiro, S. L. (2000). Stability and collapse of rapidly rotating, supramassive neutron stars: 3-D simulations in general relativity. *Phys.Rev.*, D61:044012.

[Shibata et al., 2006] Shibata, M., Duez, M. D., Liu, Y. T., Shapiro, S. L., and Stephens, B. C. (2006). Magnetized hypermassive neutron star collapse: a central engine for short gamma-ray bursts. *Phys. Rev. Lett.*, 96:031102.

[Shibata and Nakamura, 1995] Shibata, M. and Nakamura, T. (1995). Evolution of three-dimensional gravitational waves: Harmonic slicing case. *Phys. Rev.*, D52:5428.

[Shibata et al., 2011] Shibata, M., Suwa, Y., Kiuchi, K., and Ioka, K. (2011). Afterglow of binary neutron star merger. *Astrophys.J.*, 734:L36.

[Shibata and Taniguchi, 2006] Shibata, M. and Taniguchi, K. (2006). Merger of binary neutron stars to a black hole: disk mass, short gamma-ray bursts, and quasinormal mode ringing. *Phys.Rev.*, D73:064027.

[Shibata et al., 2005] Shibata, M., Taniguchi, K., and Uryū, K. (2005a). Merger of binary neutron stars with realistic equations of state in full general relativity. *Phys. Rev. D*, 71:084021.

[Shibata and Uryu, 2000] Shibata, M. and Uryu, K. (2000). Simulation of merging binary neutron stars in full general relativity: $\Gamma = 2$ case. *Phys. Rev.*, D61:064001.

[Shu and Osher, 1989] Shu, C. and Osher, S. (1989). Efficient implementation of essentially non-oscillatory shock-capturing schemes, ii. *J. Comput. Phys.*, 83:32–78.

[Sopuerta and Laguna, 2006] Sopuerta, C. F. and Laguna, P. (2006). A Finite element computation of the gravitational radiation emitted by a point-like object orbiting a non-rotating black hole. *Phys. Rev.*, D73:044028.

[Sopuerta et al., 2006] Sopuerta, C. F., Sun, P., Laguna, P., and Xu, J. (2006). A Toy model for testing finite element methods to simulate extreme-mass-ratio binary systems. *Class. Quant. Grav.*, 23:251–286.

[Staley et al., 2012] Staley, A., Baumgarte, T., Brown, J., Farris, B., and Shapiro, S. (2012). Oppenheimer-Snyder Collapse in Moving-Puncture Coordinates. *Class.Quant.Grav.*, 29:015003.

[Stark and Piran, 1985] Stark, R. and Piran, T. (1985). GRAVITATIONAL WAVE EMISSION FROM ROTATING GRAVITATIONAL COLLAPSE. *Phys.Rev.Lett.*, 55:891–894.

[Stephens et al., 2007] Stephens, B. C., Duez, M. D., Liu, Y. T., Shapiro, S. L., and Shibata, M. (2007). Collapse and black hole formation in magnetized, differentially rotating neutron stars. *Class.Quant.Grav.*, 24:S207–S220.

[Stephens et al., 2011] Stephens, B. C., East, W. E., and Pretorius, F. (2011). Eccentric Black Hole-Neutron Star Mergers. *Astrophys.J.*, 737:L5.

[Stephens et al., 2008] Stephens, B. C., Shapiro, S. L., and Liu, Y. T. (2008). Collapse of magnetized hypermassive neutron stars in general relativity: Disk evolution and outflows. *Phys. Rev.*, D77:044001.

[Stergioulas et al., 2011] Stergioulas, N., Bauswein, A., Zagkouris, K., and Janka, H.-T. (2011). Gravitational waves and nonaxisymmetric oscillation modes in mergers of compact object binaries. *Mon. Not. R. Astron. Soc.*, 418:427.

[Stergioulas and Friedman, 1995] Stergioulas, N. and Friedman, J. L. (1995). Comparing models of rapidly rotating relativistic stars constructed by two numerical methods. *Astrophys. J.*, 444:306.

[Suresh, 1997] Suresh, A. (1997). Accurate Monotonicity-Preserving Schemes with Runge Kutta Time Stepping. *J. Comp. Phys.*, 136:83–99.

[Tacik et al., 2015] Tacik, N., Foucart, F., Pfeiffer, H. P., Haas, R., Ossokine, S., Kaplan, J., et al. (2015). Binary Neutron Stars with Arbitrary Spins in Numerical Relativity.

[Takami et al., 2014] Takami, K., Rezzolla, L., and Baiotti, L. (2014). Constraining the Equation of State of Neutron Stars from Binary Mergers. *Phys.Rev.Lett.*, 113:091104.

[Takami et al., 2015a] Takami, K., Rezzolla, L., and Baiotti, L. (2015a). Constraining the Equation of State of Neutron Stars from Binary Mergers. *J. Phys. Conf. Ser.*, 600(1):012056.

[Takami et al., 2015b] Takami, K., Rezzolla, L., and Baiotti, L. (2015b). Spectral properties of the post-merger gravitational-wave signal from binary neutron stars. *Phys.Rev.*, D91(6):064001.

[Taniguchi and Shibata, 2010] Taniguchi, K. and Shibata, M. (2010). Binary Neutron Stars in Quasi-equilibrium. *Astrophysical Journal Supplement Seri*, SERIES:187.

[Tanvir et al., 2013] Tanvir, N., Levan, A., Fruchter, A., Hjorth, J., Wiersema, K., et al. (2013). A "kilonova" associated with short-duration gamma-ray burst 130603B. *Nature*, 500:547.

[Thierfelder, 2011] Thierfelder, M. (2011). *Numerical Simulations of Neutron Stars in General Relativistic Hydrodynamics*. PhD thesis, University of Jena.

[Thierfelder et al., 2011a] Thierfelder, M., Bernuzzi, S., and Brügmann, B. (2011a). Numerical relativity simulations of binary neutron stars. *Phys.Rev.*, D84:044012.

[Thierfelder et al., 2011b] Thierfelder, M., Bernuzzi, S., Hilditch, D., Brügmann, B., and Rezzolla, L. (2011b). The trumpet solution from spherical gravitational collapse with puncture gauges. *Phys.Rev.*, D83:064022.

[Thornburg, 2004] Thornburg, J. (2004). Black hole excision with multiple grid patches. *Class.Quant.Grav.*, 21:3665–3692.

[Thornburg, 2006] Thornburg, J. (2006). Event and apparent horizon finders for $3 + 1$ numerical relativity. *Living Rev. Relativity*. [Online article].

[Tichy, 2006] Tichy, W. (2006). Black hole evolution with the BSSN system by pseudo-spectral methods. *Phys. Rev. D*, 74:084005.

[Tichy, 2009] Tichy, W. (2009). A new numerical method to construct binary neutron star initial data. *Classical Quantum Gravity*, 26:175018.

[Tichy, 2011] Tichy, W. (2011). Initial data for binary neutron stars with arbitrary spins. *Phys.Rev.*, D84:024041.

[Tichy, 2012] Tichy, W. (2012). Constructing quasi-equilibrium initial data for binary neutron stars with arbitrary spins. *Phys. Rev. D*, 86:064024.

[Tolman, 1939] Tolman, R. C. (1939). Static Solutions of Einstein's Field Equations for Spheres of Fluid. *Phys. Rev.*, 55:364–373.

[Tsatsin and Marronetti, 2013] Tsatsin, P. and Marronetti, P. (2013). Initial data for neutron star binaries with arbitrary spins. *Phys.Rev.*, D88:064060.

[Tsokaros et al., 2015] Tsokaros, A., Uryū, K., and Rezzolla, L. (2015). A new code for quasi-equilibrium initial data of binary neutron stars: corotating, irrotational and slowly spinning systems. *Phys. Rev. D*, 91(10):104030.

[Uryu et al., 2009] Uryu, K., Limousin, F., Friedman, J. L., Gourgoulhon, E., and Shibata, M. (2009). Non-conformally flat initial data for binary compact objects. *Phys. Rev.*, D80:124004.

[van Meter et al., 2006] van Meter, J. R., Baker, J. G., Koppitz, M., and Choi, D.-I. (2006). How to move a black hole without excision: gauge conditions for the numerical evolution of a moving puncture. *Phys. Rev. D*, 73:124011.

[Vines and Flanagan, 2010] Vines, J. E. and Flanagan, E. E. (2010). Post-1-Newtonian quadrupole tidal interactions in binary systems. *Phys. Rev.*, D88:024046.

[Vishveshwara, 1970] Vishveshwara, C. V. (1970). Scattering of Gravitational Radiation by a Schwarzschild Black-hole. *Nature*, 227:936–938.

[Wald, 1984] Wald, R. M. (1984). *General relativity*. The University of Chicago Press, Chicago.

[Waxman, 2004] Waxman, E. (2004). Extra-galactic sources of high-energy neutrinos. *New J.Phys.*, 6:140.

[Weisberg et al., 2010] Weisberg, J., Nice, D., and Taylor, J. (2010). Timing Measurements of the Relativistic Binary Pulsar PSR B1913+16. *Astrophys.J.*, 722:1030–1034.

[Wheeler, 1964] Wheeler, J. (1964). Geometrodynamics and the issue of the final state. In DeWitt, C. and DeWitt, B., editors, *Relativity, Groups, and Topology (Les Houches, France, 1964)*, pages 316–520. Gordon and Breach, New York.

[Yamamoto et al., 2008] Yamamoto, T., Shibata, M., and Taniguchi, K. (2008). Simulating coalescing compact binaries by a new code SACRA. *Phys. Rev.*, D78:064054.

[Yang et al., 2015] Yang, B., Jin, Z.-P., Li, X., Covino, S., Zheng, X.-Z., et al. (2015). A possible Macronova in the late afterglow of the 'long-short' burst GRB 060614.

[York, 1979] York, Jr., J. W. (1979). Kinematics and dynamics of general relativity. In Smarr, L., editor, *Sources of Gravitational Radiation*, pages 83–126, Cambridge. Cambridge University Press.

[Zink et al., 2012] Zink, B., Lasky, P. D., and Kokkotas, K. D. (2012). Are gravitational waves from giant magnetar flares observable? *Phys.Rev.*, D85:024030.

Publications

Letter

[Die1] S. Bernuzzi, A. Nagar, S. Balmelli, T. Dietrich, M. Ujevic, *Quasi-universal properties of neutron star mergers*, Phys.Rev.Lett.112 (2014) 201101, arXiv: 1402.6244 [gr-qc].

[Die2] S. Bernuzzi, A. Nagar, T. Dietrich, T. Damour, *Modeling the dynamics of tidally-interacting binary neutron stars up to merger*, Phys.Rev.Lett.114 (2015) 161103, arXiv: 1412.4553 [gr-qc].

[Die3] S. Bernuzzi, T. Dietrich, A. Nagar (2015), *Towards a description of the complete gravitational wave spectrum of neutron star mergers*, Phys.Rev.Lett.115 (2015) 091101, arXiv: 1504.01764 [gr-qc].

Regular Articles

[Die4] T. Dietrich, B. Brügmann, *Solving the Hamiltonian constraint for 1+log trumpets*, Phys.Rev.D.89 (2014) 024014, arXiv:1309.3087 [gr-qc].

[Die5] D. Hilditch, T. W. Baumgarte, A. Weyhausen, T. Dietrich, B. Brügmann, P. J. Montero, E. Müller, *Collapse of Nonlinear Gravitational Waves in Moving-Puncture Coordinates*, Phys.Rev.D.88 (2013) 103009, arXiv: 1309.5008 [gr-qc].

[Die6] S. Bernuzzi, T. Dietrich, W. Tichy, B. Brügmann, *Mergers of binary netron stars with realistic spin*, Phys.Rev.D.89 (2014) 104021, arXiv:1311.4443 [gr-qc].

[Die7] T. Dietrich, S. Bernuzzi (2014), *Simulations of rotating neutron star collapse with the puncture gauge: end state and gravitational waveforms*, Phys.Rev.D.91 (2015) 044039, arXiv: 1412.5499 [gr-qc].

[Die8] T. Dietrich, S. Bernuzzi, M. Ujevic, B. Brügmann (2015), *Numerical relativity simulations of neutron star merger remnants using conservative mesh refinement*, Phys.Rev.D.91 (2015) 124041, arXiv: 1504.01266 [gr-qc].

Proceeding with peer-review

[Die9] T. Dietrich, B. Brügmann, *Spinning black hole in the puncture method: Numerical experiments*, (2014) J. Phys.: Conf. Ser. 490 012155, arXiv: 1403.5746 [gr-qc].

[Die10] S. Bernuzzi, A. Nagar, S. Balmelli, T. Dietrich, M. Ujevic, *Tidal polarizability effects in neutron star mergers*, (2015) J. Phys.: Conf. Ser. 610 012047.

Proceeding without peer-review

[Die11] N. K. Johnson-McDaniel, S. Bernuzzi, T. Dietrich, D. Hilditch, M. Thierfelder, and B. Brügmann, *Dynamics of binary neutron star mergers*, in K. Binder, G. Münster, M. Kremer (Eds.), NIC Symposium 2014, ISBN: 978-3-89336-933-1.

[Die12] B. Brügmann, S. Bernuzzi, T. Dietrich, D. Hilditch, N. K. Johnson-McDaniel, N. Moldenhauer, M. Ujevic, and A. Weyhausen, *Dynamics of binary neutron star systems*, in S. Wagner, A. Bode, H. Satzger, M. Brehm (Eds.), High Performance Computing in Science and Engineering Garching/Munich 2014, ISBN: 978-3-9816675-0-9.

Preprints

[Die13] T. Dietrich, N. Moldenhauer, N. K. Johnson-McDaniel, C. Markakis, S. Bernuzzi, B. Brügmann, W. Tichy (2015), *Binary Neutron Stars with generic Spin, Eccentricity, Mass ratio and Compactness - Quasi-equilibrium sequences and first evolutions*, arXiv: 1507.07100 [gr-qc].

[Die14] M. Bugner, T. Dietrich, S. Bernuzzi, A. Weyhausen, B. Brügmann (2015), *Solving 3D relativistic hydrodynamical problems with WENO Discontinuous-Galerkin methods*, arXiv: 1508.07147 [gr-qc].

In Preparation

[Die15] S. Bernuzzi, T. Dietrich, B. Brügmann (2015), *Exploring high-order WENO schemes in general relativistic hydrodynamics simulations of neutron star inspirals.*

Acknowledgement

I am grateful to Prof. Bernd Brügmann, who gave me the opportunity to write my thesis in his group and supported me during the last years. I am happy that he involved me into several projects not strongly related to the topic of my thesis. This allowed me to increase my knowledge, to get a better understanding of numerical relativity, and to establish new contacts.

I also want to thank in particular Dr. Sebastiano Bernuzzi for coming to my window and asking whether I want to join the group effort studying binary neutron star mergers. In this way he saved me working alone on mixed binaries and initiated a productive, friendly, and focused collaboration. In fact, I will miss Skype meetings during night and a full mailbox when waking up.

Of course I am also thankful to a large number of others, e.g., Marcus Bugner, who is the best table tennis partner I can imagine, Martin Fruhnert, who accompanied me during most of my Bachelor/Master/PhD studies and was my lucky charm during exams, Enno Harms, who deserves his title “green chancellor”, Dr. David Hilditch, for valuable discussions and his abundance of patience explaining mathematical concepts, Dr. Nathan-Kieran Johnson-McDaniel, who was the most careful proof reader I ever met, Dr. Georgios Lukes- Gerakopoulos, who gave me advice well beyond topics related to Numerical Relativity, Niclas Moldenhauer, who helped me surviving the University Village Apartments, Dr. Alessandro Nagar, who gave me at a lunch table in Paris the best introduction to the EOB model I have ever heard, Robert Röder, who joined me for a run far too rarely but always had a friendly ear, Prof. Maximiliano Ujevic Tonino, who introduced me to Rumpel and answered the question “what does the fox say”, Prof. Wolfgang Tichy, who answered always smiling SGRID and BAM related questions, Dr. Andreas Weyhausen, for not being too angry when I introduced the bamps_bam_matter.h header file.

I also thank Enno, Max, David, Matthias, Niclas, Martin, Matthias, Robert, Nathan for correcting an endless number of typos in this thesis.

Without the help, support, and love of my family and my partner Nadine, my studies would not have been possible. They deserve my grateful recognition and mean everything for me!

Additional Material

Presentations

- 16.10.2012 - (Garching) SFB/TR7 semiannual meeting: *1+log puncture data*
- 27.02.2013 - (Jena) DPG-Spring Meeting: *1+log-Trumpet Initial Data in Numerical Relativity*
- 12.07.2013 - (Warsaw) GR20/Amaldi 10: *Black Hole Spin within the moving puncture method*
- 04.09.2013 - (Prague) International Conference on Mathematical Modeling in Physical Sciences: *Spinning black hole in the puncture method*
- 20.01.2014 - (Jena) SFB/TR7-Videoseminar: *Can spin be ignored in binary neutron star mergers?*
- 27.02.2014 - (Tübingen) SFB/TR7 semiannual meeting: *Mergers of binary neutron stars with realistic spin*
- 20.03.2014 - (Berlin) DPG-Spring Meeting: *Mergers of binary neutron stars with realistic spin*
- 28.10.2014 - (Frankfurt) Astro Coffee **(invited)**: *Realistic spins and quasiuniversal relations in binary neutron star mergers*
- 05.12.2014 - (Jena) Conclusion Workshop of SFB/TR7: Gravitational Wave Astronomy: *Quasiuniversal properties of binary neutron star mergers*
- 19.01.2015 - (Potsdam) Albert-Einstein-Institut **(invited)**: *Recent progress in numerical relativity simulations of neutron star spacetimes*
- 19.03.2015 - (Berlin) DPG-Spring Meeting: *Dynamical simulations of neutron star spacetimes with conservative mesh refinement*

Research Visits

- May 2014 - Florida Atlantic University - Boca Raton, US (Florida)
- March 2015 - Institut des Hautes Études Scientifiques - Bures-sur-Yvette, France
- July 2015 - California Institute of Technology - Pasadena, US (California)

Curriculum Vitae

Personal details

Name	Tim
Surname	Dietrich
Address	Karl-Schwarzschild-Weg 1 37077 Göttingen Germany
Email	diet.tim@gmail.com
Telephone	+49/1777084084
Birth date	23th of April 1988
Nationality	German

Education

2007	High school diploma (1.0) Gymnasium Philanthropinum Dessau
2010	Bachelor of Science in Physics (1.0) Martin-Luther-University Halle-Wittenberg
2012	Master of Science in Physics (1.0) Friedrich-Schiller-University Jena
2012-2015	PhD student at the Friedrich-Schiller-University Jena

Professional Experience

2008-2010	Student assistant at the Martin-Luther-University Halle-Wittenberg
2010	Student assistant at the Interdisciplinary Center of Materials Science in Halle (Saale)
2011-2014	Research assistant for the SFB/TR-7 “Gravitational Wave Astronomy”
2015	Research assistant at the Friedrich-Schiller-University Jena
2015 -	Junior Scientist at the Max Planck Institute for Gravitational Physics Potsdam

Prizes and Scholarships

2009-2012	Scholarship of the German National Academic Foundation
2010	Gustav-Mie-Bachelor-Preis
2013-2015	Scholarship of the Landesgraduiertenstipendium Thuringia

Jena, 01.03.2016

Unterschrift

Teaching

Semester	Course	Lecturer
WS 2012/2013	Mathematische Methoden III	Prof. K. H. Lotze
SS 2013	Elektrodynamik (für Lehramt)	Prof. K. H. Lotze

Zusammenfassung

Die Verschmelzung zweier Neutronensterne ist mit einer Vielzahl von beobachtbaren Ereignissen im elektromagnetischen und Gravitationswellen-Spektrum verbunden. Während der letzten Millisekunden vor dem Zusammenstoß wird eine große Menge der Energie des Systems in Form von Gravitationswellen abgegeben. Diese Wellen können voraussichtlich in den kommenden Jahren mit dem LIGO und VIRGO-Interferometer gemessen werden. Doch obwohl bis zu 10% an Energie in Form von Gravitationswellen vom System abgegeben werden kann, sind die auf der Erde eintreffenden Signale schwach. Eine genaue theoretische Beschreibung ist nötig, um das Signal aus dem Rauschen des Interferometers herauszufiltern.

Sofern die beiden Neutronensterne noch eine ausreichend große Distanz haben und sich nicht zu schnell umeinander bewegen, existieren analytische Methoden, wie das Post-Newton Verfahren, um die Bewegung und das ausgesendete Gravitationswellensignal zu berechnen. Kurz vor dem Zusammenstoß und in der direkten Phase danach versagen diese Methoden jedoch. Nur numerische Verfahren können das System in diesem Zeitabschnitt hinreichend genau beschreiben. Dabei ist es nötig, die Einsteinschen Feldgleichungen zusammen mit den Gleichungen der allgemein-relativistischen Hydrodynamik zu lösen, was aufgrund des enormen Rechenaufwandes bisher nur auf Großrechnern möglich ist. Die vorgelegte Dissertationsarbeit beschäftigt sich genau mit diesem Problem und untersucht binäre Neutronensternsysteme mit Hilfe numerischer Simulationen.

Zu Beginn wurde der Kollaps eines einzelnen, rotierenden Neutronensternes untersucht. Ein solches System kann durch den Zusammenstoß zweier Neutronensterne oder eine Supernovaexplosion entstehen und ist von entscheidender astrophysikalischer Bedeutung. Durch verbesserte numerische Verfahren, vor allem ein zusätzlicher Korrekturschritt im adaptiven Gitterverfahren, war es möglich, den zentralen Bereich des Neutronensternes mit einer Gitterweite von ~ 6 m aufzulösen. Durch diese hohe Genauigkeit, welche alle bisherigen Simulationen übertrifft, konnte gezeigt werden, dass die Struktur des ausgesendeten Gravitationswellensignales simpel ist und nur aus einem “Precursor-Burst-Ringdown” besteht. Das bedeutet es hat die gleiche Struktur wie ein Gravitationswellensignal, das durch ein einzelnes in ein schwarzes Loch fallendes Teilchen erzeugt wird. Zudem konnte durch eine lokale Analyse der Raumzeit gezeigt werden, dass die Raumzeit nach dem Kollaps des Neutronensternes mit der Raumzeit eines einzelnen, rotierenden schwarzen Loches, welches mit den gleichen Eichbedingungen evolviert wurde, übereinstimmt.

Im Rahmen der Promotion war es auch möglich, die ersten konsistenten Neutronensternsimulationen unter Erfüllung der Zwangsbedingungen durchzuführen, bei

denen die einzelnen Neutronensterne einen Eigendrehimpuls besitzen. Dabei wurde die “Constant rotational velocity” Methode von W. Tichy verwendet. Es wurde deutlich, dass auch ein geringer und astrophysikalisch realistischer Spin Auswirkungen auf die Dynamik und das emittierte Gravitationswellensignal hat. Es konnte gezeigt werden, dass die Spin-Orbit Wechselwirkung bis zum Kontakt der Neutronensterne stärkeren Einfluss auf die Bindungsenergie als die Tidenkräfte hat, welche durch die Ausdehnung und Verformung der Neutronensterne entstehen. Zudem ist auch der aus der Verschmelzung der beiden Sterne entstandene hypermassive Neutronenstern stark durch den anfänglichen Spin beeinflusst. Während Konfigurationen mit Spin parallel zum orbitalen Drehimpuls zu einer längeren Lebensdauer des hypermassiven Neutronensternes führen, ist der gegenteilige Effekt für Systeme mit antiparallelem Spin zu beobachten. Auch die Frequenz der durch den hypermassiven Neutronenstern emittierten Gravitationswelle ist abhängig von seinem Drehimpuls. So ist die Frequenz höher (niedriger), wenn der Eigendrehimpuls der Vorgängersterne parallel (antiparallel) zum Orbitdrehimpuls war.

Weiterhin wurden Simulationes mit verschiedenen Zustandsgleichungen und Massenverhältnissen durchgeführt. Eine wesentliche Aufgabe zukünftiger Gravitationswellenastronomie ist es, die Zustandsgleichung von Materie bei supranuklearer Dichte zu bestimmen. Da solche Dichten nicht in Laboratorien erzeugt werden können, aber Neutronensterne eine solch hohe Dichte aufweisen, sind sie von besonderem Interesse. Durch verschiedene Simulationen konnte gezeigt werden, dass die Zustandsgleichung Einfluss auf das Gravitationswellensignal, den hypermassiven Neutronenstern und die in das interstellare Medium ausgestoßene Materie besitzt. Mit Hilfe der oben erwähnten Verbesserung im adaptiven Gitterverfahren konnten genaue Aussagen über die Menge an ausgestoßenem Material getroffen werden. Zudem konnte der Prozess, bei dem Material vom System abgegeben wird, genauer untersucht werden. Da weder Magnetfelder noch Neutrinos in unseren Simulationen beschrieben werden, waren nur das hohe Drehmoment und Schocks für den Ausstoß verantwortlich. Weiterhin war es möglich, Simulationen mit den bisher größten Massenverhältnissen durchzuführen. So wurde ein $1.00M_\odot - 1.50M_\odot$, und ein $0.94M_\odot - 1.94M_\odot$ System untersucht. Bei letzterem wurde Materietransfer zwischen den Neutronensternen schon vor dem eigentlichen Zusammenstoß beobachtet.

Abschließend konnte durch die Verbindung von numerischen Simulationen mit semi-analytischen Methoden gezeigt werden, dass ein verbessertes Einkörpermodell, welches vornehmlich von S. Bernuzzi und A. Nagar entwickelt wurde, das Gravitationswellensignal bis zum Zusammenstoß innerhalb der Unsicherheit der numerischen Daten hinreichend genau beschreibt. Die von dem Modell vorhergesagten quasiuniversellen Beziehungen zwischen Gravitationswellenfrequenz, Bindungsenergie, reduziertem Bahndrehimpuls, Gravitationswellenamplitude und bestimmten Tidenkop-

plungskonstanten traten auch in numerischen Simulationen auf. Hervorgerufen wird dies durch die spezielle Form des Potentials im Einkörpermodell und der Abhängigkeit von bestimmten Kopplungskonstanten, was somit einen fundamentalen Zusammenhang des Systems darstellt. Dieser Zusammenhang ist auch nach dem Zusammenstoß im hypermassiven Neutronenstern zu erkennen und kann in Zukunft genutzt werden, um eine semianalytische Beschreibung auch während dieser Phase zu konstruieren.

Selbstständigkeitserklärung

Ich erkläre hiermit, dass ich die vorliegende Arbeit selbständig, ohne unzulässige Hilfe Dritter und ohne Benutzung anderer als der angegebenen Hilfsmittel und Literatur angefertigt habe. Die aus anderen Quellen direkt oder indirekt übernommenen Daten und Konzepte sind unter Angabe der Quelle gekennzeichnet.

Bei der Auswahl und Auswertung dieser Arbeit haben mir die nachstehend aufgeführten Personen in beratender Weise unentgeltlich geholfen:

- Dr. Sebastiano Bernuzzi
- Prof. Bernd Brügmann
- Dipl.-Phys. Marcus Bugner
- Dr. David Hilditch
- Dr. Nathan K. Johnson-McDaniel
- M.Sc. Niclas Moldenhauer
- Dr. Alessandro Nagar
- Prof. Maximiliano Ujevic
- Prof. Wolfgang Tichy
- Dr. Andreas Weyhausen

In Bereichen bei denen auf Arbeit anderer zurückgegriffen wurde, ist dies ausdrücklich in der Arbeit erwähnt. Weitere Personen waren an der inhaltlich-materiellen Erstellung der vorliegenden Arbeit nicht beteiligt. Insbesondere habe ich hierfür nicht die entgeltliche Hilfe von Vermittlungs- bzw. Beratungsdiensten (Promotionsberater oder andere Personen) in Anspruch genommen. Niemand hat von mir unmittelbar oder mittelbar geldwerte Leistungen für Arbeiten erhalten, die im Zusammenhang mit dem Inhalt der vorgelegten Dissertation stehen. Die Arbeit wurde bisher weder im In- noch im Ausland in gleicher oder ähnlicher Form einer anderen Prüfungsbehörde vorgelegt.

Ich versichere ehrenwörtlich, dass ich nach bestem Wissen die reine Wahrheit gesagt und nichts verschwiegen habe.

Jena, 21.09.2015

Unterschrift